NUMERICAL INVESTIGATION OF THE INSTABILITY OF PREMIXED DUMP COMBUSTORS

by

HABIB NASRI NAJM

B.E., Mechanical Engineering
American University of Beirut
(1983)

S.M., Mechanical Engineering
Massachusetts Institute of Technology
(1986)

Submitted to the Department of
Mechanical Engineering
in Partial Fulfillment of the Requirements
for the Degree of

DOCTOR OF PHILOSOPHY

at the

MASSACHUSETTS INSTITUTE OF TECHNOLOGY

June 1989

Signature of Author _____
Department of Mechanical Engineering
May, 1989

Certified by _____
Ahmed F. Ghoniem
Associate Professor, Mechanical Engineering
Thesis Supervisor

Accepted by _____
Ain A. Sonin
Chairman, Departmental Graduate Committee

NUMERICAL INVESTIGATION OF THE INSTABILITY OF PREMIXED DUMP COMBUSTORS

by

HABIB NASRI NAJM

Submitted to the Department of Mecahnical Engineering
in Partial Fulfillment of the
Requirements for the Degree of Doctor of Philosophy
in Mechanical Engineering

ABSTRACT

Currently, the operation of premixed dump combustors, while exhibiting superior performance in efficiency and emission characteristics, is hindered by large amplitude, low frequency oscillations at equivalence ratios close to unity. The genesis of this instability is the subject of investigation in this thesis. A physical model which accounts for the most important components of flow-combustion interactions in this system is formulated assuming that the combustor is an acoustically compact trough, the flow is two dimensional, the flame is a thin front, the inlet section is charged by a constant-pressure reservoir, and the exit manifold is an acoustic oscillator. Numerical solutions at high Reynolds number are obtained using the vortex method.

Solutions of the non-reacting flow show that the dynamics are dominated by a low frequency instability of the type encountered in bluff-body wake flow. The frequency of this instability, which leads to the shedding of large vortex eddies from the recirculation zone, scales with the trough depth and the inlet flow velocity to a Strouhal number O(0.1). In the reacting flow, vorticity-flame-acoustic coupling is clearly observed. Heat release at constant exit pressure, while not appreciably changing the frequency, reduces the amplitude of the oscillations by creating favourable pressure gradients within the combustor. A similar effect is observed when the combustor exit pressure is modulated at frequencies higher than that of the natural mode. However, when the exit pressure is modulated around the frequency of the natural mode, the amplitude of oscillation grows with increasing heat release. This ultimately leads to flow reversal and the propagation of the flame into the inlet channel. Conditions leading to flame flashback conform with the instability requirement as stated by the Rayleigh criterion. The response of the acoustic oscillator to the reacting flow dynamics within the trough is shown to result in pressure modulation at the combustor exit.

Thesis Committee : Prof. A.F. Ghoniem (Chairman)
Prof. T.Y. Toong
Prof. J.A. Fay
Prof. J.R. Baron

to Laura

ACKNOWLEDGEMENTS

I wish to acknowledge the help of Prof. Ahmed Ghoniem in suggesting and guiding this research.

This work has been supported in part by the Air Force Office of Scientific Research Grant AFOSR 84-0356, the National Science Foundation Grant CBT-8709465, and the Department of Energy Grant DE-FG04-87AL44875.

I am particularly indebted to Omar Knio and Luis-Filipe Martins for their insight and criticism during many discussions, as well as their assistance in the preparation and review of this manuscript.

Above all, my family has provided continuous support and encouragement during the past four years. I would like to mention especially my mother-in-law, Jeaninne Kellogg, for the many months of selfless help in caring for our Sami and after our general welfare; and my wife, Laura, for her generous spirit, hard work, and unfailing support.

TABLE OF CONTENTS

1. INTRODUCTION

Since the early 1970's, a considerable amount of combustion and fluids research has been directed towards reducing the pollutant emissions from aircraft gas turbines (Jones, 1978). The major set of pollutants at non-idle engine conditions includes the oxides of Nitrogen, referred to cumulatively as NO_x. The levels of NO_x measured in combustor exhaust are found to increase exponentially with the flame temperature. Consequently, lowering the flame temperature, by enhanced mixing and lean combustion (low equivalence ratio), has been the goal of many investigations (the equivalence ratio of a given fuel/air mixture is: the fuel-to-air ratio in the mixture divided by the stoichiometric fuel-to-air ratio of the specific fuel). Further, in order to avoid local pockets of high fuel concentration, and hence high temperatures, it is important to achieve a "uniform" fuel/air mixture. This uniformity is best achieved if the fuel is vaporized completely during the mixing process. Consequently, combustors employing lean, premixed and prevaporized fuel/air mixtures are expected to achieve the theoretical low limit of NO_x emissions. In this work, we shall refer to these lean-premixed-prevaporized combustors simply as "premixed combustors".

In a typical premixed combustor, the mixture velocity is usually much greater than the flame velocity. Hence, special care has to be taken to anchor the flame in the combustion chamber, and prevent it from being swept away by the incoming flow. This is achieved by having a relatively stagnant region in which a pilot flame can exist and which acts as a continuous source of ignition for the high velocity gases (Cheng & Kovitz, 1957a, 1957b; and Wright & Zukoski, 1962). The separation region behind a bluff body or that downstream of a sudden expansion satisfies these conditions. In particular,

the bluff body configuration is less desirable because of the relatively high pressure drop associated with it. Hence, the typical flow geometry that has been considered in most investigations has been either a backward facing step or a cavity type geometry. (We have chosen the latter, as we shall see later). The common name used for a combustor with such a sudden expansion is a "dump" combustor. Where the "dump" is the cavity or step region.

The problem with premixed dump combustors, however, is their poor stability. Below a certain equivalence ratio, the combustion becomes unstable and "blowout" occurs, i.e. the flame is extinguished. On the other hand, if the equivalence ratio is increased beyond around 0.7, then "flashback" occurs, with the flame moving back into the inlet section. Flashback is associated with large amplitude oscillation in the combustor, and it is a very serious limitation in terms of achieving high power output (see Plee & Mellor, 1978).

Considerable effort has been invested in the understanding of flashback. Unfortunately, however, there has been no consensus on a definite explanation of its nature and the underlying flow dynamics that lead to it. The flow problem is quite complex, involving both the separating reacting flow inside the combustor, and the acoustic response of the system leading to and from the dump section. Consequently, controlling flashback by either passive or active control methods has generally been only partially successful.

While the recirculation zone in the dump is essential to the proper operation of the combustor, it turns out that its associated dynamics are the source of the flashback instability of the combustor, as we shall see later. There is considerable evidence that large scale eddy shedding in the dump section is a significant element of the combustor dynamics. Further, it seems that under conditions of high heat release, or high equivalence ratio, these eddies are energized dramatically to cause large amplitude flapping of the

flame, leading to flashback. Figure 1.1, from Vaneveld et. al. (1982), shows a typical schlieren record of "stable" combustor operation, where the organized large eddy shedding causes considerable modulation of the flame, but no severe flapping. Increasing the equivalence ratio of the incoming mixture causes a transition to different modes of oscillation, and eddy shedding frequencies. The low frequency, large amplitude, flapping mode, which is a precursor to flashback, is the "chucking" shown in Fig. 1.2, also from Vaneveld et. al. (1982). The flame is seen to lift off from the channel floor during a part of the cycle, and move a short distance into the upstream channel, before being convected back into the dump. Flashback involves further amplification of these dynamics, causing the flame to move well into the upstream channel. Figure 1.3, from the same above reference, shows a schlieren record of transition to flashback, caused by a sudden injection of extra fuel into the incoming mixture. This and similar experiments indicating the significance of the modulated recirculation zone eddy shedding to the general combustor dynamics, have prompted this work.

We will be concerned with the numerical investigation of the nature of the flashback instability and the understanding of the underlying flow dynamics leading to it. We shall look first at the non-reacting flow in a 2D cavity-type dump combustor, and then study the full reacting flow in this geometry. Particular emphasis will be given, in the reacting flow case, to the inlet and exit boundary conditions, and the coupling they provide with upstream and downstream system components.

Chapters (2) and (3) deal with the formulation of the analytical model and the numerical solution of the resulting system of equations, respectively. Chapter (4) deals with the non-reacting flow, while Chapter (5) deals with the reacting flow. A literature survey of previous work on the

non-reacting and reacting cavity flow, and general dump combustor flow, is presented in chapters (4) and (5).

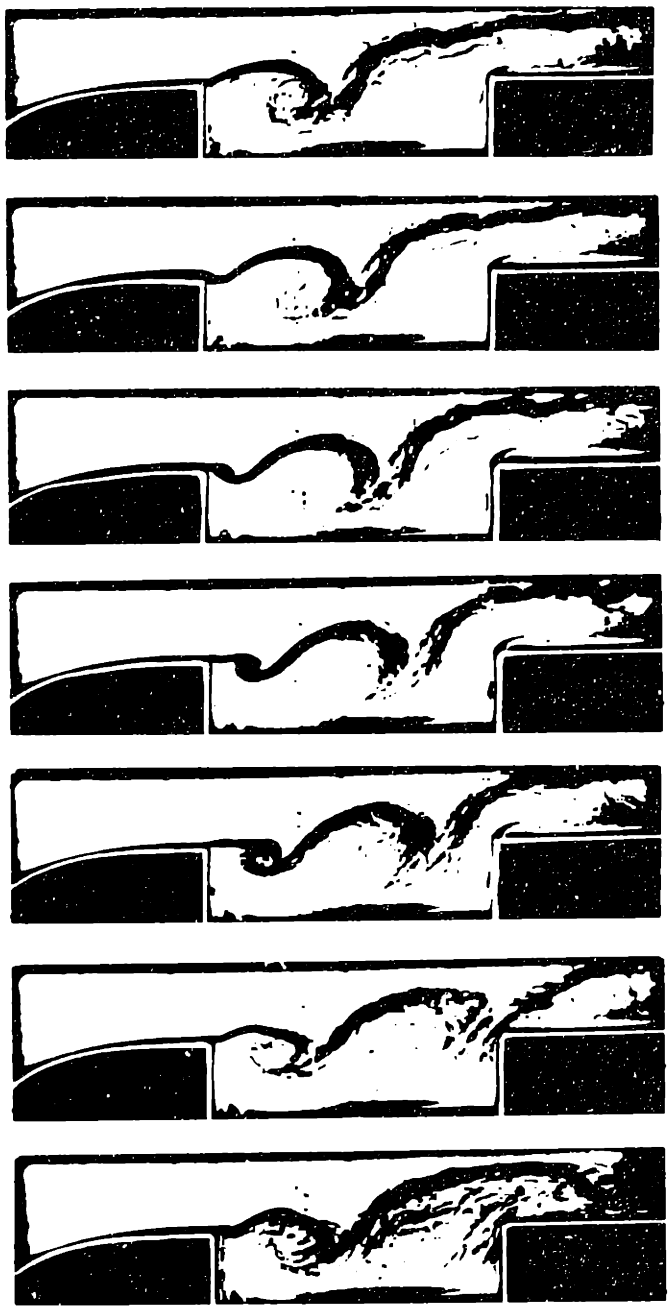

Figure 1.1 Stable combustor operation in a cavity-type dump combustor, from Vaneveld et. al. (1982). Inlet flow velocity = 9.0 m/s, Re=15000. Time interval between frames is 1 ms.

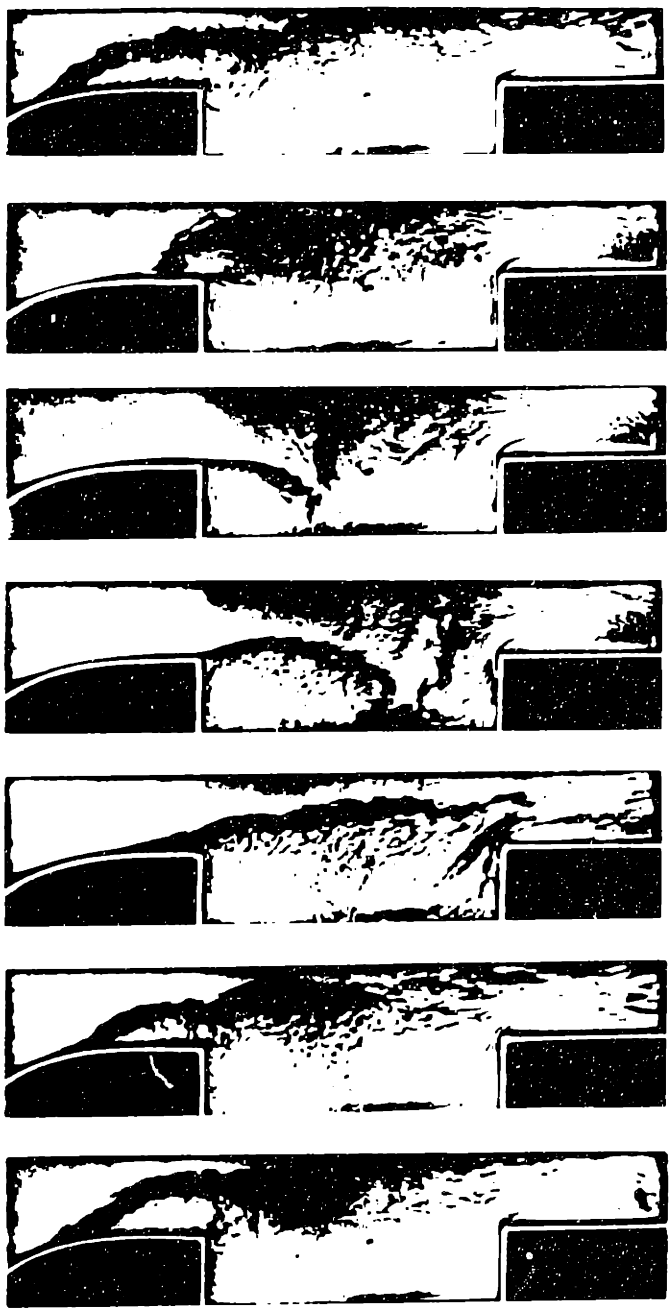

Figure 1.2 Large amplitude flapping of the flame, or "chucking", in a cavity-type dump combustor, from Vaneveld et. al. (1982). Inlet flow velocity = 9.12 m/s, Re=15000. Time interval between frames is 3 ms.

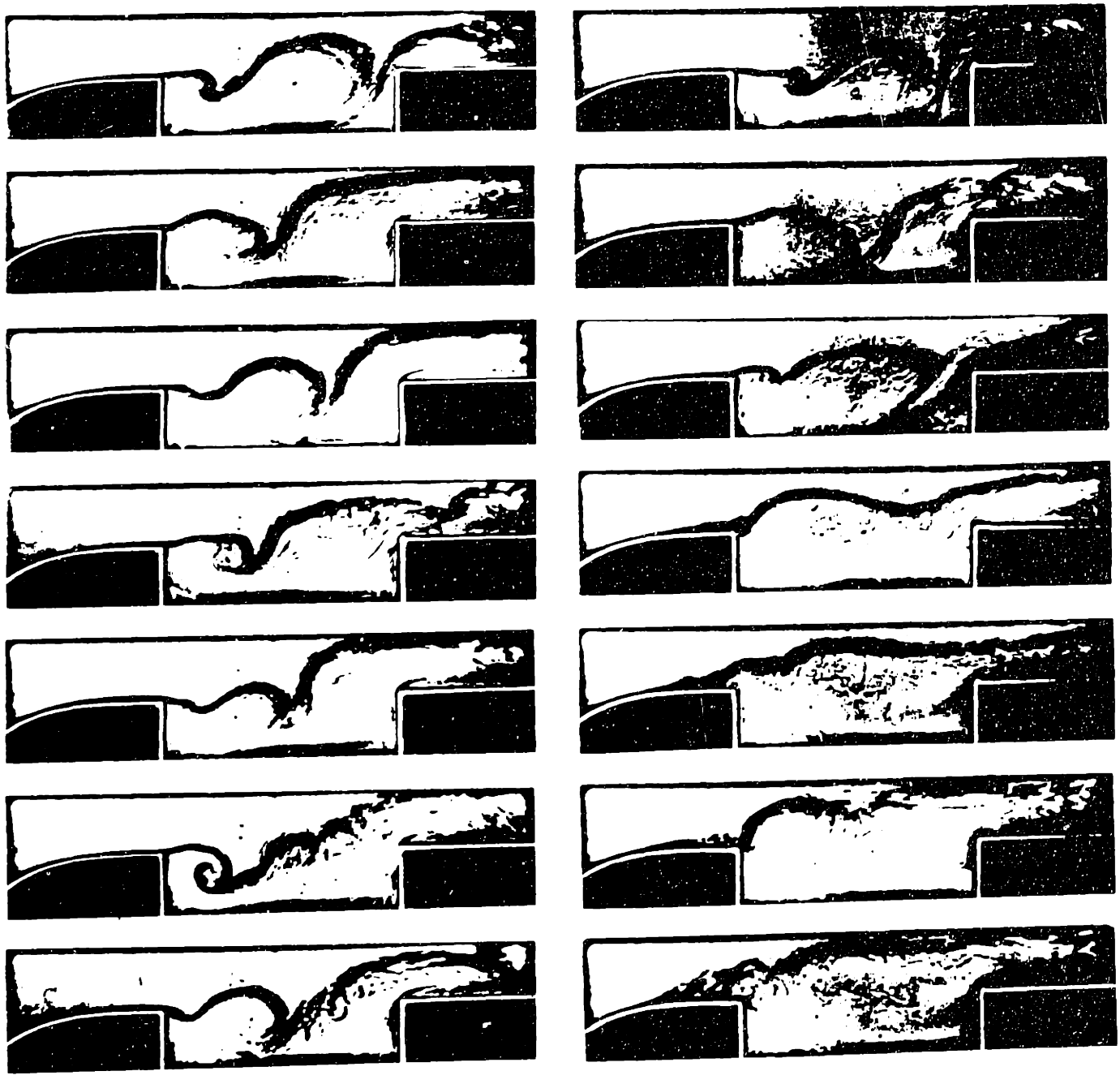

Figure 1.3 Transition to flashback in a cavity-type dump combustor, from Vaneveld et. al. (1982). Inlet flow velocity = 9.0-9.12 m/s, Re=15000. Time interval between frames is 20 ms.

2. FORMULATION - LOW MACH NUMBER, THIN FLAME COMBUSTION IN AN OPEN DOMAIN

2.1 General Equations :

The objective here is to derive a set of differential equations that describe both the flame propagation and the fluid flow in an open domain, given certain restrictive assumptions. An open domain is a domain that is open to the atmosphere, or to some large reservoir.

The discussion below follows earlier works on the topic of "slow" flame propagation in closed or open domains. Landau (1944) was among the first to propose that the flame can be considered, in the limit, as a surface separating the reactants and the products, and hence a hydrodynamic discontinuity. Later work, such as Sivashinsky (1979), combined the assumptions relevant to slow flame propagation (low Mach number), with the hydrodynamic discontinuity concept (thin flame) to derive the full set of equations that govern this flow. Ghoniem et. al (1981), Majda & Sethian (1985), Ghoniem (1986), and Knio (1984) further developed the formulation of these equations with regard to their numerical solution, and provided numerical results using the random vortex method and the SLIC (Simple Line Interface Calculation) algorithm (see also: Noh & Woodward (1976), Chorin (1980), and Barr & Ashurst (1984) concerning SLIC).

We begin by listing the set of equations that govern simple reacting flows, given the starting assumptions discussed below. This is followed by the two fundamental simplifications: the Low Mach number and the thin flame sheet limits, that allow further development of the equations.

We consider a reacting mixture consisting of two "components", reactants R and products P. The rate of reaction, i.e. the rate of burning of reactants, is assumed to be described by a first order, irreversible, unimolecular, single step, Arrhenius-rate reaction law (Strehlow, 1984;

Fristrom & Westenberg, 1965). This is clearly a major simplification, however, its reasonable validity has been demonstrated in the above reported numerical studies of combustion. Fristrom & Westenberg (pp. 324-326) suggest that a simplification that involves an "overall" reaction kinetics concept, similar to that suggested here, may be justified when there is a slow rate-determining step in the reaction which clearly dominates the situation. It should be mentioned, however, that the final result of the formulation is independent of this assumption, since we will ultimately use the laminar burning velocity as a representative of the result of chemical activity. The single step reaction assumption is only used to demonstrate the rigorous derivation of the thin flame model from the general conservation equations.

We further assume that the burnt and unburnt gas mixtures behave as perfect gases with the same molecular weights, and same constant heat conductivities, and specific heats. The viscosity, μ, is allowed to vary as a function of temperature, $\mu=\mu(T)$. The formulation is restricted to two-dimensional cartesian coordinates. Body forces are neglected, and Stokes's hypothesis is assumed to hold, i.e. the bulk viscosity is neglected, hence $p = -\sigma_m$, where p and σ_m are the thermodynamic pressure and the mean stress at a point in the fluid, respectively (Schlichting 1979).

The non-dimensionalized conservation equations that govern this flow are given in Table 2.1. Vector quantities are denoted by bold face print, while tensors are bold and underlined. Equations (2.2-6) form a set of five equations in five gas dynamic variables, namely : density, ρ, concentration of reactants, C, velocity, **u**, pressure, p, and temperature, T. When supplemented with the appropriate initial and boundary conditions, these equations determine the solution uniquely. The reference quantities for non-dimensionalization are defined in Table 2.2. Other dimensional and non-dimensional quantities are defined in Table 2.3. A tilde denotes a

dimensional variable, subscript "u" is for unburnt fluid (reactants) and subscript "b" is for burnt fluid (products). Significant non-dimensional groups are defined in Table 2.4. The derivation of the equations in Table 2.1 is described in detail in appendix A.

TABLE 2.1. GOVERNING EQUATIONS

Reaction : $R \rightarrow P$ (2.1)

Continuity : $\frac{D\rho}{Dt} + \rho \nabla.\mathbf{u} = 0$ (2.2)

Momentum : $\gamma M_o^2 \rho \frac{Du}{Dt} = - \nabla p + \frac{\gamma M_o^2}{Re_o} \nabla.\underline{\tau}$ (2.3)

Energy : $\rho \frac{DT}{Dt} - \frac{\gamma-1}{\gamma} \frac{Dp}{Dt} = - \lambda \nabla.\mathbf{q} + \frac{(\gamma-1)M_o^2}{Re_o} \Phi + \frac{Q}{\lambda} \dot{W}$ (2.4)

Species : $\rho \frac{DC}{Dt} = - \frac{\lambda}{Le_o} \nabla.\mathbf{g} - \frac{1}{\lambda} \dot{W}$ (2.5)

State : $p = \rho T$ (2.6)

where

$$\dot{W} = A\rho C\, e^{-T_a/T} \tag{2.7}$$

$$\underline{\tau} = (\tau_{ij}), \quad \tau_{ij} = \mu\left(\frac{\partial u_i}{\partial x_j} + \frac{\partial u_j}{\partial x_i} - \frac{2}{3}\delta_{ij} \nabla.\mathbf{u} \right)$$

$$\Phi = \mu\left[2\left(\frac{\partial u_1}{\partial x_1}\right)^2 + 2\left(\frac{\partial u_2}{\partial x_2}\right)^2 + \left(\frac{\partial u_1}{\partial x_2} + \frac{\partial u_2}{\partial x_1}\right)^2 - \frac{2}{3}(\nabla.\mathbf{u})^2 \right]$$

$$\mathbf{g} = - d\, \nabla C$$

$$\mathbf{q} = - k\, \nabla T$$

$$\frac{D}{Dt} = \frac{\partial}{\partial t} + \mathbf{u}.\nabla \qquad \text{and} \qquad \nabla = \left(\frac{\partial}{\partial x_1}, \frac{\partial}{\partial x_2}\right)$$

$$\nabla.\underline{\tau} = \frac{\partial \tau_{ij}}{\partial x_j} = \frac{\partial \tau_{i1}}{\partial x_1} + \frac{\partial \tau_{i2}}{\partial x_2}$$

$\delta_{ij} = 1$ for $i=j$, 0 otherwise

TABLE 2.2. REFERENCE QUANTITIES FOR NON-DIMENSIONALIZATION

$\tilde{L}$	reference length, cavity depth (m)
$\tilde{U}$	reference velocity, maximum inlet flow velocity (m/s)
$\tilde{t}_r$	reference time, $\tilde{t}_r = \tilde{L}/\tilde{U}$, (s)
$\tilde{T}_r$	reference temperature (K), chosen here to be the adiabatic flame temperature, $\tilde{T}_r = \tilde{T}_{ui} + \tilde{Q}_i/\tilde{c}_p$, where $\tilde{T}_{ui}$ is the initial (upstream-stagnation) temperature of the reactants, and $\tilde{Q}_i$ is the enthalpy of reaction at $\tilde{T}_{ui}$.
$\tilde{p}_r$	reference pressure (N/m^2), $\tilde{p}_r = \tilde{p}_{atm} = 10^5$ Pa
$\tilde{\rho}_r$	reference density (kg/m^3), here it is chosen to be the density of the products at the reference state $S(\tilde{T}_r, \tilde{p}_r)$, $\tilde{\rho}_r = \tilde{p}_r/R\tilde{T}_r$
$\tilde{d}_r$	reference mass diffusivity of reactants (kg/ms), at $(\tilde{T}_{ui}, \tilde{p}_{ui})$, where $\tilde{p}_{ui}$ is the initial (upstream-stagnation) pressure in the reactants
$\tilde{k}_r$	reference heat conductivity, (J/msK), chosen at $(\tilde{T}_{ui}, \tilde{p}_{ui})$
$\tilde{\mu}_r$	reference dynamic viscosity, (kg/ms), chosen at $(\tilde{T}_{ui}, \tilde{p}_{ui})$

TABLE 2.3 NOMENCLATURE

A normalized frequency factor, $A = \tilde{A}/\tilde{A}_r = \tilde{A}k/(\tilde{\rho}_r \tilde{c}_p \tilde{U}^2)$

$\tilde{c}_p$ specific heat at constant pressure (J/kgK), $\tilde{c}_p = \tilde{R}\gamma/(\gamma-1)$

C mass fraction (concentration) of reactants, dimensionless

d mass diffusivity of reactants, non-dimensional, $d = \tilde{d}/\tilde{d}_r$

$\tilde{E}_a$ activation energy (J/kg)

$\tilde{g}$ diffusive mass flux of reactants (kg/m^2s)

g dimensionless diffusive mass flux of reactants, $g = \tilde{g}\tilde{L}/\tilde{d}_r$

k heat conductivity, nondimensional, $k = \tilde{k}/\tilde{k}_r$

$\tilde{\lambda}$ thermal flame thickness (m), $\tilde{\lambda} = \tilde{k}/(\tilde{c}_p \tilde{U} \tilde{\rho}_r)$

p pressure, $p = \tilde{p}/\tilde{p}_r$

q conductive heat flux, $q = \tilde{q}/\tilde{q}_r = \tilde{q}\tilde{L}/\tilde{k}_r \tilde{T}_r$, $\tilde{q}$:(J/m^2s)

Q enthalpy of reaction, $Q = \tilde{Q}/\tilde{Q}_r = \tilde{Q}/(\tilde{c}_p \tilde{T}_r)$, $\tilde{Q}$:(J/kg)

$\tilde{R}$ gas constant (J/kgK), assumed same for reactants and products

t time, $t = \tilde{t}/\tilde{t}_r$, $\tilde{t}$:(s)

T temperature, $T = \tilde{T}/\tilde{T}_r$, $\tilde{T}$:(K)

T_a non-dimensional activation energy, $T_a = \tilde{E}_a/\tilde{R}\tilde{T}_r$

$\mathbf{u}=(u_1,u_2)$ dimensionless velocity, $\mathbf{u}=\tilde{\mathbf{u}}/\tilde{U}$

$\dot{W}$ dimensionless rate of production of products per unit volume, $\dot{W}=\dot{\tilde{W}}/\dot{\tilde{W}}_r$

i.e. $\dot{W} = \dot{\tilde{W}}\tilde{k}_r/\tilde{\rho}_r^2 \tilde{c}_p \tilde{U}^2$

$\mathbf{x}=(x_1,x_2)$ dimensionless coordinate, $\mathbf{x}=\tilde{\mathbf{x}}/\tilde{L}$

ρ dimensionless density, $\rho=\tilde{\rho}/\tilde{\rho}_r$

γ specific heat ratio $= \tilde{c}_p/\tilde{c}_v$

τ dimensionless shear stress tensor, $\tau = \tilde{\tau}/\tilde{\tau}_r = \tilde{\tau}\tilde{L}/\tilde{\mu}_r \tilde{U}$

Φ dimensionless viscous dissipation function, $\Phi = \tilde{\Phi}/\tilde{\Phi}_r = \tilde{\Phi}\tilde{L}^2/\tilde{\mu}_r \tilde{U}^2$

μ dimensionless dynamic viscosity, $\mu=\tilde{\mu}/\tilde{\mu}_r$

δ_{ij} kronecker delta

TABLE 2.4. NON-DIMENSIONAL GROUPS

Le_o :	Lewis number,	$Le_o = \dfrac{\tilde{k}_r}{\tilde{c}_p \tilde{d}_r}$
λ :	Flame thickness parameter,	$\lambda = \tilde{\lambda}/\tilde{L} = \dfrac{\tilde{k}_r}{\tilde{c}_p \tilde{U} \tilde{\rho}_r \tilde{L}}$
M_o :	Mach number,	$M_o = \dfrac{\tilde{U}}{(\gamma \tilde{R} \tilde{T}_r)^{1/2}}$
Re_o :	Reynolds number,	$Re_o = \dfrac{\tilde{\rho}_r \tilde{U} \tilde{L}}{\tilde{\mu}_r}$
Q :	Enthalpy of reaction,	$Q = \dfrac{\tilde{Q}}{\tilde{c}_p \tilde{T}_r}$
T_a :	Activation energy,	$T_a = \dfrac{\tilde{E}_a}{\tilde{R} \tilde{T}_r}$

2.2 Low Mach Number Limit :

Consider a state of affairs where the significant convective flow time scales are large with respect to the time scale of pressure wave propagation. If this condition is realized, then it can be assumed, to a first order approximation, that the pressure waves generated by the unsteady flow field, and the accompanying exothermic energy deposition of the combustion process are able to balance the pressure in the flow domain fast enough such that the pressure in the hydrodynamic equations may be regarded as an "averaged" quantity over the domain of interest.

If we define the convective time scale as T_c, and the "acoustic" time scale as T_a, then the above approximation is justified when:

$$\tau = T_c/T_a >> 1$$

Further, suppose that the convective dynamics are governed by some velocity u and a length, D, such that $T_c=D/u$. Similarly, write the acoustic time scale in terms of the sonic speed, c, and a relevant length Λ, such that $T_a=\Lambda/c$. In a combustion system consisting of a dump section and of piping leading to and from the dump, we shall see below that the convective length scale, D, is the depth of the dump, while the acoustic length scale, Λ, can include the whole length of the system piping. Using the Mach number M=u/c, we write the above ratio of time scales as :

$$\tau = \frac{D}{\Lambda}\frac{c}{u} = \frac{1}{M\ \Lambda/D}$$

Consequently, the requirements for achieving: $\tau >> 1$, are that (1) the Mach number is much less than unity, and (2) the length scale, D, relevant to the convective dynamics is either comparable with, or larger than, that relevant to the propagation of pressure waves, Λ, in the domain of interest.

In the following, we consider a flow field in a "compact" domain that satisfies both these conditions, and we proceed to simplify the governing equations based on an asymptotic expansion of the gas dynamic variables in terms of the square of the Mach number (see Van Dyke, 1975). The domain considered will include only the dump section, of depth D, with a small length of the inlet and exit channels leading to and from the dump, such that the overall length of the domain is comparable to D.

It is noted that, in the limit of zero Mach number, the present analysis does not require condition (2) above, since $\tau \to \infty$ for $M \to 0$, given a finite domain. However, in any useful real flow, the Mach number is not zero, but has some small value. Consequently, the analysis below is a zeroth order approximation to the actual flow equations. In particular, this approximation removes the Mach number from the flow model. If, however, despite the low Mach number, the flow field considered involves acoustic time scales that are comparable with the convective time scales, such that they play a significant role in the flow dynamics, then a flow model that does not include the speed of sound, and hence the Mach number, is not physically sound. This situation would arise, at $M << 1$, if the flow domain is such that $\Lambda/D >> 1$. In this case, a zeroth order approximation gives an unrealistic model and cannot be used. A higher order approximation is mandatory. Therefore, it should be obvious that the low Mach number model of zeroth order, as derived below and elsewhere, presupposes that, within the domain of interest, acoustic time scales are much smaller than convective time scales, and that they can be neglected. Given this understanding we now proceed to derive the model equations.

The Mach number considered in this work is $M_o = \tilde{U}/(\gamma \tilde{R} \tilde{T}_r)^{1/2}$, where $\tilde{U}$ is the maximum inlet flow velocity, and is always larger than the burning speed of the flame, $\tilde{S}_u$, ($\tilde{U}$~10-20 m/s, while $\tilde{S}_u$~0.5 m/s). Hence, M_o is larger than a

Mach number based on $\tilde{S}_u$, and it is the relevant Mach number to be used in our analysis.

Given that M_o is small, and since it appears in the equations only as $\varepsilon=\gamma M_o^2$, one should be able to expand all the gas dynamic variables in terms of ε. Let ζ denote any gas dynamic variable (ρ,**u**,p,T,...), and:

$$\zeta(\mathbf{x},t) = \zeta_o(\mathbf{x},t) + \varepsilon\zeta_1(\mathbf{x},t) + \varepsilon^2\zeta_2(\mathbf{x},t) + ... \qquad (2.8)$$

Substituting in Eq. (2.3) and gathering terms that are independent of ε, one finds that $\nabla p_o = 0$, which shows immediately that :

$$p_o = p_o(t) \qquad (2.9a)$$

This is the main result of the Low Mach number approximation. The largest component of the pressure is constant throughout the field. This result agrees readily with the assumption that M<<1 since it implies that acoustic waves travel so fast with respect to the motion of the fluid that the largest component of the pressure is equalized virtually instantaneously.

The dependence of p_o on time can be investigated easily for a confined domain by imposing the condition of fixed overall volume, see Ghoniem (1986). p_o is found to change with time due to the heat release associated with combustion.

For an open domain, the boundary conditions depend on the flow configuration both upstream and downstream of the computational domain. If the situation is such that the pressure at the domain boundary is either constant or only "slightly" varying, then we can specify p_o=const in the computational domain with good accuracy. Otherwise, p_o=$p_o(t)$ is specified by the pressure boundary conditions.

Therefore, the specific choice for the boundary conditions on the open domain determines whether p_o in the combustor is constant or a function of time. In the following, we shall assume a flow cofiguration where, for small M_o, the resulting perturbation on p_o imposed at the inlet and exit of the combustor is small enough to be neglected. Note that this does not imply that the variation of the imposed p is negligible. We do allow for imposed pressure perturbations on the boundaries, however we restrict these to be small enough to be lumped into εp_1 ($p=p_o+\varepsilon p_1+\ldots$) and hence affect the flow dynamics primarily through the momentum equation. Let us write, therefore;

$$p_o = \text{constant} \tag{2.9b}$$

We shall refer to p_o as the "base" pressure, it has also been commonly referred to as the "thermodynamic pressure". The second component of the pressure appears in the ε-component of the expansion of the momentum equation:

$$\rho_o \frac{Du_o}{Dt} = - \nabla p_1 + \frac{1}{Re_o} \nabla . \underline{\tau}_o \tag{2.10}$$

where, $\underline{\tau}_o = ((\tau_{ij})_o)$, $(\tau_{ij})_o = \mu_o \left(\frac{\partial (u_o)_i}{\partial x_j} + \frac{\partial (u_o)_j}{\partial x_i} - \frac{2}{3}\delta_{ij} \nabla . u_o \right)$

The pressure p_1 will be referred to as the hydrodynamic pressure. It is generated to balance the changes in momentum within the flow field. Its contribution to the total pressure is restricted by ε.

Applying the same procedure to the energy equation, Eq. (2.4), yields:

$$\rho_o \frac{DT_o}{Dt} = - \lambda \nabla . q_o + \frac{Q}{\lambda} \dot{W} \tag{2.11}$$

where we have used the above assumption, $dp_o/dt=0$. This fact will be implicit throughout the rest of this text.

We conclude from (2.11) that the energy balance is independent of the hydrodynamic pressure (p_1) and that the effect of the hydrodynamic dissipation is neligibly small.

The continuity and species equations and the equation of state, Eqs. (2.2,5, and 6) respectively, retain their forms to the zeroth order in ε. However, as shown by Majda and Sethian (1985), a more convenient form of the continuity equation can be obtained by differentiating Eq. (2.6), and using Eq. (2.2) for $D\rho_o/Dt$ and Eq. (2.11) for DT_o/Dt to obtain:

$$\nabla.\mathbf{u}_o = -\frac{\lambda}{p_o}\nabla.\mathbf{q}_o + \frac{Q}{\lambda p_o}\dot{W} \qquad (2.12)$$

Equation (2.12) defines combustion-hydrodynamics interactions in terms of the volumetric expansion produced by heat release.

The two modes of combustion-hydrodynamics interactions (volumetric expansion and vorticity generation) can be analyzed separately by using the Helmholz decomposition of the velocity field. Following Batchelor (1985), the instantaneous relative motion of the fluid near any point is a combination of (i) an isotropic expansion, (ii) a pure straining motion without change of volume, and (iii) a rigid-body rotation. Let us label these velocity components respectively as $\mathbf{u}_e$, $\mathbf{u}_p$, and $\mathbf{u}_\omega$. These three vector fields are characterized by the following properties,

$\nabla.\mathbf{u}_e = \Delta$, $\nabla x\mathbf{u}_e = 0$, $\mathbf{u}_e$ is defined on an infinite domain. (irrotational)

$\nabla.\mathbf{u}_p = 0$, $\nabla x\mathbf{u}_p = 0$, $\mathbf{u}_p$ is prescribed by the domain boundaries.

(solenoidal and irrotational)

$\nabla.u_\omega = 0$, $\nabla x u_\omega = \omega$, u_ω is defined on an infinite domain.

(solenoidal)

$$u_o = u_e + u_p + u_\omega \tag{2.13}$$

Where, Δ and ω are the local divergence and curl of u_o respectively. The two flow fields, u_e and u_ω, contain no information about the domain boundaries, u_p provides the required correction to have u_o conform to a specified normal velocity at boundaries. In other words:

$$u_p.n = u_o.n - (u_e + u_\omega).n \text{ , along the domain boundaries} \tag{2.13a}$$
$$= - (u_e + u_\omega).n \text{ , along fixed solid boundaries } (u_o.n=0)$$

Further, let us define the vector field $v = u_e + u_p$. Since v is irrotational, it can be expressed in terms of a potential ϕ, where $v = \nabla\phi$, and the equation governing ϕ is obtained by substituting $u_o = v + u_\omega$ into Eq. (2.12):

$$\nabla^2\phi = \frac{1}{p_o} \left(- \lambda \nabla.q_o + \frac{Q}{\lambda} \dot{W} \right) \tag{2.14}$$

Eq. (2.14) defines the first dynamic role of combustion as manifested by the volumetric expansion associated with heat release.

Moreover, taking the curl of Eq. (2.10) and noting that $\nabla x \nabla p_1 = 0$, $\nabla.\omega = 0$, $\omega = \nabla x u_o = \nabla x u_\omega$, and using Eq. (2.2) and the following two vector identities:

$$\nabla x(AxB) = (B.\nabla)A - (A.\nabla)B + A(\nabla.B) - B(\nabla.A)$$

$$\nabla x(\mathbf{A}.\nabla\mathbf{A}) = \nabla x[\ (1/2)\nabla(|\mathbf{A}|^2) - \mathbf{A}x(\nabla x\mathbf{A})\ ] = -\ \nabla x[\mathbf{A}x(\nabla x\mathbf{A})]$$

we obtain the vorticity transport equation in a 2-D, variable density field, where $\boldsymbol{\omega} = (0,0,\omega)$, as follows:

$$\frac{D}{Dt}\left(\frac{\omega}{\rho_o}\right) = -\frac{1}{\rho_o^2 Re_o}\nabla x(\nabla.\underline{\tau}_o) + \frac{1}{\rho_o^3}\nabla\rho_o x\nabla p_1 + \frac{1}{\rho_o^3 Re_o}(\nabla.\underline{\tau}_o)x\nabla\rho_o \qquad (2.15)$$

This equation defines the second part of the dynamic role of combustion. Volumetric expansion establishes a variable density field that causes a baroclinic generation of vorticity within the reaction zone. The appropriate boundary condition on the vorticity equation is $\mathbf{u}.\mathbf{s}(\mathbf{x})=0$ where $\mathbf{s}(\mathbf{x})$ is the tangential unit vector to fixed solid boundaries. This condition is used to generate vorticity along the solid boundaries to satisfy the no-slip boundary condition as explained later in the description of the vortex method.

Finally, since $\nabla.\mathbf{u}_\omega=0$, let us define the stream function ψ such that $\mathbf{u}_\omega=(\partial_2\psi,-\partial_1\psi)$. Consequently, $\nabla x\mathbf{u}_\omega = \boldsymbol{\omega} = (0,0,-\nabla^2\psi)$, or :

$$\nabla^2\psi = -\ \omega \qquad (2.16)$$

The above equations, arrived at through the low Mach number assumption, are reproduced in Table 2.5. All subscripts "o" on the gas dynamic variables will henceforth be removed, and we rewrite p_o and p_1, as P and p respectively.

TABLE 2.5. GOVERNING EQUATIONS FOR COMBUSTION

AT LOW MACH NUMBER IN AN OPEN DOMAIN

WITH CONSTANT BASE PRESSURE

$$\mathbf{u} = \mathbf{v} + \mathbf{u}_\omega, \quad \mathbf{v} = \nabla\phi, \quad \mathbf{u}_\omega = (\partial_2\psi, -\partial_1\psi) \tag{2.17}$$

$$\nabla^2\phi = \frac{1}{P}\left(- \lambda\, \nabla.\mathbf{q} + \frac{Q}{\lambda}\, \dot{W} \right) \tag{2.18}$$

$$\nabla^2\psi = - \omega \tag{2.19}$$

$$\frac{D}{Dt}\left(\frac{\omega}{\rho}\right) = \frac{1}{\rho^2 Re_o}\, \nabla\times(\nabla.\underline{\tau}) + \frac{1}{\rho^3}\, \nabla\rho\times\nabla p + \frac{1}{\rho^3 Re_o}\, (\nabla.\underline{\tau})\times\nabla\rho \tag{2.20}$$

$$\rho\frac{DT}{Dt} = - \lambda\, \nabla.\mathbf{q} + \frac{Q}{\lambda}\, \dot{W} \tag{2.21}$$

$$\rho\frac{DC}{Dt} = - \frac{\lambda}{Le_o}\, \nabla.\mathbf{g} - \frac{1}{\lambda}\, \dot{W} \tag{2.22}$$

$$P = \rho T = \text{constant} \tag{2.23}$$

2.3 Thin Flame Limit :

A useful limit of eqs. (2.17-23) arises when the following two conditions can be satisfied simultaneously : the flame thickness is small compared to the relevant dimension of the flow, and the activation energy is large. At this limit, the flame acts as a hydrodynamic discontinuity between the reactants and the products, see Landau (1944) and Sivashinsky (1979).

Physically, the limit: $\lambda \to 0$ can be achieved by letting $\tilde{k}_r$ tend to zero, (recall the definition of λ); i.e. the heat diffusion at the flame is assumed negligible in the limit of a very thin flame. Consequently, the heat released by the reaction at the flame is carried away primarily by the products of combustion leaving the flame region, and not by conduction. Further, under the condition of $\lambda \to 0$, or an infinitely thin reaction zone, the rate of reaction per unit thickness of the flame must become infinite in order to ensure a finite rate of conversion of reactants into products across the flame surface. Similarly, the significance of the "large" activation energy (T_a) is the compatibility with a narrow region (the flame) where a reaction can occur. In the limit of zero flame thickness, the reaction occurs only at the flame surface, hence the concentration of reactants (C) changes abruptly from 1 to 0 across the flame.

Before we proceed to simplify the equations in Table 2.5 by letting λ tend to zero, we introduce below some useful working relations pertaining to the flame discontinuity.

First, let (ρS) be the mass flow through the flame, and let $\mathbf{u}_f$ be the local velocity of the flame surface. We define $\mathbf{n}_f$ and $\mathbf{s}_f$: the local unit normal and tangent vectors to the flame surface, respectively. Where, $\mathbf{n}_f$ points towards the reactants, and $\mathbf{s}_f$ is oriented such that, looking along its positive direction, the reactants are on the left. Let us decompose $\mathbf{u}_f$ into

its normal (u_{fn}), and tangential (u_{fs}), components: $u_f = u_{fn} + u_{fs}$; where $u_{fn} = u_{fn}n_f$ and $u_{fs} = u_{fs}s_f$. Then, from mass conservation across the flame surface, we have :

$$\rho_u(u_{fn} - u_u.n_f) = \rho_u S_u = \rho_b(u_{fn} - u_b.n_f) = \rho_b S_b = (\rho S) \qquad (2.25)$$

where, ρ_u (ρ_b) is the density of the fluid on the unburnt (burnt) side of the flame surface, u_u (u_b) is the fluid velocity on the unburnt (burnt) side, and S_u (S_b) is the speed of propagation of the flame (by burning normal to itself into the reactants) with respect to a coordinate frame travelling at u_u (u_b), i.e. S_u (S_b) is the normal burning speed of the flame with respect to the reactants (products).

Next, if the set of points $\{\chi_f\}$ is used to construct a surface function $F(x,t)$, such that:

$$\begin{aligned} &F(x,t) = 0 && \text{for the flame surface } x = \chi_f \\ &F(x,t) < 0 && \text{in the reactants} \\ &F(x,t) > 0 && \text{in the products} \end{aligned} \qquad (2.27)$$

then $F(x,t)$ can be used to describe the motion of the flame. An equation that governs the evolution of the surface $F(x,t)=0$ is derived by using, first :

$$u_f = u_u + S_u n_f \qquad (2.28)$$

which is based on eq. (2.25), and on the fact that the flame cannot support any shear, hence that $u_u.s_f = u_f.s_f = u_b.s_f$. Equation (2.28) indicates that the motion of the flame surface is a superposition of advection with the flow

at the velocity u_u and normal propagation into the reactants (by burning) along n_f at a speed S_u.

Then, let $D_f() = \partial()/\partial t + u_f.\nabla()$, be the substantial derivative for an observer moving at the velocity of the flame surface u_f. Since, at this surface, $F(x,t) = 0$ (a constant), then :

$$D_f(F) = \partial F/\partial t + u_f.\nabla F = 0 \qquad \text{at the flame surface}$$

where,

∇F is the gradient vector of $F(x,t)$.
At every point, it is normal to the locus of points F=const and it points in the direction of increasing F.
Hence, at the flame, ∇F is normal to the flame surface, and it points towards the products.

Substituting $u_f = u_u + S_u n_f$ in $D_f(F)=0$, and given that $n_f.\nabla F = -|\nabla F|$, we get :

$$D_u(F) = \frac{\partial F}{\partial t} + u_u.\nabla F = S_u|\nabla F| \tag{2.29}$$

which is the equation governing the evolution of the flame surface by advection and by burning.

Now let us turn back to the governing equations.

A formal limit of these equations can be obtained for $\lambda \to 0$.

We begin by examining eq. (2.22). In the limit as λ tends to zero, the coefficient of the diffusive term $(\nabla.g)$ vanishes, and this term falls out of the equation. We are left with:

$$\rho \frac{DC}{Dt} = -\frac{\dot{W}}{\lambda} \quad , \quad \lambda \to 0 \tag{2.30}$$

As the flame thickness shrinks to zero, we can also write, at the flame :

$$\rho \frac{DC}{Dt} = \rho_u D_u(C) = \rho_b D_b(C) \quad , \quad \lambda \to 0 \tag{2.31}$$

where, $D_u(C) = \partial C/\partial t + \mathbf{u}_u.\nabla C$ ... on the reactants side

and, $D_b(C) = \partial C/\partial t + \mathbf{u}_b.\nabla C$ ... on the products side

and where, in the limit of zero flame thickness, the concentration field is a Heavyside function that goes from 1 in the reactants to 0 in the products at the flame surface, such that $\nabla C = (\partial C/\partial n)\mathbf{n}_f = \delta(x-\chi_f)\mathbf{n}_f$, at the flame.

Let us consider a point on the reactants side of the flame surface. Since, at that point, an observer moving with the flame speed $\mathbf{u}_f$ measures a constant concentration C=1, we have : $\rho_u D_f(C) = 0$. Hence, using eq. (2.28), we have :

$$\rho_u D_f(C) = \rho_u(\ \partial C/\partial t + \mathbf{u}_f.\nabla C\ ) = \rho_u(\ \partial C/\partial t + \mathbf{u}_u.\nabla C + S_u\mathbf{n}_f.\nabla C)$$
$$= \rho_u D_u(C) + \rho_u S_u(\partial C/\partial n) = \rho_u D_u(C) + \rho_u S_u \delta(x-\chi_f) = 0$$

i.e.

$$\rho_u D_u(C) = -\ \rho_u S_u \delta(x-\chi_f)\ ,\quad \lambda \to 0 \tag{2.32}$$

Therefore, using eqs. (2.30-32), we get

$$\lim_{\lambda \to 0} \frac{\dot{w}}{\lambda} = \rho_u S_u\ \delta(x-\chi_f) = (\rho S)\ \delta(x-\chi_f) \tag{2.33}$$

The above argument can alternatively be based on the products side, giving the same result (2.33).

Next, using eq. (2.33), and for $\lambda \to 0$, the equations in Table 2.5 can be reduced to :

$$\nabla^2\phi = \frac{QS_u}{T_u}\ \delta(x-\chi_f) \tag{2.34}$$

$$\rho\frac{DT}{Dt} = \rho_u Q S_u \, \delta(x-\chi_f) \tag{2.35}$$

$$\rho\frac{DC}{Dt} = -\rho_u S_u \, \delta(x-\chi_f) \tag{2.36}$$

Since, from eq. (2.34), $\nabla^2\phi = \nabla.\mathbf{u} = -(D\rho/Dt)/\rho$ is zero everywhere except at the flame surface, then ρ is constant everywhere on either side of the flame: $\rho=\rho_u$ in the reactants, $\rho=\rho_b$ in the products. It then follows from the state equation, $P = \rho T = \text{const}$, and from eq. (2.35), that T is constant on either side of the flame, $T=T_u$ in the reactants, $T=T_b$ in the products. And, $\rho_u/\rho_b = T_b/T_u$. Further, since $\mu=\mu(T)$, then also, $\mu=\mu_u$=const in the reactants, $\mu=\mu_b$=const in the products. Similarly, from (2.36), C is constant everywhere on either side of the flame, C=1 in the reactants, C=0 in the products, as is expected given our argument above.

In dealing with the momentum equation, however, it is first necessary to look more closely at the choice of non-dimensionalization for the viscous terms. In studying viscous dissipation in the vicinity of the flame, the characteristic length $\tilde{L}$ (in Re_o) is not a relevant length scale, instead the more significant length scale in that region is the thickness of the flame reaction zone, $\tilde{\lambda}$. Hence, in the vicinity of the flame, a more appropriate non-dimensionalization would replace $1/Re_o = \tilde{\mu}_r/\tilde{\rho}_r\tilde{U}\tilde{L}$ by λPr_o, where the Prandtl number, Pr_o, is given by:

$$Pr_o = \tilde{\mu}_r\tilde{c}_p/\tilde{k}_r$$

and, as defined earlier,

$$\lambda = \tilde{\lambda}/\tilde{L} = \tilde{k}_r/(\tilde{c}_p\tilde{U}\tilde{\rho}_r\tilde{L})$$

Clearly, λPr_o and $1/Re_o$ are equivalent.

Therefore, the momentum equation in the vicinity of the flame, and more precisely, up to the end of the hydrodyamic structure zone on either side of the flame front, see Sivashinsky (1976), should be as follows :

$$\frac{D}{Dt}\left(-\frac{\omega}{\rho}\right) = \frac{\lambda Pr_o}{\rho^2}\nabla\times(\nabla.\underline{\tau}) + \frac{1}{\rho^3}\nabla\rho\times\nabla p + \frac{\lambda Pr_o}{\rho^3}(\nabla.\underline{\tau})\times\nabla\rho \qquad (2.37)$$

On the other hand, eq. (2.20) is still the proper choice away from the flame front.

Let us now study equations (2.37) and (2.20) in the limit as the flame thickness λ tends to zero. The viscous terms drop out of (2.37) and the only term remaining on the right hand side is the local baroclinic vorticity generation term, $\nabla\rho\times\nabla p/\rho^3$. Further, rearranging terms, we get:

$$\frac{D\omega}{Dt} = -\omega\nabla^2\phi + \frac{\nabla\rho\times\nabla p}{\rho^2}$$

Then, taking the limit as $\lambda\to 0$, and using (by definition):

$$\Omega_f\,\delta(x-\chi_f) = \lim_{\lambda\to 0}\frac{\nabla\rho\times\nabla p}{\rho^2} \qquad (2.38)$$

we get, at the flame surface,

$$\frac{D\omega}{Dt} = \left(\Omega_f - \omega\frac{QS_u}{T_u}\right)\delta(x-\chi_f) \qquad (2.39)$$

Clearly, this indicates that the vorticity field has a discontinuity at the flame surface. In other words, there is a vorticity jump $\delta\omega_{u\to b}$ at the flame surface, between ω_u on the unburnt side and ω_b on the burnt side. i.e.

$$\omega_b - \omega_u = \delta\omega_{u\to b} \qquad \text{at the flame surface} \qquad (2.40)$$

The vorticity jump across a gas dynamic discontinuity in an inviscid flow has been the subject of numerous studies; see for example: Hayes (1957), Matalon & Matkowsky (1982), Emmons (1958), Chung & Law (1984), Pindera & Talbot (1986), and Berndt (1966). We will be satisfied with the statement of the expression for $\delta\omega_{u\to b}$ in the 2-D case following the derivation of Hayes (1957). The required terminology and the resulting expression are as below.

Let "s" be the coordinate along the flame surface, and recall that $(\mathbf{s}_f,\mathbf{n}_f)$ are the unit tangent and normal vectors at the flame surface, respectively. We can write : $\mathbf{u} = \mathbf{u}_n + \mathbf{u}_s$, where $\mathbf{u}$ is the fluid velocity on either side of the flame surface, and $\mathbf{u}_n = u_n\mathbf{n}_f$, $\mathbf{u}_s = u_s\mathbf{s}_f$ are the components of $\mathbf{u}$ normal and tangential to the flame surface, respectively. Note that $(u_s)_u=(u_s)_b=u_s$ along the flame, while $(u_n)_u=\mathbf{u}_u.\mathbf{n}_f$ and $(u_n)_b=\mathbf{u}_b.\mathbf{n}_f$ are not equal, as shown in eq. (2.25) above. Further, recall that $\mathbf{u}_f=\mathbf{u}_{fn}+\mathbf{u}_{fs}$ is the velocity of the flame surface, and let us define the substantial derivative for an observer moving at $\mathbf{u}_{fn}$ as:

$$D_{fn}(\,)=\partial(\,)/\partial t+\mathbf{u}_{fn}.\nabla(\,)$$

Then, according to Hayes (1957), we have :

$$\delta\omega_{u\to b} = \mathbf{n}_f \times [\ \nabla_s(\rho S)\delta(\rho^{-1}) - (\rho S)^{-1}(D_s\mathbf{u}_s + u_{fn}D_s\mathbf{n}_f)\delta(\rho)\ ] \qquad (2.41)$$

where,

$$D_s\mathbf{u}_s = (D_{fn}\mathbf{u}_s)_s + \mathbf{u}_s.\nabla_s\mathbf{u}_s$$

$$D_s\mathbf{n}_f = D_{fn}\mathbf{n}_f + \mathbf{u}_s.\nabla\mathbf{n}_f$$

∇_s = tangential component of ∇

$(\,)_s$ = tangential component of $(\,)$

$\delta\omega_{u\to b} = (\delta\omega_{u\to b})\mathbf{g}_f$, $\mathbf{g}_f = \mathbf{s}_f\times\mathbf{n}_f$

$\delta(\rho^{-1}) = 1/\rho_b - 1/\rho_u$

$$\delta(\rho) = \rho_b - \rho_u$$

At this point then, we conclude that, at the asymptotic limit of low Mach number and small flame thickness, combustion occurs across a sharp discontinuity in an inviscid, non-conducting, non-diffusive, rotational field.

In the outer flow, away from the flame, equation (2.20) can also be simplified, using $\nabla\rho = 0$ and $\nabla\mu = 0$, everywhere, and, $(\rho,\mu)=(\rho_u,\mu_u)$ in the reactants, and $(\rho,\mu)=(\rho_b,\mu_b)$ in the products. The momentum equation becomes,

$$\frac{D\omega}{Dt} = \frac{1}{Re}\nabla^2\omega \qquad (2.42)$$

where, $Re = \rho Re_\sigma/\mu = [\ (\tilde{\rho}/\tilde{\rho}_r)(\tilde{\rho}_r\tilde{U}\tilde{L}/\tilde{\mu}_r)\ ] / (\tilde{\mu}/\tilde{\mu}_r) = \tilde{\rho}\tilde{U}\tilde{L}/\tilde{\mu}$

i.e. $Re = Re_u = \tilde{\rho}_u\tilde{U}\tilde{L}/\tilde{\mu}_u$ in the reactants

$Re = Re_b = \tilde{\rho}_b\tilde{U}\tilde{L}/\tilde{\mu}_b$ in the products

Therefore, in the limit of low Mach number and thin flame in an open domain with constant base pressure P, the flow is essentially incompressible, viscous, on either side of the flame. The relevant governing equations for the whole flow field are listed in Table 2.6. In this table, we included an initial condition on the vorticity field and on the flame interface, as well as boundary conditions on the velocity along ∂D, the domain boundary.

TABLE 2.6. GOVERNING EQUATIONS FOR LOW MACH NUMBER THIN FLAME COMBUSTION IN AN OPEN DOMAIN WITH CONSTANT BASE PRESSURE

$$\frac{D\omega}{Dt} = \frac{1}{Re_u} \nabla^2\omega \qquad \text{in the reactants} \qquad (2.43)$$

$$\frac{D\omega}{Dt} = \frac{1}{Re_b} \nabla^2\omega \qquad \text{in the products} \qquad (2.44)$$

$$\omega_b - \omega_u = \delta\omega_{u\to b} \qquad \text{at the flame surface, see (2.41)} \qquad (2.45)$$

$$\mathbf{u} = \mathbf{v} + \mathbf{u}_\omega, \quad \mathbf{v} = \nabla\phi, \quad \mathbf{u}_\omega = (\partial_2\psi, -\partial_1\psi) \qquad (2.46)$$

$$\nabla^2\psi = -\omega \qquad (2.47)$$

$$\nabla^2\phi = \frac{QS_u}{T_u} \delta(x-X_f) \qquad (2.48)$$

$$\frac{\partial F}{\partial t} + \mathbf{u}_u \cdot \nabla F = S_u |\nabla F| \qquad (2.49)$$

P=constant everywhere (base pressure)

$(\rho, T, C) = (\rho_u, T_u, 1)$ in the reactants, $(\rho_b, T_b, 0)$ in the products

$$Re_u = \tilde{\rho}_u \tilde{U} \tilde{L} / \tilde{\mu}_u, \quad Re_b = \tilde{\rho}_b \tilde{U} \tilde{L} / \tilde{\mu}_b \qquad (2.50)$$

$\omega(\mathbf{x},0) = \omega_o(\mathbf{x})$

$X_f(0) = X_{fo}$

$\mathbf{u}(\mathbf{x},t) = (u_n, u_s)$ on ∂D

3. NUMERICAL SOLUTION

3.1 General Description:

The numerical solution of the equations in Table 2.6, as implemented in this study, combines the Random Vortex Method (RVM) for incompressible, viscous, 2D flow, with the Simple Line Interface Calculation (SLIC) algorithm for the propagation of the flame interface.

The two solutions are coupled by, (1) the advection part of the flame motion which uses the velocity field computed by the RVM to propagate the flame interface, and (2) the expansion field due to the heat release resulting from burning at the flame front, which contributes to the flow field computation by the RVM. A third coupling mechanism: the generation of vorticity at the flame front, is neglected.

The flow domain is a 2D cavity-in-channel geometry, as shown in Fig. 3.1. This simple geometry is intended to model the essential flow characteristics of a dump combustor. The premixed fuel and air come in from the left at xmin, they expand into the combustion chamber, the dump or cavity, and they exit through a constriction, nozzle, and leave the domain at xmax. The dump serves to stabilize the flame by anchoring it at the separation point at the upstream edge of the cavity. This stabilization is due to the separating-recirculating flow that exists in the cavity. The inlet and exit boundary conditions are critical to the validity of the flow model in simulating the operation of an actual premixed combustor. These will be discussed separately below.

As indicated in Ch. 2 and above, the fluid flow solution will use an incompressible viscous model, where the only knowledge about the burning comes from an expansion field located at the flame, and from the different Reynolds number used in the reactants and the products. Hence, the

formulation of the random vortex method, as described below, will proceed without much regard for the combustion, except for these two effects.

The combustion solution is described next, followed by a discussion of the inlet and exit boundary flow problems, and an overview of the complete solution algorithm.

3.2 Fluid Flow - Random Vortex Method:

In the Random Vortex Method solution, the vorticity field is discretized into a finite number of vortex elements whose configuration is updated every time step according to the flow equations. A Lagrangian formulation is employed, whereby advection is expressed in terms of a set of coupled ordinary differential equations while diffusion is simulated by an appropriate random walk algorithm. Numerical diffusion is minimized by avoiding the discretization of velocity gradients on a grid. The scheme is grid-free and the computations are self adaptive since vortex elements move to capture zones of large velocity gradients associated with concentration of vorticity. The degree of refinement in the discretization of the continuous vorticity field into a finite number of discrete vortex elements imposes a certain smallest resolved length scale, while the time step used in updating the vorticity field imposes a minimum time scale. The accuracy of the method in 2D high Reynolds number flows has been checked against well documented experimental data (see Najm & Ghoniem (1987), Ghoniem & Ng (1987)).

For a historical survey of the development of the random vortex method, see Ghoniem and Gagnon (1987).

In the following, we proceed to demonstrate the application of the method to the fluid flow equations listed in Table 2.6, on the computational domain D. These equations are as follows :

$$D\omega/Dt = \partial\omega/\partial t + \mathbf{u}.\nabla\omega = (1/Re)\ \nabla^2\omega \tag{3.1}$$

$$\omega = \partial u_2/\partial x - \partial u_1/\partial y \tag{3.2}$$

$$\mathbf{u} = \mathbf{v} + \mathbf{u}_\omega, \quad \mathbf{v} = \nabla\phi, \quad \mathbf{u}_\omega = (\partial\psi/\partial y, -\partial\psi/\partial x) \tag{3.3}$$

$$\nabla^2\psi = -\omega \tag{3.4}$$

$$\nabla^2\phi = (QS_u/T_u)\ \delta(\mathbf{x}-\mathbf{X}_f) \tag{3.5}$$

$$\mathbf{u} = (u_n, u_s) \text{ on } \partial D \tag{3.6a}$$

$$\omega(\mathbf{x},0) = \omega_o(\mathbf{x}) \tag{3.6b}$$

$$\chi_f(0) = \chi_{fo} \tag{3.6c}$$

We have used Re for the Reynolds number with the understanding that a different value (Re_u or Re_b) is implied depending on whether we are in the reactants or the products, respectively. Recall also that $\mathbf{u}_\omega$ is defined on an infinite (simply connected) domain, while $\mathbf{v}$ includes the required correction for the domain boundaries.

The solution of the flow equations proceeds differently for the interior region than for the no-slip "wall region". We will use the technique of viscous splitting (Beale & Majda, 1981) to break the vorticity transport equation in each region into an advection equation and a diffusion equation. The solution in the wall region will then be matched to the solution obtained in the interior to produce the full flow. In the following, we consider the solution method for each of these flow regions separately, and describe the matching of the two solutions.

3.2.1 Interior Flow:

The method of viscous splitting is applied to the vorticity transport equation (3.1) in the interior. This equation is solved, and the vorticity field is updated, at every time step, using two fractional steps: an advection step and a diffusion step. In the former, the vorticity field is updated according to the inviscid version of eq. (3.1), namely :

$$\partial\omega/\partial t + \mathbf{u}.\nabla\omega = 0 \tag{3.7}$$

along with eq's (3.2-5,3.6b&c) and the boundary condition $\mathbf{u}.\mathbf{n} = u_n$, on ∂D, where $\mathbf{n}$ is the unit outward normal to ∂D. We then update the vorticity by the diffusion step, which refers to the solution of the equation :

$$\partial\omega/\partial t = (1/Re)\nabla^2\omega \tag{3.8}$$

This is eq. (3.1) with $\mathbf{u}=\mathbf{0}$.

Combining these two solutions provides a solution of (3.1) in the interior. Let us now consider each fractional step individually.

3.2.1.1 Advection:

Let us list again the relevant equations for the (inviscid) advection of the vorticity field in the domain interior. These are :

$$D\omega/Dt = \partial\omega/\partial t + \mathbf{u}.\nabla\omega = 0 \tag{3.9}$$

$$\omega = \partial u_2/\partial x - \partial u_1/\partial y = \nabla x u \tag{3.10}$$

$$\mathbf{u} = \mathbf{v} + \mathbf{u}_\omega \tag{3.11}$$

$$\mathbf{v} = \nabla\phi \tag{3.12}$$

$$\mathbf{u}_\omega = (\partial\psi/\partial y, -\partial\psi/\partial x) \tag{3.13}$$

$$\nabla^2\psi = -\omega \tag{3.14}$$

$$\nabla^2\phi = (QS_u/T_u)\ \delta(x-\chi_f) \tag{3.15}$$

$$u.n = u_n \quad \text{on } \partial D \tag{3.16a}$$

$$\omega(x,0) = \omega_o(x) \tag{3.16b}$$

$$\chi_f(0) = \chi_{fo} \tag{3.16c}$$

Equation (3.9) is simply a statement of the Helmholz theorem, namely that, in an inviscid flow, the vorticity is advected along particle paths. Its solution follows immediately from the knowledge of the velocity field (u) at every point in the fluid. Therefore, the main issue here is the determination of the velocity u from eq's (3.11-15) and the boundary and initial conditions (3.16). Let us discuss the solution for each of $\mathbf{u}_\omega$ and v separately. Recall that $\mathbf{u}_\omega$, the solution of eq's (3.13,3.14), is the inviscid velocity field due to a specified distribution of vorticity in an unbounded, simply connected, domain, while v, the solution of eq's (3.12,3.15), is the potential flow corresponding to specified volume fluxes at the domain boundaries and to a specified source field at the flame interface. The sum of these two velocity components gives the required velocity u to be used in

advecting the vorticity field. We begin below by looking at the solution for u_ω.

3.A Inviscid Flow Field due to a Specified Vorticity Field in a Simply Connected Unbounded Domain

The solution of the Poisson equation (3.14) in a simply connected unbounded fluid domain at rest at infinity is given in terms of the Green function of the Poisson equation (F. John, 1982, p. 151):

$$\psi(\mathbf{x},t) = \int G(\mathbf{x}-\mathbf{x}')\,\omega(\mathbf{x}',t)\,d\mathbf{x}' \tag{3.17}$$

where $d\mathbf{x}' = dx'dy'$, and, for a general vector argument $\mathbf{x} = (x,y)$,

$$G(\mathbf{x}) = -(1/2\pi)\,\ln(r), \qquad r = |\mathbf{x}| \tag{3.18}$$

The integration is performed over the area where ω is nonzero. The velocity distribution is recovered by substituting eq. (3.17) into eq. (3.13):

$$\mathbf{u}_\omega(\mathbf{x},t) = \int \mathbf{K}(\mathbf{x}-\mathbf{x}')\,\omega(\mathbf{x}',t)\,d\mathbf{x}' = \mathbf{K}(\mathbf{x})*\omega(\mathbf{x},t) \tag{3.19}$$

where,

$$\mathbf{K}(\mathbf{x}-\mathbf{x}') = \left(\partial G(\mathbf{x}-\mathbf{x}')/\partial y \;,\; -\partial G(\mathbf{x}-\mathbf{x}')/\partial x \right)$$
$$= -(1/2\pi)\,\left(y-y' \;,\; -(x-x') \right) \,/\, |\mathbf{x}-\mathbf{x}'|^2$$

or, for a general vector argument $\mathbf{x} = (x,y)$,

$$\mathbf{K}(\mathbf{x}) = -(1/2\pi)\,(y,-x)/r^2, \qquad r=|\mathbf{x}| \tag{3.20}$$

$\mathbf{K}$ is the integral kernel of the Poisson equation, and * denotes convolution. In the Lagrangian description of the flow, we follow the motion of material

points. Let us write $\chi(\alpha,t) = (x(t),y(t)) = x(t)$ for the trajectory followed by the particle which is at point $\alpha = (\alpha_1,\alpha_2)$ at time t=0 (α_1 and α_2 are the "Lagrangian coordinates" of the particle). Hence, the map $\alpha \to \chi(\alpha,t)$ (the fluid flow map) advances each fluid particle from its position at time t=0 to its position at time t. From the definition of the velocity field of the fluid:

$$\frac{Dx(t)}{Dt} = \frac{\partial \chi(\alpha,t)}{\partial t} = u_\omega(\chi(\alpha,t),t), \quad \chi(\alpha,0) = \alpha \tag{3.21}$$

Further, using eq. (3.9), we have : $\omega(\chi(\alpha,t),t) = \omega(\alpha,0)$, or, equivalently, $\partial\omega(\chi(\alpha,t),t)/\partial t = 0$ (see also Chorin & Marsden, 1979, p.34). Given this fact, and since the flow is incompressible, we can write the right hand side of eq. (3.21), based on eq. (3.19), as follows:

$$\begin{aligned} u_\omega(x,t) = u_\omega(\chi(\alpha,t),t) &= \int K[\chi(\alpha,t)-\chi(\alpha',t)]\ \omega(\chi(\alpha',t),t)\ J(\alpha',t)\ d\alpha' \\ &= \int K[\chi(\alpha,t)-\chi(\alpha',t)]\ \omega(\chi(\alpha',t),t)\ d\alpha' \\ &= \int K[\chi(\alpha,t)-\chi(\alpha',t)]\ \omega(\alpha',0)\ d\alpha' \end{aligned} \tag{3.22}$$

where, $J(\alpha,t)$ is the Jacobian of the fluid flow map and $J = 1$ for an incompressible fluid (Chorin & Marsden, 1979, p.14). Eq. (3.21) is a set of uncountably many ordinary differential equations which, when supplemented with eq. (3.22), provides a solution of the Euler equations in the unbounded domain. In order to reduce this to a finite number of equations, we will use the standard Riemann sum approximation (Greenberg, 1978) to the integral in eq. (3.22). Therefore,

$$\begin{aligned} u_\omega(x,t) \sim \hat{u}_\omega(x,t) &= \sum_{j=1}^{N} K[x-\hat{\chi}_j(\alpha_j,t)]\ \Gamma_j = \sum_{j=1}^{N} K(x-x_j)\Gamma_j \\ &= \frac{1}{2\pi}\sum_{j=1}^{N} \Gamma_j \frac{[\ -(y(t)-y_j(t))\ ,\ x(t)-x_j(t)\ ]}{|x-x_j|^2} \end{aligned} \tag{3.23}$$

where we have used $x_j = x_j(t) = (x_j(t), y_j(t)) = \hat{\chi}_j(\alpha_j, t)$, and where :

$$\Gamma_j = \omega(\alpha_j, 0)\delta A_j \tag{3.24}$$

and α_j is the centroid of the area element δA_j, belonging to the grid introduced in the α plane to partition the region where $\omega(\alpha, 0)$ is nonzero.

Now let, $g(x) = \sum_{j=1}^{N} \delta(x - x_j)\Gamma_j$, where δ is the Dirac Delta function. Then, since $K(x - x_j) = \int \delta[(x - x_j) - x']\, K(x')\, dx'$, we have :

$$\begin{aligned} K(x) * g(x) = [K*g](x) = [g*K](x) &= \sum_{j=1}^{N} \Gamma_j \int \delta[(x - x_j) - x']\, K(x')\, dx' \\ &= \sum_{j=1}^{N} K(x - x_j)\Gamma_j \end{aligned} \tag{3.25}$$

Hence, by eq. (3.23), we have:

$$\hat{u}_\omega(x,t) = \sum_{j=1}^{N} \hat{u}_\omega^j(x,t) = K(x) * \left(\sum_{j=1}^{N} \delta(x - x_j)\Gamma_j \right) \tag{3.26}$$

Then, comparison with eq. (3.19) gives that $\hat{u}_\omega(x,t)$ is the velocity corresponding to a collection of point vortices with circulation Γ_j and coordinates $x_j(t) = \hat{\chi}_j(\alpha_j, t)$, i.e.,

$$\omega(x,t) = \sum_{j=1}^{N} \delta(x - x_j)\ \Gamma_j \tag{3.27}$$

In eq. (3.23), the expression for $\hat{u}_\omega^j(x,t)$ is the well known Biot-Savart law for the velocity induced by a straight line vortex (Batchelor, 1985)

Therefore, one possible numerical method for solving Euler's equation in an unbounded domain consists of replacing eq. (3.21) by the system of ordinary differential equations:

$$\frac{Dx_i}{Dt} = \frac{\partial \hat{\chi}_i(\alpha_i, t)}{\partial t} = \hat{u}_{\omega,i}(t), \qquad \hat{\chi}_i(\alpha_i, 0) = \alpha_i \tag{3.28}$$

where, $\hat{u}_{\omega,i}(t)$, from (3.23), is the velocity induced by the contribution of all point vortices at point vortex i. Since a point vortex in our 2D model represents a straight line vortex in 3D space, then it does not induce a velocity on itself (Batchelor, 1985, p.511), and we have :

$$\hat{u}_{\omega,i}(t) = \sum_{\substack{j=1 \\ j\neq i}}^{N} \hat{u}^{j}_{\omega,i}(t) = \sum_{\substack{j=1 \\ j\neq i}}^{N} \Gamma_j \, K(x_i - x_j)$$

$$= \frac{1}{2\pi} \sum_{\substack{j=1 \\ j\neq i}}^{N} \Gamma_j \, \frac{[\, -(y_i(t)-y_j(t)) \, , \, x_i(t)-x_j(t) \,]}{|x_i - x_j|^2} \qquad (3.29)$$

with $x_i = \hat{\chi}_i(\alpha_i,t) = (x_i(t),y_i(t))$, $x_j = \hat{\chi}_j(\alpha_j,t) = (x_j(t),y_j(t))$, and where N is the total number of point vortices. Thus, at each instant, the $\hat{\chi}_j$'s should approximate the exact coordinates χ_j's of the point vortices if the method is to converge. The algorithm (3.28,3.29) is called the point vortex method. It was introduced by Rosenhead (1932) to study the behavior of vortex sheets.

Since the kernel $K(x)$ is singular at $x=0$, the velocity, $\hat{u}_{\omega,i}$, tends to infinity as the distance between the point vortices approaches zero. This can cause the method to break down. To see how this happens, consider an approximation to a vortex tube consisting of a large number of point vortices (vortex lines when extended in the third dimension). Following eqs. (3.28,3.29), it can be seen that, when separated from one another by a short distance, the vortices will wind around each other because of the singularities on the right hand side of those equations. This was confirmed computationaly by Kuwahara & Takami (1973). The standard point vortex method of Rosenhead thus fails due to a spurious interaction of vortices at close

range. To overcome this difficulty, Chorin (1972) first suggested that "blobs" of finite area, rather than points of vorticity, be considered. Hence, eq. (3.27) is modified to :

$$\omega(\mathbf{x},t) = \sum_{j=1}^{N} \Gamma_j \, f_\delta(\mathbf{x}-\mathbf{x}_j) \tag{3.30}$$

where the "core function" f_δ is a radially symmetric function of small support, such that $\int f_\delta d\mathbf{x}=1$, and where,

$$f_\delta(\mathbf{x}) = \delta^{-2} \, f(r/\delta), \qquad r = |\mathbf{x}| \tag{3.30a}$$

Thus, f_δ, which has the dimension of (1/area), approximates the 2D Dirac delta function as $\delta \to 0$. The "core radius", δ, represents the cutoff radius such that f_δ is "small" or zero for $r > \delta$.

It is worthwhile noting a few points about δ and f_δ before we proceed. In order to approximate a given continuous vorticity distribution accurately, 2δ is often chosen to be larger than the separation between the centers of adjacent discrete vortex elements (Ghoniem & Gagnon, 1987). This allows for a margin of overlap between vortex elements. Further, the core function, f, plays a similar role as interpolating polynomials in finite difference schemes and base functions in finite-element formulations. By requiring f to be radially symmetric, the approximation in eq. (3.30) is at least second order (Hald, 1985).

With the introduction of the cutoff function, the velocity field (3.26) for the point vortex method is then replaced by :

$$\hat{\mathbf{u}}_\omega(\mathbf{x},t) = \mathbf{K}(\mathbf{x}) * \sum_{j=1}^{N} f_\delta(\mathbf{x}-\mathbf{x}_j)\Gamma_j = \mathbf{K}(\mathbf{x}) * \omega(\mathbf{x},t) \tag{3.31}$$

or,

$$\hat{u}_{\omega}(x,t) = \sum_{j=1}^{N} K_{\delta}(x-x_j)\ \Gamma_j \tag{3.32}$$

where, $x = \hat{X}(\alpha,t)$, $x_j = \hat{X}_j(\alpha_j,t)$, and :

$$K_{\delta}(x-x_j) = K(x)*f_{\delta}(x-x_j) = \int K(x-x')\ f_{\delta}(x'-x_j)\ dx' \tag{3.33}$$

Hence, the kernel $K(x)$ is replaced by a smoothed kernel $K_{\delta}(x)$ which is bounded at $x=0$, such that (Ghoniem & Gagnon, 1987):

$$K_{\delta}(x) = -\frac{1}{2\pi}\ \frac{(y,-x)}{r^2}\ \kappa(r/\delta) \tag{3.34}$$

with,

$$\kappa(r) = 2\pi \int_0^r r'\ f(r')\ dr' \tag{3.35}$$

We can then compute the vortex element trajectories by solving the system of ordinary differential equations (3.28). From eq. (3.32), the velocity at the center of the vortex element (blob) i due to all the other vortex elements j is equal to :

$$\hat{u}_{\omega,i}(t) = \sum_{\substack{j=1 \\ j\neq i}}^{N} \hat{u}^{j}_{\omega,i}(t) = \sum_{\substack{j=1 \\ j\neq i}}^{N} \Gamma_j\ K_{\delta}(x_i-x_j) \tag{3.36}$$

The algorithm (3.28,3.36) is called the <u>vortex element method</u>. From eq. (3.30) we have Chorin's interpretation of the vortex method (Chorin, 1972), namely, that the vorticity is approximated by a sum of vortex elements (blobs) of common shape f_{δ} centered at $x_j(t) = \hat{X}(\alpha_j,t)$, and with strength Γ_j.

We shall use the vortex core function suggested by Chorin (1972), defined by:

$$f(r) = \begin{cases} 1/2\pi r \\ 0 \end{cases} \quad \text{and} \quad K(r) = \begin{cases} r & \text{for } r \le 1 \\ 1 & \text{for } r > 1 \end{cases} \tag{3.37}$$

Consequently, the velocity at (x,t) due to blob j, using eq. (3.32), is :

$$\hat{u}^j_\omega(x,t) = \Gamma_j K_\delta(x-x_j) = \begin{cases} \dfrac{-\Gamma_j}{2\delta\pi} \dfrac{(y-y_j, x_j-x)}{|x-x_j|} & r \le \delta \\ \dfrac{-\Gamma_j}{2\pi} \dfrac{(y-y_j, x_j-x)}{|x-x_j|^2} & r > \delta \end{cases} \tag{3.38}$$

or, in polar coordinates (r,θ), with origin at $x_j(t)$,

$$\hat{u}^j_\omega(r,\theta) = \hat{u}^j_\omega(r) = (u_r, u_\theta) = \begin{cases} (0, \Gamma_j/2\delta\pi) & r \le \delta \\ (0, \Gamma_j/2\pi r) & r > \delta \end{cases} \tag{3.39}$$

Therefore, for $r > \delta$, the velocity field induced by a vortex blob of strength Γ_j at x_j is identical to that due to a point vortex of the same strength and location. For $r \le \delta$, the velocity is constant at the value $\Gamma_j/2\delta\pi$ corresponding to $r = \delta$, which is the maximum velocity induced by the vortex.

The vorticity distribution corresponding to the above velocity field due to vortex element j is found to be :

$$\omega_j(r,\theta) = \omega_j(r) = \begin{cases} \Gamma_j/2\delta\pi r & \text{for} \quad r \le \delta \\ 0 & \text{for} \quad r > \delta \end{cases} \tag{3.40}$$

The stream function associated with this velocity field is :

$$\psi_j(r,\theta) = \psi_j(r) = \begin{cases} (\Gamma_j/2\pi)\ (1-r/\delta) & \text{for} \quad r \le \delta \\ (-\Gamma_j/2\pi)\ \ln(r/\delta) & \text{for} \quad r > \delta \end{cases} \tag{3.41}$$

3.B Potential FLow

The potential flow problem involves the solution of eq's (3.12,3.15) using the boundary condition (3.16a). These equations are repeated below for convenience :

$$\mathbf{v} = \nabla\phi \tag{3.12}$$

$$\nabla^2\phi = (QS_u/T_u)\ \delta(\mathbf{x}-\chi_f) \tag{3.15}$$

$$\mathbf{u}.\mathbf{n} = u_n \quad \text{on } \partial D \tag{3.16a}$$

where, $\mathbf{u} = \mathbf{v} + \mathbf{u}_\omega$, $u_n = 0$ on fixed solid walls, $u_n = u_{in}$ far upstream in the inlet channel, and $u_n = u_{out}$ far downstream in the exit channel.

Given $\mathbf{u}_\omega$, (we drop the "^" in the remainder of this text), the condition (3.16a) can be written :

$$\mathbf{v}.\mathbf{n} = \nabla\phi.\mathbf{n} = u_n - \mathbf{u}_\omega.\mathbf{n} \tag{3.42}$$

On the other hand, in order to deal with the right hand side of eq. (3.15) it is useful to recall the splitting of the potential flow field $\mathbf{v}$ into the two potential flow fields $\mathbf{u}_e$ and $\mathbf{u}_p$, eq. (2.13) above. Namely,

$$\mathbf{v} = \mathbf{u}_e + \mathbf{u}_p \tag{3.42a}$$

where,

$\nabla.\mathbf{u}_e \neq 0$, defined on an unbounded (simply connected) domain

$\nabla.\mathbf{u}_p = 0$, prescribed by the domain boundaries

Therefore, let $\mathbf{u}_e = \nabla\phi_e$, and $\mathbf{u}_p = \nabla\phi_p$, then split the above problem into two problems as follows :

$$\phi = \phi_e + \phi_p$$

$$\mathbf{v} = \nabla\phi = \nabla\phi_e + \nabla\phi_p = \mathbf{u}_e + \mathbf{u}_p$$

where ϕ_e is the solution of :

$$\nabla^2\phi_e = (QS_u/T_u)\ \delta(\mathbf{x}-\chi_f) \tag{3.42b}$$

on an unbounded simply connected domain. (The χ_f are bounded so that $\nabla\phi_e \to 0$ as $\mathbf{x}\to\infty$). While ϕ_p is the solution of :

$$\begin{aligned} &\nabla^2\phi_p = 0 && \text{on the domain D} \\ &\mathbf{u}_p.\mathbf{n} = \nabla\phi_p.\mathbf{n} = u_n - \mathbf{u}_\omega.\mathbf{n} - \mathbf{u}_e.\mathbf{n} && \text{on } \partial D \end{aligned} \tag{3.42c}$$

From the specification of the two problems, it is clear that ϕ, the sum of the two potentials, satisfies the initial problem (3.15,3.42).

The solution of (3.42b) is described in Appendix C. The flow field $\mathbf{u}_e$ is represented approximately by a finite set of "source-blobs" that are the result of discretizing the expansion field along the flame. The flow field of a source-blob differs from that of a 2D point source by the smoothing associated with a specified cutoff (core) radius analogous to what was used above with the vortex blobs. The expression for $\mathbf{u}_e(\mathbf{x},t)$ for N_s source-blobs, where source j is located at $\mathbf{x}_j$ and has strength q_j, is as follows :

$$\mathbf{u}_e(\mathbf{x},t) = \sum_{j=1}^{N_s} \mathbf{u}_{ej} = \sum_{j=1}^{N_s} \frac{q_j}{2\pi} \frac{\mathbf{r}_j}{|\mathbf{r}_j|^2}\, g(|\mathbf{r}_j|/c_j) \tag{3.42d}$$

where, $\mathbf{r}_j = \mathbf{x}-\mathbf{x}_j$, and g(r) is the core function, given by :

$$g(r) = \begin{cases} 1 & \text{for } r > 1 \\ r & \text{for } r \le 1 \end{cases} \tag{3.42e}$$

The solution of problem (3.42c), leading to the full solution of the advection flow field (the velocity $\mathbf{u}$, eq. 3.11), is dealt with in the

following. The solution of (3.42c) amounts to satisfying the prescribed boundary fluxes on the computational domain boundary ∂D, given the two flow fields $\mathbf{u}_\omega$ and $\mathbf{u}_e$ and the specified normal velocity value on ∂D, u_n. As stated above u_n is specified to be : zero on solid walls, u_{in} far upstream ($x \to -\infty$), u_{out} far downstream ($x \to +\infty$). Note that in both limits, $\pm \infty$, $\mathbf{u}_\omega$ and $\mathbf{u}_e$ tend to zero, hence $\mathbf{u}_p \cdot \mathbf{n} = u_n$.

Several methods exist for solving this problem. Since the domain geometry considered is relatively simple, we have chosen to use conformal mapping. This method avoids a discretization error in the computation of boundary fluxes, and is quite efficient for simple geometries. For the geometry at hand, however, no analytical conformal map exists; hence, a code that computes the Schwartz-Christoffel mapping numerically was used. This code was provided by Trefethen (1979).

The solution, as implemented here, begins by mapping the flow domain, along with the two flow fields $\mathbf{u}_\omega$ and $\mathbf{u}_e$, from the physical complex plane ($w=x+iy$) to the upper half plane, referred to as the transform plane, ($\zeta=\xi+i\eta$), where $i=(-1)^{1/2}$. The domain walls are mapped to the ξ-axis, while the domain itself is mapped to the region : $\eta > 0$. A vortex/source inside the domain in the physical plane maps to a vortex/source with the same strength in the transform plane and vice versa.

Next, given $\mathbf{u}_\omega$ and $\mathbf{u}_e$, we proceed to satisfy the boundary conditions, namely, the inlet-exit flows and the impenetrable walls.

Under stable operating conditions, when no bulk flow reversal occurs in the combustor, the inlet flow, coming from an "infinite" upstream channel, corresponds to a source at $x=-\infty$. The inlet flow rate and the extra volume generated by the expansion sources at the flame interface are both vented to a sink, which is located downstream at $x=+\infty$, (again, for stable combustor operation). These roles of source and sink may be interchanged depending on

the pressure boundary conditions upstream and downstream of the combustor, as will be discussed in section 3.4 below. In the following discussion, with no loss of generality, we will assume stable operation; hence an upstream source and a downstream sink. By the choice of the mapping, the two limits, $x=-\infty$ and $x=+\infty$, are mapped to two points on the ξ-axis in the transform plane. Hence, the imposition of the inlet and exit boundary conditions involves specifying the proper source and sink strengths at these two points in the ζ-plane.

In order to enforce $u_n=0$ on the ξ-axis in the ζ-plane (except at the inlet and exit source and sink singularities), the normal flux on this axis due to each vortex/source in the upper half plane is cancelled by an artificial identical vortex/source image of the same strength (opposite sign for the vortices) in the lower half plane, at the same normal distance from the ξ-axis. Therefore, solving (3.42c) amounts to finding the velocity induced at any point in the -unbounded simply connected- transform plane by :

1) the images of the vortices

2) the images of the flame sources

3) the inlet and exit flow source and sink and the image of each.

This gives the velocity $\mathbf{u}_p$ in the ζ-plane. The final velocity $\mathbf{u}$ in the physical plane is arrived at by, (1) adding the velocities induced by the vortices and the flame sources themselves (the flow fields $\mathbf{u}_\omega$ and $\mathbf{u}_e$) in the ζ-plane, and (2) mapping the final result to the physical plane. This is done below, after a brief description of the terminology.

The Schwartz-Christoffel technique utilizes the "complex velocity" concept where, for $\mathbf{u}=(u_1,u_2)$, the complex velocity is $W=u_1-iu_2$. To be more precise, consider a point $w=x+iy$, which maps to $\zeta=\xi+i\eta$. Let the total velocity at w, in the physical plane, be $\mathbf{u}=(u_1,u_2)$, while the corresponding velocity at ζ in the transform plane be $\sigma=(\mu,\nu)$. Then the complex velocities, $W=u_1-iu_2$ at w, and $S=\mu-i\nu$ at ζ are related by the transformation as follows:

$$W(w) = S(\zeta)\ F(w) \tag{3.43}$$

where $F(w)=d\zeta(w)/dw$ is the transformation function that maps the w-plane to the ζ-plane (see Hildebrand, 1976; Nehari, 1975). Below, the evaluation of S due to a distribution of vortices, sources, and sinks in the ζ-plane is described.

We begin by developing eq. (3.38) to use complex numbers and to give the complex velocity due to a finite number of vortex elements ($j=1,\ldots N_v$) in the ζ-plane. To use a more concise notation, let us retain $\kappa(r/\delta)$ so that one expression will suffice for all r.

The radial symmetry of the core function f, corresponding to a blob j in the physical plane, is not preserved, in general, when the blob is mapped to the ζ plane. For simplicity, and following the practice adopted in earlier works (e.g. Ghoniem & Gagnon, 1987), we neglect this disruption of radial symmetry, and use a circular core in the ζ plane, with radius β_j given by :

$$\frac{\beta_j}{\delta} = |F(w_j)|, \quad F(w_j) = \left(\frac{d\zeta}{dw}\right)_{w=w_j}$$

Therefore, the velocity due to vortex element j at $\zeta_j=\xi_j+i\eta_j$ in the ζ plane, induced at a point $\zeta=\xi+i\eta$, is given by:

$$\sigma_\omega^j = \Gamma_j\ K_\delta(\zeta-\zeta_j) = \frac{-\Gamma_j}{2\pi}\frac{(\eta-\eta_j,\xi_j-\xi)}{|\zeta-\zeta_j|^2}\ \kappa(|\zeta-\zeta_j|/\beta_j) = (\mu_\omega,\nu_\omega) \tag{3.44}$$

or, using $R^j=\zeta-\zeta_j$, and introducing $S_\omega^j=\mu_\omega^j-i\nu_\omega^j$, we get :

$$\begin{aligned} S_\omega^j &= \frac{-\Gamma_j}{2\pi}\frac{(\eta-\eta_j)+i(\xi-\xi_j)}{|R^j|^2}\ \kappa(|R^j|/\beta_j) \\ &= \frac{-i\Gamma_j}{2\pi}\frac{(\xi-\xi_j)-i(\eta-\eta_j)}{R^jR^{j*}}\ \kappa(|R^j|/\beta_j) = \frac{-i\Gamma_j}{2\pi R^j}\ \kappa(|R^j|/\beta_j) \end{aligned} \tag{3.45}$$

where, $R^{j*} = (\xi-\xi_j)-i(\eta-\eta_j)$ is the complex conjugate of R^j.

Therefore, the complex velocity in the ζ-plane, at the point (ζ,t), due to N_v vortices and their N_v images in the lower half plane, is given by :

$$S_\omega(\zeta,t) = \sum_{j=1}^{N_v} (-i\Gamma_j/2\pi R^j)\kappa(|R^j|/\beta_j) + \sum_{j=1}^{N_v} (i\Gamma_j/2\pi \bar{R}^j)\kappa(|\bar{R}^j|/\beta_j) \qquad (3.46)$$

where, $\bar{R}^j = \zeta-\zeta^{j*}$.

Note that a blob and its image are assigned identical core functions with the same core radius β_j in the ζ plane. This is necessary in order that they may cancel each other's normal velocity at the wall ($\eta=0$) whatever their distance from the wall. As noted above, the only difference between a blob and its image, in the ζ plane, is the sign of the circulation assigned to each.

The complex velocity due to a distribution of sources and sinks can be found similarly. We recall eq. (3.42d) above, for the velocity induced by a source blob in an unbounded simply connected domain. This equation is equally valid for a sink, with $q_j < 0$. By the same reasoning employed above, we assume that the core function $g(r)$ retains its radial symmetry in the ζ-plane. The core radius in the ζ-plane (γ_j) is found from that in the w-plane (c_j), as done above for the vortices, by :

$$\frac{\gamma_j}{c_j} = |F(w_j)|, \quad F(w_j) = \left(\frac{d\zeta}{dw}\right)_{w=w_j}$$

Let us write (3.42d) in the ζ-plane. Consider a source (or sink) blob j, at ζ_j, of strength q_j, and core radius γ_j. The velocity $\sigma_e=(\mu_e,\nu_e)$ induced by it at a point ζ, following (3.42d), is :

$$\sigma_e^j = (\mu_e^j,\nu_e^j) = \frac{q_j}{2\pi} \frac{(\xi-\xi_j,\eta-\eta_j)}{|\zeta-\zeta_j|^2} g(|\zeta-\zeta_j|/\gamma_j) \qquad (3.47)$$

where,

$$g(r) = \begin{cases} r & \text{for } r \leq 1 \\ 1 & \text{for } r > 1 \end{cases}$$

hence, the complex velocity $S_e^j = \mu_e^j - i\nu_e^j$ is given by:

$$S_e^j = (q_j/2\pi)\, g(|R^j|/\gamma_j)\, R^{j*}/|R^j|^2 = q_j\, g(|R^j|/\gamma_j)/2\pi R^j \qquad (3.48)$$

where,

$$R^j = (\xi-\xi_j)+i(\eta-\eta_j) = \zeta-\zeta_j \qquad (3.49)$$

Therefore, the complex velocity induced by N_s sources and sinks and their images is given by :

$$S_e = \sum_{j=1}^{N_s} q_j\, g(|R^j|/\gamma_j)/2\pi R^j + \sum_{j=1}^{N_s} q_j\, g(|\bar{R}^j|/\gamma_j)/2\pi \bar{R}^j \qquad (3.50)$$

where, $\bar{R}^j = \zeta-\zeta^{j*}$. Note that this summation includes all the sources and sinks in the flow, including those on the ξ-axis (the inlet flow source and the exit sink, with $c = \gamma = 0$), where $R^j = \bar{R}^j$. Hence, a source (or sink on the ξ--axis is counted twice. Further, analogous to what was done with the blobs, each source and its image are assigned the same core radius γ_j, in the ζ plane.

Finally, the total complex velocity at a point due to the vorticity distribution (eqs. 3.13,3.14) and the potential flow (expansion sources and boundary conditions) eqs. 3.15,3.16a, in the ζ-plane, is given by :

$$S(\zeta) = \mu - i\nu = S_\omega + S_e$$

$$= \sum_{j=1}^{N_v} \frac{i\Gamma_j}{2\pi} \left(\frac{-\kappa(|R^j|/\beta_j)}{R^j} + \frac{\kappa(|\bar{R}^j|/\beta_j)}{\bar{R}^j} \right)$$

$$+ \sum_{j=1}^{N_s} \frac{q_j}{2\pi} \left(\frac{g(|R^j|/r_j)}{R^j} + \frac{g(|\bar{R}^j|/r_j)}{\bar{R}^j} \right) \qquad (3.51)$$

In order to map the complex velocity to the physical plane, we use equation (3.43) above, to arrive at $W=u_1-iu_2$, i.e.

$$W(w) = S(\zeta)F(w)$$

The above discussion provided an expression for the velocity $\mathbf{u}(\mathbf{x},t)$, eq. (3.11), at any point in the fluid <u>except</u> at the center of a vortex blob. We need to compute $\mathbf{u}_i$ (the advection velocity of blob i) in order to update the velocity field. The computation of $\mathbf{u}_i$ in the ζ-plane is in fact identical to that at any point $\mathbf{x}$, except that the summation over the N_v blobs in eqs. (3.46) and (3.51) excludes the case j=i, while the summation over the images still includes the image of blob i. Further, the mapping of the complex velocity to the physical plane involves an additional term when the point in question is the center of a vortex blob. Namely, for a blob i,

$$W(w_i) = S(\zeta_i)F(w_i) - (i\Gamma_i/4\pi)\,(dF/d\zeta)_{w_i} = u_1 - iu_2 \qquad (3.52)$$

and,

$$\mathbf{u}_i(t) = \mathbf{u}(\chi_i(\alpha_i,t),t) = (u_1,u_2) \qquad (3.53)$$

The justification for this extra term is explained in Appendix B.

Therefore, we have found the advection velocity $\mathbf{u}$, at every point in the physical plane. The next section describes the use of these velocities in updating the locations of the vortex blobs in the computational domain at every time step.

3.C Updating the Vorticity Field in the Interior by Advection

Each vortex blob is advected by its above computed advection velocity ($u_i(t)$) according to eq. (3.9), which states that vortex elements are simply advected with the material particles. Note that $u_i(t)$ is the solution of equations (3.11-15) and the potential boundary condition (3.16a), at some time $t=n\Delta t$, given the initial conditions (3.16b,c).

The location of vortex element i, $x_i(t)$, is updated according to :

$$(\partial x_i(t)/\partial t)_{adv} = u_i(t) \tag{3.54}$$

The time integration of this equation is done using the modified Euler (also known as Huen's) method (Gerald & Wheatley, 1984). Using a time step Δt, the algorithm is as follows :

For, $i=1,\ldots,N_v$:

$$\begin{aligned} x_i^{n+1/2} &= x_i^n + \Delta t u_i^n \\ x_{i,adv}^{n+1} &= x_i^n + \Delta t(u_i^n + u_i^{n+1/2})/2 \end{aligned} \tag{3.55}$$

where, $x_i^n = (x_i(n\Delta t), y_i(n\Delta t))$

$u_i^n = (u_{i,1}(n\Delta t), u_{i,2}(n\Delta t))$

$x_i^{n+1/2}$ = intermediate location of vortex blob i

$u_i^{n+1/2}$ = u_i corresponding to the intermediate vorticity distribution ($x_i^{n+1/2}$) but using the flame source distribution and inlet and exit conditions used to compute u_i^n (those at $t=n\Delta t$).

$x_{i,adv}^{n+1}$ = location of blob i at $t=n\Delta t$ due to advection alone.

This technique is second-order accurate in time. Sethian (1984) comments on the necessity of a second-order time integration scheme such as the above for updating the vortex blob locations by advection.

3.2.1.2 Diffusion:

The transport of vorticity due to diffusion is expressed by the second fractional step expressed above in eq. (3.8). In the Random Vortex Method, the effect of diffusion is implemented by the dispersion of a finite number of vortex elements with finite and constant vorticity according to 2D Gaussian Statistics (Chorin, 1972; Milinazzo & Saffman, 1977; Saffman & Baker, 1979; Ghoniem & Sherman, 1985; Ghoniem & Gagnon, 1987).

The algorithm is based on the fact that the Green function of the 1D form of eq. (3.8), given by :

$$G(x,t) = (Re/4\pi t)^{1/2} \exp(-x^2 Re/4t) \tag{3.56}$$

is identical to the probability density function of a Gaussian random variable η with a zero mean and a standard deviation of $\sigma=(2\Delta t/Re)^{1/2}$, namely:

$$P(\eta;t) = (1/2\sigma^2\pi)^{1/2} \exp(-\eta^2/2\sigma^2) \tag{3.57}$$

In 2D, the Green function of eq. (3.8) is given by :

$$G'(x,y,t) = (Re/4\pi t) \exp(-(x^2+y^2)Re/4t) \tag{3.58}$$

which is equivalent to :

$$G'(x,y,t) = G(x,t)G(y,t) \tag{3.59}$$

where G(x,t) and G(y,t) have the same form as in eq. (3.56) above. The corresponding probability density function is the product of two 1D probability density functions:

$$P'(\eta_x,\eta_y;t) = P_1(\eta_x;t)P_2(\eta_y;t) \tag{3.60}$$

where P_1 and P_2 are give by eq. (3.57) above. Thus the solution of eq. (3.8) is simulated stochastically by a 2D displacement of the vortex elements in two perpendicular directions using two sets of independent Gaussian random numbers, each having a zero mean and a standard deviation of ($\sigma=(2\Delta t/Re)^{1/2}$).

The random walk algorithm is compatible with vortex schemes because of its Lagrangian grid-free form. It can also be applied in regions of large gradients near fixed solid boundaries to move vortex elements which are generated to satisfy the no-slip boundary condition without excessive numerical diffusion since it does not depend on the resolution of a grid. Ghoniem and Sherman (1985) discuss in detail the stochastic solutions of the diffusion equation with different boundary conditions, its application to the reaction-diffusion equation, and to the combined heat and momentum diffusion that arises in natural convection.

In the Random Vortex Method, the diffusive transport of vortex elements is simulated stochastically by adding to their convective motion an extra displacement drawn from a Gaussian population with zero mean and a standard deviation σ. The total transport of vortex elements is obtained by adding the two fractional displacements :

$$x_i^{n+1} = x_{i,adv}^{n+1} + \eta_i \qquad (3.61)$$

where, $\eta=(\eta_1,\eta_2)$ is the random displacement vector,

x_i^{n+1} = new location of blob i in the domain interior (at $t=(n+1)\Delta t$)

3.2.2 Wall Region:

In the context of the Random Vortex Method, the "wall region" refers to a very thin region extending only a few σ's (random walk standard deviations) from the domain walls, where the discretization of the vorticity field uses vortex sheets instead of blobs, the latter being used in the bulk of the flow domain.

Vorticity is generated at the walls to satisfy the no-slip boundary condition (Lighthill, 1963; Payne, 1958). This scheme of vorticity generation was used by Chorin (1972) in the Random Vortex Method to satisfy the viscous boundary condition at solid walls. The vorticity generated along the wall is discretized into elements separated by a distance "h". To improve the resolution, the required circulation generated at each wall station is distributed among several elements (sheets) such that each has a certain maximum circulation Γ_m. These sheets leave the wall by diffusion, to become part of the interior vorticity field at later times, when they are converted into vortex blobs of appropriate core radius to satisfy compatibility between the interior and wall regions. The wall region (also referred to below as the sheet region) has a thickness Δ_s.

By the nature of the solution in the wall region, we will use the wall velocity computed from the above interior flow calculation as a specified U_∞ for the boundary layer equations. We will not need to use the Helmholz decomposition, eq. (3.3), of the velocity field. It will be sufficient to write down the curl of the Navier-Stokes equations and the continuity equation as starting points. Further, since Δ_s is typically much less than the cell size used for the flame propagation algorithm, we will not consider the expansion field of any flame sources in the sheet region, rather the effect of the expansion field will be present via U_∞. Therefore, the relevant equations are:

$$\partial\omega/\partial t + \mathbf{u}.\nabla\omega = (1/Re)\ \nabla^2\omega \tag{3.62}$$

$$\partial u/\partial x + \partial v/\partial y = 0 \tag{3.63}$$

$$\omega = \partial v/\partial x - \partial u/\partial y \tag{3.64}$$

where $\mathbf{u}=(u,v)$, and $Re=Re_u$ (Re_b) in the reactants (products).

In this section, the coordinate system (x,y) is used to represent the parallel and the normal to the wall, respectively. Points (x,0) belong to the wall. Coordinate transformation is employed whenever necessary for converting velocities and point coordinates from the domain coordinate system (Fig. 3.1) to the coordinate system of each wall and vice versa.

We now proceed to describe the solution of the above equations in the wall region. We use Prandtl's boundary layer approximation to simplify eqs. (3.62,3.64). This approximation is based on the fact that the cross stream dimension of the boundary layer is much smaller than its stream-wise dimension. Consequently, we find : $\partial v/\partial x \ll \partial u/\partial y$ and $\partial^2\omega/\partial x^2 \ll \partial^2\omega/\partial y^2$, and the above equations simplify to :

$$\partial\omega/\partial t + \mathbf{u}.\nabla\omega = (1/Re)\ \partial^2\omega/\partial y^2 \tag{3.65}$$

$$\partial u/\partial x + \partial v/\partial y = 0 \tag{3.66}$$

$$\omega = -\ \partial u/\partial y \tag{3.67}$$

Similarly to what was done in the domain interior, our solution is split into two fractional steps. First, we update the vorticity with respect to the advection component by solving :

$$\partial\omega/\partial t = -\mathbf{u}.\nabla\omega \tag{3.68}$$

$$\partial u/\partial x + \partial v/\partial y = 0 \tag{3.69}$$

We assume the u velocity component "infinitely" away from the wall to be given (U_∞) and require that, at the solid walls, $u=(u_s,u_n)=(0,0)$, hence we impose a "no-slip" condition at the walls..

Next, we update the vorticity field with respect to the diffusion term $\partial^2\omega/\partial y^2$, i.e.

$$\partial\omega/\partial t = (1/Re)\ \partial^2\omega/\partial y^2 \qquad (3.70)$$

Given the above stated "no-slip" boundary condition, vorticity has to be generated at the walls to force the u-velocity there to be zero. The wall region acts as a transition zone from the still fluid (at y=0) to the high speed fluid in the interior. Vorticity created at the wall diffuses into the domain interior (Morton, 1984). This is in contrast to flow in the interior (where $\omega=\partial v/\partial x-\partial u/\partial y$) where neither velocity component dominates the motion of the vorticity. Consequently, it is inappropriate to use vortex blobs to discretize the vorticity field within the wall region, since each blob generates a radially symmetric rotation of fluid around its center. Instead, we use vortex sheets, which are surfaces parallel to the solid walls across which the tangential velocity changes abruptly. In the following (see Chorin, 1978), we describe the discretization of the vorticity field into sheets, and discuss the properties of the sheets.

Let us consider one of the domain walls. Discretize this wall into sections of length "h". The vorticity generated on one such section is found by calculating the circulation around a rectangle of length h, and infinitesimal width, as in the diagram below :

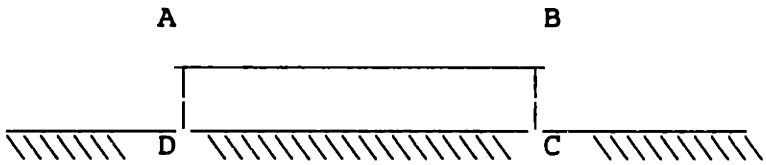

Side CD is coincident with the wall section of length h. The velocity on side CD is specified to be zero (no-slip), while that on side AB is the wall velocity computed from the domain interior (u_s). The circulation around ABCD is given by :

$$\Gamma = - \int_B^A u_s ds + 0 + 0 + 0 = - \bar{u}_s h \qquad (3.71)$$

where $\bar{u}_s$ is the mean value of u_s over the length h. We will assume the variation of u_s over h is approximately linear, and hence use the velocity computed at the mid point (M_i) of each wall section (i) of length h to be $\bar{u}_s$ for that section. To improve the resolution, the circulation computed at each section (i) is divided among several sheets, all generated with the same initial coordinates (at M_i), same length h, and same circulation Γ_m (+ve for counter clockwise rotation). Where Γ_m is specified a priori, as the maximum allowed vortex strength. These sheets move away from the wall by diffusion to become part of the interior vorticity at a later time. The coordinates of a given sheet are, by convention, those of its center (midpoint).

The vorticity distribution inside the wall layer (eq. 3.67) is thus approximated by a number of vortex sheets of length h and circulation Γ_m, which remain parallel to the wall while transporting velocity jumps δu, such that :

$$\delta u = u^+ - u^- \qquad (3.72)$$

where u^+ (u^-) is the velocity above (below) the sheet.

If the circulation per unit length carried by sheet j is γ_j (also called sheet "strength") then :

$$\gamma_j = \Gamma_j / h = - \delta u_j \qquad (3.73)$$

Using the same core function concept implemented above, we thus write the vorticity distribution due to collection of N sheets as follows:

$$\omega(x,t) = \sum_{j=1}^{N} \gamma_j \, f_\Delta(x-x_j) \tag{3.74}$$

where $x_j = x_j(t) = (x_j(t),y_j(t)) = \chi(\alpha_j,t)$. $(x_j(t),y_j(t))$ are the coordinates of the center of sheet j (with lagrangian coordinate α_j) at time t. f_Δ is the "vortex sheet core function" which is defined by :

$$f_\Delta(x-x_j) = \delta(y-y_j) \; [\; H(x-x_j^L) - H(x-x_j^R) \;] \tag{3.75}$$

where $x_j^L = x_j - h/2$, and $x_j^R = x_j + h/2$, are the x-coordinates of the left and right extremities of sheet j, respectively. $\delta(y)$ is the Dirac delta function, and H(x) is the Heaviside step function (Greenberg, 1978), defined by :

$$H(x) = \begin{cases} 1 & \text{for } x > 0 \\ 1/2 & \text{for } x = 0 \\ 0 & \text{for } x < 0 \end{cases} \tag{3.76}$$

That this choice of core function is appropriate can be easily checked by finding the circulation around a rectangle with area A, and with side lengths h and Δ_s, containing a single sheet j entirely. Namely, we expect to get : $\int_A \omega \, dA = \Gamma_j = h\gamma_j$. This is verified below :

$$\begin{aligned} \int_A \omega \, dA &= \int_{x_j^L}^{x_j^R} \int_0^{\Delta_s} \gamma_j \, f_\Delta(x-x_j) \, dy \, dx \\ &= \gamma_j \int_{x_j^L}^{x_j^R} [\; H(x-x_j^L) - H(x-x_j^R) \;] \, [\int_0^{\Delta_s} \delta(y-y_j) \, dy \;] \, dx \\ &= \gamma_j \int_{x_j^L}^{x_j^R} [1-0][1] \, dx = \gamma_j \, h = \Gamma_j \end{aligned} \tag{3.77}$$

Integration of eq. (3.67) in the y-direction, from y=0 to y_j, gives the u-velocity distribution in the wall region, given u=0 at the wall, namely :

$$u(x,y) = \int_0^y \frac{\partial u}{\partial y'}\, dy' = -\int_0^y \omega\, dy'$$

$$= \sum_{j=1}^{N} \gamma_j\, K_\Delta(x-x_j) \qquad (3.78)$$

where, $K_\Delta(x-x_j) = -\int_0^y f_\Delta(x'-x_j)\, dy', \quad [\, x'=(x,y')\,]$

$$= -H(y-y_j)\,[\,H(x-x_j^L) - H(x-x_j^R)\,] \qquad (3.79)$$

Another formulation for this velocity integral, which is more useful in terms of finding the actual slip velocity at the wall due to a given interior flow and a distribution of sheets, is found by integrating eq. (3.67) from y to Δ_s, instead of 0 to y. This formulation is, in fact, the one utilized in the code for driving the wall velocity to zero by generation of sheets. The velocity at the edge of the sheet region (x,Δ_s), is $U_\Delta(x)$. Since the sheet region is very thin, we simply use the wall velocity computed from the interior flow for U_Δ. The integration from y to Δ_s gives :

$$u(x,y) = U_\Delta(x) + \int_y^{\Delta_s} \omega(x,y')\, dy'$$

$$= U_\Delta(x) + \sum_{j=1}^{N} \gamma_j\,[1-H(y-y_j)]\,[H(x-x_j^L)-H(x-x_j^R)] \qquad (3.80)$$

The total velocity at the wall (due to the interior flow and the sheets) is given by :

$$u(x,0) = U_\Delta(x) + \sum_{j=1}^{N} \gamma_j\,[H(x-x_j^L)-H(x-x_j^R)] \qquad (3.81)$$

3.2.2.1 Sheet Advection

Let us compute the velocity induced at the center of a sheet i due to the interior flow and the influence of all other sheets. We average over the sheet length of sheet i :

$$\bar{u}_i = \bar{u}(x_i,y_i) = \frac{1}{h} \int_{x_i^L}^{x_i^R} u(x,y_i)\, dx$$

$$= \bar{U}_\Delta(x_i) + \sum_{j=1}^{N} \gamma_j \, [1-H(y_i-y_j)] \, D_{ij} \qquad (3.82)$$

where, $$\bar{U}_\Delta(x_i) = \frac{1}{h} \int_{x_i^L}^{x_i^R} U_\Delta(x)\, dx \cong U_\Delta(x_i) \qquad (3.83)$$

and, $$D_{ij} = \frac{1}{h} [(\Delta_{ij}+h)\, H(\Delta_{ij}+h) - 2\Delta_{ij}\, H(\Delta_{ij}) + (\Delta_{ij}-h)\, H(\Delta_{ij}-h)]$$

$$\Delta_{ij} = x_i - x_j \qquad (3.84)$$

Note, it can be easily shown that :

$$D_{ij} = \begin{cases} 1 - |\Delta_{ij}|/h & \text{for } |\Delta_{ij}| < h \\ 0 & \text{for } |\Delta_{ij}| \geq h \end{cases} \qquad (3.85)$$

The above expression for $\bar{u}_i$ can be developed further to give :

$$\bar{u}_i = U_\Delta(x_i) + \frac{1}{2}\gamma_i + \sum_{\substack{j=1 \\ y_j > y_i}}^{N} \gamma_j \, D_{ij} \qquad (3.86)$$

$\gamma_i/2$ is the self induced velocity of sheet i, and the summation on the right hand side of the above equation includes only those sheets that are further away from the wall than sheet i (higher than sheet i). Sheets closer to the wall than sheet i (lower than it) have no influence on it. It is also

noted that the velocity $U_\Delta(x_i)$ is found by interpolation or extrapolation from the computed wall velocities using the nearest two wall points.

The v-velocity component of a vortex sheet is computed by integrating the continuity equation, (3.69). Let us define I(x) as follows :

$$I(x) = \int_0^{y_i} u(x,y)\, dy \tag{3.87}$$

Then, we have :

$$v(x,y_i) = - \frac{\partial I(x)}{\partial x} \tag{3.88}$$

or,
$$\bar{v}_i = \bar{v}(x_i,y_i) = \frac{1}{h} \int_{x_i^L}^{x_i^R} v(x,y_i)\, dx \tag{3.89}$$

i.e.
$$\bar{v}_i = - \frac{1}{h} \left[I(x_i^R) - I(x_i^L) \right] \tag{3.90}$$

At this point we make another approximation, namely we use $\bar{I}(x)$ instead of I(x) in this last equation. $\bar{I}(x)$ is the mean of I(x) over $x \pm h/2$, i.e.:

$$\bar{I}(x) = \frac{1}{h} \int_{x-h/2}^{x+h/2} I(x')\, dx' = \int_0^{y_i} \bar{u}(x,y)\, dy \tag{3.91}$$

where,
$$\bar{u}(x,y) = U_\Delta(x) + \sum_{j=1}^{N} \gamma_j \left[1-H(y-y_j)\right] D_{xj} \tag{3.92}$$

$$D_{xj} = \begin{cases} 1 - |x-x_j|/h & \text{for } |x-x_j| < h \\ 0 & \text{for } |x-x_j| \geq h \end{cases} \tag{3.93}$$

Then, $\bar{I}(x)$ is found to be :

$$\bar{I}(x) = y_i U_\Delta(x) + \sum_{j=1}^{N} \gamma_j D_{xj} \min(y_i,y_j) \tag{3.94}$$

and, $\bar{v}_i$ is :

$$\bar{v}_i = - \frac{1}{h} \left[\bar{I}(x_i+h/2) - \bar{I}(x_i-h/2) \right] \tag{3.95}$$

Equations (3.86) and (3.95) give the velocity induced at the center of each vortex sheet i, due to the interior flow and all other sheets j.

At this point we can update the sheet locations using the advection step, eq. (3.68). Given the locations x_i^n at time $t=n\Delta t$, we find the intermediate locations, due to advection alone, $x_{i,adv}^{n+1}$, at time $t=(n+1)\Delta t$. We use Euler's method for this time integration :

$$x_{i,adv}^{n+1} = x_i^n + \Delta t\, \bar{u}_i^n \tag{3.96}$$

$$y_{i,adv}^{n+1} = y_i^n + \Delta t\, \bar{v}_i^n \tag{3.97}$$

3.2.2.2 Sheet Diffusion

To update the vorticity in the wall region with respect to the diffusion equation (3.70), we use, as with the blobs, a random walk algorithm. We allow each sheet to undergo a jump in the y-direction, either positive or negative, which is selected from a Gaussian distribution with zero mean and standard deviation $\sigma = (2\Delta t/Re)^{1/2}$. Note that diffusion takes place only in the direction normal to the wall. Without the diffusion term, the sheets would never leave the boundary, since $\mathbf{u}=(0,0)$ at the wall, by construction. The random walk diffuses the sheets away from the wall to join other sheets in the wall region. The position of sheet i is updated by the random walk, starting with the intermediate location found above due to advection alone, as follows :

$$x_i^{n+1} = x_{i,adv}^{n+1} \tag{3.98}$$

$$y_i^{n+1} = y_{i,adv}^{n+1} + \eta_i \tag{3.99}$$

where η_i is the random jump.

3.2.3 Matching the Interior and Wall Region Solutions :

As mentioned above, one element of the matching between the Interior flow and the wall flow solutions is the use of the wall velocity U_Δ, computed from the interior flow alone, as the driving outer flow velocity for the boundary layer computations within the sheet region. This allows the interior flow to determine the production of vorticity within the boundary layer.

Another mechanism for matching between the two flow regions is the transfer of vorticity from the wall region to the interior by allowing those vortex sheets located at a distance greater than Δ_s from the wall to become vortex blobs. When a vortex element is converted from sheet to blob, or vice versa, its total circulation Γ_m is conserved. A blob is converted to a sheet if it moves closer than Δ_s to a wall. By selecting Δ_s to be 2-3 times the standard deviation of the random jumps implemented in the diffusion algorithm it is unlikely that a blob will move outside the domain due to a random jump in one time step. If, due to very high convective blob velocities, this does happen, then the offending blob is deleted.

A menacing part of the diffusion of sheets is that they may diffuse down into the wall, since the random jumps used to simulate diffusion can be negative. Following previous practice, the new locations of these sheets are found by appropriate reflection back into the domain (see Ghoniem et. al., 1982).

The determination of the blob core radius is done also to have proper matching between the interior and wall regions. The rational here is to have the same wall velocity induced by a vortex element at distance Δ_s from the wall whether that element is a sheet or a blob. This ensures a smooth transition from sheet to blob or vice versa, in terms of the wall velocities. Given that Δ_s is, by construction, much smaller than a blob core radius, δ,

and, given the choice of blob core function f_δ used here, this smoothness condition requires that δ and h be related by :

$$\delta = h/\pi \tag{3.100}$$

To demonstrate this assertion, consider a solitary sheet in the wall region, in an otherwise stagnant fluid, of circulation $\Gamma_m = h\gamma > 0$. The velocity induced by this sheet at the wall, irrespective of its wall coordinate y, is $u_{sh} = u^-$, where:

$$\delta u = u^+ - u^- = -\Gamma_m/h$$

Since $u^+ = 0$ (stagnant fluid in the interior, solitary sheet), then :

$$u_{sh} = u^- = \Gamma_m/h$$

Next, consider a solitary blob with the same circulation $\Gamma_m > 0$, along with its image with respect to the wall. Let the blob lie at $y=\Delta_s$ from the wall. Its image is then at the same distance on the other side of the wall. Since $r=\Delta_s < \delta$, for both the blob and its image, then the tangential velocity at the wall due to both of them is given by (eq. 3.39) :

$$u_b = 2\,\Gamma_m/2\delta\pi = \Gamma_m/\delta\pi$$

substituting $\delta=h/\pi$, we get :

$$u_b = \Gamma_m/h = u_{sh}$$

Hence, the velocity induced on the wall due to a blob or sheet at Δ_s is the same, and the transition from sheet to blob or vice versa causes no sudden velocity changes at the wall.

Finally, we may summarize the process of generation and propagation of vorticity implemented in this work, as follows :

1) Find the total velocity for each blob, eqs. (3.52,3.53).

2) Find U_Δ at the walls, and use it to find the total sheet velocity, eqs. (3.86,3.95).

3) Create vorticity to satisfy the no-slip boundary condition at the walls.

4) Update the sheet locations by eqs. (3.96-3.99), and the blob locations by eqs. (3.55,3.61).

3.3 Combustion Solution:

This section concerns the numerical description of the motion of the flame interface, as governed by eq. (2.29) above. The motion of the flame can be split into two components : advection and burning. Advection is simply the motion of the flame interface as a passive material surface with the local flow velocity. Burning, on the other hand, is the motion of the flame into the reactants with respect to an observer moving with the reactants immediately ahead of the flame. The reactants burn and are converted into products. As a result of the exothermic combustion reaction, heat is generated at the flame. The products of combustion are at a higher temperature, and lower density, than the reactants; i.e. the fuel and air mixture expands upon burning. In our thin flame model, this expansion of the fluid crossing the flame zone occurs only at the flame interface. The flame expansion field (eq. 2.34 above) is discretized here into a finite number of 2D point sources, which are distributed along the flame interface. The implementation of these sources is also described below.

3.3.1 Resolution and Propagation of the Flame Interface:

Various methods exist for the numerical description of the shape and evolution of interfaces between fluids. The algorithm implemented in this work is based primarily on the SLIC (Simple Line Interface Calculation) method introduced by Noh & Woodward (1976), and later implemented by Chorin (1980) for flame propagation and advection with increased spatial resolution. This method uses a finite set of horizontal and vertical straight line segments on a 2D rectangular grid to construct the flame interface, and an alternating direction scheme to advect the interface. SLIC has been used successfully in earlier works for tracking flame surfaces, see for example Barr & Ashurst (1984), Ghoniem et. al. (1982), Knio (1984), and Majda & Sethian (1985).

The information provided by SLIC includes the amount of products, or reactants, in each cell of the computational grid, and, for cells containing the flame interface, it includes some indication of the shape of the interface, be it horizontal, vertical, corner, or a neck. SLIC does not provide the local slope or curvature of the flame interface. The slope of the interface is useful for visualization purposes, while the curvature is needed to provide a means for varying the burning speed and/or computing the flame stretch along the flame interface. After Markstein (1964), the variation of the laminar burning speed, S_u, with curvature, is taken as :

$$S_u = S_n(1-\Lambda/R_F) \tag{3.101}$$

where S_n is the laminar burning speed of a planar flame, $\Lambda=\Lambda(T_u,P)$ is the Markstein length (Markstein, 1964), and R_F is the local radius of curvature of the flame. The VOF (Volume of Fluid) method introduced by Hirt & Nichols (1981) is used in part here to find the slope of the flame interface in a cell based on the information provided by SLIC for that cell and its closest neighbors. These slopes are used to construct a smoother flame interface than that provided by SLIC, which is then used to find the local radius of curvature of the flame (see Knio, 1984).

Our implementation of SLIC and VOF for the determination and propagation of the flame interface follows closely that of Knio (1984). Consequently, the discussion below will skim over many details stressing only the added modifications and/or deviations from earlier works as well as the general algorithm structure.

We begin by discretizing the domain using a uniform grid, with cell size given by $\Delta x = \Delta y = h_f$. The cells are numbered by rows i=1,2,...N and columns j=1,2...M. The center of cell (i,j) is at (x_i,y_j). Each cell is assigned a fractional index f_{ij} which indicates the amount of products in the cell.

Hence, $f_{ij}=1$ for a cell full of products, $f_{ij}=0$ for a cell full of reactants, and $0<f_{ij}<1$ for "fractional" cells, i.e. cells that contain some reactants and some products. These fractional cells contain the flame interface. Other index arrays are used to describe the form of the SLIC interface within a cell.

The propagation of the flame interface is done using two fractional steps based on eq. (2.29). Considering a set of points $\{\chi_f\}$ that identify the flame interface, the following expression, which is based on eq. (2.28), is clearly equivalent to (2.29), namely :

$$\frac{d\chi_f(t)}{dt} = u_f(\chi_f) = u_u(\chi_f) + S_u(\chi_f)n_f(\chi_f) \tag{3.102}$$

where, we recall, $u_f(\chi_f)$ is the local velocity of the flame interface, $u_u(\chi_f)$ is the fluid velocity on the reactants side of the flame interface, $S_u(\chi_f)$ is the local burning speed of the flame, and $n_f(\chi_f)$ is the local unit normal to the flame interface pointing towards the reactants, all defined at $x=\chi_f(t)$.

Using eq. (3.102), we write the fractional step for burning as :

$$\frac{d\chi_f(t)}{dt} = S_u(\chi_f)n_f(\chi_f) \tag{3.103}$$

While the advection step is given by :

$$\frac{d\chi_f(t)}{dt} = u_u(\chi_f) \tag{3.104}$$

The propagation of the flame by burning, normal to itself as indicated in eq. (3.103), can be implemented using the classical Huyghens principle for wave propagation (see Thompson, 1984). Consider a flame front that forms the boundary ∂D_1 between a region of products D_1 and a region of reactants comprising the rest of the computational domain D. Given flame propagation by burning only, the motion of ∂D_1 at every point is given by the local S_u along

the outward normal n_f. Using the construction of Huyghens, successive flamefronts are drawn as the envelopes of the circular flamelets of radii $S_u\Delta t$, and centers along ∂D_1. Consequently, (see Chorin, 1980) if we let f^n denote the concentration field given by the set of cell fractions f_{ij}, for all (i,j), at time $t=n\Delta t$, and use an advection operator A, where $A_\theta(f^n)$ is the new value of f obtained from f^n by advection with a uniform velocity field of magnitude S_u and angle θ with the x-axis (neglecting the variation of S_u for now), then the new f_{ij} due to the burning step is given by :

$$(f_{ij}^{n+1})_{brn} = \max_{0\leq\theta\leq 2\pi} [\ A_\theta(f_{ij}^n)\ ] \tag{3.105}$$

This statement is equivalent to Huyghens principle. Further, as shown by Chorin (1980), propagation in eight normal directions is sufficient to yield reasonably accurate results, in the 2D case. The maximum is thus taken over a discrete set of eight cases, in addition to the case of no motion, as follows:

$$(f_{ij}^{n+1})_{brn} \cong B(f_{ij}^n) = \max_{k=0\to 8} [\ A_\theta(f_{ij}^n)\ ] \tag{3.106}$$

where, $\theta=k\pi/4$, $A_0(f^n)=f^n$, and B refers to the burning operator. The stability condition for this burning algorithm is expressed as a courant condition (Chorin, 1980), namely :

$$\Delta t \leq \Delta x/\max(S_u) \tag{3.107}$$

Given the variation of S_u along the flame interface, the above process of maximization of fractions, eq. (3.106), is still feasible, albeit involving extensive bookkeeping. See Knio (1984) for details.

The flame advection algorithm used by Chorin (1980) and Knio (1984) involves moving the flame SLIC interface by the velocity computed on the

midpoint of the cell wall on the reactants side of the interface. This velocity is used to propagate the flame, along the directions of the coordinate axes, in an alternating direction scheme. Alternate time steps involve propagation in the X-Y then Y-X directions. This scheme has been adopted here with a modification that involves splitting the velocity field into two components and propagating the flame with each in a fractional step approach. The two velocity components are given by :

$$u = \mu + \nu \tag{3.108}$$

where μ is the combined velocity due to the vorticity field and the potential flow boundary conditions of zero flow into solid walls and a specified inlet and exit flow rates for the computational domain. ν is the flow field due to the flame expansion sources and their corresponding potential boundary conditions as for μ. The estimation of the interface velocity in the μ-propagation step involves interpolation between the μ velocities computed at the cell wall midpoints. This interpolation, which is admissible because μ is continuous at the flame interface, provides better accuracy than the one sided estimation of interface velocity. This latter extrapolation is implemented in the estimation of the ν-velocity at the flame interface. Given the large amplitudes of velocity involved in the μ field, this improved accuracy is desirable.

Therefore, the advection process proceeds as follows :

1) time step n, advect by the ν field in X then in Y direction.

2) time step n, advect by the μ field in X then in Y direction.

3) time step n+1, advect by the ν field in Y then in X direction.

4) time step n+1, advect by the μ field in Y then in X direction.

5) time step n+2, repeat step 1), etc ...

The stability condition for the advection step is again a courant type condition :

$$\Delta t \leq \Delta x/\max|\mathbf{u}| \tag{3.109}$$

3.3.2 Implementation of the Expansion Sources at the Flame:

We recall the above discussion (section 3.B) on the potential flow solution, which made use of the discretization of the flame expansion field into source blobs based on the demonstration in Appendix C. Our purpose here is to describe the implementation of these sources, in terms of the combustion solution.

In refering to Appendix C, we will use the subscript k instead of j, since j is already used in the (i,j) nomenclature of the combustion cells.

We begin by describing the evaluation of the source strengths q_k.

If we identify the elemental areas, A_k (A_j in Appendix C), with the computational cells (i,j) used to propagate the flame, then we can show :

$$q_k = \Delta f_{ij}\ \Delta x^2\ (\rho_u/\rho_b - 1)\ /\ \Delta t \tag{3.114}$$

where, $$\Delta f_{ij} = B(f_{ij}) - f_{ij}$$

The demonstration of this expression is as follows. Consider cell k(i,j). Consider that, at time $t=n\Delta t$, it has a volume V_u of reactants and V_b of products (per unit length in the 3^{rd} dimension). Let ΔV_u be the volume of fluid swept by the flame interface, in this cell, by burning into the reactants in one time step. Then the new volumes of reactants and products, before taking expansion into account, are: $V_u' = V_u - \Delta V_u$ and $V_b' = V_b + \Delta V_u$, respectively. Note also that $\Delta V_u = \Delta f_{ij} \Delta x^2$.

However, by mass conservation, we must have that for a volume ΔV_u of reactants that has been burnt, the corresponding volume of created products, ΔV_b, is given by :

$$\Delta V_b = \Delta V_u \ \rho_u/\rho_b \tag{3.115}$$

The new volume of products due to burning in the cell should be, therefore, given by $V_b^* = V_b + \Delta V_b$. Hence, the amount of volume that needs to be added by the expansion field in cell k(i,j), in the time step Δt, is given by :

$$\Delta V_k = V_b^* - V_b'$$

$$= \Delta V_b - \Delta V_u = (\rho_u/\rho_b - 1)\ \Delta V_u \tag{3.116}$$

And, since, by definition,

$$q_k = \Delta V_k/\Delta t \tag{3.117}$$

we arrive at (3.114)

In fact, in order to refine the spatial discretization of the expansion field, the source strength q_k is actually distributed among 1 to 4 sources along the flamelet straight line segment (given by VOF) depending on the length of this segment. Thus a cell in which burning occurs may contain from 1 to 4 sources whose cumulative strength corresponds to the amount of burning in the cell at that time step.

Another point that was left unanswered in Appendix C is the determination of the maximum velocity (V_m) assigned to an expansion source at the flame. This is discussed below.

Let us look at the velocities immediately before and after a small section of the flame of length ds, with respect to an observer moving with the flame at that location. The reactants are seen to move towards the flame at speed S_u, while the products move away at S_b. From mass conservation across the flame, we have

$$S_b = (\rho_u/\rho_b)\, S_u \tag{3.118}$$

Then, from a volume balance across the flame, we get that the rate of expansion (volume generation), per unit length along the flame, is given by :

$$S_b - S_u = (\rho_u/\rho_b - 1)\, S_u \tag{3.119}$$

We assume that this expansion is isotropic. Then, it follows that half of it is directed ahead of the flame and half behind it. Hence, the velocity due to the expansion field immediately before or after the flame is given by :

$$V_q = (1/2)(\rho_u/\rho_b - 1) S_u \tag{3.120}$$

Consequently, we set the velocity in the core of the source blobs to be $V_m = V_q$.

3.4 Inlet and Exit Boundary Conditions:

As explained above, the vortex method solution, as applied to the problem at hand, requires the specification of the inlet and exit flow rates (at $-\infty$ and $+\infty$ respectively, in the physical plane). These flow rates correspond to the relevant Source and Sink strengths in the ζ plane. In an actual combustor, however, the inlet and exit flow rates are not independently specified variables, rather, they depend on the flow conditions upstream and downstream. If the inlet flow is supplied by some reservoir, then the stagnation pressure of the reservoir, the shape and properties of the inlet section, and the time dependent flow configuration in the combustor, all contribute to the specification of the inlet flow rate at any instant of time. The same can be said for the exit flow rate.

Including the upstream and downstream flow configurations in the computational domain increases the complexity and cost of the numerical solution prohibitively. An easier option is to use some simplified flow model for the inlet and exit flow problems. This model has to include the relevant physical processes that determine the inlet and exit flow rates, and yet be simple enough so as not to increase the computational burden considerably.

As a first step towards such a model, we have to choose the flow geometry upstream and downstream. Experimental combustors have used a variety of choices. Typical upstream configurations use a compressor followed by a plenum chamber with flow straighteners and screens to obtain a roughly uniform flow with low turbulence intensity. The flow is then directed into the combustion section through a smooth contraction. The downstream configuration may or may not have a constriction (wide or narrow) that defines the end of the combustion chamber. This is followed by a long exhaust pipe leading to the atmosphere. A significant element of the flow dynamics in a long pipe, whether upstream or downstream, is that the time scales

associated with the streamwise propagation and reflection of pressure waves are comparable to the convective time scales in the combustor. Hence, the pipe can enhance the flow dynamics in the combustor by acting as a forced resonator.

With all the above in mind, we have chosen the inlet and exit configurations as follows. At the inlet, we assume the flow to be coming from an infinite reservoir at a fixed P_o, while at the exit we consider that we have a long 1-D channel exiting to the atmosphere, see Fig. 3.2. Each of these will be discussed in more detail below.

3.4.1 Inlet Boundary Condition

The essential requirement from the upstream boundary condition is to provide a flow rate into the channel at xmin (see Fig. 3.1) which is dependent on the flow picture inside the computational domain at every time step. Hence, for example, if, given a certain inlet flow rate, there is a severe pressure surge in the combustor, the inlet flow should slow down and then reverse, causing fluid to move back into the upstream reservoir. The configuration shown in Fig. 3.2, is sufficient for this purpose.

More precisely, our implementation of this boundary condition at every time step involves solving one of two different incompressible flow problems, depending on the sign of the inlet flow rate Q_{in}^{n-1}(= Q_{in} at the previous time step).

For $Q_{in}^{n-1} > 0$, i.e. for flow from the reservoir into the combustor, we solve the simple inviscid flow problem depicted in Fig. 3.3 for the new flow rate Q_{in}^{n} into the channel. The solution utilizes the unsteady Bernoulli integral written between points "a" and "b" shown in Fig. 3.3. The resulting equation, written in non-dimensional form, is as follows :

$$\frac{P_a}{\rho} + \frac{V_a^2}{2} + \left(\frac{\partial\phi}{\partial t}\right)_a = \frac{P_b}{\rho} + \frac{V_b^2}{2} + \left(\frac{\partial\phi}{\partial t}\right)_b \qquad (3.121)$$

The non-dimensionalization uses the same reference quantities U, L_r, and ρ_r, as used in the development of the cavity flow equations. Namely, U is a nominal inlet velocity, L_r is the cavity depth, and ρ_r is the density of the premixed reactants (which is the density of the incompressible fluid considered here). The reference pressure is chosen to be $p_r = \rho_r U^2$. Clearly, the non-dimensional density used above is given by : $\rho=1$. It is kept as ρ for clarity.

The pressure at "a", which is at a "large" distance (=50H) from the channel entry, is assumed to be the fixed stagnation pressure, $P_a = P_o$, while the velocity, $\mathbf{u}_a$, is assumed negligible, hence $V_a = |\mathbf{u}_a| = 0$. The pressure at "b", P_b, is the pressure computed from the combustor flow field at xmin (Fig. 3.1). This is done by integrating the streamwise pressure gradient, $\partial p/\partial x$, along the channel centerline from xmax to xmin. The pressure at xmax is known from the exit boundary condition solution, while $\partial p/\partial x$ is computed at discrete points along the centerline, from the prevailing flowfield. As discussed above, the flowfield is computed from the vortices and their images, the flame sources and their images, and the specified inlet flow rate into the channel. Hence, in particular, P_b depends on the channel inlet flow rate. $\mathbf{u_b} = (V_b,0)$ is the velocity at point "b", it is directly related to the inlet flow rate as mentioned below, and it is an unknown. ϕ is the flow potential at a point, such that : $\mathbf{u}(\mathbf{x},t) = \nabla\phi(\mathbf{x},t)$. The determination of ϕ involves the solution of the Laplace equation $\nabla^2\phi=0$ for the flow geometry in Fig. 3.3. This is easily done using Schwartz-Christoffel mapping to the upper half transform plane. If this mapping is designed such that the point $(+\infty,0)$ in the physical (w) plane maps to (0,0) in the transform (ζ) plane, and point "b" at w=0+i0 maps to ζ=0+i ($i=(-1)^{1/2}$), then the above equation can be simplified to the following ordinary differential equation:

$$\frac{P_o}{\rho} + B\frac{dq}{dt} = \frac{P_b}{\rho} + \frac{1}{2}A^2q^2 \tag{3.122}$$

where, q = channel inlet flow rate

$$V_b = Aq, \quad A = \frac{1}{\pi}\,\mathrm{Im}\left[\left(\frac{d\zeta}{dw}\right)_{w=w_b}\right], \quad w_b = 0+i0, \quad \mathrm{Im}(x+iy)=y$$

$$\phi_a = Bq, \quad B = \frac{\ln(|\zeta_a|)}{\pi}$$

$$P_b = P_b(q)$$

This equation is solved for $q^n = Q_{in}^n$ using an implicit discretization as follows :

$$\frac{P_o}{\rho} + B\frac{(q^n - q^{n-1})}{\Delta t} = \frac{P_b^n}{\rho} + \frac{1}{2}A^2(q^n)^2 \tag{3.123}$$

where the only unknown is q^n, since $P_b^n = P_b^n(q^n)$. Further development gives :

$$f(q^n) = (q^n)^2 - 2bq^n + c = 0 \tag{3.124}$$

where, $b = B/(A^2\Delta t)$

$$c = c(q^n) = 2bq^{n-1} - 2(P_o - P_b^n)/(A^2\rho) \tag{3.125}$$

The solution of this implicit equation in q^n is found using a simple Newton iteration scheme, with q^{n-1} providing an initial guess at every time step. The solution gives $q^n = Q_{in}^n$. If this is found to have a negative value then the solution is repeated using the reverse flow formulation as discussed below.

For the case of reverse flow, i.e. when $Q_{in}^{n-1} < 0$, we consider the upstream flow as a jet exiting into an infinite reservoir. We enforce the presence of the reservoir by setting the static pressure, P_b, in the exiting jet to be equal to P_o. Hence, the correct reverse flow rate, q^n, is that which gives P_b

$= P_{xmin} = P_o$ in the computational domain. Recall that P_b is computed by integrating $\partial p/\partial x$ from xmax to xmin, and is a function of the vortical and expansion fields as well as the flow rate at the channel inlet, q^n. The reverse flow problem is solved for q^n using Newton's iteration on the equation :

$$f(q^n) = P_b^n(q^n) - P_o = 0 \tag{3.126}$$

Again, here, if the solution $q^n = Q_{in}^n$ is found to have a positive value, then the flow has reversed and gone back into the cavity, the solution is repeated using the above positive Q_{in}^n formulation.

In each of the above two cases, forward or reverse flow, we required the computation of P_b from the flow inside the computational domain, between xmin and xmax, and for a given inlet flow rate q. As q is changed for each iteration of the Newton method, the vortical and expansion fields are frozen at their given state at the present time step. Hence, for each iteration, using q^n and the frozen vortical and expansion fields, P_b is found by integrating the x-momentum equation from xmax to xmin along the channel center line. The flow velocities at points along this line are computed cheaply for each iteration since the only changing element of the flow field is q^n. Special care is taken in computing ∇u and $\nabla^2 u$ when the path of integration crosses by or across the flame front, since the velocity field is discontinuous along the flame. In the vicinity of the flame interface one sided derivatives are computed so as not to cross the discontinuity. Further, the relevant Reynolds number is used in computing $\partial p/\partial x$ from the x-momentum equation, depending on whether the point considered is in the reactants or the products. The pressure jump across the flame discontinuity is also taken

into account in the computation of the pressure integral. The integration from xmax to xmin gives :

$$P_{in} = P_b^n = p_{ex} - \int_{xmin}^{xmax} (\frac{\partial p}{\partial x})\, dx \qquad (3.127)$$

where the computation of $\partial p/\partial x$ uses proper non-dimensionalization. p_{ex} is the pressure at the domain exit, at xmax, and it is assumed to be known, given the downstream boundary condition, as discussed below.

3.4.2 Exit Boundary Condition

The exit boundary condition problem involves the computation of the combustor exit pressure, $p_{ex}(t)$, at xmax.

One option, which we make use of extensively in studying the combustor flowfield (Ch. 5) is to specify a given $p_{ex}(t)$ as a forced pressure at the combustor exit. In reporting numerical results based on this model, which we call the uncoupled model, we will specify p_{ex} to be either constant at P_{atm} or a sinusoidal function of time of specified amplitude and frequency.

On the other hand, as mentioned above, it is instructive to consider a simplified downstream flow model for the computation of $p_{ex}(t)$. Specifically, we shall use an inviscid compressible 1D channel flow model to connect the cavity exit, xmax, to the atmosphere. In the following, we refer to this downstream channel as the "1D oscillator". The exit flow rate from the combustor provides a time varying inlet flow velocity to the oscillator. In turn, the pressure computed from the oscillator at its inlet provides the required $p_{ex}(t)$ for the combustor flow computation. This combined flow model is referred to below as the "coupled" system.

In the following, we discuss the derivation and implementation of the 1D oscillator solution. At the outset, we stress the simplicity of this flow model. We assume that no combustion takes place in this channel, and we neglect all viscous dissipation. We also restrict the dynamics to the

streamwise direction (1D). The boundary conditions at the inlet and exit of the oscillator, discussed below, are also very simple. The point of this whole exercise is to couple the combustor flow with a system that can act as a forced acoustic resonator, and hence to illustrate a feasible coupling mechanism in actual systems between the combustor and the piping leading to and from it.

We begin by writing the dimensional 1D inviscid gas dynamics equations for a perfect gas, assuming negligible conduction heat transfer, from Appendix A. Note that "~" denotes a dimensional quantity. The conservation equations, and state equation, are as follows :

Mass :
$$\frac{\partial \tilde{\rho}}{\partial \tilde{t}} + \tilde{u}\frac{\partial \tilde{\rho}}{\partial \tilde{x}} + \tilde{\rho}\frac{\partial \tilde{u}}{\partial \tilde{x}} = 0 \qquad (3.128)$$

Momentum :
$$\frac{\partial \tilde{u}}{\partial \tilde{t}} + \tilde{u}\frac{\partial \tilde{u}}{\partial \tilde{x}} + \frac{1}{\tilde{\rho}}\frac{\partial \tilde{p}}{\partial \tilde{x}} = 0 \qquad (3.129)$$

Energy :
$$\frac{\partial \tilde{T}}{\partial \tilde{t}} + \tilde{u}\frac{\partial \tilde{T}}{\partial \tilde{x}} - \frac{1}{\tilde{\rho}\tilde{c}_p}\left(\frac{\partial \tilde{p}}{\partial \tilde{t}} + \tilde{u}\frac{\partial \tilde{p}}{\partial \tilde{x}}\right) = 0 \qquad (3.130)$$

State :
$$\tilde{p} = \tilde{\rho}\tilde{R}\tilde{T} \qquad (3.131)$$

where, $\tilde{R}=\tilde{c}_p-\tilde{c}_v$ is the ideal gas constant.

Eqs. (3.128-131) can be manipulated to give the following system of three equations in 3 unknowns, (ρ,u,T) :

$$\frac{\partial \tilde{\rho}}{\partial \tilde{t}} + \tilde{u}\frac{\partial \tilde{\rho}}{\partial \tilde{x}} + \tilde{\rho}\frac{\partial \tilde{u}}{\partial \tilde{x}} = 0 \qquad (3.132)$$

$$\frac{\partial \tilde{u}}{\partial \tilde{t}} + \frac{\tilde{c}^2}{\gamma\tilde{\rho}}\frac{\partial \tilde{\rho}}{\partial \tilde{x}} + \tilde{u}\frac{\partial \tilde{u}}{\partial \tilde{x}} + (\gamma-1)\tilde{c}_v\frac{\partial \tilde{T}}{\partial \tilde{x}} = 0 \qquad (3.133)$$

$$\frac{\partial \tilde{T}}{\partial \tilde{t}} + \frac{\tilde{c}^2}{\gamma \tilde{c}_v} \frac{\partial \tilde{u}}{\partial \tilde{x}} + \tilde{u} \frac{\partial \tilde{T}}{\partial \tilde{x}} = 0 \tag{3.134}$$

where $\gamma = \tilde{c}_p / \tilde{c}_v$, and $\tilde{c}^2 = \gamma \tilde{R} \tilde{T}$. $\tilde{c}$ is the speed of sound in the fluid.

Next, we non-dimensionalize these equations using the following reference quantities, velocity, $\tilde{U}$, length, $\tilde{L}$, density $\tilde{\rho}_r$, temperature, $\tilde{T}_r$, pressure, $\tilde{p}_r = \tilde{\rho}_r \tilde{R} \tilde{T}_r$, and time, $\tilde{t}_r = \tilde{L}/\tilde{U}$. Where, $\tilde{U}$, $\tilde{\rho}_r$, $\tilde{T}_r$ are chosen as typical values of the velocity, density and temperature at the combustor exit, i.e. at the inlet to the 1D oscillator; and $\tilde{L}$ is the length of the oscillator. We arrive at the following set of 3 dimensionless equations written in vector form :

$$\frac{\partial w}{\partial t} + \underline{A} \frac{\partial w}{\partial x} = 0 \tag{3.135}$$

where, $w = [\rho, u, T]^T$ is the unknown column vector, $p = \rho T$, and $\underline{A}$ is a coefficient matrix given by:

$$\underline{A} = \begin{vmatrix} u & \rho & 0 \\ T/\gamma \rho M_o^2 & u & 1/\gamma M_o^2 \\ 0 & (\gamma - 1)T & u \end{vmatrix} \tag{3.136}$$

where, $\rho = \tilde{\rho}/\tilde{\rho}_r$, $u = \tilde{u}/\tilde{U}$, $T = \tilde{T}/\tilde{T}_r$, $t = \tilde{t}/\tilde{t}_r$, $x = \tilde{x}/\tilde{L}$, $M_o = \tilde{U}/\tilde{c}_o = \tilde{U}/(\gamma \tilde{R} \tilde{T}_r)^{1/2}$, and $T/M_o^2 = \tilde{c}/\tilde{U} = c$. Note, c is the dimensionless speed of sound in the fluid.

Equation (3.135) is solved numerically using the SCM (Split Coefficient Method). This method combines both finite difference techniques and the method of characteristics. The implementation used here is based on the exposition of Anderson et. al. (1984).

The method uses a uniform grid between x=0 and 1, where x=0 is at the combustor exit, or the oscillator inlet (xmax in combustor coordinates), and x=1 is the oscillator exit to the atmosphere. Eq. (3.135) is discretized in time and space using finite differences. For convenience we use a first order discretization in time and space.

The discretization of the time derivative is straightforward :

$$(\frac{\partial w}{\partial t}) \tilde{=} (w_i^{n+1} - w_i^n)/\Delta t \qquad (3.137)$$

where Δt is the time step, $w_i^n = w(x_i, t^n)$, and $t^n = n\Delta t$.

The evaluation of the space derivative uses a properly selected splitting of the coefficient matrix. For each of the three components of w, at a given point in space ($x_i = i\Delta x$, $\Delta x = 1/(N-1)$, $i = 1,2,...N$) and a given instant in time, $t^n = n\Delta t$, the choice of discretization for the x-derivative depends on the direction of the relevant characteristic. The choices are either upwind or downwind differencing.

Therefore, the method proceeds by splitting the coefficient matrix $\underline{A}(x_i, t^n)$ into two matrices, $\underline{A}^+$ and $\underline{A}^-$, such that :

$$\underline{A}_i^n = \underline{A}^+ + \underline{A}^- \qquad (3.138)$$

$$(\frac{\partial w}{\partial t}) + \underline{A}^+ (\frac{\partial w}{\partial x})^+ + \underline{A}^- (\frac{\partial w}{\partial x})^- = 0 \qquad (3.139)$$

where $(\partial w/\partial x)^+$ is discretized using backward differences (upwind), i.e.

$$(\frac{\partial w}{\partial x})^+ \tilde{=} \frac{w_i^n - w_{i-1}^n}{\Delta x} \qquad (3.140)$$

while $(\partial w/\partial x)^-$ is discretized using forward differences (downwind):

$$(\frac{\partial w}{\partial x})^- \tilde{=} \frac{w_{i+1}^n - w_i^n}{\Delta x} \qquad (3.141)$$

The slopes of the characteristics at every point in x-t space determine the splitting of $\underline{A}$. These slopes are in turn given by the eigenvalues of $\underline{A}$, namely :

$$\lambda_1 = u, \quad \lambda_2 = u+c, \quad \lambda_3 = u-c \tag{3.142}$$

Furthermore, for each eigenvalue λ_j, a left eigenvector L_j exists, and is found from :

$$L_j^T (\underline{A} - \lambda_j \underline{I}) = 0 \tag{3.143}$$

where $\underline{I}$ = diag(1,1,1) is the identity matrix.

Using eq. (3.143), the L_j's are found to be :

$$\begin{aligned} L_1^T &= [\ (1-\gamma)c/\gamma\rho,\ 0,\ c/\gamma T\ ] \\ L_2^T &= [\ c/\gamma\rho,\ 1,\ c/\gamma T\ ] \\ L_3^T &= [\ -c/\gamma\rho,\ 1,\ -c/\gamma T\ ] \end{aligned} \tag{3.144}$$

After Anderson et. al. (1984), the splitting of $\underline{A}$ into $\underline{A}^+$ and $\underline{A}^-$ uses :

$$\underline{A}^+ = \underline{T}\ \underline{\Lambda}^+\ \underline{T}^{-1}, \qquad \underline{A}^- = \underline{T}\ \underline{\Lambda}^-\ \underline{T}^{-1} \tag{3.145}$$

where $\underline{T}^{-1}$ is a 3x3 matrix given by :

$$\underline{T}^{-1} = \begin{vmatrix} L_1^T \\ L_2^T \\ L_3^T \end{vmatrix} \tag{3.146}$$

and $\underline{\Lambda}^+$ ($\underline{\Lambda}^-$) is a diagonal matrix that contains the positive (negative) eigenvalues, such that $\underline{\Lambda}^+ + \underline{\Lambda}^- = \underline{\Lambda}$ = diag(λ_1,λ_2,λ_3). Thus, if for example,

$0 < u < c$, then $\underline{\Lambda}^+ = \text{diag}(u, u+c, 0)$ and $\underline{\Lambda}^- = \text{diag}(0, 0, u-c)$. While, if $-c < u < 0$, then $\underline{\Lambda}^+ = \text{diag}(0, u+c, 0)$ and $\underline{\Lambda}^- = \text{diag}(u, 0, u-c)$.

Given $\underline{A}^+$ and $\underline{A}^-$ at each (x_i, t^n), eq. (3.139) is solved for w_i^{n+1} in the interior (i=2,3,... N-1), using eqs. (3.137,3.140,3.141), to give :

$$w_i^{n+1} = w_i^n - \frac{\Delta t}{\Delta x} \left[(\underline{A}^+)_i^n (w_i^n - w_{i-1}^n) + (\underline{A})_i^n (w_{i+1}^n - w_i^n) \right] \qquad (3.147)$$

The boundary conditions at $x_1=0$ and $x_N=1$ are dictated by the slopes of the characteristics at these points, at time t^n. Thus, for example, if $0 < u_1^n < c$, then, at time t^n, the characteristics corresponding to $\lambda_1 = u$ and $\lambda_2 = u+c$ have positive slopes (λ_1, λ_2) in x-t space, and are thus pointing from outside the domain towards (x_1, t^{n+1}), while the third characteristic, $\lambda_3 = u-c$, has a negative slope (λ_3) and points from inside the domain towards (x_1, t^{n+1}). Consequently, two of the gas dynamic variables $(\rho, u, T)^n$ have to be specified at (x_1, t^{n+1}), while the third has to be found from the compatibility condition for the λ_3 characteristic. A similar reasoning is used for the case of $u < 0$ at (x_1, t^n), and for the two cases of positive or negative u_N at (x_N, t^n).

The compatibility condition for each of the three characteristics, λ_j, is the relationship between the gas dynamic variables that has to be satisfied along the characteristic. The condition for each λ_j is found using the corresponding vector $\mathbf{L}_j$ introduced above, from the following expression (see Anderson, 1984) :

$$\mathbf{L}_j^T \left(\frac{\partial \mathbf{w}}{\partial t} + \lambda_j \frac{\partial \mathbf{w}}{\partial x} \right) = 0 \qquad (3.148)$$

Note that the result of the left hand side is a scalar expression. The resulting compatibility conditions are given by :

$$\frac{\partial \ln(\rho T/\rho^\gamma)}{\partial t} + u \frac{\partial \ln(\rho T/\rho^\gamma)}{\partial x} = 0 \qquad \text{for } \lambda_1 = u \qquad (3.149)$$

$$\frac{\partial \ln(\rho T)}{\partial t} + (u+c)\frac{\partial \ln(\rho T)}{\partial x} + \frac{\gamma}{c}\left[\frac{\partial u}{\partial t} + (u+c)\frac{\partial u}{\partial x}\right] = 0 \quad \text{for } \lambda_2 = u+c \tag{3.150}$$

$$\frac{\partial \ln(\rho T)}{\partial t} + (u-c)\frac{\partial \ln(\rho T)}{\partial x} - \frac{\gamma}{c}\left[\frac{\partial u}{\partial t} + (u-c)\frac{\partial u}{\partial x}\right] = 0 \quad \text{for } \lambda_3 = u-c \tag{3.151}$$

We summarize the specification of the boundary conditions at every time step as follows. We implicitly assume that $|u_i| < c$, then :

$$\text{- at } x_1=0 \;\Big|\; \begin{array}{ll} \text{if } u_1^n > 0 & \text{specify } u_1^{n+1} \text{ and } T_1^{n+1} \quad (3.152) \\ \text{if } u_1^n < 0 & \text{specify } u_1^{n+1} \quad (3.153) \end{array}$$

$$\text{- at } x_N=1 \;\Big|\; \begin{array}{ll} \text{if } u_N^n > 0 & \text{specify } p_N^{n+1} \quad (3.154) \\ \text{if } u_N^n < 0 & \text{specify } p_N^{n+1} \text{ and } T_N^{n+1} \quad (3.155) \end{array}$$

where, $p=\rho T$.

The velocity u_1^{n+1} in (3.152,3.153) is the known space averaged flow speed at the combustor exit at t^n, while the pressure at the oscillator exit, p_N^{n+1} in (3.154,3.155), is specified to be atmospheric. The specification of the temperature at the oscillator inlet and exit, T_1^{n+1} and T_N^{n+1}, in (3.152) and (3.155), is not straightforward. In the actual system, T_1 is a time varying quantity depending on the amount of products versus unburnt reactants leaving the combustor at a given time. On the other hand, the combustion does not stop at the combustor exit. It continues as the mixture is convected downstream. Obviously, our simple non-reacting 1D oscillator model cannot account for this extra burning and the associated heat release. We have chosen to use an inlet temperature T_1 that assumes the fluid at that location to be at the products' temperature, T_b, which is a fixed quantity, hence $T_1 = T_b$. Again, while this is clearly not the actual situation, it suffices for

the present purpose of constructing a simple 1D oscillator to examine the general features of the combustor-system coupling. Further, given the low Mach number flow considered in this work, the temperature variations along the 1D oscillator are expected to be relatively small. Consequently, the exit temperature, T_N, is specified to be the products' temperature, T_b, as well. The flow reversal at the exit ($u_N < 0$, in 3.155), if it occurs, is expected to be intermittent, occuring only during a fraction of the flow oscillation cycle. It is therefore expected to be short lived, since the period of the flow oscillation is merely a fraction of a second (see for example Vaneveld et. al., 1982). Hence, it seems reasonable to assume that the flow rushing into the pipe at x_N, from the atmosphere, consists of hot products, still at T_b.

Finally, the initial conditions used for the gas dynamic variables (ρ,u,T) are given by: $\rho=\rho_b$, u=1, $T=T_b$.

3.5 Overall Solution Algorithm:

In the following we present an overview of the algorithm used in the implementation of the numerical solution described above.

We describe the sequence of tasks that are executed by the code at each time step. The previous time step is t_{n-1}, while the present one is t_n. We use $\{\Omega^{n-1}\}$ as the set of vortices in the computational domain at the previous time step. Similarly for the sources ($\{S^{n-1}\}$). We use VOF as an abbreviation for the "Volume of Fluid" method, discussed in the description of the combustion solution above. Other symbols follow easily, or are explained below.

The algorithm, at each time step, is as follows :

1) Begin a new time step, $t_n = n\Delta t$.
2) Get the new exit pressure, $P_{ex}-P_{atm}$, from the downstream boundary condition.
3) Get the new inlet flow rate, Q_{in}, and inlet pressure P_{in} from the upstream boundary condition, using the cavity flow field : $(\{\Omega^{n-1}\},\{S^{n-1}\},Q_{in})$.
4) Find Umax, from the flow field : $(\{\Omega^{n-1}\},\{S^{n-1}\},Q_{in})$, on the combustion grid. Use Umax to find the suitable (stable) combustion time step Δt_f, and hence to set the number of combustion time steps per vorticity time step $J=\Delta t/\Delta t_f$.
5) Do the combustion calculation in J time steps Δt_f.
   5.a) For j=1 to J, where : $t_j = t_{n-1} + j\ \Delta t_f$.
   5.b) Advect the products by the dilatation flow field : $\{S^{j-1}\}$.
   5.c) Advect the products by the flow field : $(\{\Omega^{n-1}\},Q_{in})$
   5.d) Using VOF, find the burning speed in every cell, $S_u(i,j)$.
   5.d) Propagate the flame by burning into the reactants, find Δf_{ij}.
   5.e) Find the new flame interface by VOF.

5.f) Generate the new sources $\{S^j\}$ from Δf_{ij} in every cell.

5.g) goto (5.a).

6) Remember two source fields, the one from the previous time step $\{S^{n-1}\}$, and the new one $\{S^n\}$ from the last combustion time step $\{S^n\}=\{S^J\}$.

7) Generate new vortex sheets at the domain walls, using the flow field : $(\{\Omega^{n-1}\},\{S^{n-1}\},Q_{in})$, and propagate them by advection and diffusion. Those that become new blobs are set aside, refer to them as $\{\Omega_{new}\}$.

8) Update the locations of the vortices: $\{\Omega^{n-1}\}$, by advection, using the flow field : $(\{\Omega^{n-1}\},\{S^{n-1}\},Q_{in})$, and then by diffusion. Deal with those that enter sheet layers or leave the domain.

9) Form the new set of vortices $\{\Omega^n\}$ from those left after step (8) above, and from $\{\Omega_{new}\}$ (step 7). The complete new flow field is given by : $(\{\Omega^n\},\{S^n\},Q_{in})$. This is flow field for time t_n.

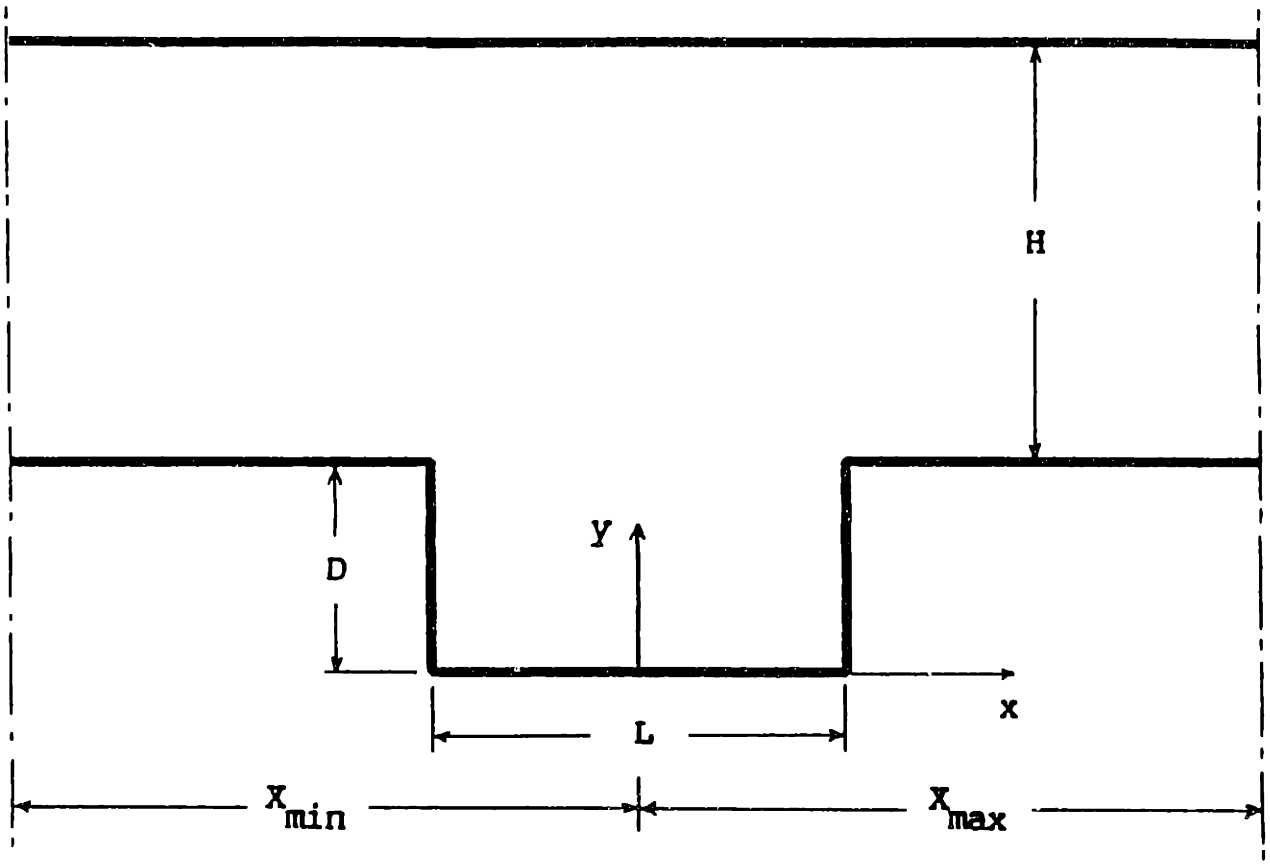

Figure 3.1 - Nomenclature and geometry of dump combustor

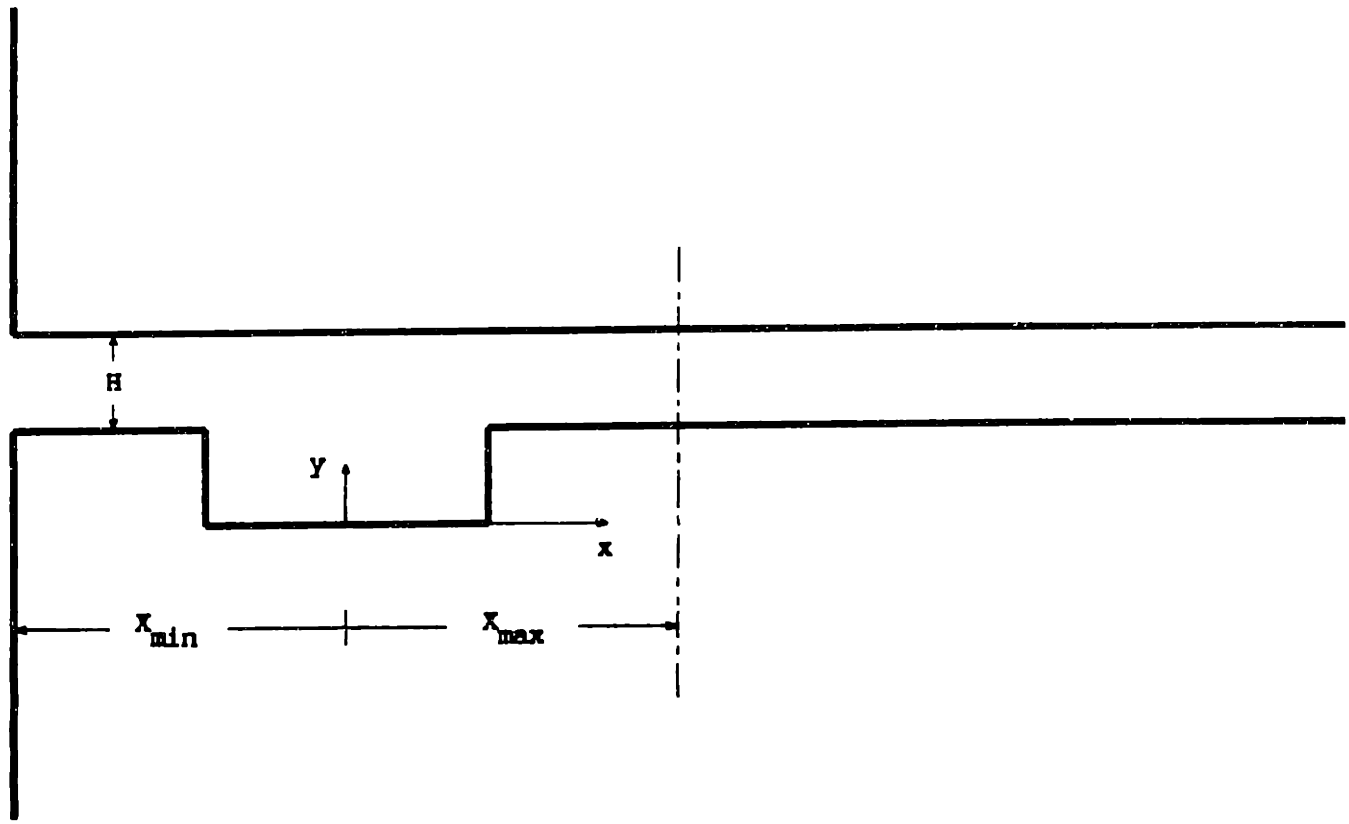

Figure 3.2 - Upstream and downstream flow configurations.

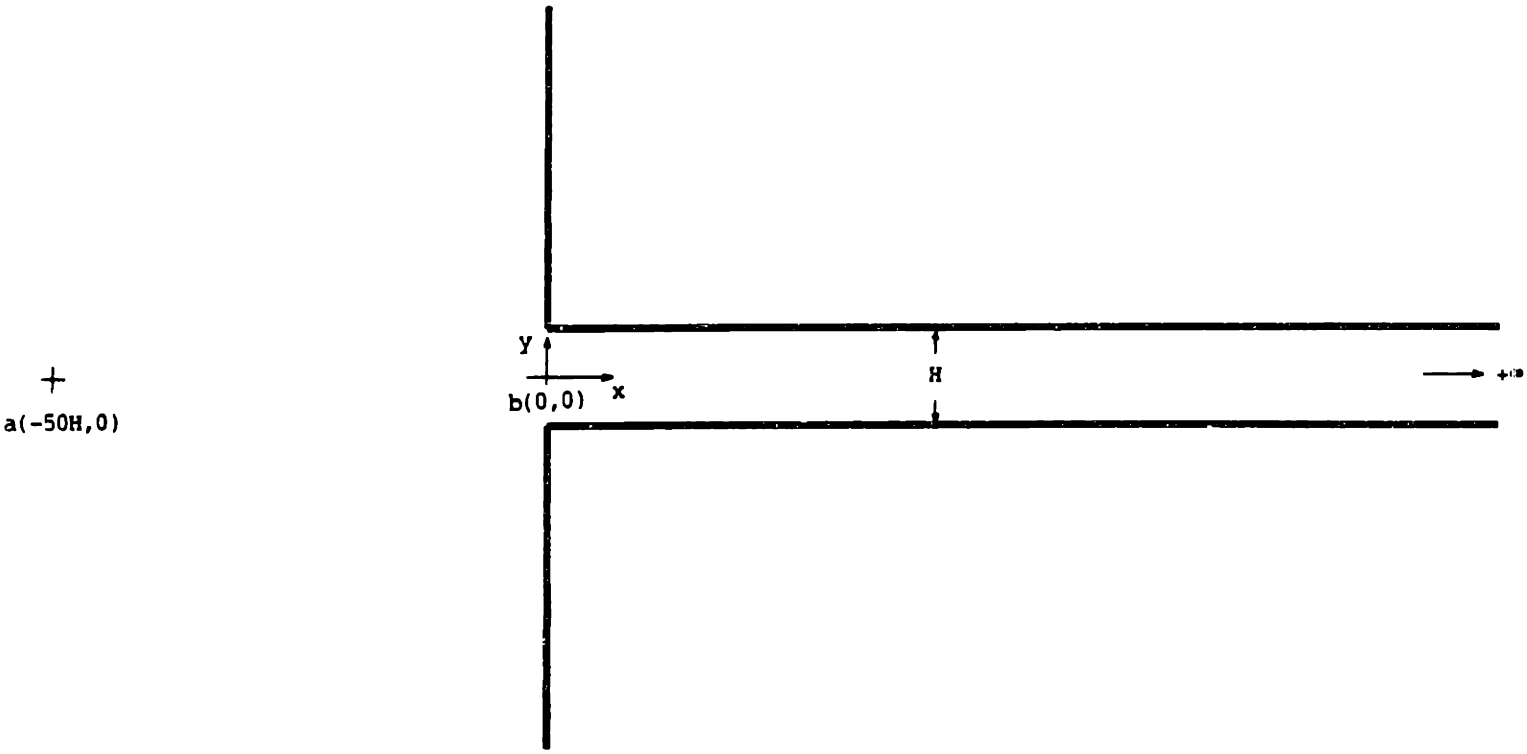

Figure 3.3 - Inlet flow boundary condition.

4. NON-REACTING FLOW

Let us now consider the non-reacting flow in a dump combustor. The study of the underlying dynamics of this flow, given the exclusion of the effects of heat release, is a good introduction to the more complex reacting case.

In the following discussion, we shall be concerned with the dynamics of low Mach number, hence incompressible, fluid flow in geometries that exhibit the essential features of a dump combustor flow configuration. These features include: (1) the shear layer starting at the upstream edge of the dump and separating the fast mainstream fluid from the slower recirculating fluid in the dump; (2) the recirculation zone in the dump; and (3) the constraint presented by the existence of the constriction at the downstream end of the dump. Because of these diverse features of the flow field, the discussion below will touch upon several flow configurations that stress one or more such features in particular. These configurations include free shear layers, forced and impinging shear layers, backward-facing step, cavity, and bluff-body flows. Because of the assumed incompressibility of the working fluid, we shall look at experimental results from both air and water flows.

For consistency in extrapolating the results to combustor flows, we are interested in high Reynolds number dynamics. Namely, $Re=UD/\nu > 1000$, where D is depth of the dump, U is the mainstream flow velocity at the upstream edge of the dump, and ν is the kinematic viscosity of the fluid. At these Reynolds numbers, both the shear layer and the recirculation zone are highly unstable. This instability results in the shedding of vortical structures at certain characteristic frequencies. At low Reynolds numbers, $Re=O(100)$, the instability of the flow tends to become insignificant due to the high viscous dissipation, which acts to diffuse vortical structures before they grow to significant sizes. Our results exhibit a trend towards higher instability,

hence more coherent vortical structures and significant flow oscillation, as the Reynolds number is increased. For Re > 1000, we have found the flow field to vary little with the Reynolds number, as is generally expected for high Reynolds number flows. The majority of our results use Re=2500, except in cases where comparison with experimental data dictates otherwise.

The numerical study reported herein uses the 2D cavity-in-channel flow configuration in Fig. 3.1, repeated here for convenience in Fig. 4.1. The numerical solution is as described in Chapter 3, with $u_e=0$ and Re fixed everywhere (non-reacting flow). The choice of a 2D model obviously restricts the range of phenomena that can be studied, by suppressing flow instability as well as vortex stretching in the 3^{rd} dimension. This is not a severe restriction, however, since (1) the significant dynamics of shear layer flows correspond to the large scale, roughly 2D, flow structures (see Brown & Roshko, 1974; Oster & Wygnanski, 1982) and (2) the large scale dynamics of recirculation zones, as in the wake behind a bluff body, are expected to be also sufficiently two dimensional. Both of these flows, on the other hand, have no walls downstream of the separation point. In particular, the recirculation zone behind a step or in a cavity does not display the same degree of 2D organization as a bluff body flow, since the flow structures lose their coherence upon interaction with the walls downstream. On the other hand, the significant low frequency, albeit broad peaked, oscillations in these flows are still determined by the large scale 2D dynamics.

The upstream and downstream boundary conditions used in the computations below do not include the pressure boundary conditions described in Chapter 3. Instead, we choose a simple upstream boundary condition that involves specifying the inlet velocity profile at xmin, and a downstream boundary condition that involves the deletion of vortex elements beyond the end of the computational domain, x=xmax. The reason for using these simple boundary

conditions is to ensure a less complicated flow field, especially since for low Mach number non-reacting flow acoustic phenomena are generally negligible.

In the following numerical study and accompanying discussion we shall stress one aspect of the cavity geometry that is found to be most significant in determining the flow dynamics. This is the cavity aspect ratio : length/depth or L/D ratio. As we shall see below, short, or deep, cavities exhibit dynamics that are quite different from those of long, or shallow, cavities. In fact, we will try to demonstrate that there are two significant mechanisms that determine the unsteady oscillations of cavity flows. These are the instability of the shear layer and that of the recirculation zone. As the cavity length is decreased to a fraction of the depth, the shear layer instability, modulated by the impingement at the downstream cavity edge, dominates over that of the recirculation zone. The structure of the recirculation zone tends to a relatively quiescent eddy for small L/D. On the other hand, as the length of the cavity is increased with respect to the depth, the recirculation zone gains dominance until, by $L/D > 4$, the flow resembles a step flow or a wake behind a bluff body, where the shedding frequency of the recirculation zone is clearly dominant.

We begin below by a review of previous studies on shear layers, including free, forced and impinging shear layers, as well as cavity, step, and bluff body flows. The present numerical results and conclusions are then reported, with a clear distinction between the short and long cavity cases.

4.1 Background :

The Kelvin-Helmholtz instability leads to the formation of large scale vortical structures in free shear layers at a wide range of frequencies. The mode observed most frequently is the natural or most unstable frequency, f_n, which corresponds to a Strouhal number of $St_n = f_n \theta_o / U_s \sim 0.033$, where θ_o is the momentum thickness of the undisturbed layer and U_s is the mean velocity in the layer. In fact, the value of St_n depends on the velocity distribution within the initial shear layer, thus some variation in the above value is observed.

The behavior of a shear layer forced by controlled external excitation applied by oscillating the free streams has been studied extensively, e.g., Ho and Huang (1982) and Ghoniem and Ng (1987). Results show that the shedding frequency is the harmonic of the forcing frequency closest to the most unstable frequency of the shear layer. Thus, as the forcing frequency, f_f, is decreased, the rollup frequency, or the response frequency of the shear layer, f_r, experiences jumps which correspond to the harmonics of the forcing frequency, $n f_f$, where n is an integer. These shed eddies are, however, forced to pair in a collective manner to form eddies at the forcing frequency.

A shear layer impinging on a downstream wedge experiences forcing due to the upstream influence of the disturbance generated by the impingement of flow structures on the wedge. This flow was studied experimentally by Hussain and Zamman (1978), and Ziada and Rockwell (1982). The impinging shear layer was found to exhibit jumps in its oscillation frequency with the variation of impingement length, L, mainstream velocity, U_o, and separating boundary layer momentum thickness, θ_o. These jumps correspond to changes in the number of waves, or eddies, which exist simultaneously within L. The eddy impingement frequency, f_i, which is the same as the feedback frequency from the

downstream edge, f_f, is also the same as the rollup frequency, in all frequency stages. The feedback frequency plays the role of a forcing frequency.

The instability of cavity flows has been the subject of various studies. Ghaddar (1985) suggests that it is a result of the interaction between the shear layer Kelvin-Helmholtz instability and the channel flow Tollmien-Schlichting (T-S) waves. Schadow & Wilson, (1985) and Schadow et. al. (1984), working on a step flow with a downstream constriction, suggest that the shedding frequency is determined by the acoustic properties of the apparatus. On the other hand, cavity flow oscillations have been observed in essentially incompressible flow, and when the upstream flow was free of significant T-S oscillations, suggesting that other frequency selection mechanisms may exist; see, for example, Rockwell and Knisely (1979), and Knisely and Rockwell (1982).

Knisely and Rockwell (1982) found, for a planar ramp-cavity geometry with L/D around 2.0, that $L/\lambda = n$, where λ is the wavelength of the dominant oscillation. The dominant frequency was found to experience jumps with the variation of L/θ_o, such that the dominant Strouhal number, $St = f\,\theta_o/U_o$, was in the range: 0.011 - 0.018. Several lower amplitude oscillation frequencies, which are fractions of the dominant frequency, were also observed depending on the range of L/θ_o. It was concluded that at least some of the observed short cavity dynamics can be explained by the impingement feedback process as with the shear layer-wedge system.

Sarohia (1977) studied oscillations in an axisymmetric cavity flow, with $L/D < 1.1$, where D is the depth of the cavity, and found $L/\lambda = n + 1/2$. The cavity depth, was found to affect the dynamics if it is less than 5 - 10 δ_o, where δ_o is the boundary layer thickness at the upstream separation edge, defined as the point where $u/U_o = 0.99$. The flow dynamics in these cavities,

which identify as short cavities, are apparently dominated by the shear layer instability, as manifested by the shedding of small scale eddies, on the order of magnitude of the original shear layer thickness.

Ethembabaoglu (1973) conducted an investigation covering a relatively wide range of rectangular cavity lengths, $L/D = 0.3 - 5.5$, where D is the depth of the cavity. This study was done at high Reynolds number, $U_o D/\nu = 7 - 9 \times 10^5$. The dominant frequency was found to exhibit one jump, while maintaining an overall decrease with increasing L/D. The value of fD/U_o was in the range: 0.2 - 1.5, for the above range of L/D. Neary and Stephanoff (1987) report a Strouhal number $fD/U_o = 0.24$ for flow over a rectangular cavity with $L/D = 3.5$ and Re_D around 2500. In the above two studies the flow was such that $D/\delta_o \leq 3$, thus these cavities were shallow with respect to the separating boundary layer.

More recently, Gharib and Roshko (1987) and Gharib (1987) report an experimental study of flow in a short axisymmetric cavity, where they identify dynamics similar to those described by Rockwell and Knisely for short cavities. They also describe the flow in a long axisymmetric cavity, with L/D=1.4, as being similar to a wake flow. Specifically, they report flow visualization results which indicate that, in this flow regime, the axisymmetric cavity shear layer becomes highly asymmetric, and no longer reattaches onto the downstream corner. The reattachement point is observed to be below the downstream corner. Further, the cavity flow is observed to be unstable on a large scale, comparable to the depth D. Generally, they suggest that the flow field in this regime begins to show some resemblance to a 3-dimensional bluff-body wake.

Other studies on long cavities include the numerical investigation of Kailasanath et. al (1986) where a cavity with $L/D = 11.6$ was used, with fD/U_o

= 0.09, and that of Menon and Jou (1987), where fD/U_o = 0.1 with a cavity where L/D = 10 approximately.

Evidently, cavity flows are complicated beyond impinging shear layer flows by the existence of recirculating eddies inside the cavity. According to the experimental information cited above, the frequency of oscillation depends on L, D, U_o, and θ_o. For a cavity in a channel, the channel height, H, may also be important. Further, for high Mach number flows, channel and cavity acoustics may also contribute to the frequency selection mechanism.

While the flow structure and instability mechanism for short cavities appear to be understood on the basis of the impinging shear layer mechanism, the dynamics of flow in longer cavities are not well understood despite the above investigations. The flow dynamics in long cavities appear to be inherently different from those in short cavities due to the interaction between the separating shear layer and the cavity floor, 3D effects, as well as the instability of the recirculation zone and the concomitant shedding of large scale eddies. The relevance of recirculation zone dynamics in long cavities is expected since, in the limit of large L/D, the cavity flow must tend to a step flow configuration, where the recirculation bubble is known to exhibit oscillation and large scale shedding of vortical structures.

Other flows whose dynamics are determined by a recirculation bubble have also been studied extensively, and their results may be used to shed some light on the dynamics of long cavities. Both step flows and bluff-body flows fall within this category.

In step flows, the work of Tani et. al (1961), and Honji (1975), provided some of the early indications about the transient structure of the recirculation bubble in a non-reacting flow over a backward-facing step. Later work on the same configuration, such as Driver et. al. (1987), Eaton and Johnston (1981), Pitz and Daily (1981), and Schadow et. al. (1984), found

fD/U_o to be in the range 0.04-0.16, i.e. roughly : $fD/U_o = O(0.1)$. The onset of 3D instabilities masks the 2D recirculation zone instability in these flows, resulting in a frequency spectrum that is broad peaked around the Strouhal number of 0.1.

Bluff body flows are found to exhibit similar dynamics. Works by Kiya and Sasaki (1983,1985), Parker and Welsh (1983), and Cherry et. al (1984) found the Strouhal number fD/U_o to be in the range 0.1-0.2, where D is here the dimension of the bluff body normal to the undisturbed flow direction. Again, $fD/U_o = O(0.1)$.

These results, along with the above long cavity results, agree on an order of magnitude of 0.1 for the Strouhal number fD/U_o. This suggests that the recirculation bubble may be the common mechanism that defines the dynamics of all these flows.

The role of the recirculation bubble in defining the dynamics of long and short cavity flows is demonstrated in the following exposition of our numerical results. We illustrate the accuracy of the model by comparisons with experimental measurements, and we elaborate on the nature of the dominant instability mechanism for a wide range of values of L/D (2.0-8.0).

4.2 Results :

Results have been obtained for various values of L/D, L/θ_o, and H/D. The purpose of our analysis is to define the mechanism of oscillation at different values of these parameters and determine the corresponding frequency in each case.

The following discussion deals with the dynamics of short and long cavities separately. It is difficult to define a value for L/D at which one can distinguish between a short and a long cavity. We will make this distinction based on the dynamics of the separating shear layer. If the shear layer impinges on the downstream edge before it reaches the bottom wall, we call this case a short cavity. If the shear layer impinges on the bottom wall first, even though this may happen intermittently, this is a long cavity. By experimenting with various values of L/D, we found that $L/D > 2$, corresponds to a long cavity. The long cavity case is more interesting for the dump combustor analysis, given typical combustor geometries. On the other hand, we start by analyzing results for the $L/D = 2$ case because it represents a more natural extension of the impinging shear layer analysis.

Where dimensionless numerical parameters and results are reported, the reference quantities used are as follows. The reference length is the cavity depth D. The reference velocity is the upstream spatial-mean streamwise velocity U_m, where the product of U_m and the channel height is the fixed prescribed upstream inlet flow rate per unit depth in the 3rd dimension. The reference time is D/U_m, and the reference circulation is $U_m D$.

4.2.1 Short Cavity :

This is the case for which $L/D < 2$; the separating shear layer impinges on the downstream edge before it reaches the bottom wall. In the following, we compare the numerical results on the mean velocity with experimental measurements, and study the dynamics of the shear layer in terms of the rollup of vortex eddies.

4.2.1.1 Mean Velocity Profiles :

The experimental measurements of the mean velocity profiles within a rectangular cavity, reported by Sinha (1978) and Rockwell and Knisely (1979), were used to check the accuracy of the numerical solution. Figure 4.2 shows a comparison between the numerical results and the measurements of Sinha (1978). The parameters used in his wind tunnel experiment are : $L/D = 2.0$, $\delta_o/D = 0.56$, and $U_oD/\nu = 2140$, where, as in Fig. 4.1, δ_o is the boundary layer thickness at the upstream edge of the cavity, and U_o is the main stream velocity in the channel at that location. Relevant numerical parameters used in our simulation are: $h_s/D = 0.25$, $\Gamma_m/U_mD = 0.0208$, $\Delta t U_m/D = 0.1$, and $\Delta_s/D = 0.0207$; where h_s is the length of a vortex sheet, Γ_m is its circulation, U_m is the spatial mean flow velocity in the upstream channel, and Δ_s is the thickness of the sheet region. Vortex elements were deleted at $xmax/D = 4$. The experimental value of the boundary layer thickness at the step was achieved in the numerical simulations by varying the inlet channel length and the boundary layer thickness at xmin. The computations were performed until a stationary state was reached, and a sample of 1050 time steps was collected to obtain the average velocity distributions.

Figure 4.2 shows good agreement between the computed profiles and the experimental results, most notably within the shear layer. Two places where disagreement is noticeable are the lower parts of profiles (2) and (3). Within this region, the experimental profiles are less certain, which was

noted by the author and is evident in profile (2) in the figure where two values of the velocity were reported at the same location. The disagreement in the boundary layer region of profile (6) is probably due to both three dimensional effects and to the fact that, in the numerical simulation, vorticity is deleted at xmax/D = 4.0 for computational efficiency.

The comparison between the computed mean velocity profiles and those measured by Rockwell and Knisely (1979) is shown in Fig. 4.3. In this experiment, water was used in the flow over a cavity in a channel without a top wall. The experimental flow and geometry specifications are: θ_0/D = 0.014, L/D = 2, U_oD/ν = 7571. Relevant numerical parameters are: h_s/D = 0.25, Γ_m/U_mD = 0.0208, $\Delta tU_m/D$ = 0.1, Δ_s/D = 0.015 and xmax/D = 4. The figure depicts the normalized velocity u/U_{max} plotted against a normalized coordinate $(y-y_{1/2})/\theta$, at x/D = 0.92. Here U_{max} is the maximum velocity at the specified x-location, x and y are as defined in Fig. 4.1, $y_{1/2}$ is the value of y at which u/U_{max} = 0.5, and θ is the shear layer momentum thickness at the specified x location, between u=0 and $u=U_{max}$. The comparison between the two profiles shows excellent agreement in the shear layer. No experimental data is provided in the recirculation zone.

The mean velocity profiles for a short cavity indicate that a separating shear layer exists between the main stream and the cavity fluid, while a recirculating flow dominates the downstream region of the cavity. The long-time-average streamlines computed from the results of the above run with U_oD/ν = 7571, plotted in Fig. 4.4, support this conclusion and reveal further detail of the mean flow structure. This plot shows the dominant eddy residing in the downstream part of the cavity, as well as a smaller upstream corner counter-rotating eddy. These results are in general agreement with previous observations, see for example Hardin and Mason (1977), Ghaddar et. al.

(1986), and Ethembabaoglou (1973). The time dependent flow structure is discussed in detail below.

4.2.1.2. Short Cavity Dynamics :

The flow dynamics in a short rectangular cavity, L/D = 1-2, were investigated experimentally by Rockwell and Knisely (1979). They reported that the flow displayed jitter in the location of impingement of the shear layer eddies on the downstream cavity edge which, they suggested, could be due to low frequency modulation by the adjacent recirculation zone of the cavity, as well as three dimensional effects. Despite this jitter, a peak in the frequency spectrum was identified at $f\theta_o/U_o = 0.016$.

Knisely and Rockwell (1982) studied a modified cavity in which the upstream cavity edge was replaced by a slanting ramp in order to reduce the noise and to enhance the organization of the rollup process. They used L/D = 2. In this study, it was found that two stages of oscillation, depending on the value of L/θ_o, may occur. The frequency spectrum, in either stage, displayed a dominant, largest amplitude peak, which corresponded to the frequency of shear layer eddy rollup, along with other lower frequency peaks at lower amplitudes. The dominant Strouhal number, $St = f\theta_o/U_o$, in either stage, was in the range: 0.011-0.018, depending on the value of L/θ_o.

The first stage described above corresponds to a flow structure which we will refer to as a one-eddy system. In this regime, a single eddy occupied most of the impingement length, with a smaller eddy being shed from the upstream edge. The flow structure which corresponds to the second stage will be referred to as a two-eddy system. Here, two eddies existed simultaneously within the impingement length. In both Rockwell & Knisely (1979) and Knisely & Rockwell (1982), the separating shear layer impinged on the downstream edge, and δ_o/D was small enough, 0.1-0.2, to minimize the interaction between the shear layer eddies and the cavity floor. The modulation of the shear layer dynamics by the recirculating eddies inside the cavity was observed in both stages in the form of low frequency overall flapping of the layer.

The results of the numerical simulations for the dynamics of the short cavity are now discussed. The relevant numerical parameters are: $h_s/D = 0.20$, $\Gamma_m/U_m D = 0.0167$, $\Delta t U_m/D = 0.05$, $\Delta_s/D = 0.011$, $xmax/D = 4.0$. The flow parameters are: $U_o/U_m = 1.026$, $U_m D/\nu = 7500$, and $\theta_o/D = 0.02$. Figure 4.5 shows a sequence of time frames depicting the evolution of the flow structure in terms of the distribution of the vortex elements in the interior of the domain, with a straight line segment originating at the center of each element proportional to and in the direction of its velocity. Within this period, four eddies, marked by short arrows, are shed from the separating shear layer. The mean period between two sheddings is $T = 1.17$, corresponding to a Strouhal number $St = f\theta_o/U_o = 0.0166$.

Within a period of 27.0, a total of 15 eddies were shed. These eddies can be classified in two groups, depending on their frequency, size, speed of propagation and overall influence on the flow field. The shedding shown in Fig. 4.5 involves the smaller, faster, and hence more frequent eddies that travel in the shear layer along the top of the cavity, with little effect on the recirculating flow within the cavity. Ten such eddies were observed, nine of which had $S_t = 0.013 - 0.019$, with a distribution skewed towards higher frequencies, while one eddy was observed at $St = 0.04$. This range of Strouhal numbers, 0.013-0.019, where most of the shear layer eddy shedding occured is in general agreement with the above experimental data.

In the following, we analyze the flow structure observed in the shear layer and within the cavity during the most frequent shedding. In Fig. 4.5, the centers of the separating shear layer eddies are marked with an arrow. In Fig. 4.6, the edge of the shear layer is indicated by a solid line, while the velocity vectors are plotted with respect to a coordinate system moving at $0.5\ U_m$. Plotting the vorticity field with respect to this moving coordinate system serves to indicate the extent and structure of the shear layer in

terms of vortex structures. Both figures show the presence of two eddies within the impingement length. According to the above distinction between the two regimes in a short cavity, this picture suggests that the dynamics fall in a two-eddy regime. Moreover, in the laboratory reference frame, we note the existence of two large recirculating eddies within the cavity, a counter clockwise rotating eddy downstream of the backward-facing step, and a clockwise rotating eddy which occupies the other side of the cavity. A smaller eddy also resides at the bottom corner of the forward-facing step in the downstream end of the cavity. The shear layer eddies flow over these two large recirculation eddies that act as a buffer between the shear layer and the bottom wall of the cavity. This is an important distinction between the short cavity and the long cavity dynamics. In the mean velocity reference frame, the separating shear layer eddies rollup, growth, and impingement on the downstream edge is shown. The dark line defines the demarcation between the vorticity laden fluid and the mainstream irrotational flow.

It should be noted that the rollup of the separating shear layer was induced by its instability. The "white" noise, which exists in the computations due to the discrete nature of the numerical method and the random noise associated with the simulation of diffusion, acts as small amplitude perturbations at a wide range of frequencies. The fact that some eddies were shed at frequencies different from the most preferred frequency, St = 0.016, shows that, as in the case of a free shear layer, the separating shear layer is unstable to a range of frequencies.

The dynamics of the larger, slower, and hence less frequent eddies are illustrated in Fig. 4.7. This sequence of frames shows the shedding of one such eddy. Within a time period of 27.0, five slow eddies were observed, with St as low as 0.004. Comparison of the frames shown in Fig. 4.7 with Fig. 4.5 suggests that fundamental differences exist between the mechanism of eddy

shedding in each. The eddy forming at the separation edge in Fig. 4.7 travels slower than the shear layer eddies in Fig. 4.5 because it generally exists at a lower level within the cavity. It grows to become significantly larger than the shear layer eddies, and its interaction with the recirculating eddy in the downstream side of the cavity leads to a significant flapping of the shear layer above the cavity. This activity does not inhibit the smaller shear layer eddies which are seen to shed and ride on the stronger wave. This overall picture is reminiscent of the experimentally observed modulation of the separated shear layer dynamics by the low frequency oscillation of the recirculation zone within the cavity (Rockwell and Knisely, 1979). It seems that this slow shedding is the mechanism responsible for the low frequency oscillation of the recirculation zone within the cavity and the flapping of the shear layer.

Figures 4.8 and 4.9 show the instantaneous streamlines in a sequence of frames corresponding to Figs. 4.6 and 4.7, respectively, for fast and slow shedding. These plots indicate again the difference between the two modes of instability. Ghaddar et. al. (1986) report streamline plots that are similar to the slow shedding in Fig. 4.9.

The spectrum of frequencies evident in the above visual observations can be seen quantitativly by studying the flow velocity fluctuations at specific points. Figure 4.10 shows the u-velocity fluctuation at one station in the shear layer above the cavity close to the downstream edge ($x/D = 0.95$, $y/D = 1.0$) and the corresponding frequency spectrum. The two plots indicate the existence of strong low frequency oscillation, along with weaker high frequency dynamics. It is noted that the experimental results for the $L/D = 2$ ramp-cavity geometry of Knisely & Rockwell (1982), while showing a similar spread in frequencies, find a higher amplitude for the frequency peak corresponding to the shear layer eddy rollup than the modulation frequency.

The difference between the two results indicates that the recirculation zone dynamics of the geometries considered are different. The investigation in Rockwell & Knisely (1979) used an actual cavity, but they report spectra for a shorter cavity than the one considered here, namely $L/D = 1.1$.

The frequency peak with the highest amplitude in the spectrum in Fig. 4.10 occurs at a Strouhal number, $St = f\theta_o/U_o = 0.004$, or a frequency $fD/U_m = 0.22 = 1/4.5$. This frequency corresponds roughly to the long period oscillation observed in the velocity trace in Fig. 4.10, and to the period of large eddy shedding in Fig. 4.7.

The mean observed streamwise propagation velocity of the slow eddies within the cavity length, i.e. the phase velocity at their frequency, was found to be: $c/U_m=0.33$. Hence, the oscillation wavelength corresponding to the frequency $fD/U_m=0.22$ is $\lambda/D=1.5$. Consequently, we find $fL/c=L/\lambda=1.33$. This result, when interpreted in terms of the formulation: $L/\lambda=[n,n+1/2]$, suggests a value of the integer $n=1$, hence indicating a first stage oscillation, or a one eddy system within the cavity length in the recirculation zone. This conclusion is in agreement with our definition of a one eddy system, as demonstrated by observing the flow structure in Fig. 4.7, where the large recirculating eddy in the downstream end of the cavity occupies most of the cavity length while the smaller eddy is being shed at the upstream edge.

The dynamical results indicate that both the "shear layer" and "recirculation zone" modes of instability exist for the cavity geometry with $L/D = 2$. It is also evident that the shear layer does not interact directly with the bottom wall of the cavity; the recirculation eddies within the cavity form a buffer between the shear layer and the cavity floor, hence the reference to this geometry as a short cavity. This is not the case for a cavity with $L/D > 2$, as discussed below.

4.2.2 Long Cavity - Dynamics of Recirculation Zones :

For cavities most often used in combustion applications, $L/D > 4$. As we mentioned before, it is expected that in this case the flow dynamics will be different from those of a short cavity since the separated shear layer, driven by the flow within the cavity, will reach the bottom wall before impinging on the other side of the cavity. We have performed several simulations for different values of L/θ_o since it was initially suspected that, as in the case of short cavity, the thickness of the boundary layer would control the dynamics within the trough. Fig. 4.11 shows a series of frames for the flow field for the case with $L/D = 4$, $L/\theta_o = 183$, $Re_D = U_m D/\nu = 2500$, and $U_o/U_m = 1.04$. The numerical parameters used in this case are, $h_s/D = 0.25$, $\Delta t U_m/D = 0.1$, $\Gamma_m/U_m D = 0.0208$, $\Delta_s/D = 0.0179$, and $xmax/D = 4$.

The numerical results reveal that: (1) the flow structure appears to be completely different from that observed in the short cavity case and, in particular, the large eddies which resided permanently in the left and right hand sides of the trough in the short cavity are now in constant transition; and (2) the dominant frequency of oscillation is associated with the motion of the recirculation eddy away from the step and the rollup of another eddy. This motion is periodic, and all the events associated with a single period are repeated every cycle. In the following we examine one complete cycle of events for the sample of frames for time 70 - 83 shown in Fig. 4.11.

At time 70, the flow structure consists of a large leading eddy moving towards the cavity edge and a satellite counter-clockwise rotating eddy which resides between the leading eddy and the step. There are also two small shear layer eddies flowing on the top side of these two eddies. Between time 71 and 79, a new trailing eddy, with its own satellite counter clockwise rotating eddy, forms at the step while the leading eddy is moving into the downstream edge. The trailing eddy starts as a rollup eddy in the separating

shear layer, however, instead of moving on top of the large eddies, it is pushed downwards by a strong flux of channel fluid into the cavity and is anchored at the step, growing by entraining more of the vortical fluid delivered by the shear layer. During its growth, the shear layer rolls up on its upper side, shedding small eddies, as shown in time 74 - 79, which are engulfed by the growing anchored eddy.

At time 77, the interaction between the trailing eddy and the step corner results in the generation of another satellite counter clockwise rotating eddy. As the trailing eddy grows by entraining more vortical fluid and engulfing the separating shear layer eddies, its satellite counter clockwise eddy grows. The trailing eddy then moves downstream, and a gap is generated between it and the step side wall, as seen in time 79 - 81. Within the next part of the cycle, the separating shear layer at the step will "dip" into the cavity and shed a new eddy that will become the new trailing eddy, while the first eddy will become the leading eddy.

We now describe the development of the leading eddy, which takes place on the right hand side of the trough while the trailing eddy is growing on the left hand side. As soon as the trailing eddy separates from the step, it ceases to entrain vortical fluid from the shear layer, as shown in time 72 - 74. Instead, it becomes the leading eddy and starts to entrain non vortical fluid from the main stream, as well as some of the vortical fluid from its satellite counter rotating eddy. The leading eddy tends to exert a strong strain field on its satellite, causing it to get engulfed in its own field, as shown in time 73 -78. This causes a substantial increase in the leading eddy size in the cross stream direction. During the final stages of the leading eddy within the trough, it collides with the downstream edge of the cavity, rides over the edge, and leaves almost in its entirety, as shown in time 76 -79.

The instantaneous streamline plots corresponding to the above sequence of frames are shown in Fig. 4.12. These plots emphasize the large scale structures more than the small structures since, by construction, they involve some smoothing of the vorticity field. The shedding cycle of the large scale leading and trailing eddies in the recirculation zone is clearly illustrated. On the other hand, the curvature of the streamlines above the cavity represents the same shedding cycle in terms of a velocity wave propagating downstream.

The long cavity acts as a shallow trough in which the separating shear layer experiences large amplitude flapping on top of the recirculating eddy. This severe flapping causes the shear layer to interact directly with the cavity floor during part of the cycle, as opposed to the flapping observed in the short cavity case where the shear layer did not interact with the floor. The recirculation zone is observed to shed eddies that form, grow, leave the step and are then replaced, hence causing the flapping of the shear layer. The flapping action seems to dominate over the shedding of the eddies from the separating shear layer. While these eddies are still shed at a fast rate as in the $L/D = 2$ case, they do not move along the top of the cavity towards the downstream edge as in Fig. 4.5. Instead, they are instantly engulfed by the recirculating zone eddies. Hence, the shear layer eddies seem to have a negligible influence on the flow field. In fact, most of the entrainment of fluid from the main stream takes place within the eddies generated in the recirculation zone, as shown in Fig. 4.13 in which a dark line is drawn to indicate the boundary between the vortical fluid and the fluid being entrained from the main stream. As in the short cavity case, the long cavity instability mechanism involves both shear layer and recirculation zone modes of instability, however, the latter mode is clearly dominant.

It is interesting to note, concerning the recirculation zone structure in Fig. 4.13, that it is reminiscent of the entrainment contours in free shear layers.

The average velocity profiles within the cavity are shown in Fig. 4.14, plotted $u(x,y)/U_{max}(x)$ against $(y-y_{1/2})/\theta(x)$. The profiles exhibit strong self-similarity within the shear layer, $0<u<U_{max}$. The mean streamlines are shown in Fig. 4.15, where a well defined mean recirculation bubble, similar to that behind a step or a bluff body, is evident. The spatial growth of the recirculation eddies, shown in terms of the average momentum thickness $\theta(x)$, is depicted in Fig. 4.16. The figure shows a plot of θ/θ_o vs. $(x-x_{eup})/\theta_o$ for five x locations along the cavity length, $x/D = -2, -1.95, -1, 0$, and 1; where $x_{eup}/D = -2$ is the x location of the upstream cavity edge. The two phases of development of the eddy, involving its being either the trailing or the leading eddy, are clearly shown in this figure. In the first phase, the trailing eddy grows by entraining vortical fluid and engulfing small rollup eddies shed by the separating shear layer. When the trailing eddy is separated from the step, it ceases to grow. In the second phase, the trailing eddy becomes the leading eddy, and it grows by entraining fluid from the main stream and engulfing the vortical fluid from its satellite counter rotating eddy.

The organization of this process is best exhibited in Fig. 4.17 and 4.18. In Fig. 4.17, a time trace of the streamwise velocity component is shown at coordinates $(x/D,y/D) = (-1.95,1.0)$, $(-1.0,1.0)$, $(1.0,1.0)$, and $(1.95,1.0)$, i.e., all traces are taken along the top of the cavity. The time traces show the remarkable organization of the recirculation eddy shedding process at a dimensionless time period of 12.5. Fig. 4.18 shows the spectra for the fluctuation in the streamwise velocity at the same stations chosen above. The highest amplitude peak occurs at $St = f\theta_o/U_o = 0.0016$, which is an order of

magnitude smaller than the shear layer most unstable Strouhal number. Furthermore, since $\theta_o/D = 0.0218$ and $U_o/U_m = 1.040$, the dimensionless frequency corresponding to this peak is $fD/U_m = St_D = 0.08 = 1/12.5$. Hence, this peak corresponds to the frequency of recirculation eddy shedding. The spectra also show lower amplitude peaks corresponding to the harmonics of this frequency.

The mean streamwise propagation speed for the recirculation zone eddies, c, was measured to be $c/U_m = 0.21$. This was done by tracking the centers of the eddies as they propagate downstream in the cavity. This value of c leads to $fL/c = L/\lambda = 1.52$, which, as was noted for the recirculation eddy shedding in the $L/D = 2$ case, indicates a value of $n = 1$, a first stage oscillation, and a one eddy system in the recirculation zone. A one eddy system is evident in the flow structure shown in Fig. 4.11.

In order to investigate the significance of L/θ_o on the cavity dynamics for long cavities, we repeated the above numerical simulation with $L/\theta_o = 119$ and 217, i.e. with $\theta_o/D = 0.034$ and 0.018. Fig. 4.19 shows velocity traces and fluctuation spectra of the two cases. The corresponding frequencies of oscillation of the recirculation zone are the same as in the above results for the intermediate case, $L/\theta_o = 183$, to within the frequency resolution affordable to us: $\pm(0.004 - 0.007)$. The peak Strouhal numbers ($f\theta_o/U_o$) are different because θ_o is different among the three cases. The values of the Strouhal number defined as fD/U_m, however, are : $St_D = 0.085$ and 0.086, essentially the same as the 0.08 value for L/θ_o=183, given our frequency resolution. The flow fields in both cases looked the same as in Fig. 4.11. A sample of 130 time steps is shown in Fig. 4.20 for $L/\theta_o = 217$. These results indicate that the value of θ_o, within the range investigated herein, is irrelevant to the dynamics of the flow field in the long cavity case, as is suggested by the dominance of the recirculating zone instability over the

shear layer instabitlity. On the other hand, it is expected that, for any L/D, a value of θ_o/D exists beyond which θ_o becomes the dominant factor in the cavity dynamics. In this work we restrict ourselves to cases where θ_o/D is in the above range of values.

The effects of varying H/D and xmax/D on the flow in the L/D=4 cavity were also investigated. Varying H/D was done in order to ascertain whether the frequency selection in the chosen flow geometry was affected by the specific choice of channel height, as opposed to being an intrinsic cavity selection. H/D was changed from the value used above (H/D=2.0) to H/D=1.0, with no major effect on the dynamics, fD/U_m=0.092. The study of the effect of xmax/D on the dynamics is more of a numerical question. Specifically, the issue is whether our choice of xmax, the point at which vortex blobs are deleted, for the above runs affects the flow dynamics in a significant manner. The value of xmax/D was varied from the above value of 4.0 to 8.5. The resulting Strouhal number for the dynamics was St_D = 0.087, which is again not very different from the 0.08 value found above.

Next, in order to study the transition between the short cavity and the long cavity cases, we investigated the intermediate case of L/D = 3. In this case, the flow parameters are, L/θ_o = 96, Re_D = 2500, and U_o/U_m = 1.06. The numerical parameters used are, h_s/D = 0.25, $\Delta t U_m/D$ = 0.1, $\Gamma_m/U_m D$ = 0.0208, Δ_s/D = 0.0179, and xmax/D = 4. The dynamics of the flow field is shown in Fig. 4.21. The highest peak in the frequency spectrum (not shown), which corresponds to the recirculation zone oscillation shown in Fig. 4.21, is fD/U_m = 0.09 = 1/11.1. The phase speed was measured to be: c/U_m = 0.16, indicating an $fL/c = L/\lambda$ = 1.69, i.e. a one eddy system in the recirculation zone.

The sequence of frames shown in Fig. 4.21 illustrates dynamics common to the two cases studied above, L/D = 2, and 4. In the time period 70 -75, the

trailing eddy is seen to move downstream while growing in size by entraining both non-vortical fluid and shear layer eddies, indicated by arrows. It is noted that the development of the flow structure starting at time 75 in Fig. 4.21, is similar to that observed in Fig. 4.11 starting at time 70. The trailing eddy becomes the leading eddy as a new trailing eddy starts forming at time 76, Fig. 4.21. The effect of shorter cavity length in the L/D = 3 case of Fig. 4.21 as compared to Fig. 4.11 is to change the subsequent development of the leading eddy. This eddy, in Fig. 4.11, grows in size to the point where its core is at the level of the channel floor, before it collides with the downstream cavity step. Subsequent to this collision, the eddy climbs the step in its entirety, including, in particular, its core. In Fig. 4.21, because of the shorter distance of travel before collision, the leading eddy is smaller, and its core is within the cavity when it arrives at the downstream step, at time 77-78. In this case, the result of the collision is the destruction of the eddy, as its top fluid is sheared off by the faster channel flow, while its core and bottom fluid are trapped within the cavity. Eventually, the vortical fluid trapped in the cavity is dragged away, however, the eddy structure is lost. This process, while sharing with the L/D = 4 case the fact that all the vortical fluid comprising the leading eddy eventually leaves the cavity, to be replaced by a new eddy, also shares with the L/D = 2 case, Fig. 4.7, the fact that the downstream/leading eddy is sheared off at the top by channel fluid. Compare, for example, Fig. 4.7, time 118.5, and Fig. 4.21, time 78.

It is obvious, from studying this intermediate case, how decreasing the cavity length would decrease the amplitude of flapping of the shear layer. When L decreases, the recirculating eddies have less time to grow before impinging on the downstream edge, and hence will grow to smaller final size. The smaller recirculation eddy size at impingement causes smaller vertical

displacement of the shear layer at that location, hence weaker flapping. This explains the dominance of the recirculation zone instability, manifested by the flapping, over the shear layer instability, in long cavities.

Finally, it is instructive to look at the flow dynamics as the cavity length goes beyond L/D=4. We have looked at two cases in particular, L/D=6 and 8. The results of these two cases are useful in order to fully understand the frequency selection mechanism in long cavities. The results presented hitherto show that the flow intability in long cavities is primarily a recirculation zone instability involving shedding of large eddies from the recirculation zone that completely dominate the smaller shear layer eddies. We have not, however, determined how the frequency of recirculation zone shedding is selected. It is not yet clear whether the cavity recirculation bubble is shedding eddies at its "natural" frequency or if it is somehow "forced" by the impingement of these eddies at the downstream cavity edge, in a manner similar to the organization of an impinging shear layer.

Two observations on the results for long cavities, L/D = 3 and 4, suggest that the shedding is actually natural, not organized by impingement forcing. First, in looking at the L/D = 4 flow dynamics, e.g. in Fig. 4.11, it is evident that the trailing eddy begins forming when the leading eddy moves away from the step causing a strong dip of the shear layer into the cavity. Thus, the formation of a new eddy is not a result of impingement of the leading eddy with the downstream corner. Secondly, it is noted that in going from L/D = 3 to L/D = 4 there is only a minor change in $St_D = fD/U_m$. This relative invariance of f with the impingement length L suggests that the former is not dependent on the latter.

The results for L/D = 6 and 8 confirm the above two observations. The flow dynamics are almost identical to those at L/D = 4. The Strouhal number

St_D in both cases is around 0.08, as it is for $L/D = 4$, and the evolution of the flow structures, their development, interaction and downstream motion, are all similar to the $L/D = 4$ case. Hence, it is evident that for $L/D > 3$, the cavity flow dynamics are fully determined by the natural oscillation of the recirculation bubble within the cavity, and are therefore independent of L/D. For $L/D < 3$, the cavity length is short enough to constrain the size of the recirculation bubble and hence to affect its shedding frequency.

The dynamics of the $L/D = 8$ case are illustrated in the series of frames in Fig. 4.22 and in the u and v spectra in Fig. 4.23. In this run, $Re_D = 2500$, $U_o/U_m = 1.067$, $\theta_o/D = 0.026$, and the numerical parameters are: $h_s/D = 0.333$, $\Delta t U_m/D = 0.1$, $\Gamma_m/U_m D = 0.0278$, $\Delta_s/D = 0.0179$, and $xmax/D = 6.0$. The long time average streamlines are shown in Fig. 4.24, to indicate the unconstrained length of the recirculation bubble given the specific flow parameters.

The variation of St_D for all the L/D cases considered is shown plotted in Fig. 4.25. This plot shows the strong decline of fD/U_m for $L/D = 2$-3, followed by a relatively fixed value around 0.08 for $L/D > 3$, as the cavity flow approaches that behind a backward facing step.

4.3 Conclusions :

Numerical simulation of the 2D incompressible flow over a cavity in a channel at high Reynolds number shows that the large scale dynamics of cavity flows involve two coexisting flow instabilities: the shear layer instability and recirculation zone instability. If the recirculation zone were quiescent, the flow field over a cavity would resemble a shear layer impinging on a downstream wedge, with the resulting organization due to disturbance feedback from eddy impingement downstream. However, recirculation zones are not quiescent. They have been observed to display significant oscillation in various flow configurations. Our results illustrate how this oscillation modulates the shear layer dynamics, causing a low frequency flapping of the shear layer. The amplitude of flapping increases with the length-to-depth ratio of the cavity, while the effect of the shear layer rollup at the separation edge, which coexists with this global flapping, becomes increasingly negligible. We have also shown that the mechanism which drives the oscillation of the recirculation zone is the shedding and downstream migration of large scale eddies within the cavity.

Our results show that eddy shedding from the long cavity ($L/D > 3$) recirculation zone is similar to that from the recirculation bubble in a backward facing step or behind a bluff body. All three flow configurations exhibit recirculation zone shedding at a Strouhal number $fD/U_m = O(0.1)$, a manifestation of a generic recirculation bubble instability. We note that this shedding process was found to be independent of θ_o, the momentum thickness of the boundary layer at the upstream separation edge, for $\theta_o/D = O(0.01)$. We restrict our conclusions to this range of θ_o. We suspect that θ_o would become a relevant parameter in the long cavity dynamics if it were of the order of magnitude of the cavity depth D, however, we are not concerned with this range of values.

The shedding of large scale eddies from the recirculation zone at low frequency strongly resembles the processes observed in the unstable modes of operation of a dump combustor (Keller et al., 1981; Vaneveld et. al., 1982). While heat release may affect the shedding frequency, and the rate of growth and the size of the large eddies downstream, the results of the numerical simulations suggest that the mechanism of the combustor instability is strongly tied to the instability of the recirculation zone in the dump.

One interesting aspect of the reacting flow is the higher organization of the recirculation zone eddies that is observed experimentally. Generally, low frequency peaks in non-reacting flow spectra are much broader than those measured in reacting flows. We suspect the reason to be that, in the reacting case, the unsteady flame acts as a distributed acoustic source. This acoustic energy is stored in the pressure waves that travel up and down the pipes upstream and downstream of the combustor. Consequently, the combustor experiences significant pressure forcing, which may cause the organization of large eddy shedding to be enhanced. In the non-reacting case this feedback forcing is absent and the large 2D structures tend to breakdown due to interaction with the walls and 3D instabilities.

In the next chapter we deal with the full reacting flow dynamics.

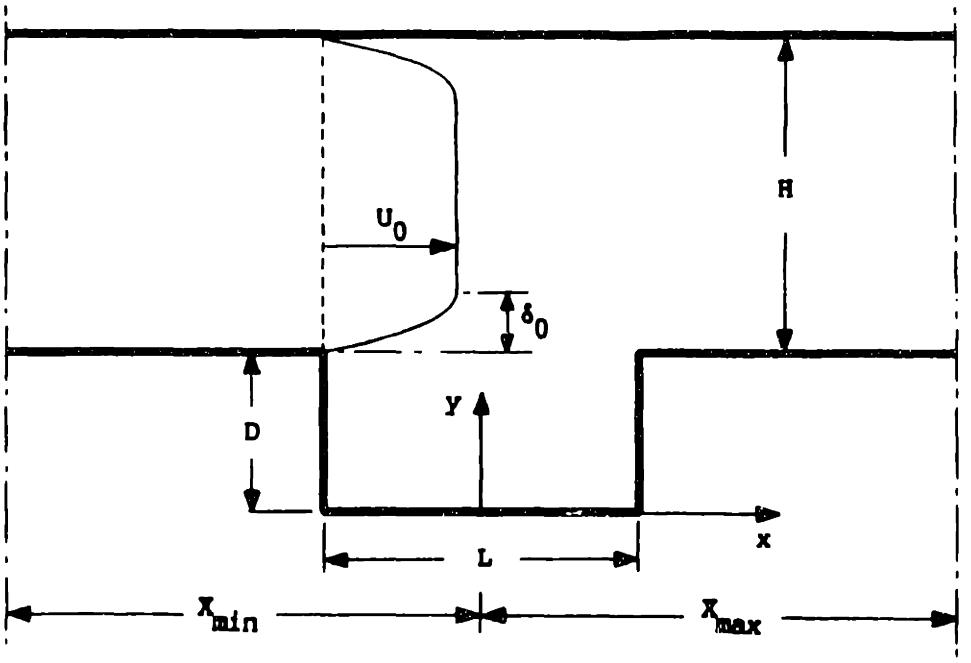

Figure 4.1 A schematic diagram of the geometry of the cavity in a channel, showing the coordinate system and the parameters used to define the flow and the dimensions of the computational window.

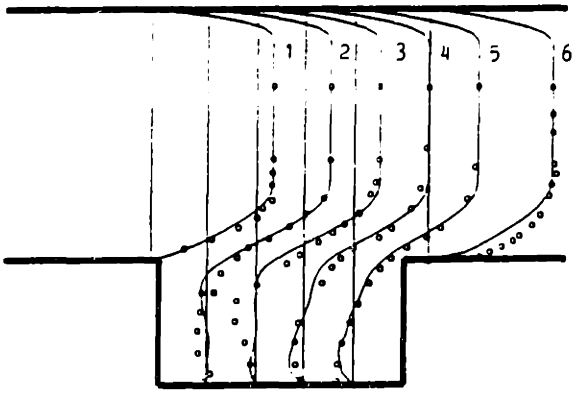

Figure 4.2 A comparison between the computed mean velocity profiles, shown in solid lines, and the measurements of Sinha (1978), shown in open circles (o) for a flow at $Re = U_0D/\nu = 2140$, $L/D = 2$.

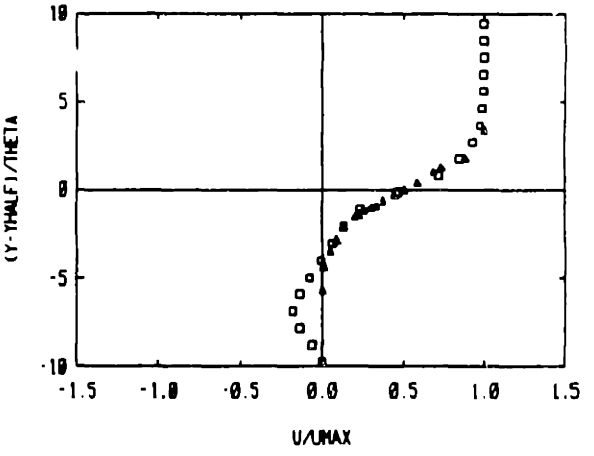

Figure 4.3 A comparison between the numerical solution, indicated by squares (□), and Rockwell and Knisely's measurements (1979), shown by triangles (Δ), of the mean velocity profile within a cavity with $L/D = 2$, and $Re = U_0D/\nu = 7571$, at $x/D = 0.92$.

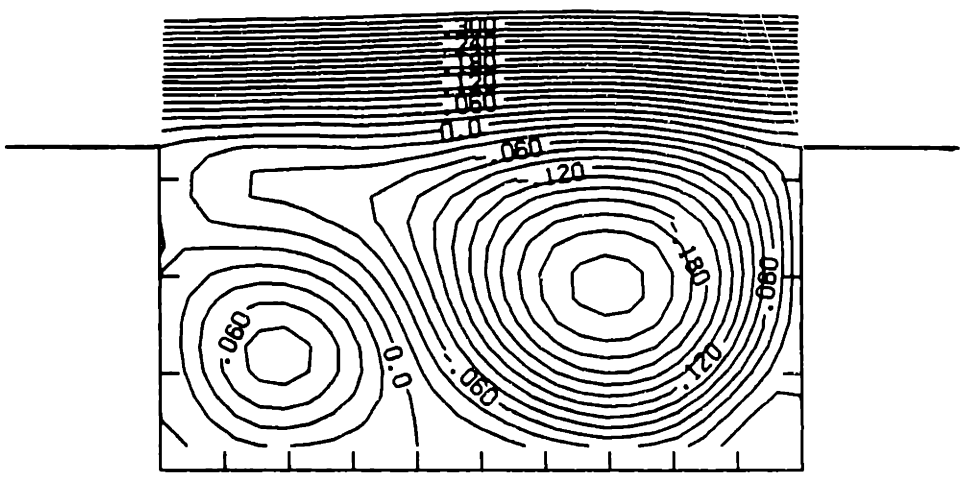

Figure 4.4 Long time average streamlines, time 101.0 to 143.5, corresponding to the numerical results used in Fig. 4.3.

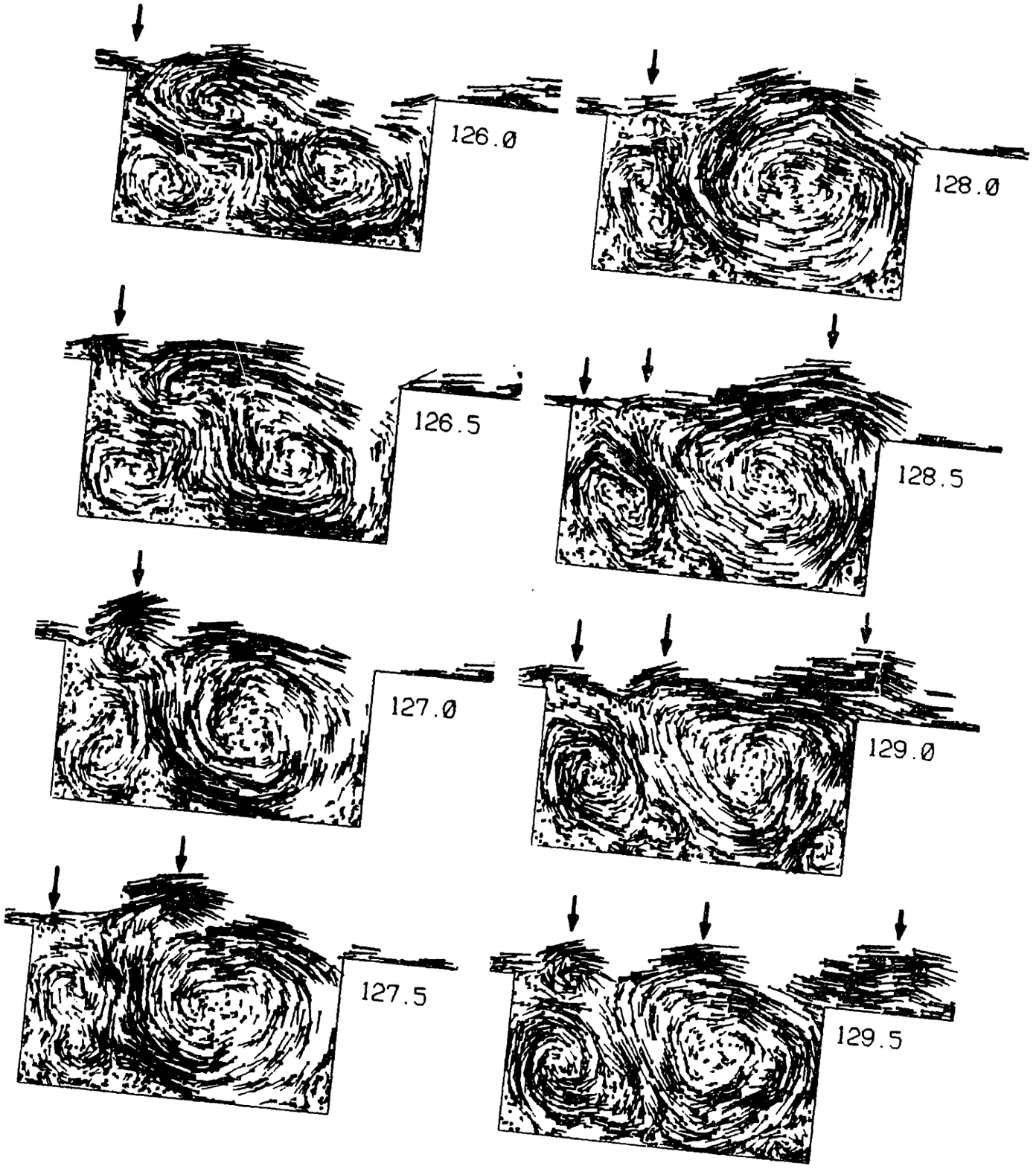

Figure 4.5 For caption see next page.

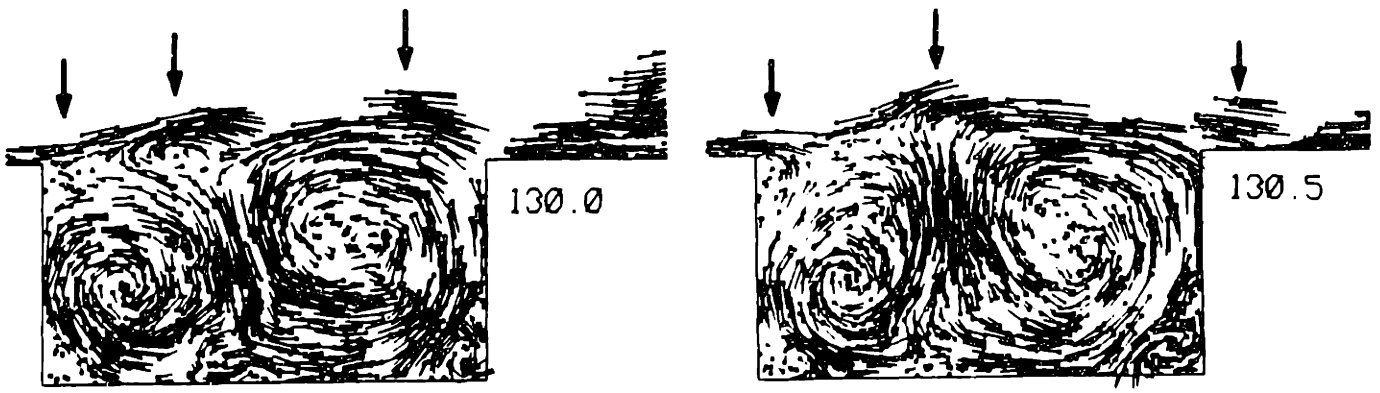

Figure 4.5 A sequence of time frames (continued from the previous page) showing the flow field, presented in terms of the vortex elements and their velocity vectors, for the flow over a cavity with L/D = 2 at Re_D = 7500. The arrows indicate the centers of the shear layer eddies. Note the presence of two resident eddies within the trough, and the two shear layer eddies over the impingement length.

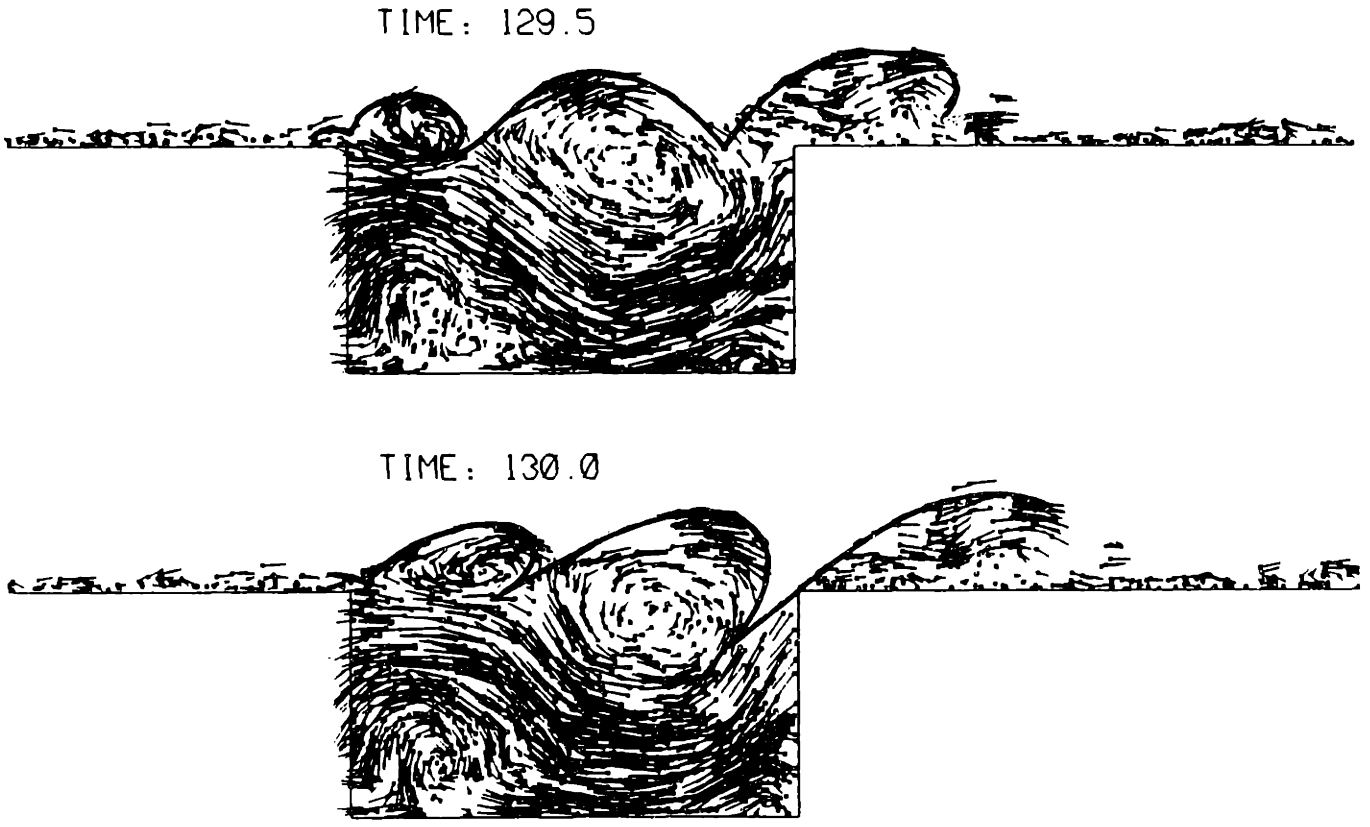

Figure 4.6 Two time frames of the flow depicted in Fig. 4.5, with the vortex elements velocity measured with respect to $U_\infty/2$. A solid line, which is drawn as a demarcation of the separating shear layer, outlines a two-wave (eddy) system over the cavity.

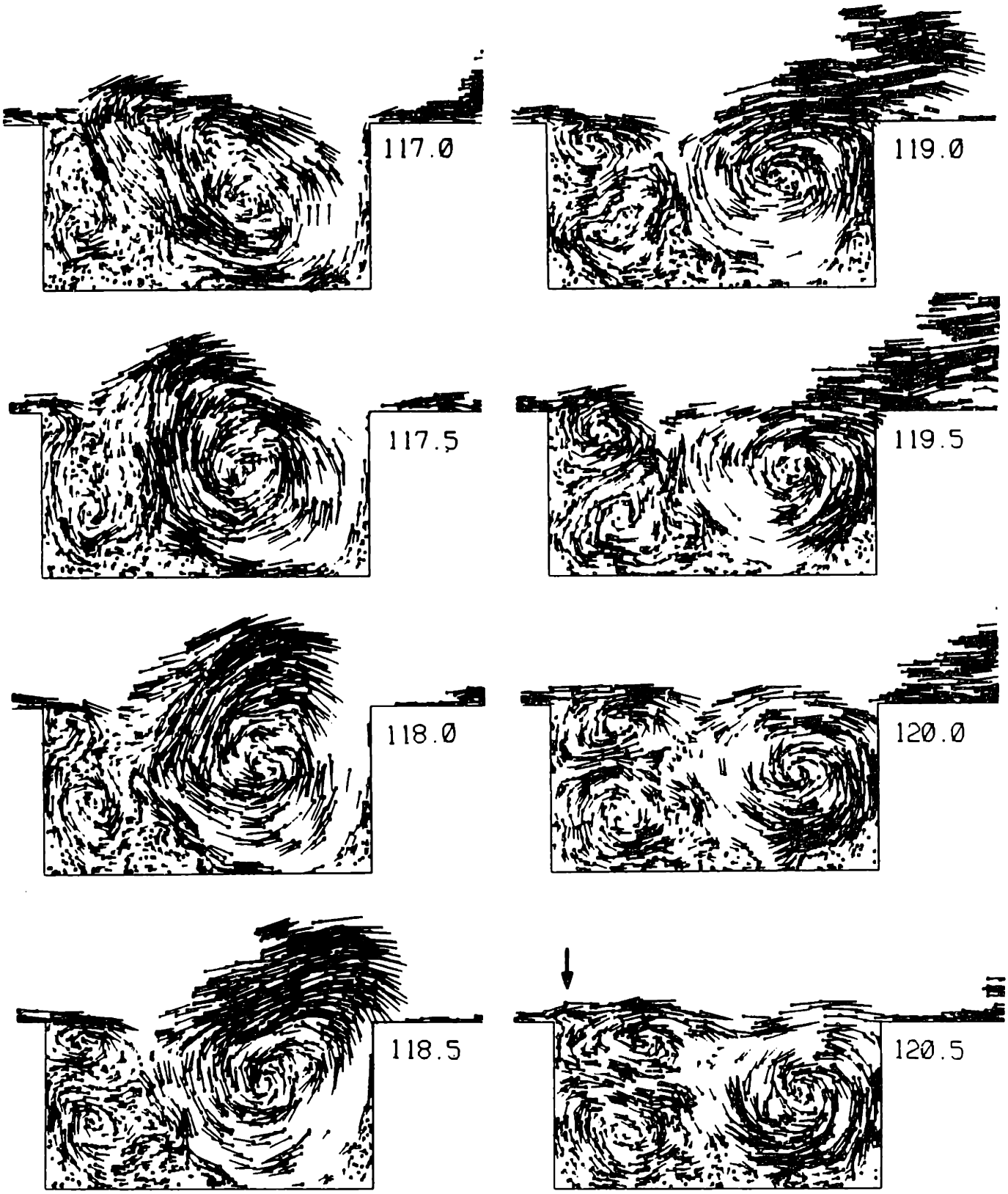

Figure 4.7 For caption see next page.

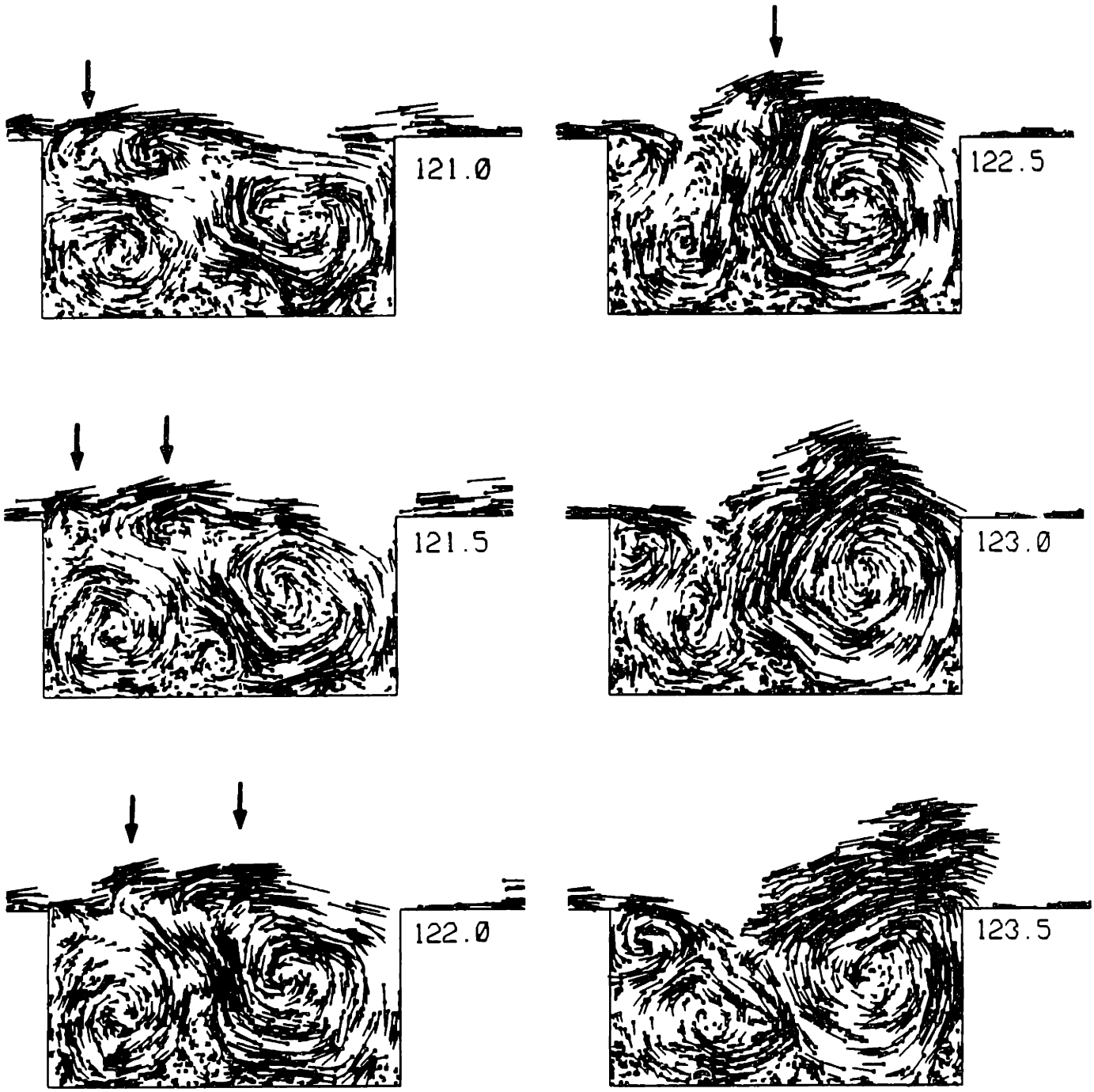

Figure 4.7 A sequence of time frames (continued from the previous page) showing the flow field at the conditions of Fig. 4.5, exhibiting the shedding of a slow eddy within the cavity.

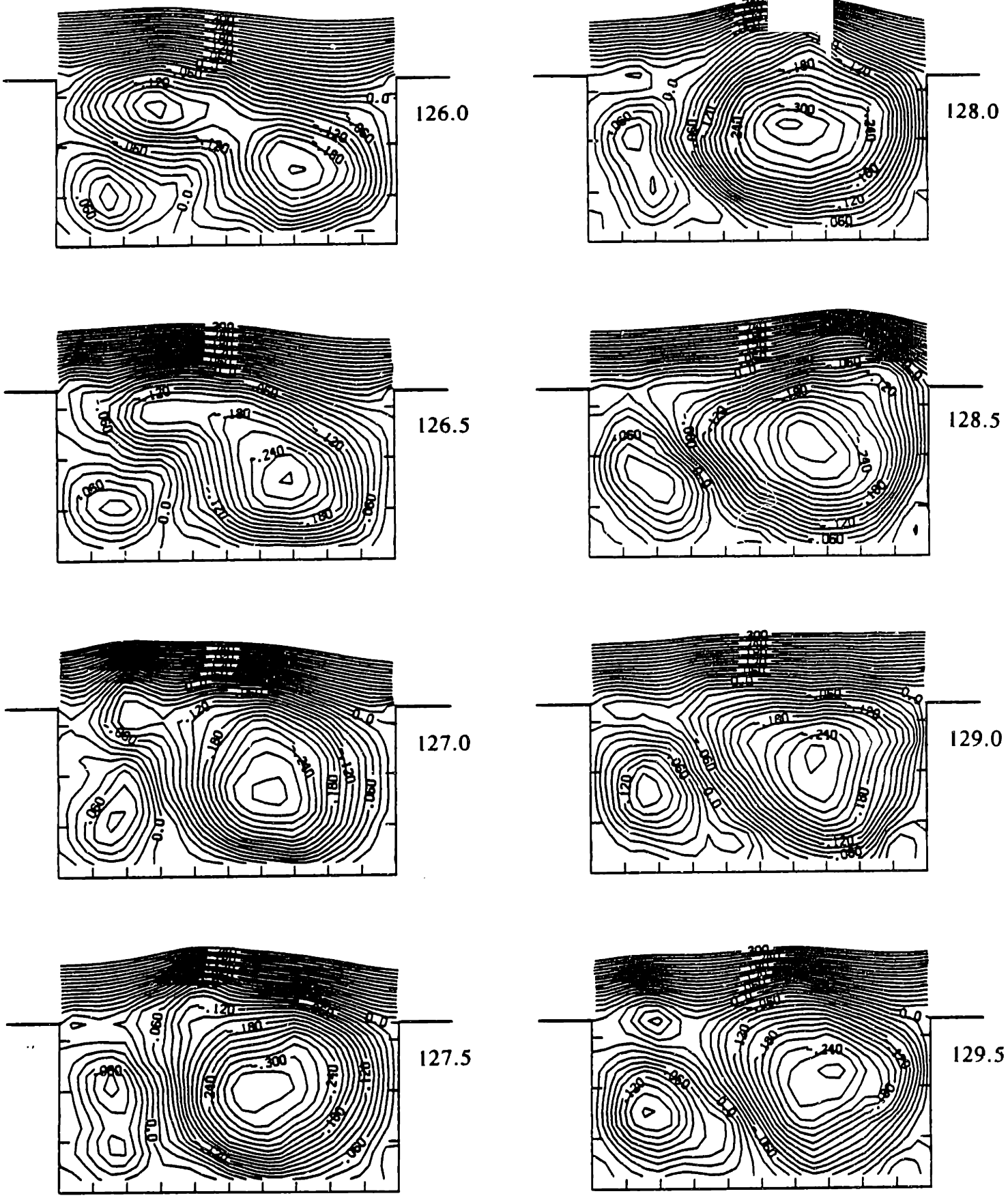

Figure 4.8 For caption see next page.

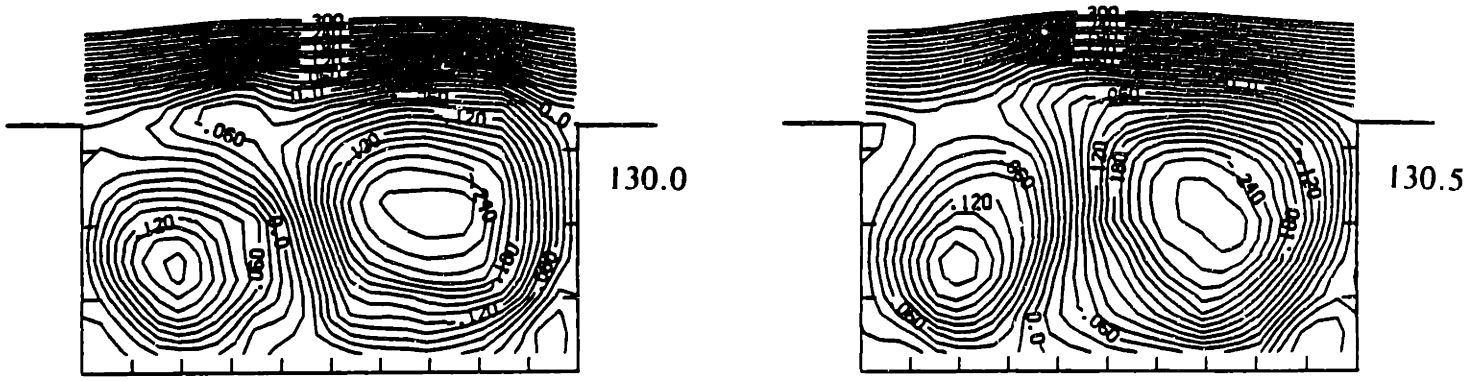

Figure 4.8 A sequence of time frames (continued from the previous page) showing the instantaneous streamlines corresponding to the vorticity plots in Fig. 4.5.

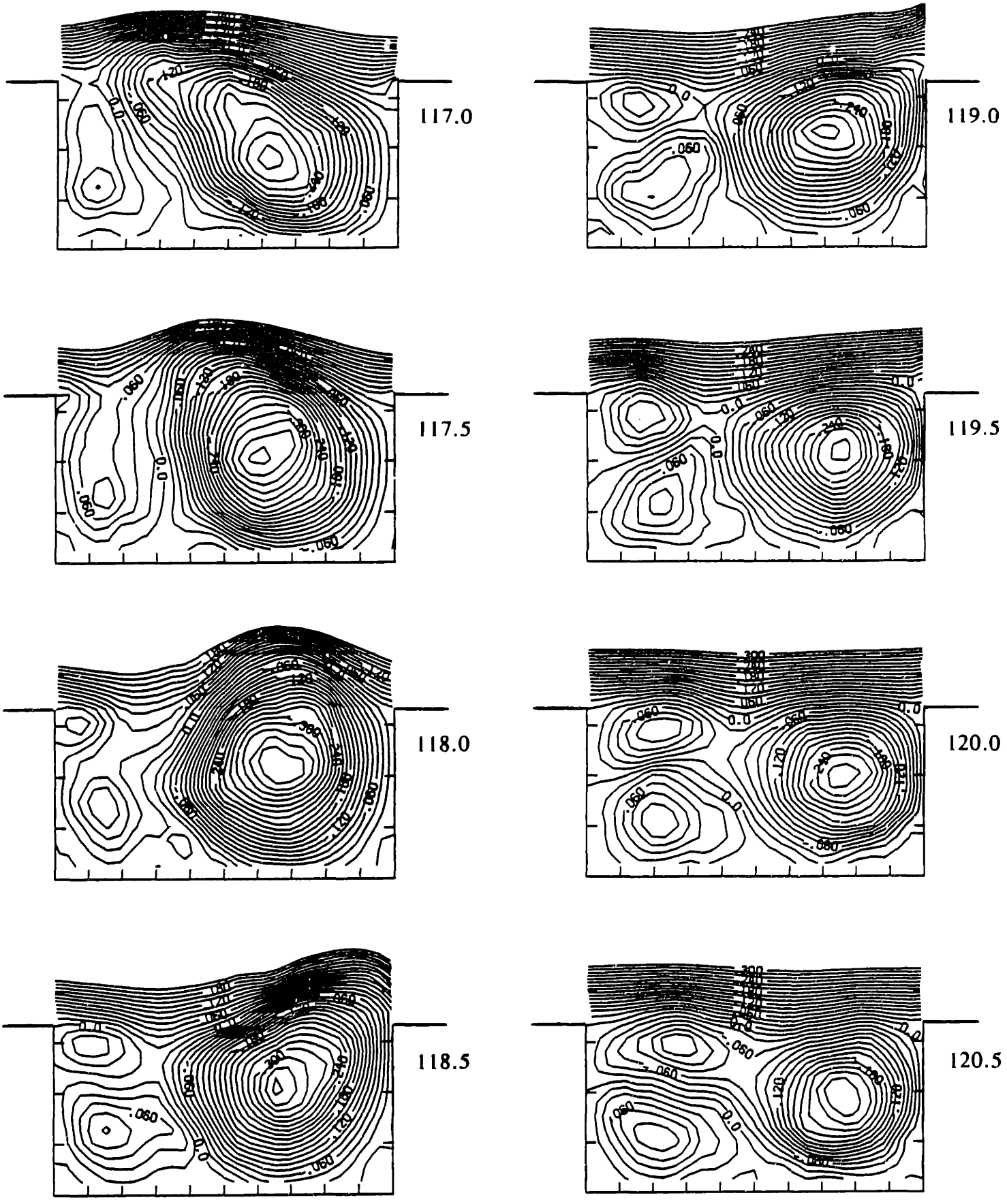

Figure 4.9 For caption see next page.

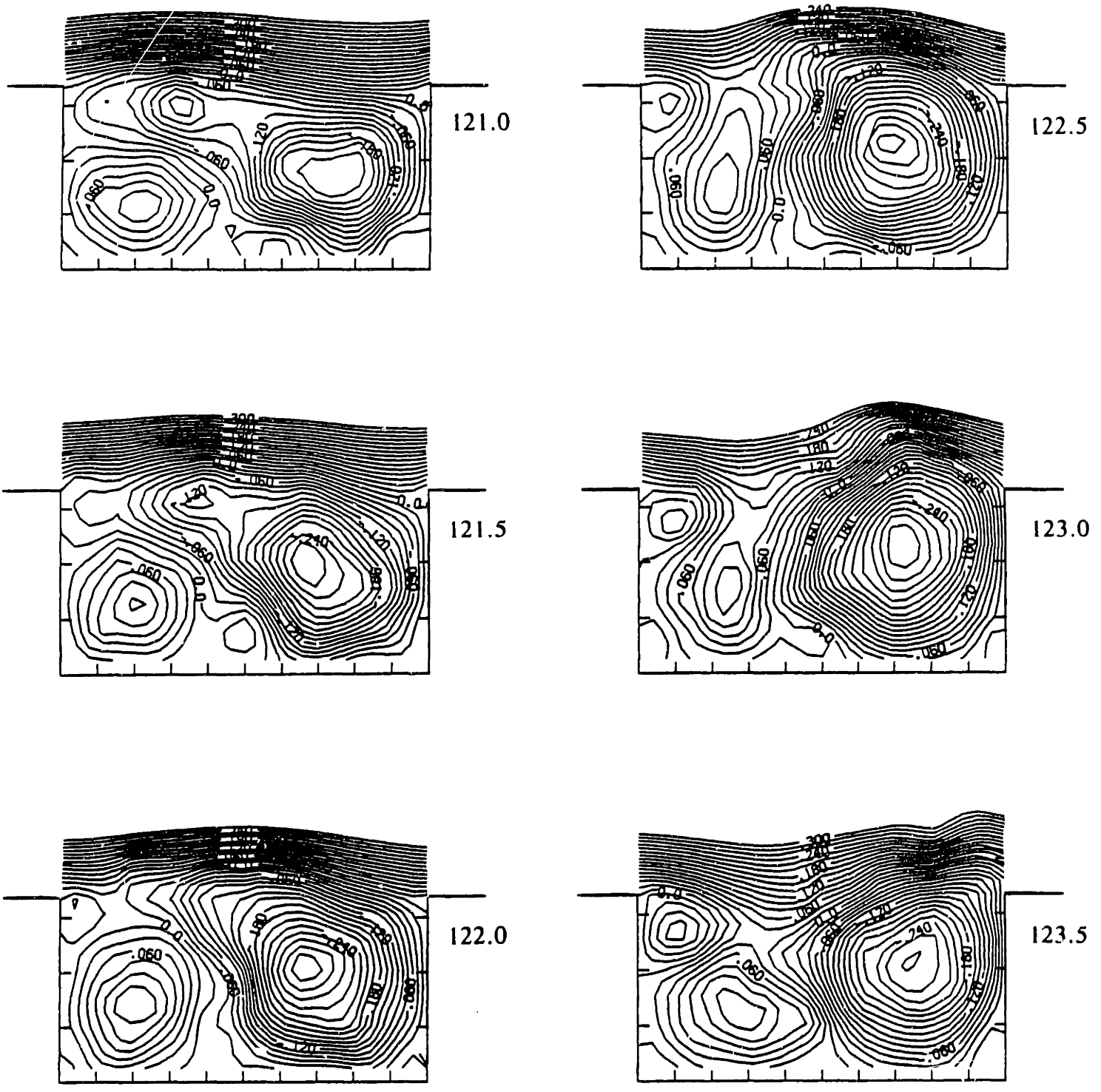

Figure 4.9 A sequence of time frames (continued from the previous page) showing the instantaneous streamlines corresponding to the vorticity plots in Fig. 4.7.

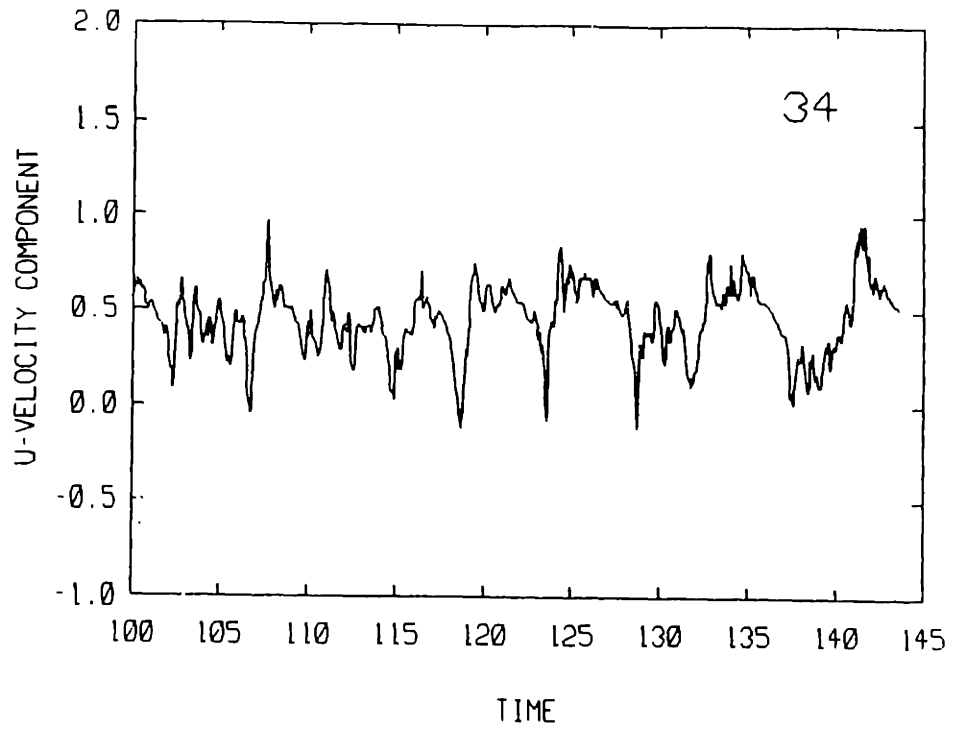

(a)

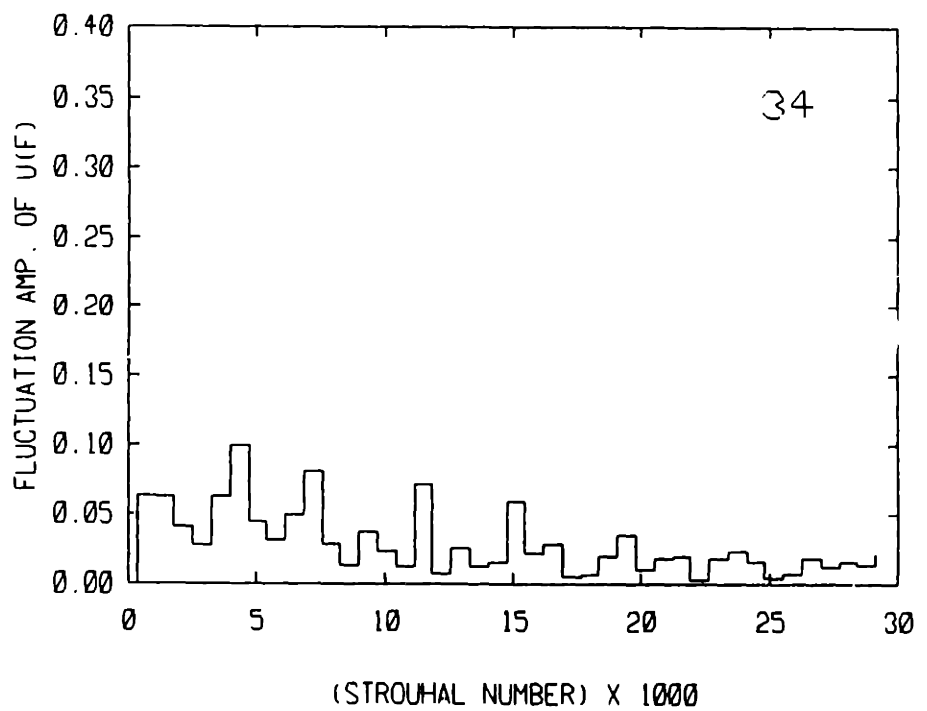

(b)

Figure 4.10 Velocity fluctuation (a) and frequency spectrum (b) for a cavity with $L/D = 2.$, $L/\theta_o = 100$ at $x/D = 0.95$, $y/D = 1.0$.

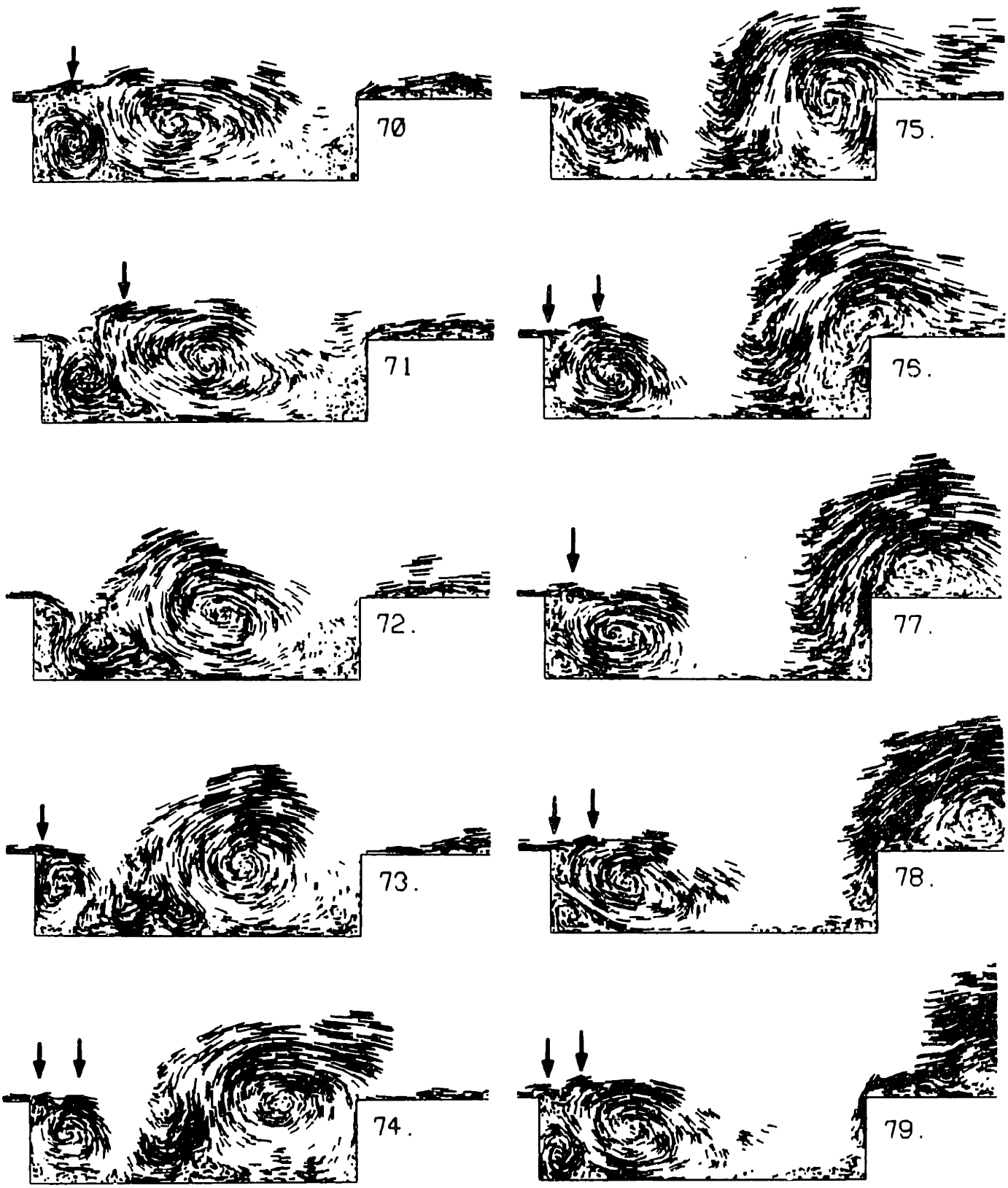

Figure 4.11 For caption see next page.

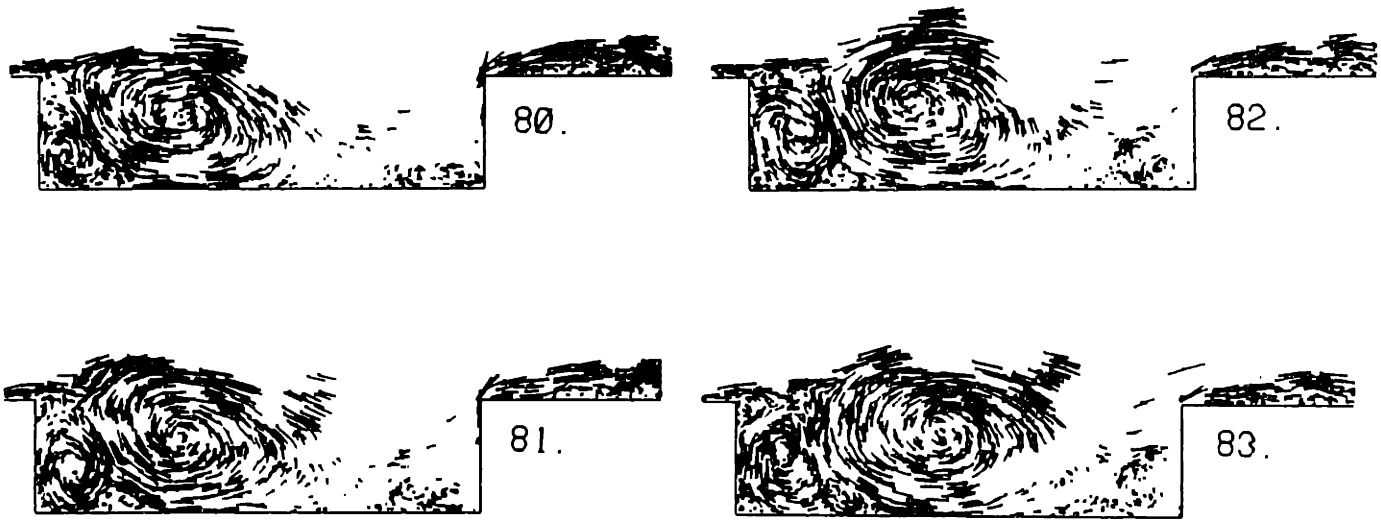

Figure 4.11 A sequence of time frames (continued from the previous page) showing the flow field, in terms of the vortex elements and their instantaneous velocity vectors, for a flow over a long cavity with $L/D = 4$, $L/\theta_o = 183$, and $Re_D = 2500$. The arrows indicate the eddies within the shear layer as they are shed and engulfed by the trailing, clockwise rotating eddy. Note the leading and trailing eddies, and their satellite counter clockwise rotating eddies.

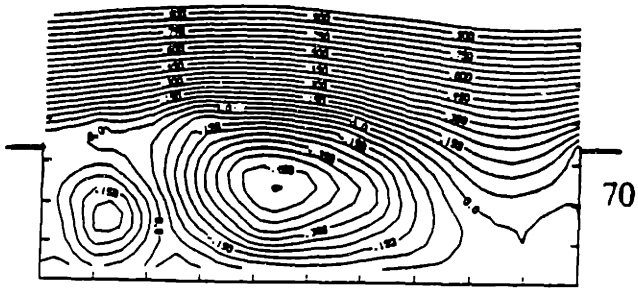
70.

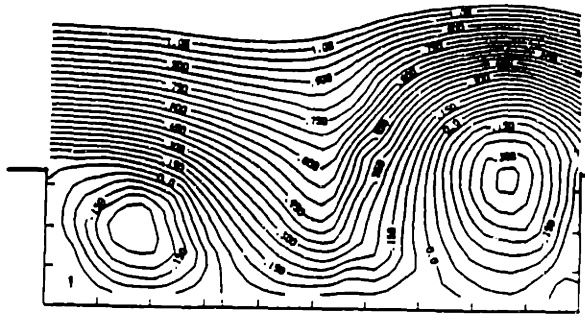
75.

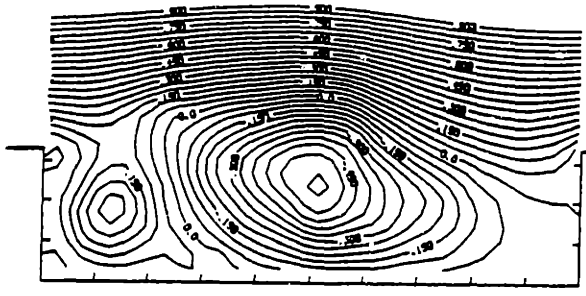
71.

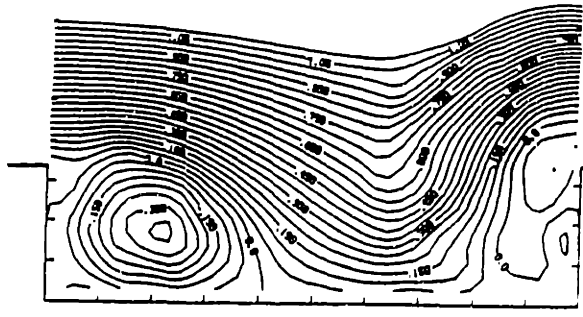
76.

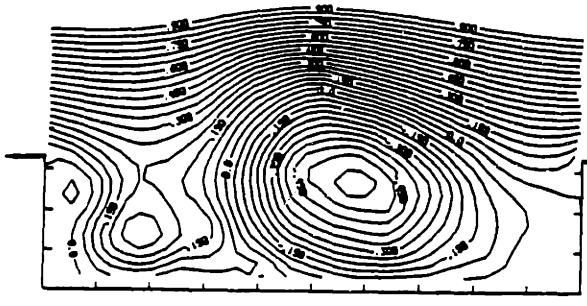
72.

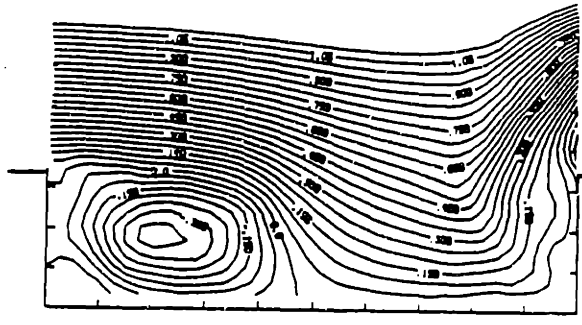
77.

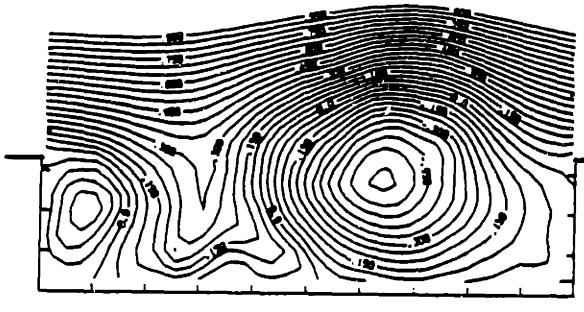
73.

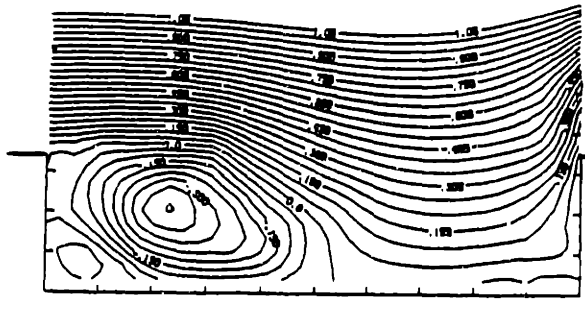
78.

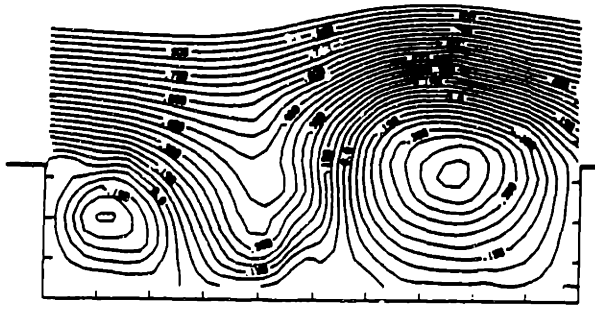
74.

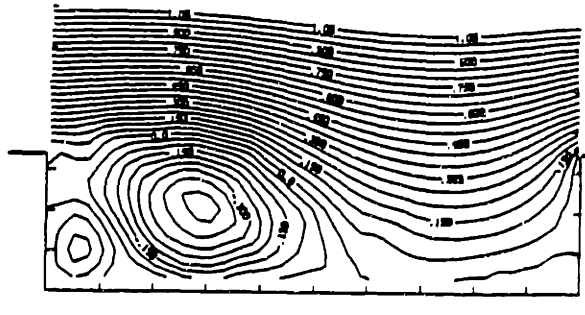
79.

Figure 4.12 For caption see next page.

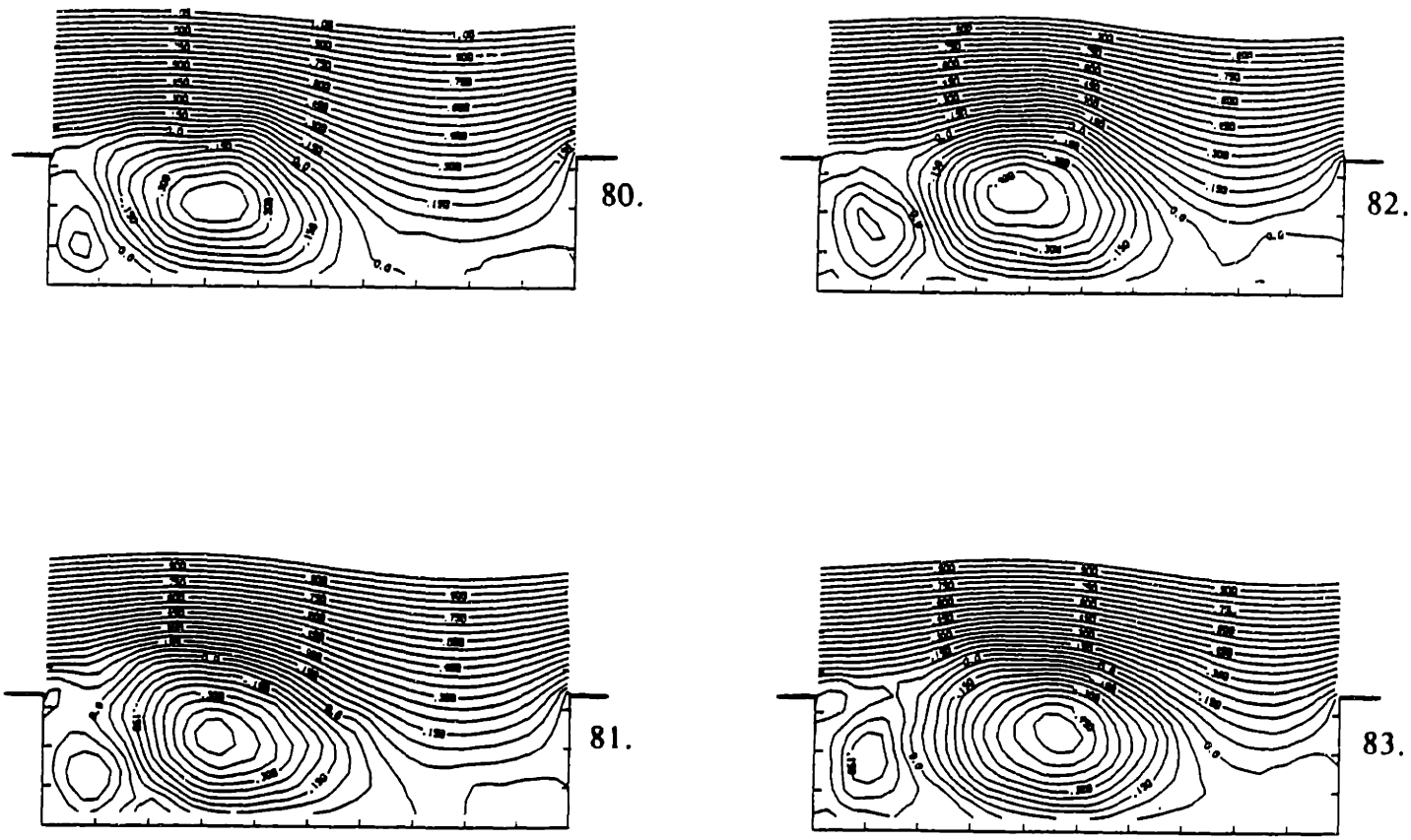

Figure 4.12 A sequence of time frames (continued from the previous page) showing the instantaneous streamlines corresponding to the vorticity plots in Fig. 4.11.

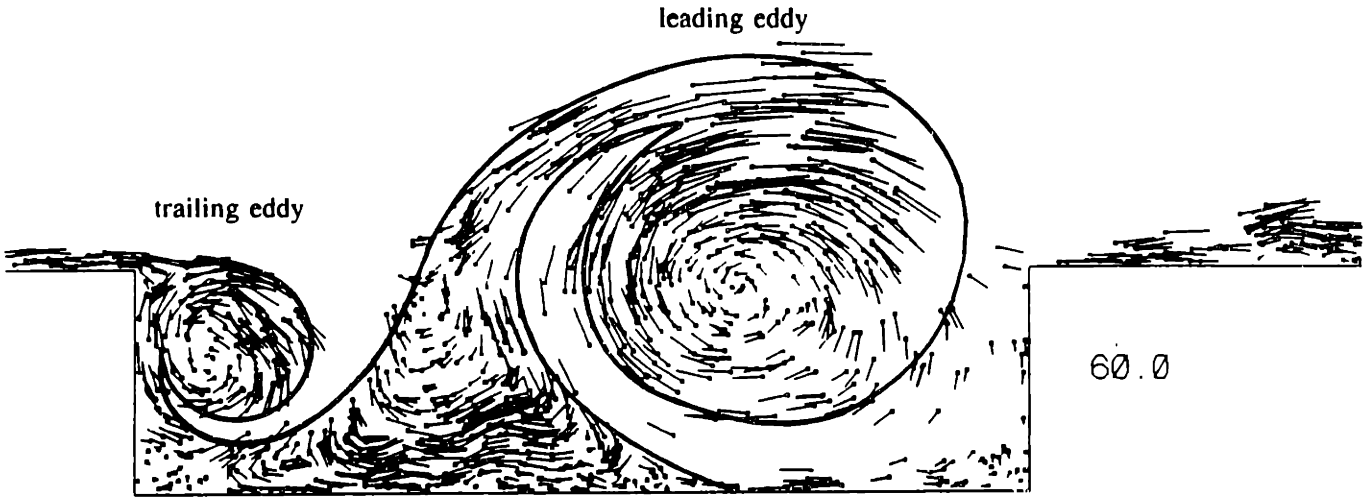

Figure 4.13 The flow field at the same conditions as in Fig. 4.11, with a line depicting the boundary between the vortex-laden flow and the potential flow entrained from the main stream.

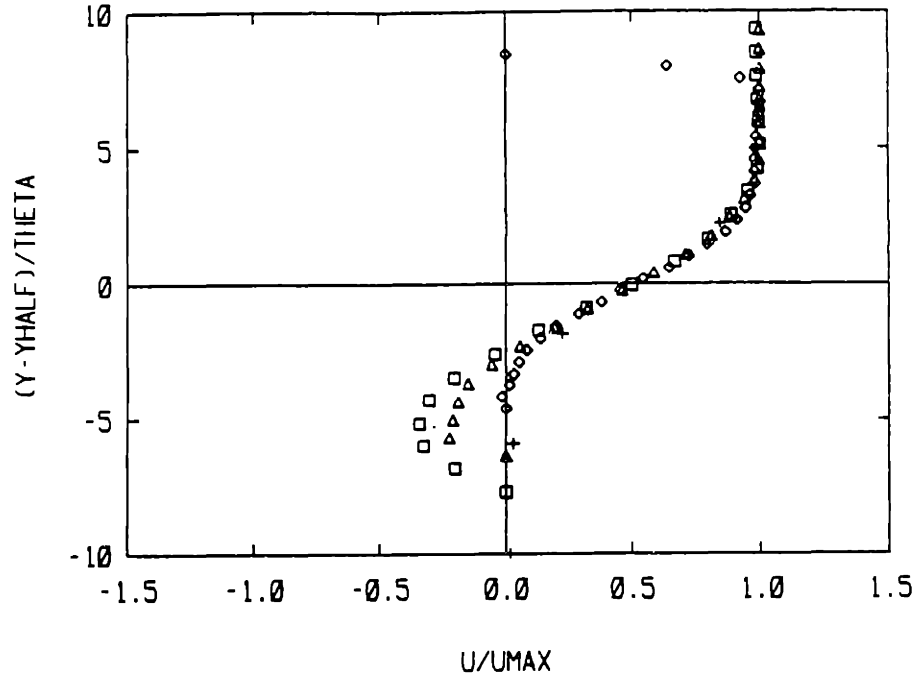

Figure 4.14 The mean velocity profiles of the flow depicted in Fig. 4.11, exhibiting the self similarity of the flow within the shear layer formed by the eddies shed from the recirculation zone. x/D = -1.9 (+), x/D = -1.0 (□), x/D = 0.0 (Δ), x/D = 1.0 (◇).

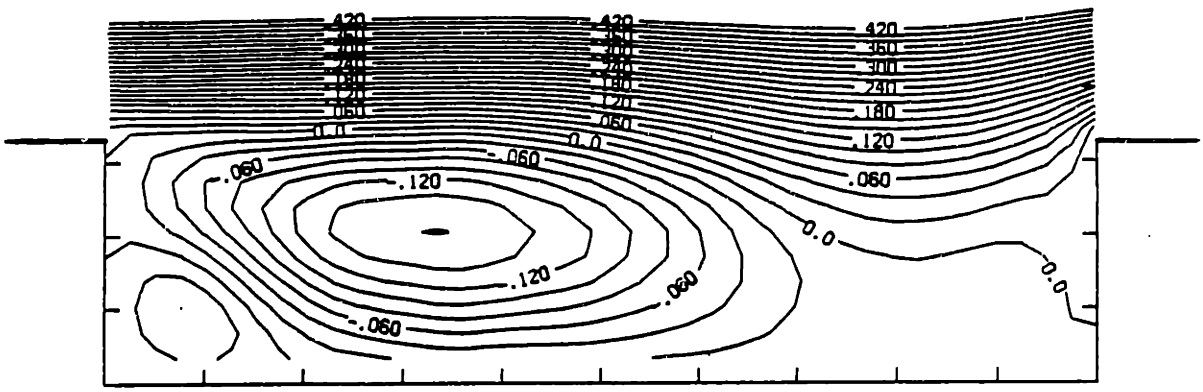

Figure 4.15 Long time average streamlines, time 69.0 to 135.0, of the flow depicted in Fig. 4.11.

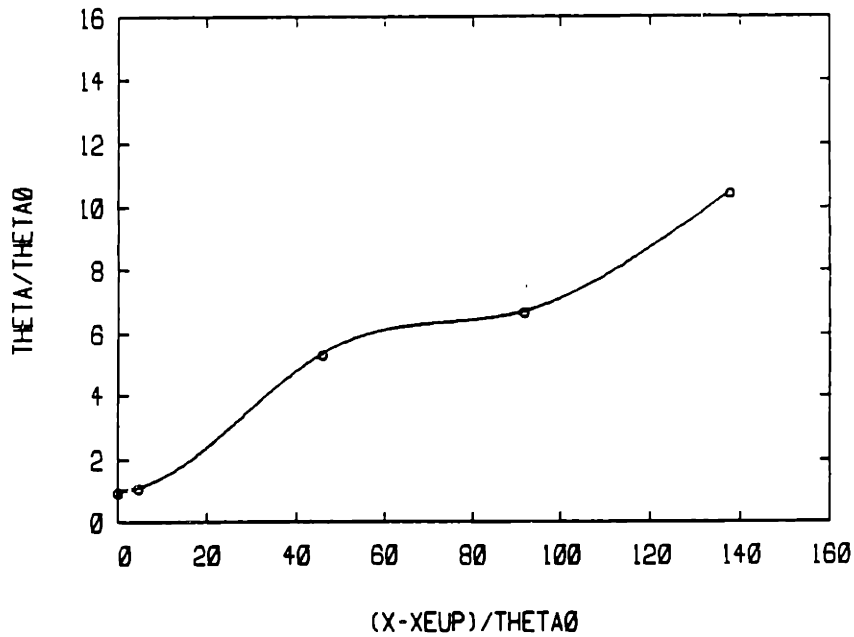

Figure 4.16 The growth of the momentum thickness, θ, versus streamwise distance, for the flow field shown in Fig. 4.11.

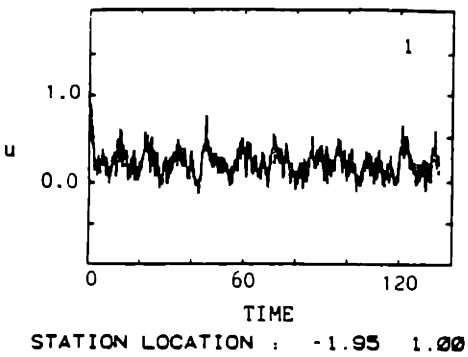

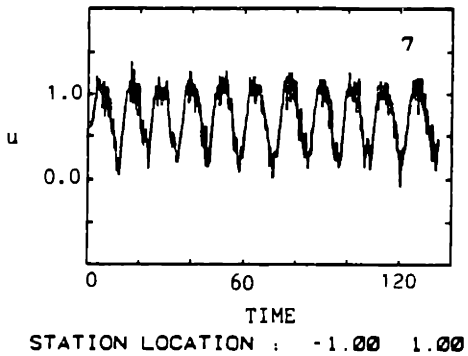

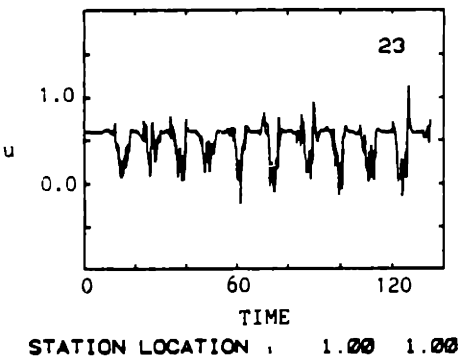

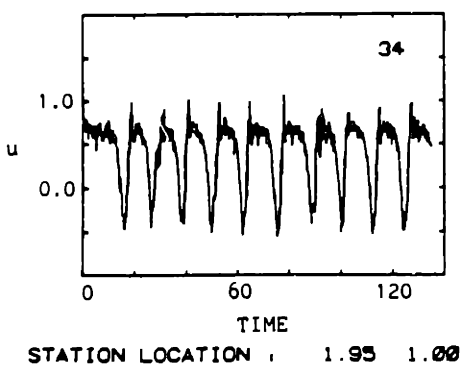

Figure 4.17 Time traces of the streamwise velocity at points along the top of the cavity, for the flow field of Fig. 4.11, showing the oscillation produced by the shedding of eddies from the recirculation zone. The numbers under each figure indicate the x and y coordinates, respectively.

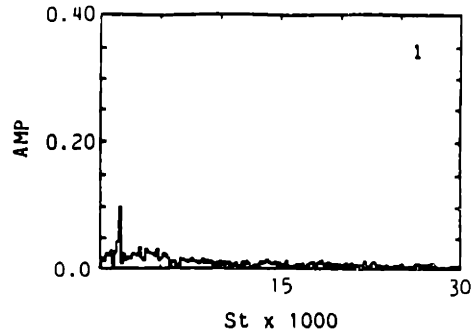

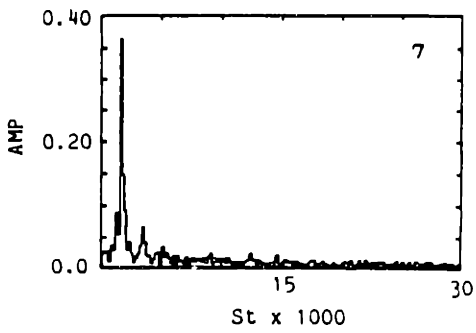

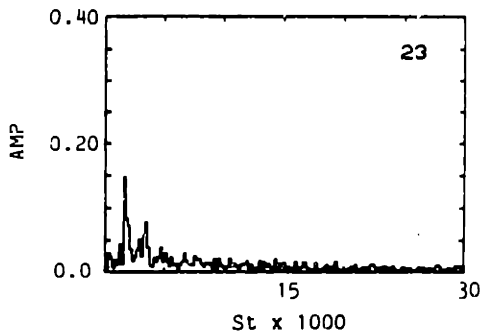

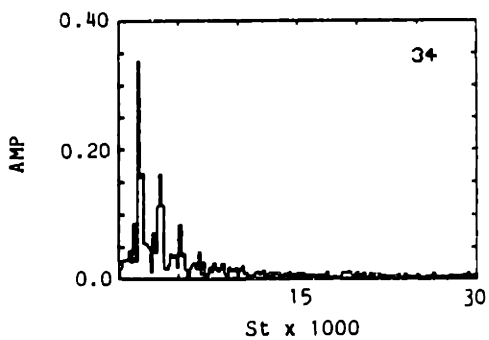

Figure 4.18 Spectra of the streamwise velocity fluctuation for the same points as in Fig. 4.17, plotted against the Strouhal number based on the boundary layer momentum thickness and mainstream velocity at the step.

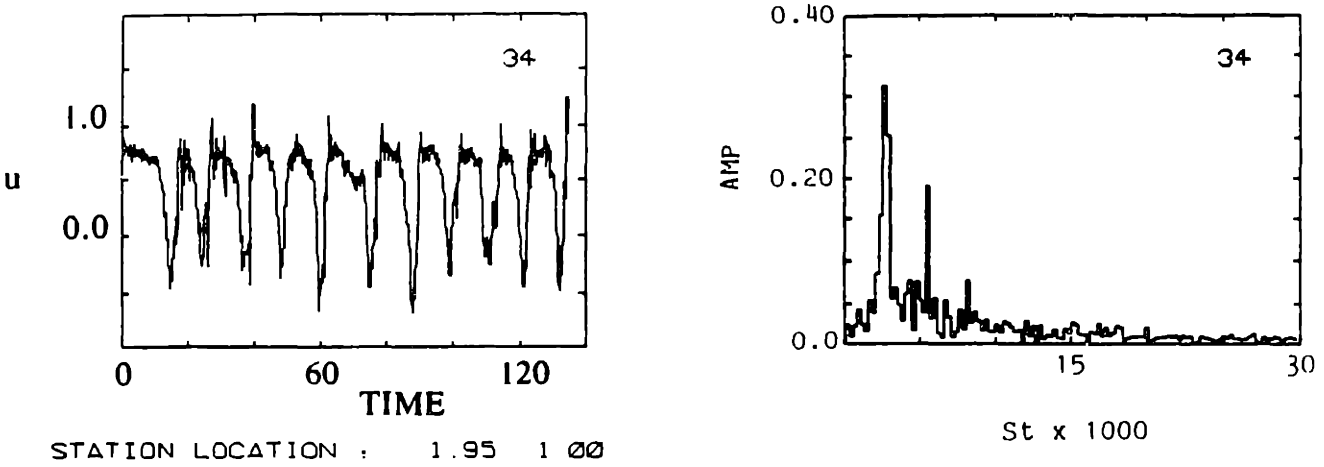

(a)

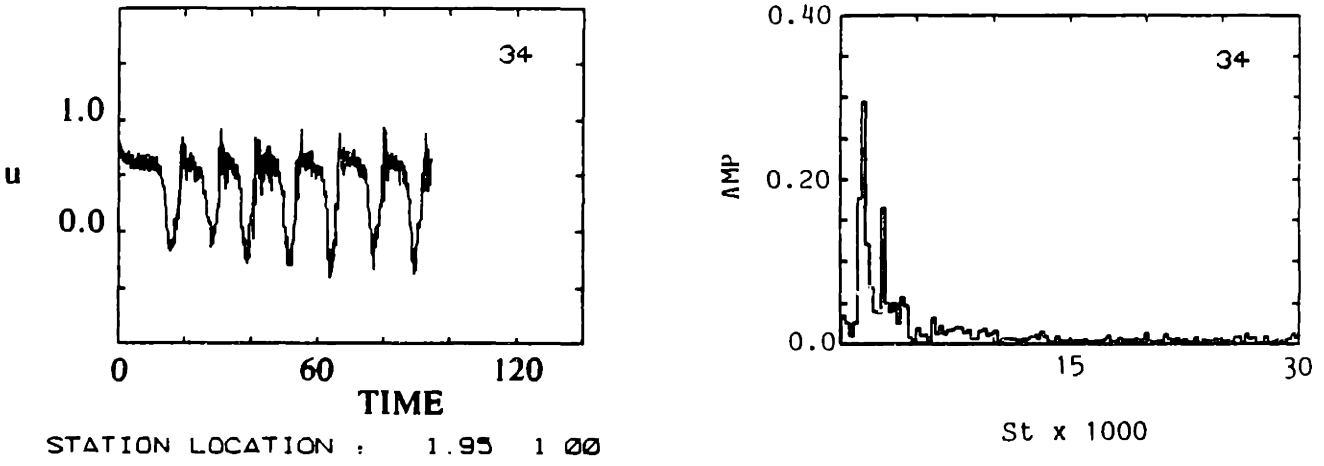

(b)

Figure 4.19 Time trace and spectra of the streamwise velocity for L/D = 4 and (a) L/θ_o = 119; and (b) L/θ_o = 217.

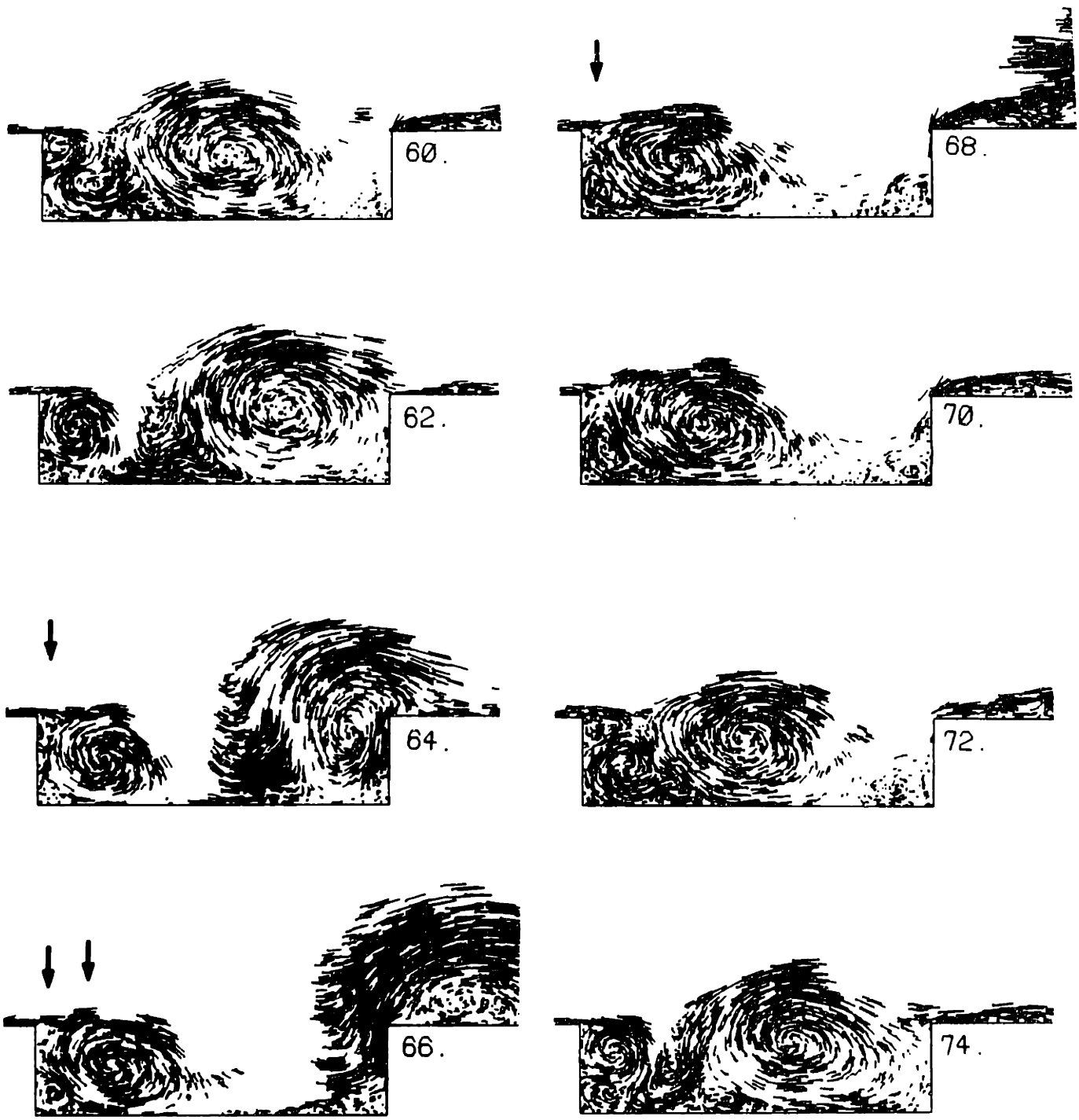

Figure 4.20 The flow field, shown in terms of the vortex elements and their instantaneuos velocity vectors, over a cavity with $L/D = 4$; $L/\theta_o = 217$; and $Re_D = 2500$. Arrows show the separating shear layer eddies.

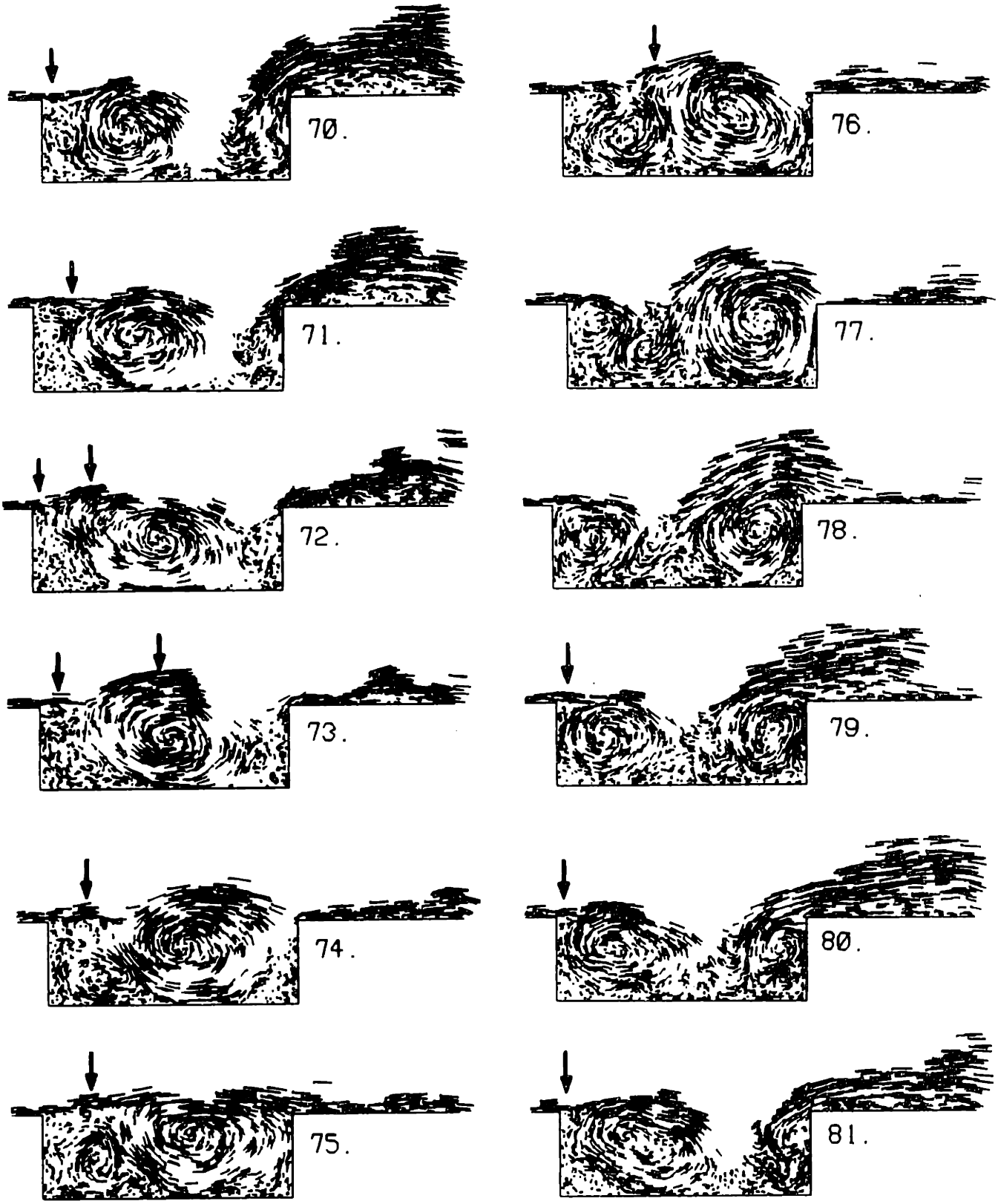

Figure 4.21 The flow field, shown in terms of the vortex elements and their instantaneuos velocity vectors, over a cavity with $L/D = 3$; $L/\theta_o = 96$; and $Re_D = 2500$. Arrows show the separating shear layer eddies.

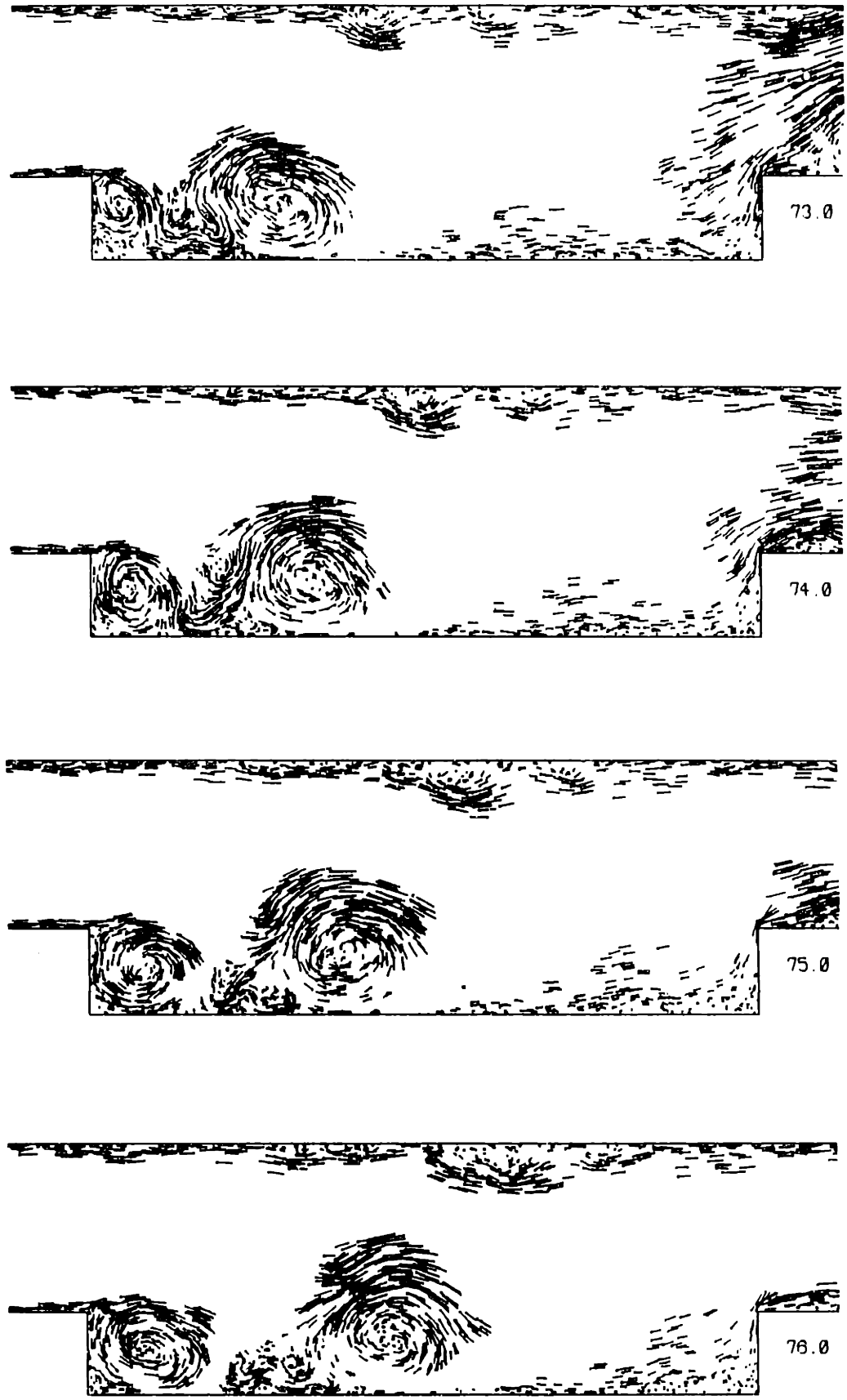

Figure 4.22 Continued on next page.

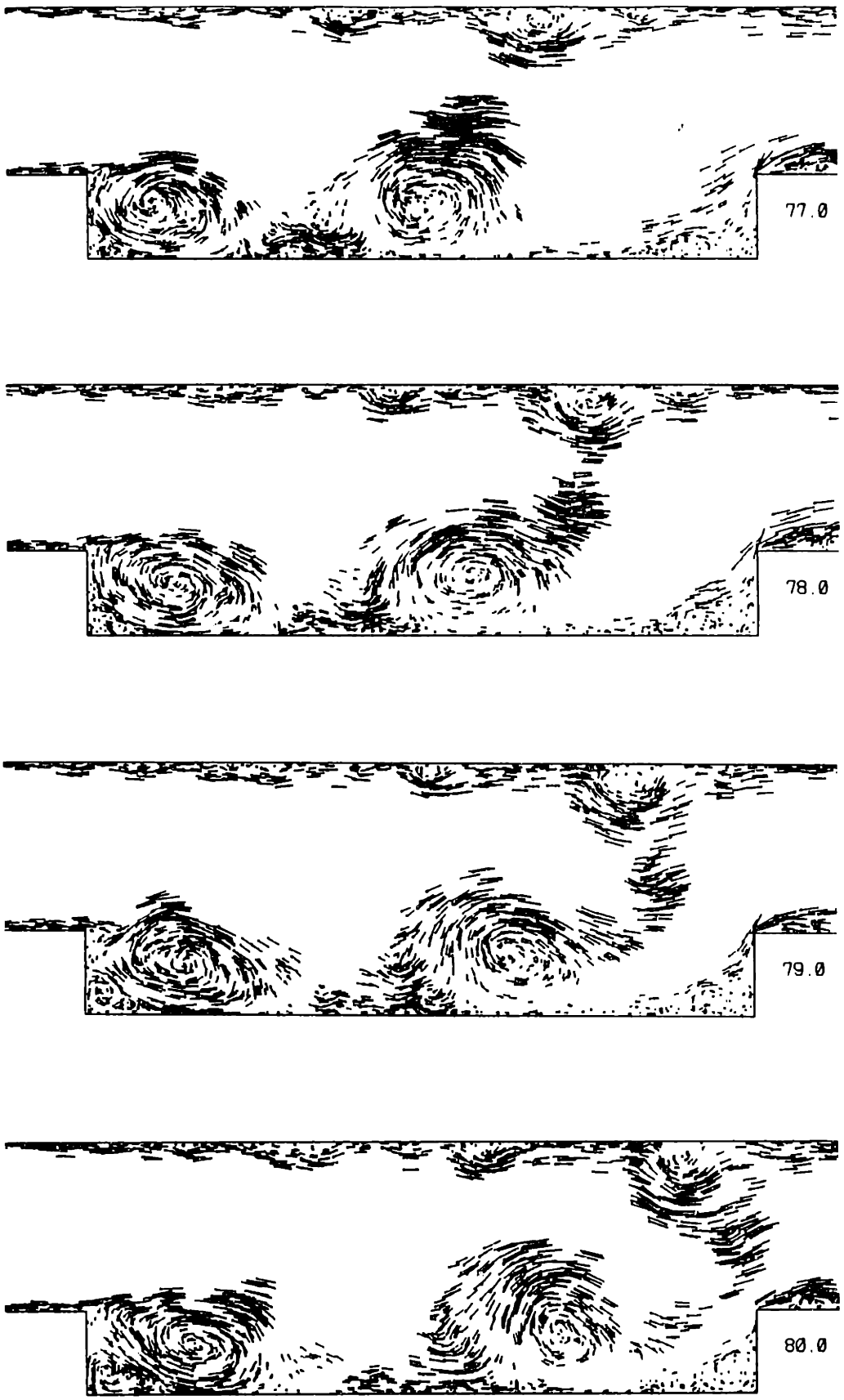

Figure 4.22 Continued on next page.

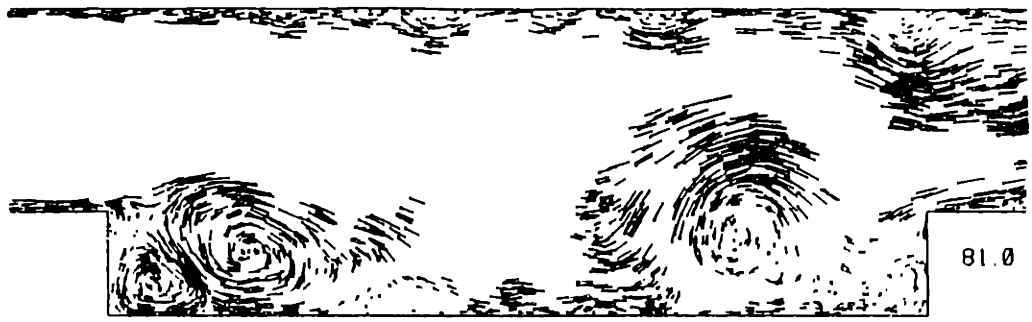

Figure 4.22 Continued on next page.

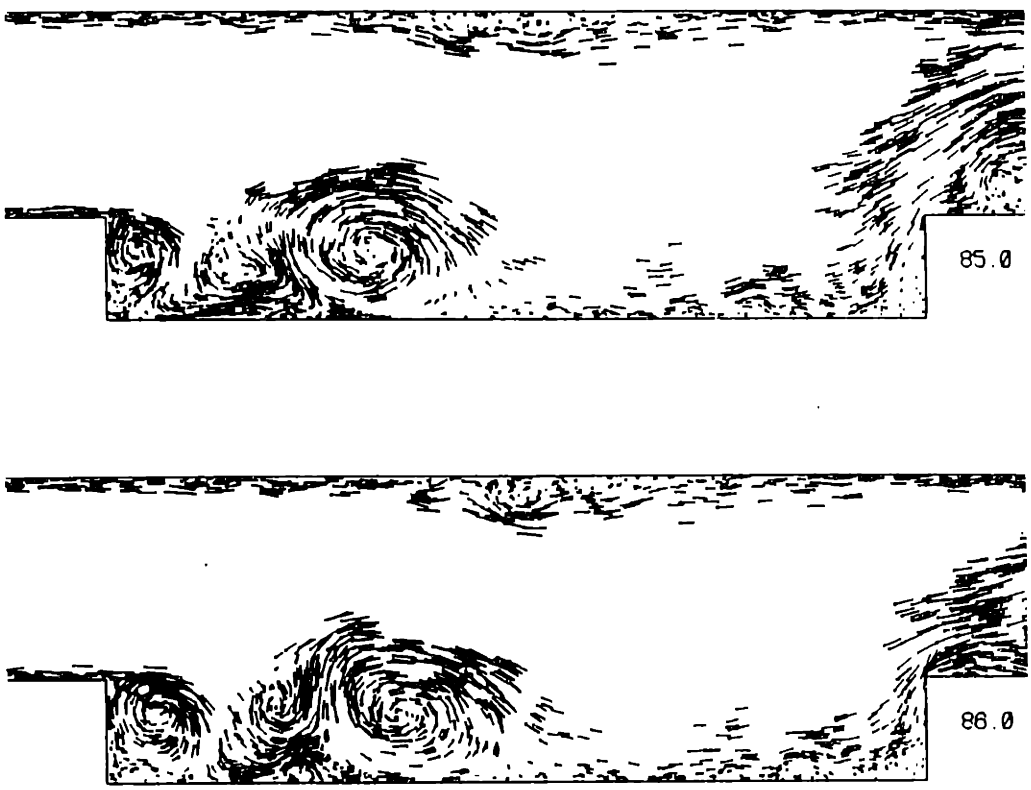

Figure 4.22 A sequence of time frames (continued from the previous three pages) showing the flow field, in terms of the vortex elements and their instantaneous velocity vectors, for a flow over a long cavity with L/D = 8, and Re_D = 2500.

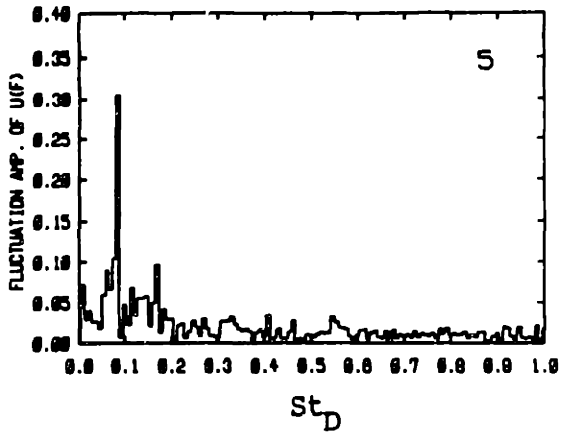

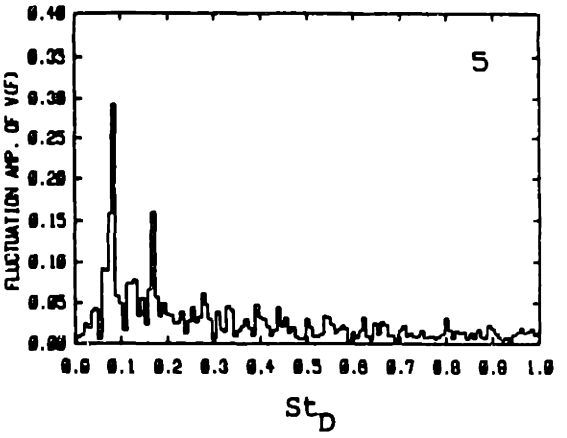

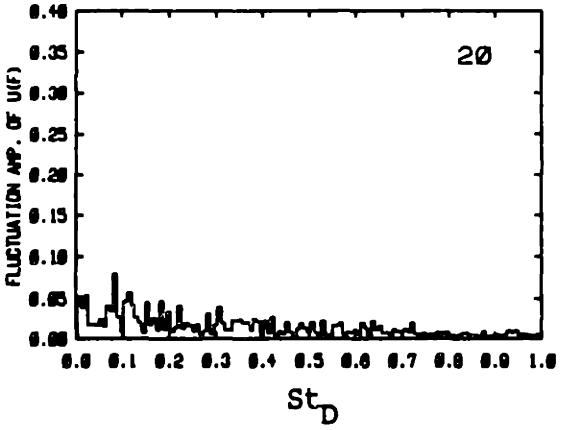

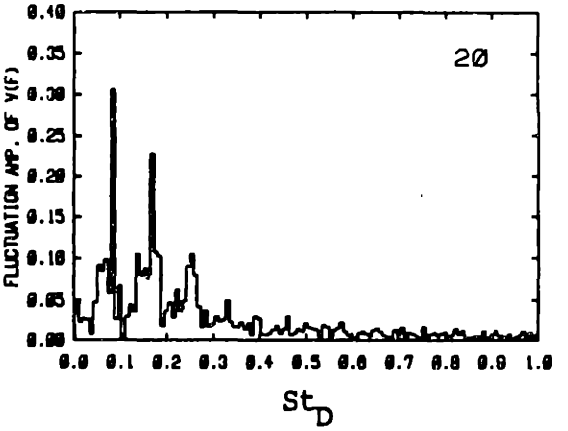

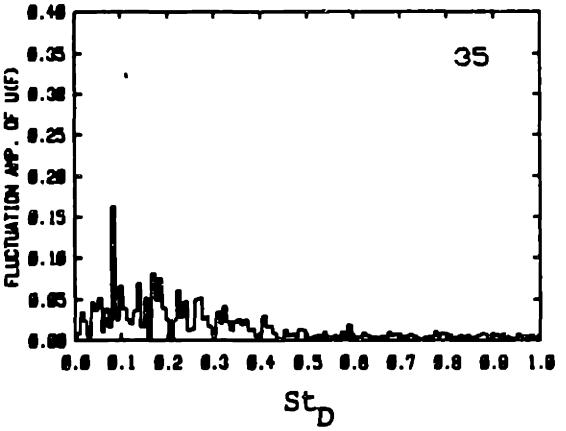

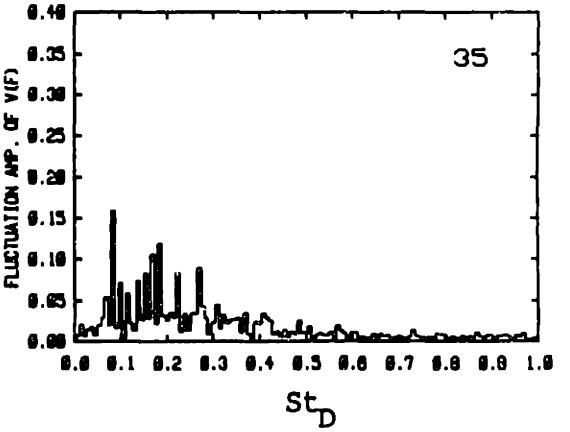

Figure 4.23 Spectra of the u and v velocity fluctuation, for the flow depicted in Fig. 4.22, at three points along the top of the cavity. The top row of plots corresponds to $(x/D,y/D) = (-3.0,1.0)$, the middle row to $(0.0,1.0)$, while the bottom row is at $(3.0,1.0)$. St_D is the Strouhal number based on the mean inlet velocity and the cavity depth. The highest peak in each of the above plots is at $St_D = fD/U_m = 0.085$.

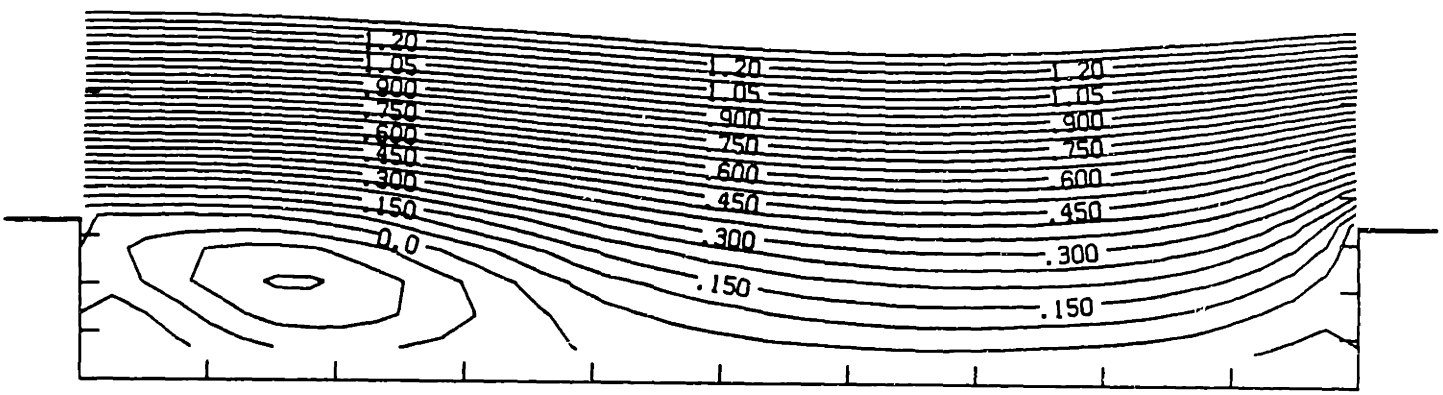

Figure 4.24 Long time average streamlines, time 20.0 to 150.0, computed from the flow field depicted in Fig. 4.22.

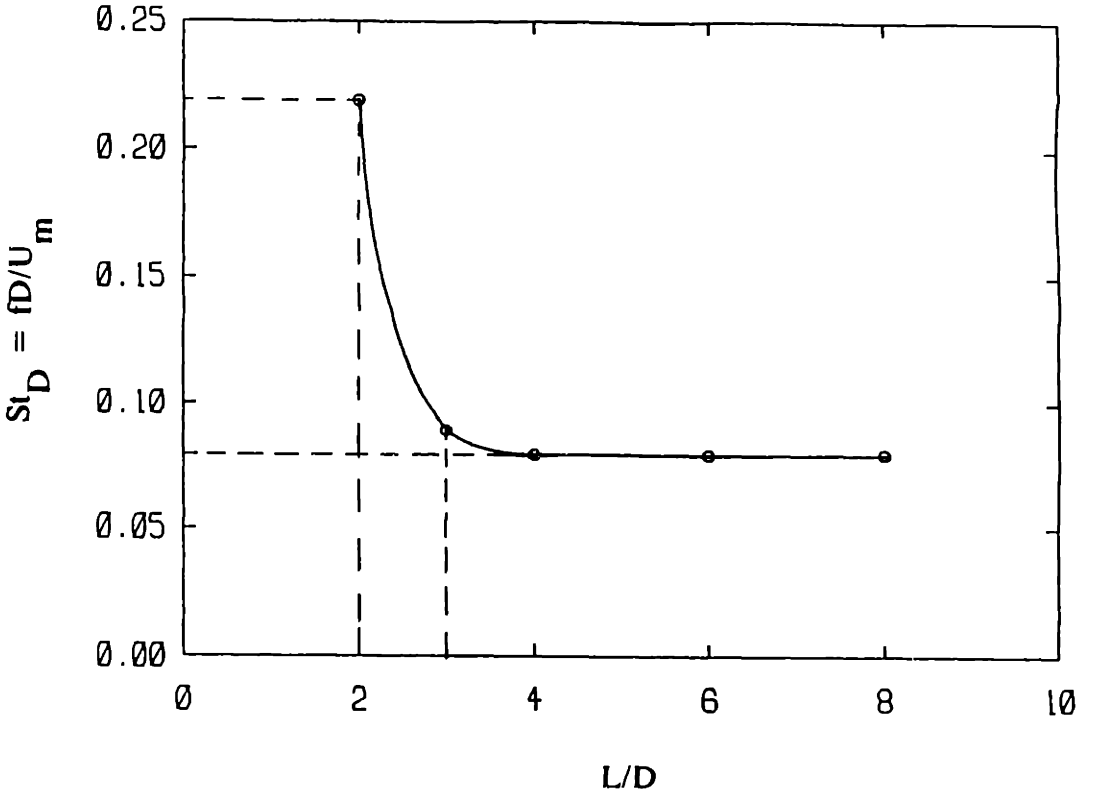

Figure 4.25 The variation of $St_D = fD/U_m$ versus L/D for all the cases studied.

5. REACTING FLOW

5.1 Background :

As mentioned earlier, the overwhelming problem with premixed dump combustors operating at relatively high, although less than stoichiometric, equivalence ratios is the "flashback" instability. Flashback, briefly introduced in Chapter 1, is an instability that results in the motion of the flame upstream into the inlet duct. It is accompanied by low frequency, large amplitude flow and pressure oscillation in the combustor. In the following, we give an extensive review of previous investigations into the nature of flashback in premixed dump combustors, and present our understanding and interpretation of this data.

It is worthwhile to note at the outset that the flashback we refer to here is not the "classical" flashback (Lewis & Von Elbe, 1961). Classical flashback involves the upstream motion of the flame along walls, in the boundary layers, due to the local low convective velocity. This is clearly not the case in the majority of reported flashback observations in premixed dump combustors. Instead, as reported in the review of Plee & Mellor (1978), flashback in premixed dump combustors is generally associated with either preignition, autoignition, or convective flow reversal. Furthermore, the latter phenomenon, flow reversal, is the one observed in all controlled laboratory experiments involving simple model geometries such as a backward facing step or a cavity.

Let us examine the combustor flow dynamics in general, under non-flashback conditions, and then consider the mechanism of transition to flashback.

Premixed dump combustor flows have been found to involve large scale, organized, vortex structures (eddies) that are shed from the upstream edge region of the dump and modulate the flame interface as they grow and move downstream. As evidenced by Schlieren pictures of many experimental investigations, the flame region lies generally at the edges of these eddies (e.g. Ganji & Sawyer, 1979, 1980; Keller et. al., 1981;, Vaneveld et. al., 1982; Yu et. al., 1989, 1987; Smith & Zukoski, 1985;, McManus et. al., 1987, 1989; Pitz & Daily, 1981, 1983). Furthermore, the eddies have been observed at various frequencies and were classified as different modes of oscillation of the combustor (see Keller et. al., 1981, Vaneveld et. al., 1982).

The problem of understanding these various modes of oscillation has been a daunting task tackled by many investigators. The dynamics of the underlying non-reacting flow, as indicated in Chapter 4, involve complicated interaction between the shear layer and the recirculation zone instabilities. The existence of the flame presents the added complication of the expansion field due to the combustion heat release as well as the acoustic response of the piping system upstream and downstream of the combustor, given the acoustic source distribution associated with the flame front.

The equivalence ratio, ϕ, of the incoming fuel/air mixture has been found to determine the specific mode of oscillation exhibited by the combustor. When ϕ is small, relatively high frequency, low amplitude oscillations are observed. As ϕ is increased, lower frequencies gain dominance, leading to large scale, low frequency flapping of the flame, which finally causes severe flow reversal and flashback. This low frequency oscillation, in which the flame position undergoes strong flapping but stays anchored at the desired region, has been studied widely as the significant precursor to flashback. It is a sustainable mode of operation, since the flow reversal is weak, and

occurs for a fraction of the oscillation cycle, hence the flame does not move far upstream into the inlet duct.

The following quote from Ganji & Sawyer (1979) is typical of observations made during transition to flashback: "Flashback is brought about by a coupling between the combustion and fluid mechanical processes which produces an instability in the flow. Flashback appears to start with an overexpansion of the large eddies inside the combustor which augments the recirculation of reactants into the recirculation zone behind the step. This in turn causes a lifting of the flame from the edge of the step and increases eddy growth. This process repeats until pressure pulsations occur which are sufficient to stagnate or possibly reverse the flow into the combustor allowing the flame to move into the inlet section upstream of the step." Similar dynamics have been reported by Vaneveld et. al. (1982), Keller et. al. (1981).

Given all this, the major unresolved issue is still the identification of the mechanism that leads to amplified instabilities and determines the frequencies of the combustor oscillation, both at high and, in particular, at low frequencies. It has been suggested by many studies that this frequency selection is determined by the acoustic characteristics of the combustor and piping system (Smith & Zukoski, 1985; Kailasanath & Gardner, 1986, 1987; Menon & Jou, 1987; Jou & Menon, 1987). The prevailing conviction has been that the acoustic power radiated from the unsteady flame feeds energy into the resonant acoustic modes of the system. This resonant pressure oscillation, which is fed back to the combustor, is believed to determine the frequency of the organized eddies shed from the shear layer and recirculation zone.

While we agree in part with this scenario, we will try to demonstrate that even if the higher modes of oscillation of the combustor correspond to "acoustic" modes of the system, the more dangerous low-frequency

oscillations, which lead to flashback, are determined by the dynamics of the recirculation zone in the dump. Thus, while the higher modes are "system" instabilities, the low-frequency mode that leads to flashback is a "combustor" instability in the sense that it is predetermined by the flow configuration in the dump (the inlet flow speed and the depth of the dump).

The dynamics of non-reacting incompressible recirculation zones are discussed in Chapter 4, and they generally involve the following scaling of the frequency of eddy shedding from the recirculation zone : $fD/U = St = O(0.1)$, where D is the cavity depth and U is the mean inlet velocity. Here, one has to be careful to recall that this Strouhal number, in non-reacting flows and, by extrapolation, in reacting flows, is not sharply defined but rather observed to be roughly around 0.1. The specific low frequency selected within this range may depend on other variables, including the acoustic response of the system, but it will always be such that $St=O(0.1)$, and it will always involve the amplification of the recirculation zone oscillations. Similarly, we must stress that our numerical investigation in Chapter 4 has found $St=O(0.1)$ for recirculation zones at incompressible conditions. Hence, we are considering combustor flows at relatively low Mach numbers. We are not making predictions about high Mach number flow fields.

Furthermore, the inlet flow rate in our non-reacting flow study was fixed, and U_m, used in Chapter 4, was simply the spatial mean velocity at the inlet plane. In the reacting case, where the upstream boundary condition is a specified stagnation pressure rather than the inlet flow rate, U_m is a function of time. We have chosen to use the time average value of U_m to be the mean velocity, U, used in the definition of St above.

The above claim, that the recirculation zone provides a generic low frequency "combustor" instability independent of other system components, is

quite general, and we shall try to provide justification for it by examining previous experimental findings before discussing our numerical results.

Generally, available experimental measurements of oscillation spectra within dump combustors exhibit two or more large amplitude peaks. As ϕ is increased, the lower frequency peak gains dominance. The accompanying time traces exhibit the familiar "beating" which corresponds to the superposition of two or more frequencies (Choudhury et. al. 1981; Yu et. al., 1989). The remarkable observation however, is that the reported Strouhal numbers for the lowest peak are found to always lie around 0.1, as indicated by the compilation of results in Table 5.1. These results are from various experimental and computational studies using different combustor and system configurations. The fact that St~0.1 is the single common result among all of them. On the other hand, the higher frequency peaks, not reported in the Table, and other details vary widely depending on the specific overall system considered. We believe that this system dependent variation has been at the root of the general inability to comprehend the operation of dump combustors.

Therefore, based on the above, we maintain that flashback occurs as a result of amplification of the inherent recirculation zone dynamics, and that this amplification occurs as the pressure oscillation in the system approaches the natural low frequency of the recirculation zone eddies. In the following we attempt to verify this hypothesis by conducting numerical experiments using the full reacting flow model. We begin by the case of fixed atmospheric exit pressure, p_{ex}, and examine the flow dynamics. This is followed by a forcing study in which p_{ex} is specified to be a given sinusoidal forcing function and we examine the effects of higher heat release given different frequencies of exit pressure modulation.

Table 5.1

Yu. et. al., 1989	Double expansion, with constriction at exit D=2.5cm, L=5.8-12.5 cm, U=12.2-16.3 m/s ϕ=0.65, dominant St = 0.09-0.15. L/D is found to change St slightly. e.g. for U=12.2 m/s, (L=5.8 cm, St=0.15), while (L=12.5 cm, St=0.10)
McManus et. al., 1987 and 1989	Backward facing step, D=2.0 cm, U=8.5 m/s ϕ=0.70, St=0.10 even when forced at a much higher St.
Gangi & Sawyer, 1978	Backward facing step, D=2.55 cm, U=13.2 m/s St=0.10, low frequency flapping Pressure oscillation amp. >> dynamic head
Smith & Zukoski 1985	Backward facing step, D=1.9 cm, U=22.0 m/s, ϕ=1.0 St=0.16 for U=22 m/s St=0.09 (same f), for U=40 m/s, and with changes to some acoustic characteristics of the system., although a new peak appears also slightly larger St. St=0.20 for U=50 m/s frequency depends on the amplitude of inlet velocity fluctuation.
Schadow et. al. 1987	Axisymmetric ducted jet, D=3.2 cm, non-reacting, U=38 m/s, St=0.12 reacting, U=37 m/s, St=0.13
Kailasanath et. al. 1986, 1987	Axisymmetric ramjet, step - constriction, computational. D=3.2 cm, U=50 m/s, St=0.09, lowest peak.
Vaneveld et. al. 1982	2D cavity, D=2.54 cm, U=9.12 m/s, St=0.15 low frequency chucking

5.2 Results :

The geometry used here is again that of Fig. 3.1, along with the upstream and downstream pressure boundary specifications. The computational grid used for the propagation and advection of the products of combustion is a uniform, square grid with $\Delta x/D = \Delta y/D = 0.1$.

We will denote the reference velocity by U_r, and the reference density by ρ_r. We use the dynamic pressure $\rho_r U_r^2$ as the reference pressure p_r for the boundary condition pressure computation, and we will report gauge pressure values, measured with respect to atmospheric pressure, $P_{atm}=10^5$ Pascals. Hence, a pressure $p/p_r=1.0$, for example, corresponds to an absolute dimensional value of $P_{atm}+1.0p_r$. We refer to the stagnation pressure in the upstream reservoir as p_o.

As indicated in Chapter 2, the Reynolds numbers in the reactants (Re_u) and the products (Re_b) are different. In fact, given their definitions in Table 2.6, we have :

$$Re_b/Re_u = (\rho_b/\rho_u)(\mu_u/\mu_b) \tag{5.1}$$

Further, given eq. (2.23), we have : $\rho \propto 1/T$. Using this relation, and assuming $\mu \propto T^{1/2}$ (see Tien & Lienhard, 1979), we get :

$$Re_b/Re_u = (\rho_b/\rho_u)^{3/2} \tag{5.2}$$

Therefore, in the reacting case, the Reynolds number used in the products is a fraction of that in the reactants, where this fraction is given by the 3/2 power of the density ratio ρ_b/ρ_u.

The results are obtained for a fixed cavity geometry, L/D=4.0, H/D=1.0, xmin/D=-4.0, xmax/D=4.0. These parameters will be implicit in the discussion below.

Further, the same dimensional reference quantities are used in all the reacting flow results below. The reference density and viscosity (dynamic) are those of the reactants, and have the values : ρ_r=1.2 kg/m^3, and μ_r=2.0x10^{-5} Ns/m^2. The reference length is the cavity depth, D=2.5 cm. The reference velocity is U_r = 6.67 m/s, and the reference gauge pressure is p_r=53.33 Pa.

In the following we begin by examining the reacting flow results for the unforced case, where the exit pressure is atmospheric.

5.2.1 The Unforced Case :

The main issue here is to determine the effect of the heat release due to combustion on the flow dynamics, given a specified fixed exit pressure, p_{ex}=0 (gauge), i.e. atmospheric exit pressure.

We begin by examining a flow case with the following specifications :

Upstream stagnation pressure : $p_o/p_r = 2.02$ (p_o=107.73 Pa-gauge)

Reynolds number in reactants : $Re_u = U_r D/\nu_u = 10^4$

Density ratio across flame : $\rho_u/\rho_b = 4$

Reynolds number in products : $Re_b = U_r D/\nu_b = 1250$

Normal burning speed : $S_u/U_r = 0.05$ (S_u=33.33 cm/s)

We also use the following numerical parameters :

Sheet length : $h_s/D = 1/3$

Sheet strength : $\Gamma_m/U_r D = 0.0278$

Time step : $\Delta t U_r/D = 0.05$

Sheet layer thickness : $\Delta_s/D = 0.0095$

The flow dynamics for this case are illustrated in the sequence of time frames of the vorticity field and the flame interface shown in Fig. 5.1. Although the products and reactants are not labeled specifically, it is implicit that the area underneath the flame, within the cavity and beyond, contains the products. The inlet stream is all reactants. The flame interface is drawn as a thick line for visualization purposes. The same earlier convention is used with the vortices, namely, each vortex element is depicted with a small circle, and its velocity is delineated by a straight line segment originating at its center and with its length and direction corresponding to the magnitude and direction of the velocity vector at that point.

For comparison, Fig. 5.2 shows a similar sequence of frames illustrating the recirculation zone eddy shedding for non-reacting flow in the same geometry, although at lower Reynolds number, $Re=U_r D/\nu=1250$, and lower upstream stagnation pressure, $p_o/p_r=1.0$. Note that the reference velocity and pressure used for this case are different from those for the reacting flow cases. They are : $U_r=0.83$ m/s, and $p_r=0.83$ Pa. All other reference quantities are identical to those in the reacting flow. Relevant numerical parameters are : $h_s/D=1/2$, $\Gamma_m/U_r D=0.0417$, $\Delta t U_r/D=0.05$, $\Delta_s/D=0.0134$.

The dynamics of the recirculation zone in the reacting case are similar in many respects to those of the non-reacting flow. Eddies are shed at the upstream edge of the dump, they grow by entraining shear layer vorticity, then detach and move downstream as they continue to grow by entraining essentially irrotational fluid until they collapse at the downstream edge.

Further, the flame is observed, as was found experimentally, to ride on the outer edge of the recirculation zone. In other words, the large eddies modulate the flame interface as they grow and move downstream. Similarly, small shear layer eddies are observed to modulate the flame at a smaller scale, which is superposed on the larger scale modulation, see for example time 37.0 in Fig. 5.1. As with the non-reacting flow pictures, these smaller eddies are engulfed by the large trailing eddy forming in the upstream end of the cavity.

The reacting flow does differ, however, from the non-reacting flow in that the size and "coherence" of eddies within the recirculation zone are both diminished due to the flow field associated with the flame. By the "coherence" of an eddy we refer to the degree to which the eddy holds the vortical fluid within it together as one structure, distinct from the rest of the flow field. In the non-reacting flow, Fig. 5.2, the eddies displayed higher coherence and attained larger sizes than those in Fig. 5.1. This

difference is also observed in the time trace and spectral analysis of the velocity along the top of the cavity. Let us consider the u-velocity at y/D=1.0, and x/D=-1.0,1.0. Figures 5.3 and 5.4 show the time traces and frequency spectra for the reacting flow at these two points respectively, while Figures 5.5 and 5.6 show the same results for the non-reacting flow. The dominant low frequency peak at each station in Fig. 5.4 has lower amplitude than that in Fig. 5.6. At x/D=-1.0, the amplitude of the dominant peak in the reacting case is u/U_r=0.137 or u/U=0.109, while that in the non-reacting case has u/U_r=0.414, u/U=0.370. Similarly, at x/D=1.0, the dominant peak has an amplitude of u/U_r=0.117, u/U=0.093, in the reacting case as compared to u/U_r=0.346, u/U=0.309, in the non-reacting case. As will be indicated below, these peaks do correspond to the recirculation zone eddy shedding in each case. Clearly then, both the time traces and spectra show a better organization in the non-reacting flow than in the reacting flow.

In fact, we find that increasing the amount of burning, hence the heat release, beyond that used above, causes further reduction in the size and coherence of the recirculation zone eddies, giving a rather quiescent recirculation region in the dump - as long as the exit pressure is fixed. Thus, our numerical results indicate that, for a fixed exit pressure, the heat release associated with combustion acts to dampen the instability of the shear layer and recirculation zone.

These observations are in agreement with available experience for combustion systems with no significant acoustic feedback, see for example, Williams (1985) and Glassman (1987). One mechanism that has been suggested to explain this stabilization is that the Reynolds number in the recirculation zone is lower than that in the mainstream due to the increased temperature in the products. The lower Reynolds number is expected to cause the separation bubble to become more stable in the reacting case than in the non-reacting

case. However, the value of the Reynolds number used in the above non-reacting flow is precisely that used in the products in the reacting case (recall eq. 5.2 above). Therefore, it is not the lower Reynolds number in the products that dampened the instability of the recirculation zone. The only other possible mechanism in our model is the expansion field due to the flame. It seems that this expansion field acts to accelerate the flow leaving the dump region by imposing a more favourable streamwise pressure gradient, and that this tends to dampen the growth of the recirculation zone instability. The flow acceleration due to heat release is clearly exhibited by the increase in the size of the velocity vectors leaving the cavity in Fig. 5.1. Figure 5.7, from Lewis and Von Elbe (1961) p. 439, shows the pressure gradient and mean recirculation bubble size corresponding to reacting and non-reacting flow around a cylinder. This figure illustrates the correlation between the pressure gradient and the degree of growth of the recirculation zone instability. We suggest that this same mechanism is at work in the flow at hand. This mechanism is well known in other flow arrangements such as, for example, the stabilization of boundary layers by flow acceleration and favourable pressure gradients. Figure 5.1 illustrates that the growth of the boundary layer on the top wall, which can be compared to that in Fig. 5.2, is drastically reduced due to heat release and the concomitant flow acceleration. Similarly, for plane shear layers, streamwise pressure gradients are known to strongly affect the growth of the shear layer; reducing it for a favourable pressure gradient and enhancing it otherwise (Masutani et. al., 1978, 1988).

Clearly, this stabilization is not significant in systems where the combustion can couple with the system acoustics causing sustained pressure oscillations in the combustor and its inlet and exit piping. In such cases, the pressure feedback due to the acoustic resonance forced by the flame may

upset the stabilization caused by the expansion field by enhancing the organized eddy shedding from the recirculation zone. See for example the flow pictures of Vaneveld et. al. (1982).

Therefore, we have shown that for a fixed exit pressure, hence no acoustic resonance feedback or pressure forcing, the reacting flow exhibits oscillation corresponding to eddy shedding from the recirculation zone similar to the non-reacting flow shedding but with lower coherence and strength. Further, increasing the amount of burning causes further stabilization of the recirculation zone. We therefore conclude that this system cannot achieve the large amplitude fluctuations leading to flow reversal and flashback. Clearly, the downstream exit pressure is crucial in determining the dynamics to be seen in the combustor. The investigation of the influence of this pressure is handled in the next section. Before we go there, however, it is instructive to analyze the "natural" dynamics of the present model in some more detail. This will shed light on the nature of the combustor flow oscillation and allow further comparison with experimental results.

Let us begin by observing the shedding frequency of the recirculation zone eddies in the reacting case versus that in the non-reacting flow. These shedding processes are found to correspond to the dominant Strouhal number peaks in Figs. 5.4 and 5.6, respectively. The Strouhal number in each of these plots is based on the cavity depth and on the time average mean inlet velocity U, for the time span considered. We expect, from the results in Chapter 4 and from our literature review, that both spectra should exhibit dominant peaks in the vicinity of St=0.1. This is indeed the case, the dominant peak in the non-reacting case, Fig. 5.6, is at St=0.089$\pm$0.012, while that in the reacting case, Fig. 5.4, is at St=0.119$\pm$0.012 at x/D=-1.0, and St=0.099$\pm$0.012 at x/D=1.0, being well centered around 0.1 for the whole range

of x/D. In the non-reacting case, St=0.089 corresponds to a dimensionless time period of 10, which is evident in the vorticity dynamics shown in Fig. 5.1 (compare times 33.0 and 42-43.0, to see how the flow repeats itself with this period). As for the reacting case, St=0.1 corresponds to a time period of 8, which is again evident in Fig. 5.2, as for example, between the frames at times 35.0 and 43.0. Therefore, the Strouhal number, O(0.1), of recirculation zone eddy shedding, which corresponds to the lowest frequency, highest amplitude peak in the frequency spectra, is not significantly different in the reacting case from that in the non-reacting case. It is also noted that, for the reacting flow, the peaks at St~0.2 and 0.1 are of comparable size while in the non-reacting flow the low frequency mode carries almost three times as much energy as the high frequency mode.

Next, we examine both the pressure in the combustor and the inlet flow rate, Q_{in}, as functions of time. For the sake of comparison with experimental measurements, we look at the pressure in the channel, at its centerline, above the upstream step of the cavity, P_{step}. The pressure trace corresponding to the conditions of Fig. 5.1 is shown in Fig. 5.8. Figure 5.8a shows the actual pressure data computed in the run, while Fig. 5.8b shows a smoothed version of the same trace. Both traces are plotted against time. The smoothing helps to bring out the low frequency oscillations of the pressure by filtering out the high frequency noise. This noise, which is evident in Fig. 5.8a, is due to the the unsteady flow field as well as the discrete nature of the numerical scheme and the random walk algorithm for the simulation of diffusion. Note that the pressure is obtained by integrating $\partial p/\partial x$, which is computed from the x-momentum equation and thus involves differentiation of the velocity field. The inlet flow rate, Q_{in}, is plotted in Fig. 5.9. This trace contains less high frequency noise than the pressure trace. This is clearly due to the inertia of the fluid and the concommitant

time delay required for it to accelerate due to a given pressure gradient. Figure 5.10a shows the superposition of the Q_{in} and P_{step} traces. It is found from this plot that Q_{in} leads P_{step} by, roughly, a quarter of a period of oscillation. This observation is in agreement with the experimental measurements of Yu et. al. (1989), for a cavity with a constriction at the exit and an "long" upstream pipe inlet section.

The superposition of Q_{in} and P_{step} is blown up in Fig. 5.10b, for a time segment from 32.0 to 44.0. This segment corresponds to the shedding cycle shown in Fig. 5.1. Let us compare the two figures. The pressure in Fig. 5.10b reaches a minimum at times 33 and ~41. In Fig. 5.1, these times are seen to correspond to a flow condition where the trailing eddy is growing in the upstream region of the dump, while the leading eddy has collapsed at the downstream edge. This is accompanied by an acceleration of the inlet flow into the combustor, as is evident in the significant positive slope of the Q_{in} trace at time 41, for example. The rise in the inlet flow manifests itself in the vorticity plots as a strong downward flux of vortex elements into the cavity. This is seen at times 34-35, and 41-42 in Fig. 5.1. The trace of Q_{in} attains a peak at times 35 and 42. As the flow acceleration decreases, to reach this peak, the pressure is seen to rise steeply. The maximum pressure is attained roughly at times 37 and 44, a 1/4 period (2 time units) after the Q_{in} peak. At this point, the flow rate is experiencing strong deceleration. Time frame 37.0 in Fig. 5.1 indicates that this corresponds to a situation where the large eddy reaches its maximum size on its journey to the downstream edge. As the eddy arrives at the downstream edge, the flow rate reaches its minimum (time 38-40), and the pressure is falling steeply. The eddy disintegrates at the downstream step (time 40-41), as the flow rate starts to rise again, and the pressure reaches its minimum.

At this time, a new trailing eddy is forming in the upstream region of the cavity, and the cycle is repeated.

Therefore, the eddy shedding process is closely associated with specific flow rate and pressure oscillations within the combustor. The flow rate into the combustor attains a maximum as the trailing eddy leaves the step and moves downstream, while the minimum flow rate corresponds to the leading eddy arriving at the downstream step prior to its disintegration. The pressure, P_{step}, on the other hand, reaches its highest value when the eddy is largest after it has detached from the upstream step and before arriving at the downstream step. Clearly, this high pressure causes the minimum flow rate soon after when the eddy reaches the downstream edge. The minimum pressure corresponds to the situation where the trailing eddy has formed but is still close to the upstream edge, while the leading eddy has disintegrated at the downstream step. One more time we see that the oscillations of the separating shear layer and recirculation zone are not necessarily related to the impingement of the large eddy at the downstream edge but to the flow processes involving the leading and trailing eddies in the cavity.

The strongest oscillation of Q_{in} and P_{step} occurs at the frequency of the recirculation zone eddy shedding, St=0.1. This is well illustrated by the spectra shown in Fig. 5.11a, for Q_{in}, and Fig. 5.11b, for P_{step}.

A significant component of the combustor operation involves the total rate of heat release and its relationship to the combustor flowfield. The rate of expansion, or rate of volume release, is a direct indicator of the heat release in our model. For the reacting flow case considered, the volume release rate is found to oscillate with the large scale flow dynamics. This oscillation is shown in Fig. 5.12a, where we have plotted the rate of volume release versus time. While a considerable amount of energy exists at various

frequencies, the spectral analysis reveals a dominant Strouhal number that is close to 0.1, as in Fig. 5.13.

In order to investigate the nature of these oscillations, let us examine first Fig. 5.12b. This plot shows the variation in the overall number of flame segments, or flamelets, in the combustor as a function of time. This is an indicator of the overall flame length (or area, given the 3rd dimension). A comparison between this plot and that of the volume release rate in Fig. 5.12a reveals that the two quantities are in phase, in fact they follow each other closely. Hence, we find that the instantaneous amount of heat release from the combustor varies directly as the instantaneous flame length. This is expected since the rate of burning is given by : $\int S_u dl$ over the flame length. When the flame is contorted and fragmented by the flow field, its overall length increases, and hence the amount of burning, and heat release, increase accordingly.

The flame is contorted both by the shear layer eddies and by the large recirculation zone eddies. Both these mechanisms can be observed in our results. Consequently, it is difficult to point to a definite time within a shedding cycle that will exhibit the highest heat release. Note in particular that flame modulations by the shear layer eddies, although initially small, grow with time as they move downstream along the flame and hence become significant. In the majority of the cycles observed, however, the flame seemed to attain its highest contortion, producing the highest heat release, when the recirculation zone eddy is largest, having detached from the upstream step, and moving downstream. This is reasonable in the light of our previous discussion about the mechanism of growth of the eddy in this part of the cycle. Namely, the large eddy grows by entraining fluid from the mainstream, hence by entraining reactants and stretching the flame interface and increasing its area.

To illustrate the relationship between the flow dynamics and the overall rate of heat release, let us look at the vorticity plots corresponding to the heat release maxima in Fig. 5.12. After the flow startup time (0-10), these are found to occur at times : 19.0, 22.0, 31.0, ~39.0, and 43.5. The vorticity field at time 39.0 is shown as part of the sequence in Fig. 5.1, while the rest are shown in Fig. 5.14. As we shall see, some of these frames exhibit the above large detached eddy situation and the concomitant flame contortion, while others correspond to flame contortion due to growth of shear layer modulations. Frame 19.0 shows the eddy at an early phase, but the flame interface is quite contorted due to the downstream growth of perturbations. Similarly, frame 39.0, in Fig. 5.1, exhibits significant contortion due to shear layer eddies, both upstream and downstream, while the recirculation zone eddy is at the downstream step. On the other hand, each of the frames 22.0, 31.0, 43.5, shows a large detached eddy traveling downstream, as described above, at the time of maximum heat release. As mentioned in our above comparison between the inlet flow rate and step pressure traces and the vorticity frames, this part of the shedding cycle, exhibiting high heat release and a large detached eddy in the dump, corresponds roughly to a maximum in the pressure. The correspondence between the pressure peaks and heat release peaks is evident, at least for some of the heat (volume) release peaks in Fig. 5.15, where the pressure and volume release traces are superposed. In fact, Yu et. al. (1989) find that the rate of heat release lags the pressure by roughly 1/4 of the period. Hence, the heat release should peak shortly after the pressure does. At least three of the peaks in Fig. 5.15 (times 7.0, 31.0, and 39.0) display this phase lag. The time segment corresponding to the two peaks at times 31.0 and 39.0 is blown up in Fig. 5.16a to illustrate this 1/4 period phase shift. Furthermore, given the above demonstrated phase relationship between the

pressure and the inlet flow rate, it is evident that the heat release is roughly 1/2 period (180 degrees) out of phase with the inlet flow rate, as shown in Fig. 5.16b for the same time segment in Fig. 5.16a.

The heat release minima, on the other hand, are found to correspond to situations where the flame is least contorted. From Fig. 5.12, consider the minima at times 15.5, 26.0, 28.0, 36.0, 42.0, and 46.0. The vorticity plots at times 15.5, 26.0, 28.0, and 46.0 are shown in Fig. 5.17, while those at 36.0, and 42.0 are in Fig. 5.1. These frames illustrate the lower fragmentation and contortion of the flame interface at these times, and hence the lower heat release.

Finally, let us look at the flow rate leaving the combustor, namely Q_{out}. The variation of this quantity with time and the corresponding frequency spectrum are shown in Fig. 5.18. The dominant frequency corresponds to St=0.079$\pm$0.012 which is again in the vicinity of 0.1, this is expected since both Q_{in} and the volume release rate have been found to exhibit this Strouhal number.

The significance of Q_{out} is that it acts as a forcing function for the downstream system components that may exhibit a characteristic acoustic resonance response. Clearly, given this oscillation in Q_{out} feeding into the exit piping, the pressure at the exit plane (xmax) is not expected to be fixed at atmospheric or any other pressure level. Instead, it must exhibit oscillations that depend on the flowfield and geometry.

This brings us to the next topic. In order to investigate the effect of having an oscillating exit pressure on the combustor dynamics, we conducted the forcing study discussed in the next two sections. This study involves imposing a specified exit pressure waveform, hence removing the effect of the flow field on p_{ex}, but retaining the effect of p_{ex} on the combustor dynamics. This is a simpler case to tackle as opposed to the fully coupled case.

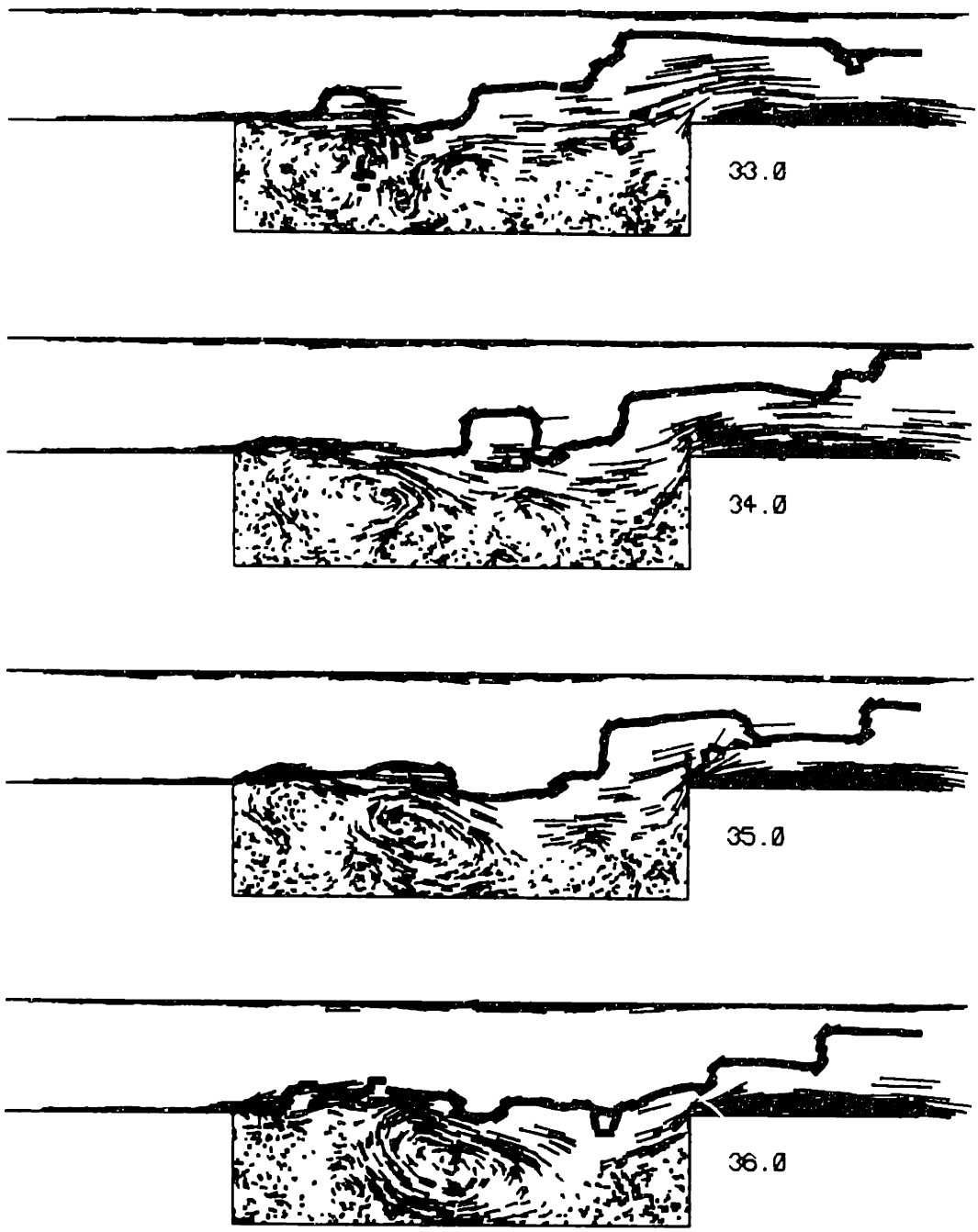

Figure 5.1 For caption see next page.

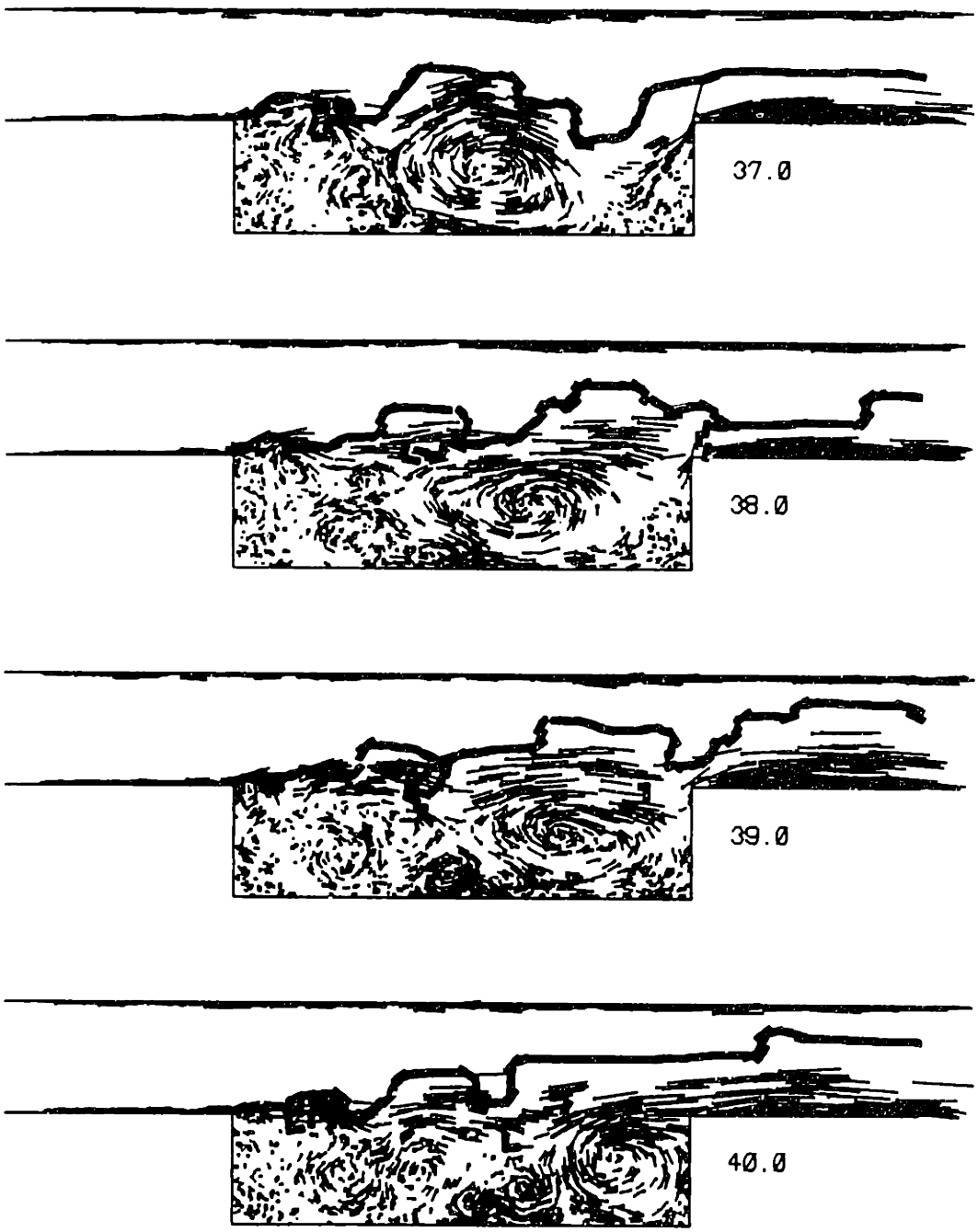

Figure 5.1 For caption see next page.

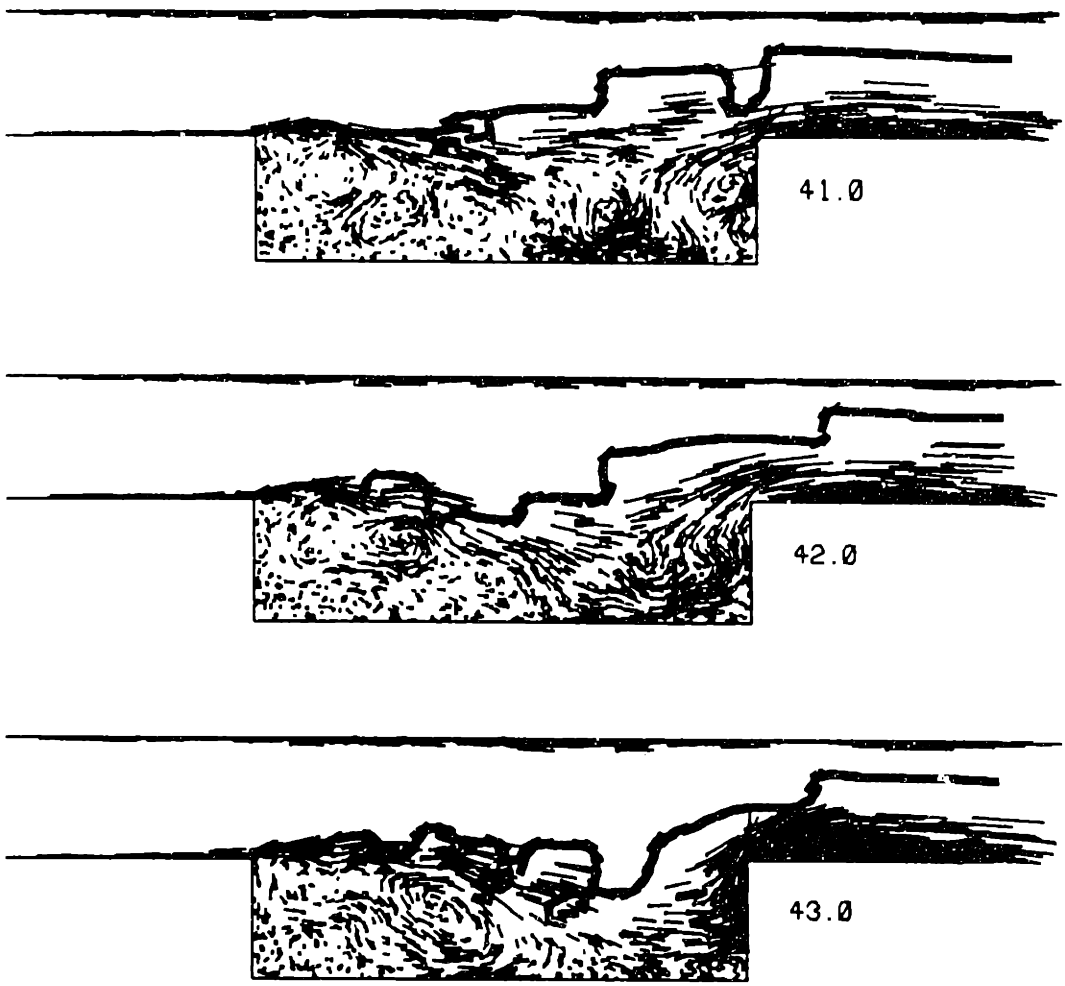

Figure 5.1 A sequence of time frames (continued from the previous page) showing the combustor flow field, presented in terms of the vortex elements, their velocity vectors, and the flame interface. The exit pressure is atmospheric, fixed.

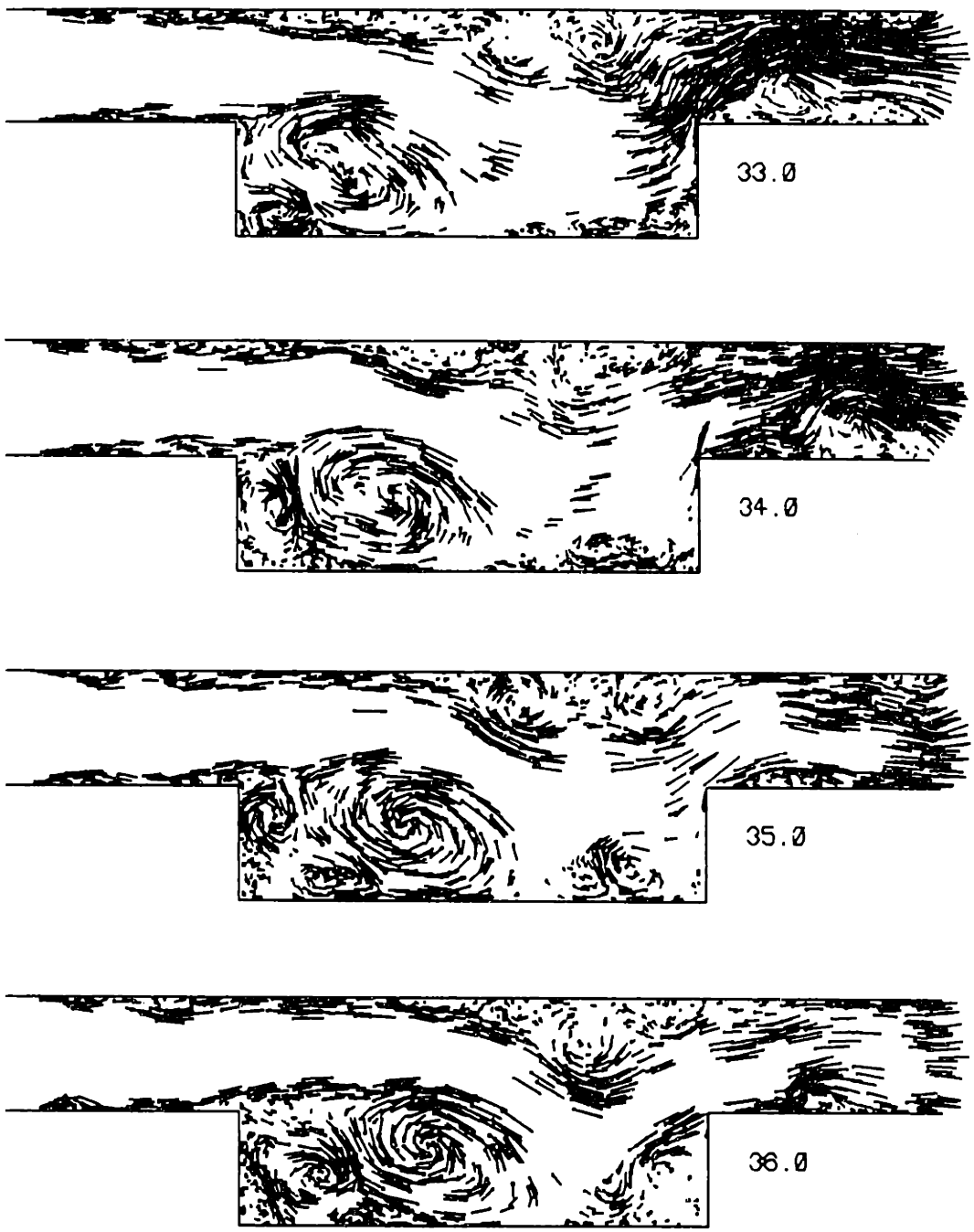

Figure 5.2 For caption see next page.

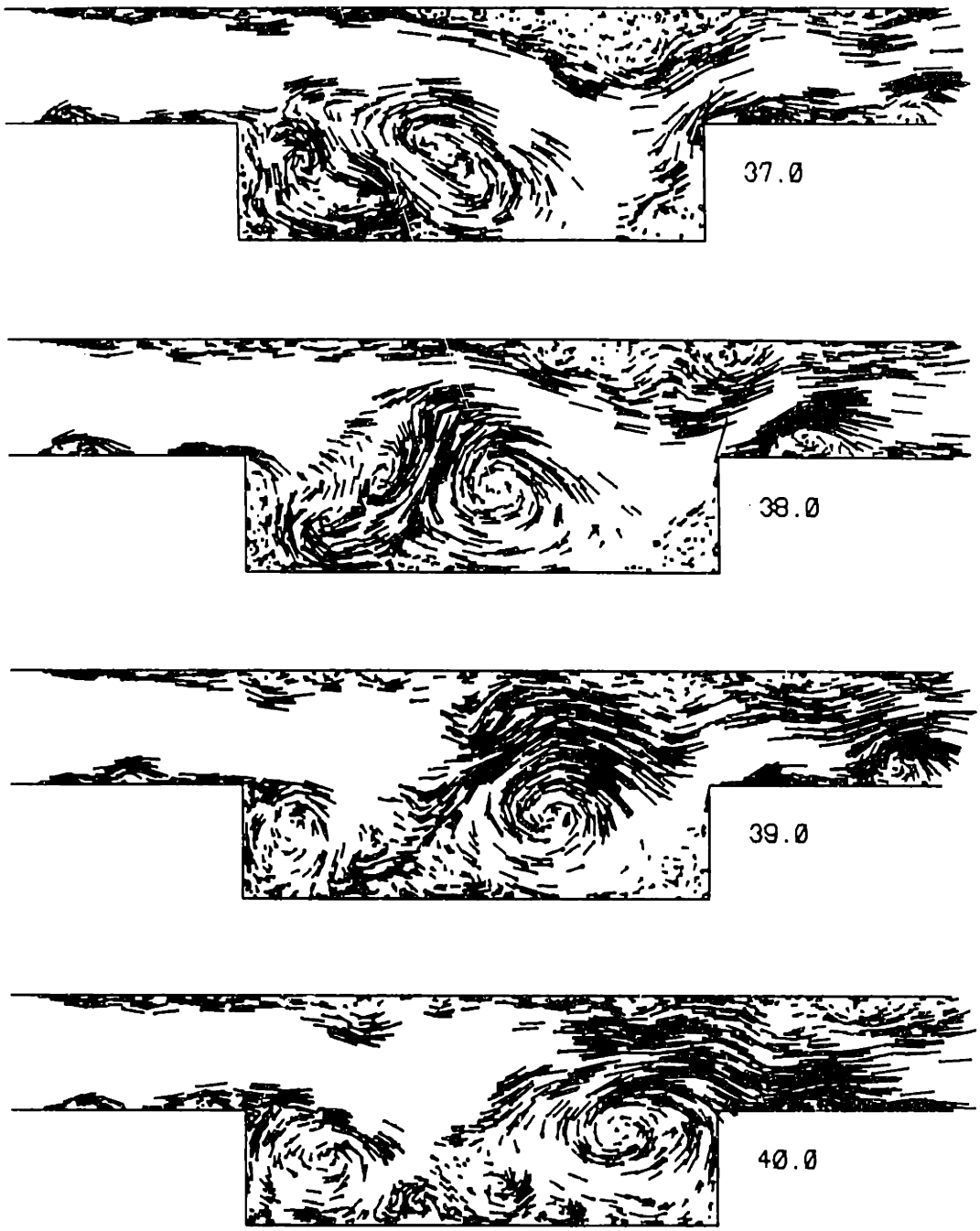

Figure 5.2 For caption see next page.

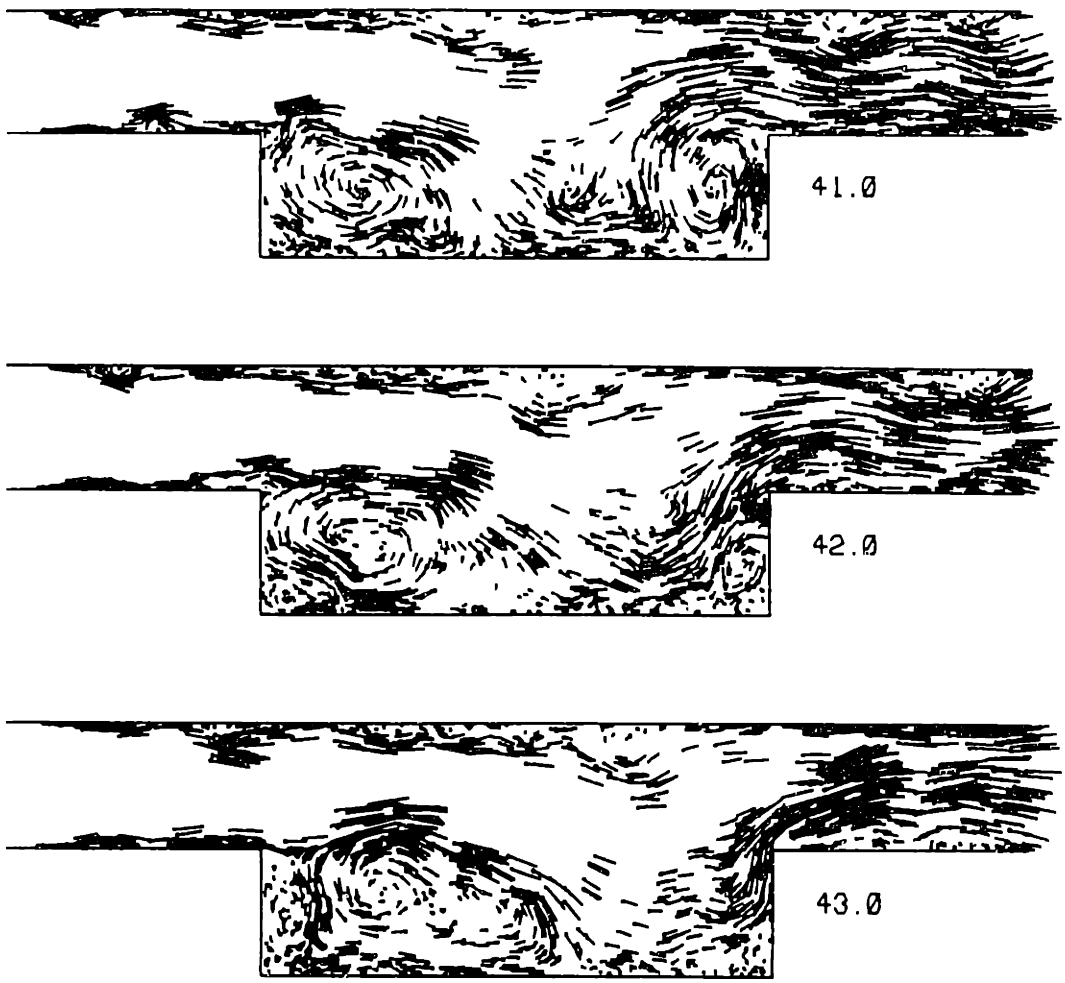

Figure 5.2 A sequence of time frames (continued from the previous page) showing the non-reacting flow field in the combustor geometry, presented in terms of the vortex elements and their velocity vectors. The exit pressure is atmospheric, fixed. The upstream boundary condition is, as with the reacting flow case, a specified stagnation pressure.

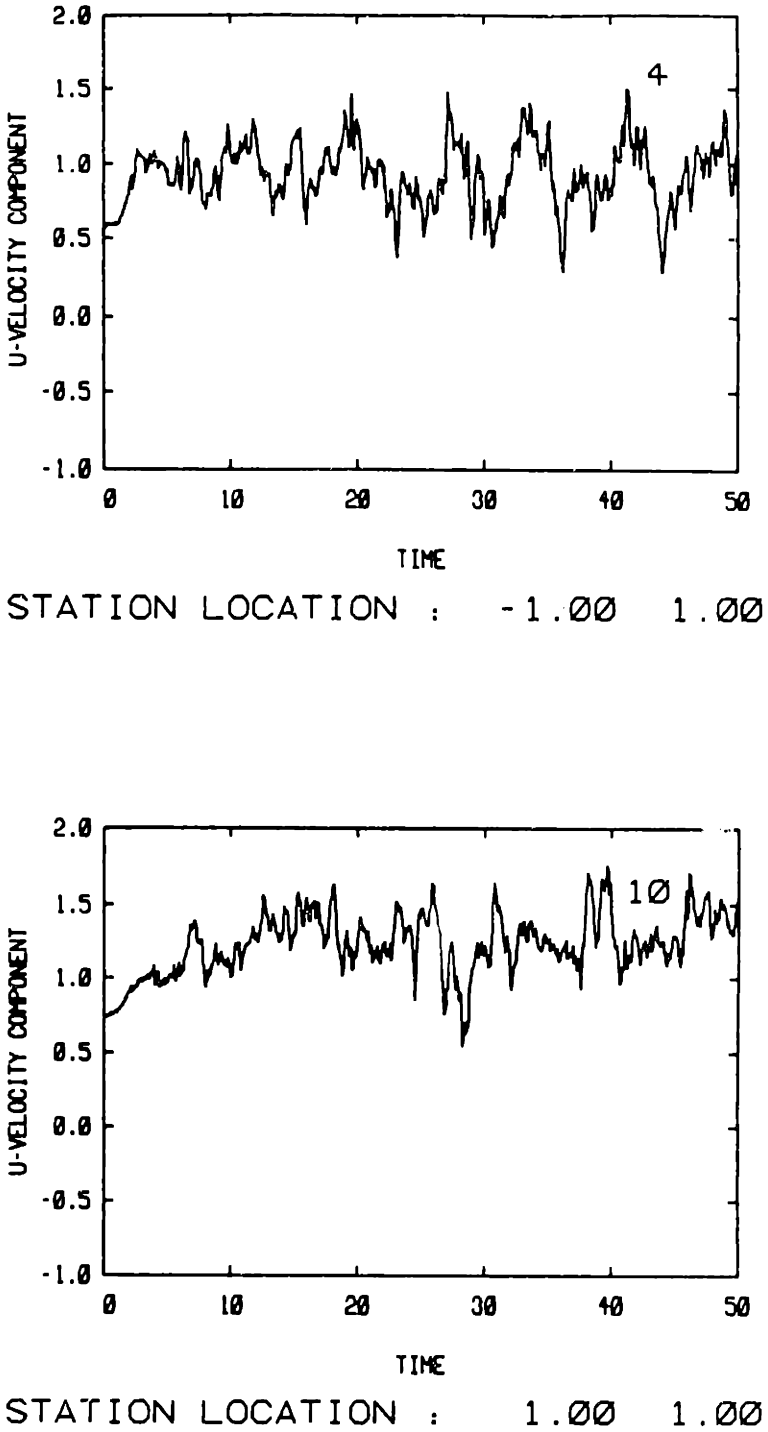

Figure 5.3 Time traces of the streamwise velocity at two points along the top of the cavity, for the reacting flow field of Fig. 5.1. The numbers identifying the station location are the x and y coordinates, respectively.

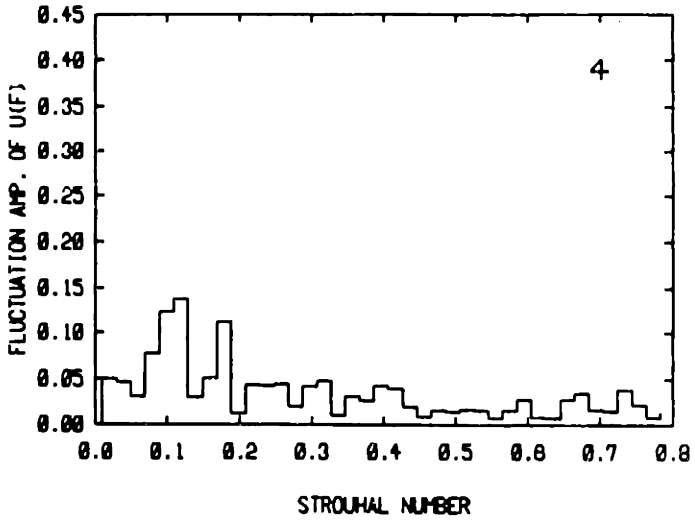

X=-1.000, PEAKS= 0.119 0.179 0.020

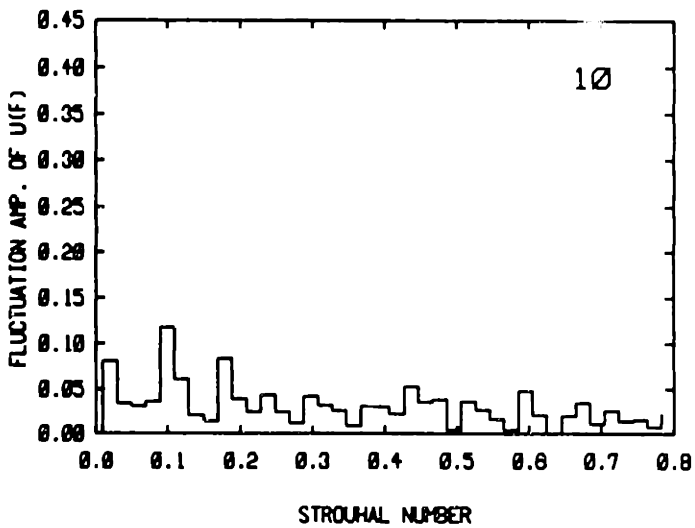

X= 1.000, PEAKS= 0.099 0.179 0.020

Figure 5.4 Spectra of the streamwise velocity fluctuation, computed from the time trace in Fig. 5.3, for the time period 10.0-50.0. The Strouhal number used is based on the cavity depth and the mean inlet flow velocity for the time period considered. The dominant peak is around St=0.1 in both plots.

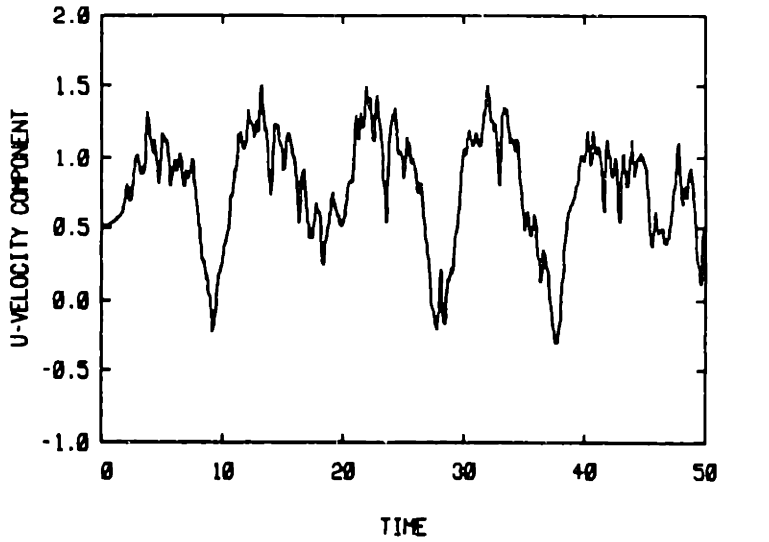

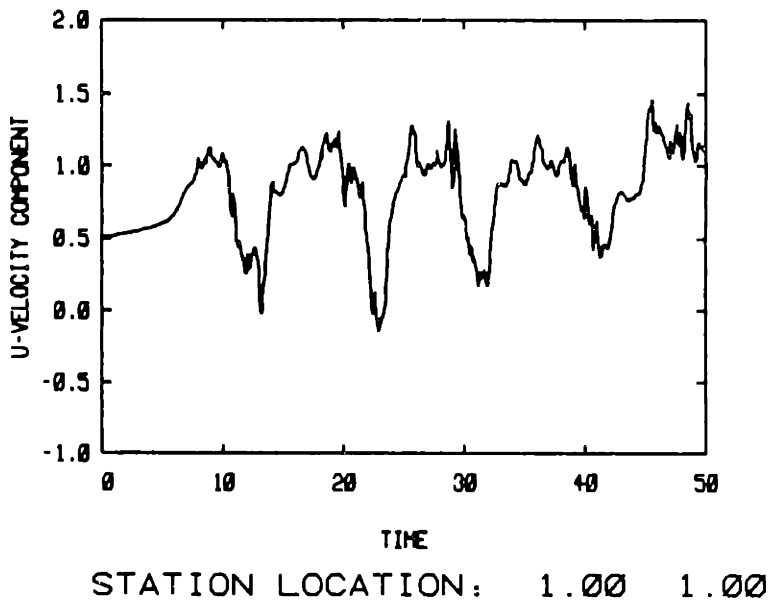

Figure 5.5 Time traces of the streamwise velocity at two points along the top of the cavity, for the non-reacting flow field of Fig. 5.2. The numbers identifying the station location are the x and y coordinates, respectively.

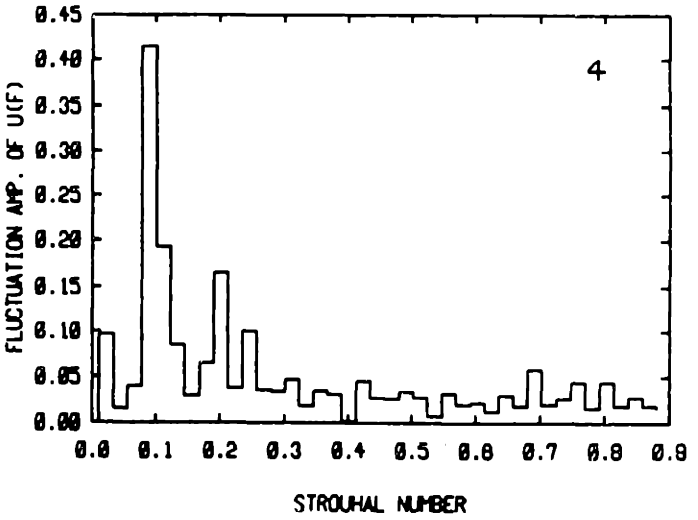

X= -1.000, PEAKS= 0.089 0.201 0.246

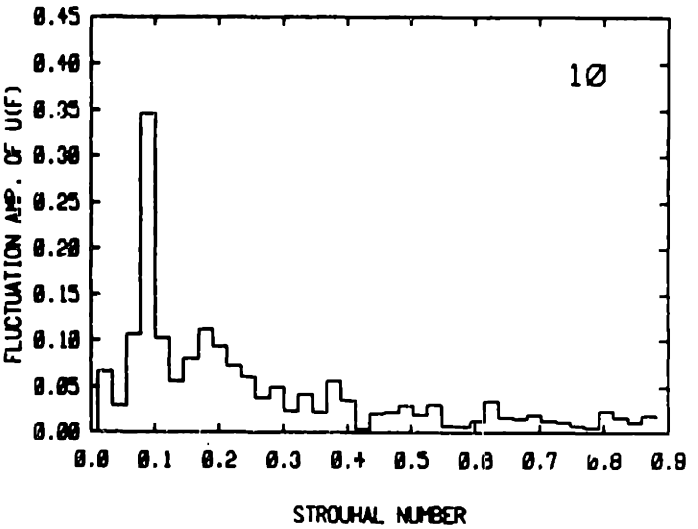

X= 1.000, PEAKS= 0.089 0.179 0.022

Figure 5.6 Spectra of the streamwise velocity fluctuation, computed from the time trace in Fig. 5.5, for the time period 10.0-50.0. The Strouhal number used is based on the cavity depth and the mean inlet flow velocity for the time period considered. The dominant peak is around St=0.1 in both plots.

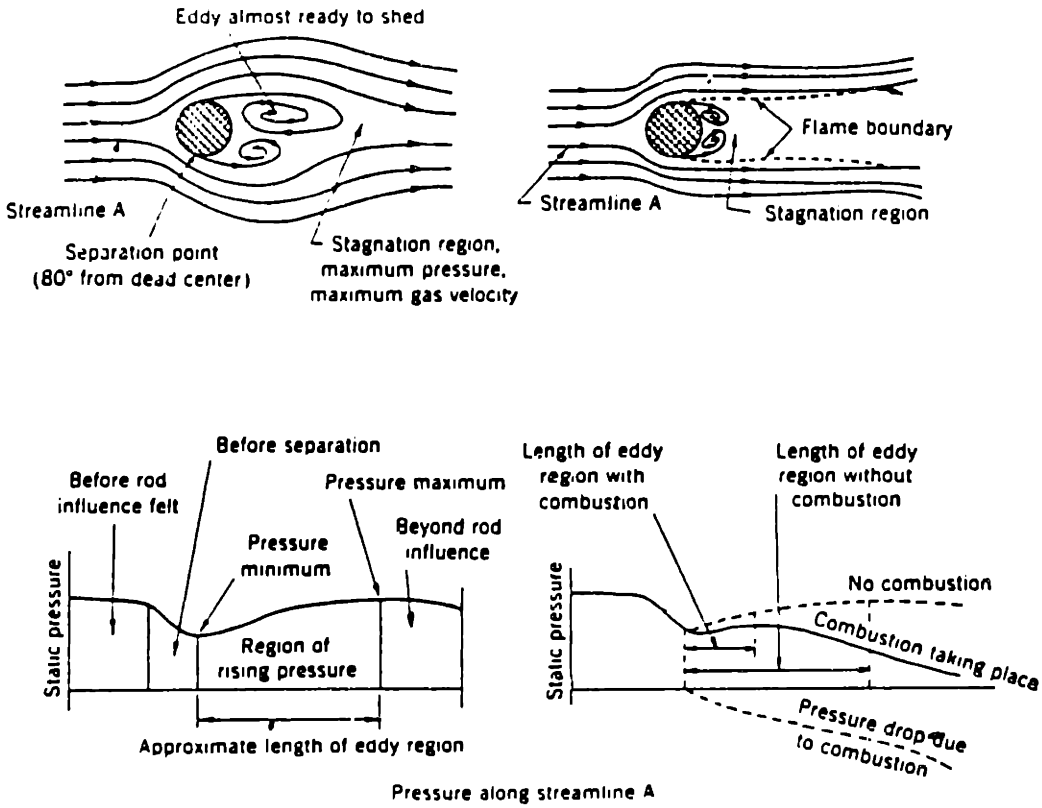

Figure 5.7 Schematic streamline plot and pressure profile for non-reacting (left) and reacting (right) flow around a cylinder, from Lewis and Von Elbe (1961) p. 439. Note the favourable pressure gradient and reduced recirculation zone size in the reacting case versus the non-reacting case.

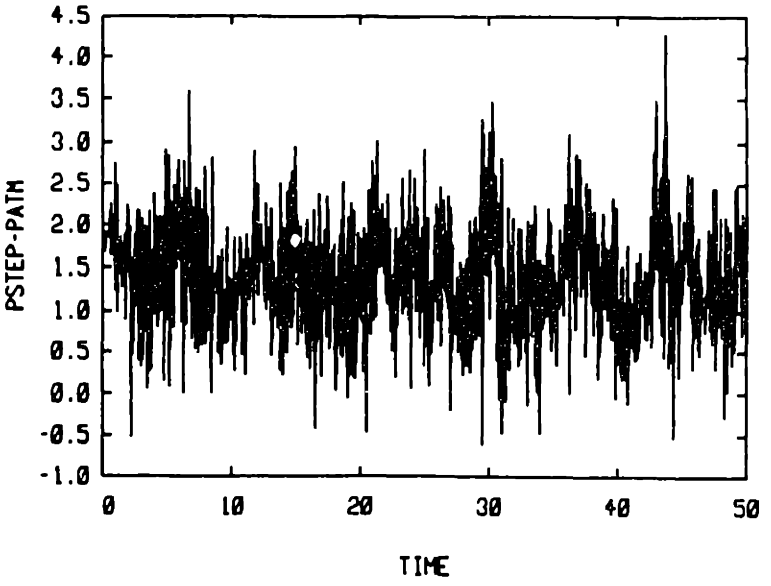

(a)

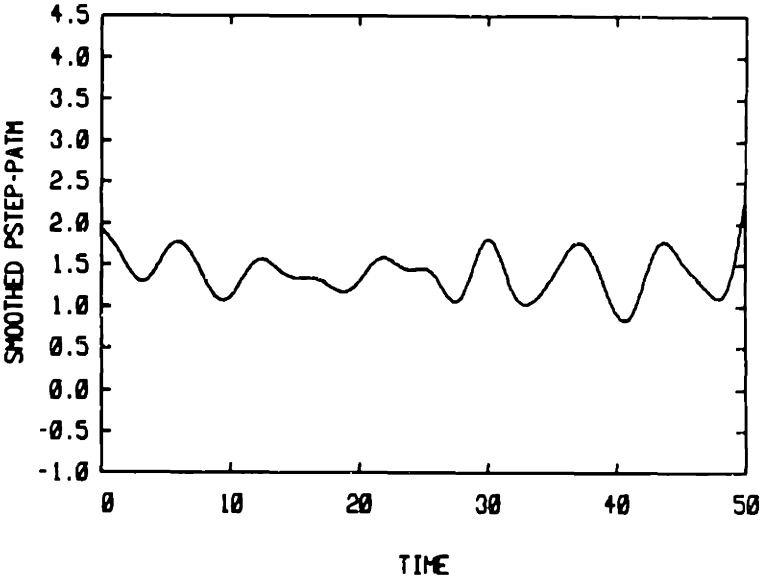

(b)

Figure 5.8 The pressure trace (channel centerline) at the upstream step (a) and the same trace after smoothing (b) plotted versus time, for the reacting flow of Fig. 5.1.

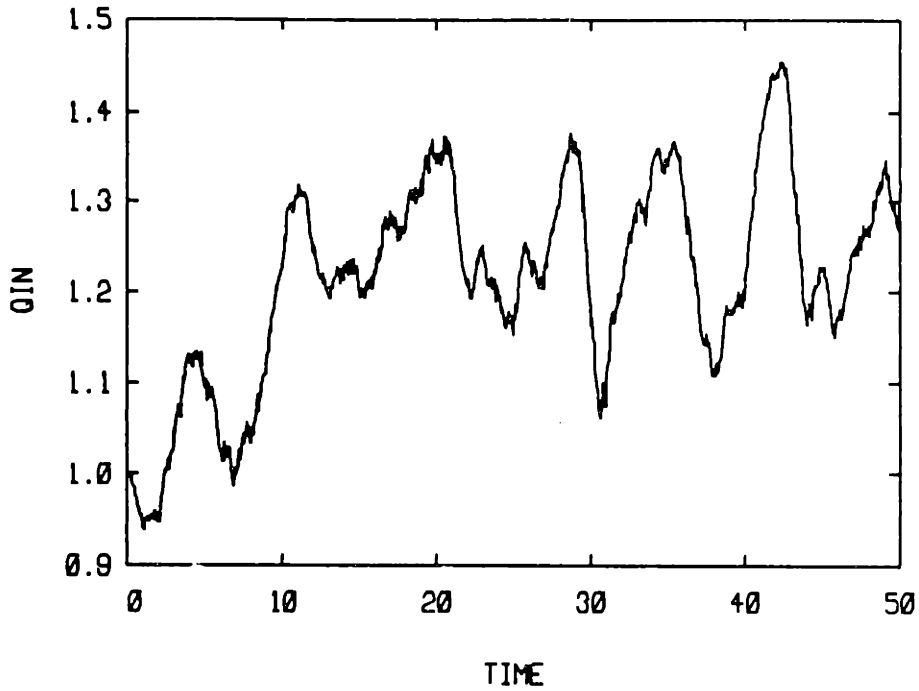

Figure 5.9 The inlet flow rate at xmin plotted against time, for the reacting flow of Fig. 5.1.

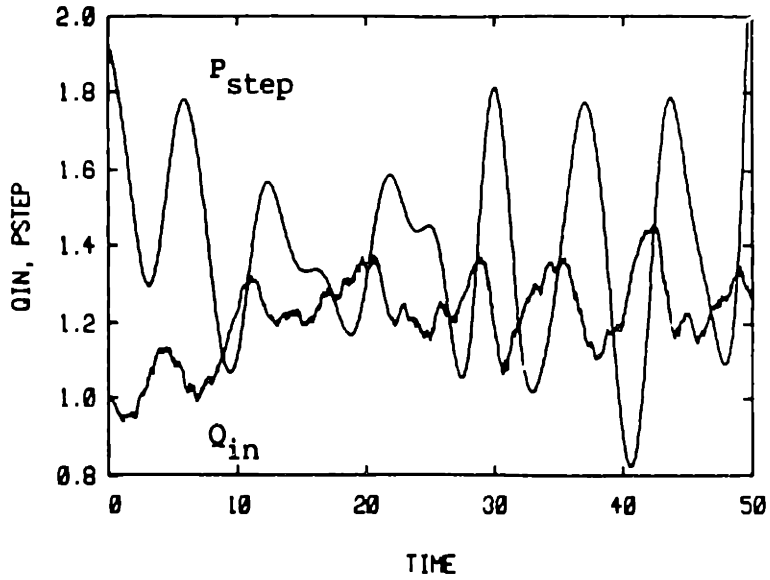

(a)

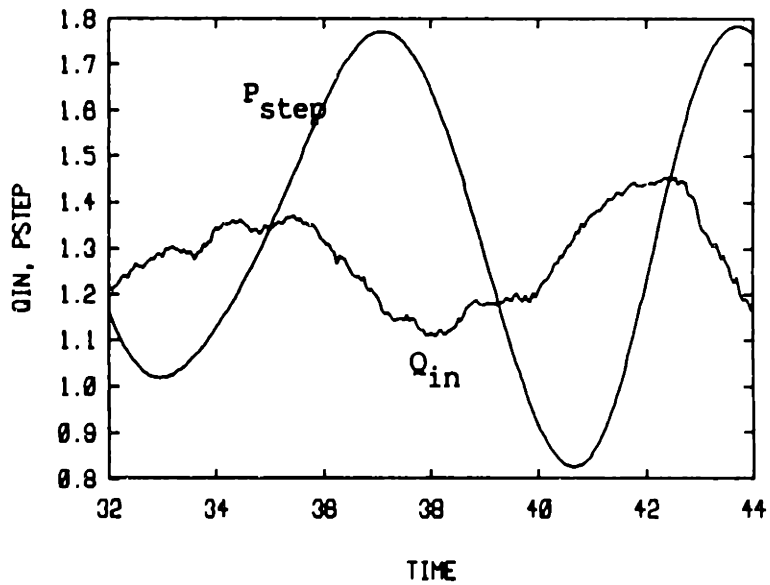

(b)

Figure 5.10 (a)- The inlet flow rate and upstream step pressure plotted against time, for the reacting flow of Fig. 5.1. (b)- A close up segment of the plot in (a) for the time span corresponding to the shedding cycle in Fig. 5.1.

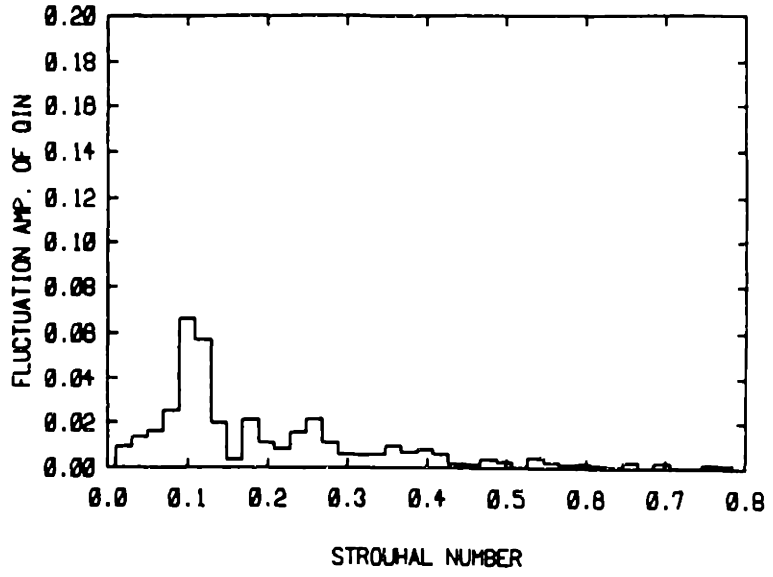

(a)

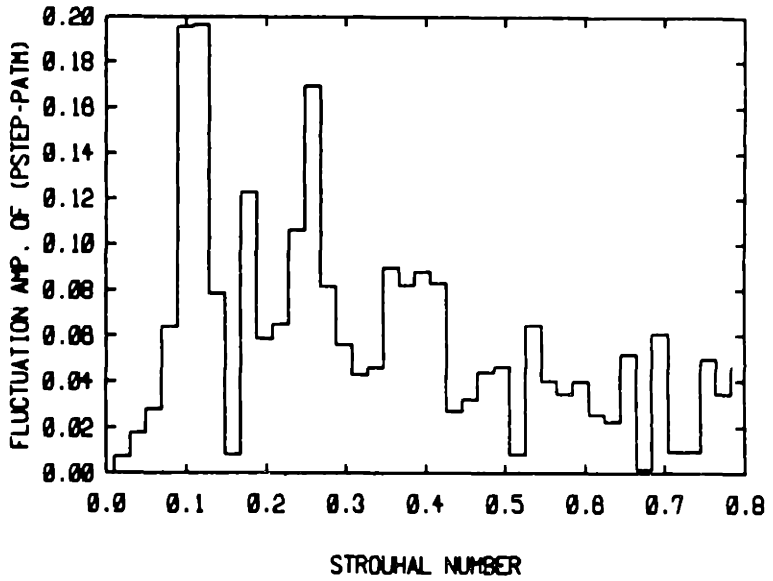

(b)

Figure 5.11 Spectra of the inlet flow rate (a) and upstream step pressure (b), computed from the corresponding time traces in figures 5.9 and 5.8a,for the time period 10-50. The Strouhal number used is based on the cavity depth and the mean inlet flow velocity for the time period considered. Both plots exhibit a dominant peak around St=0.1.

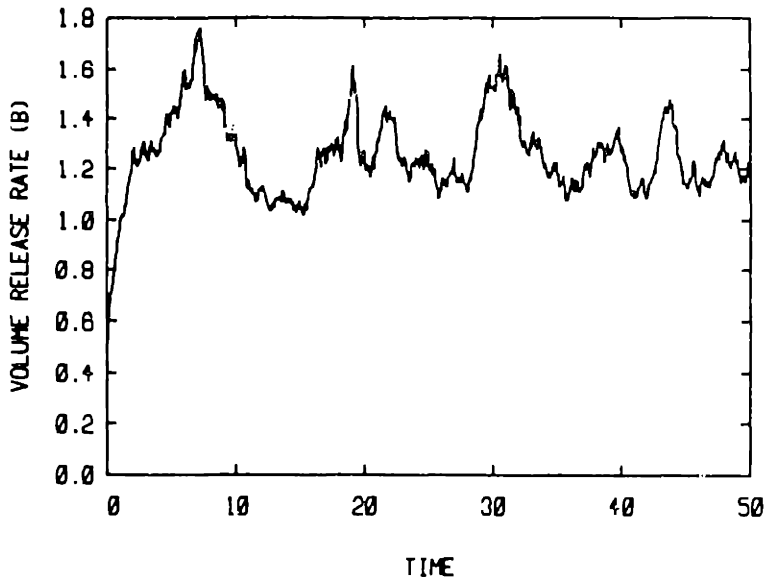

(a)

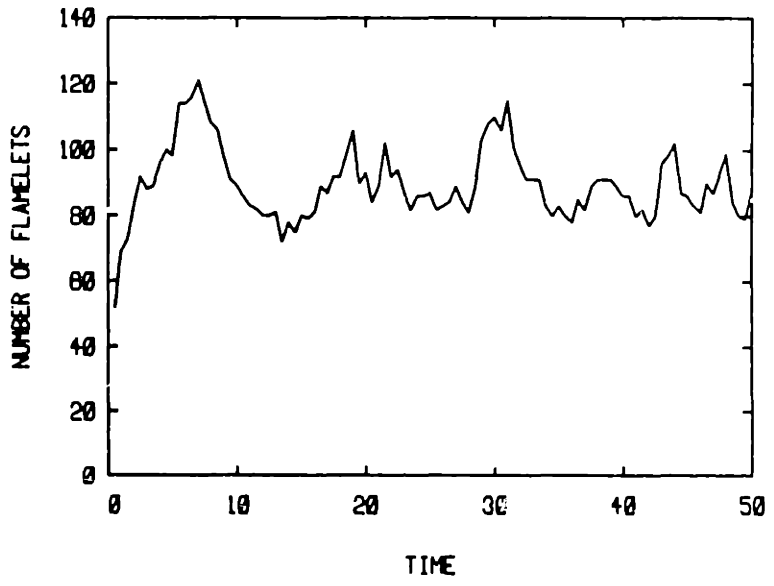

(b)

Figure 5.12 The rate of volume release (heat release) in the combustor (a), and the total number of flame segments (b), plotted against time, for the reacting flow field shown in Fig. 5.1.

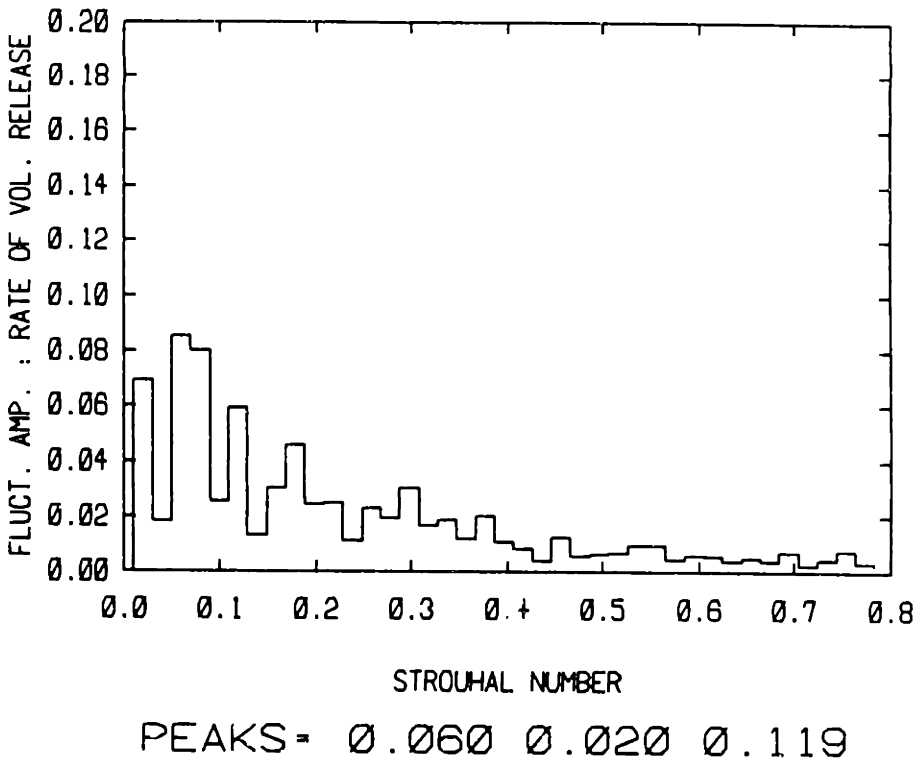

Figure 5.13 Spectrum of the rate of volume release (heat release) in the combustor, computed from the time trace in Fig. 5.12a, for the time period 10-50. The Strouhal number used is based on the cavity depth and the mean inlet flow velocity for the time period considered. The dominant peak is around St=0.1.

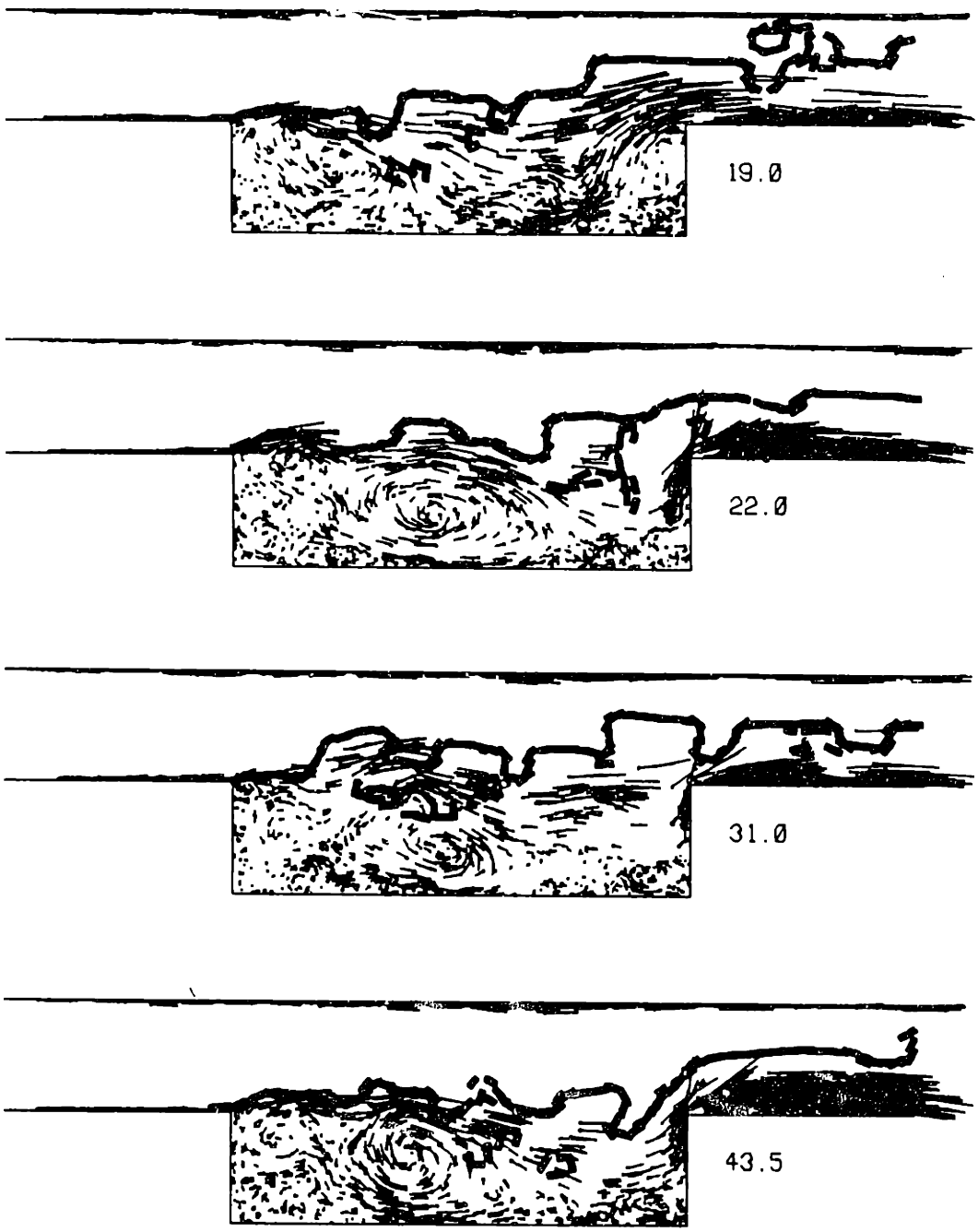

Figure 5.14 Instantaneous frames of the reacting flow field of Fig. 5.1, at times corresponding to heat release maxima in Fig. 5.12, depicting the flame fragmentation and contortion at these times.

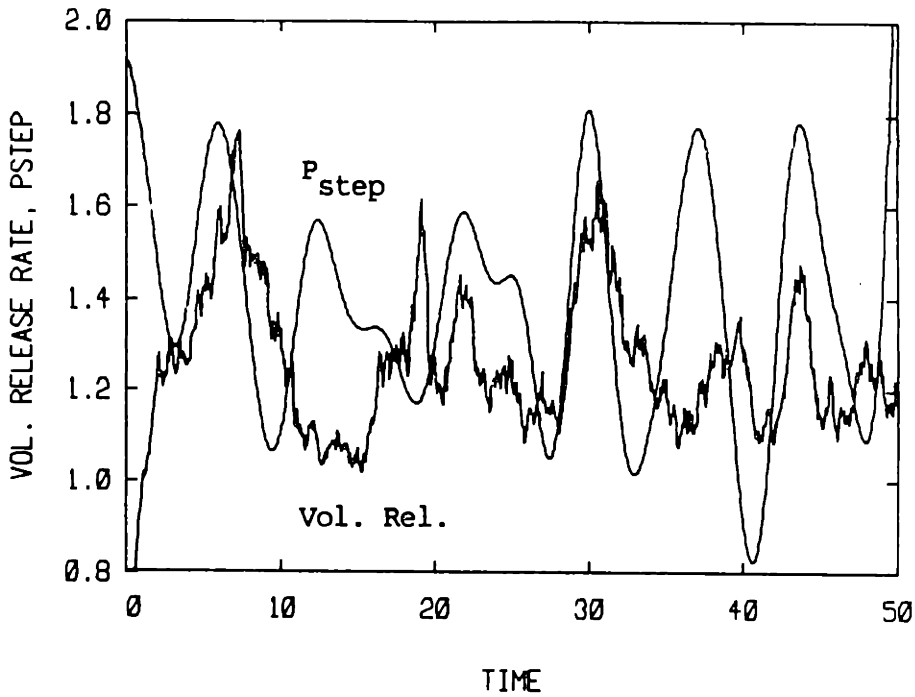

Figure 5.15 The rate of volume release (heat release) and the upstream step pressure plotted against time, for the reacting flow rate of Fig. 5.1.

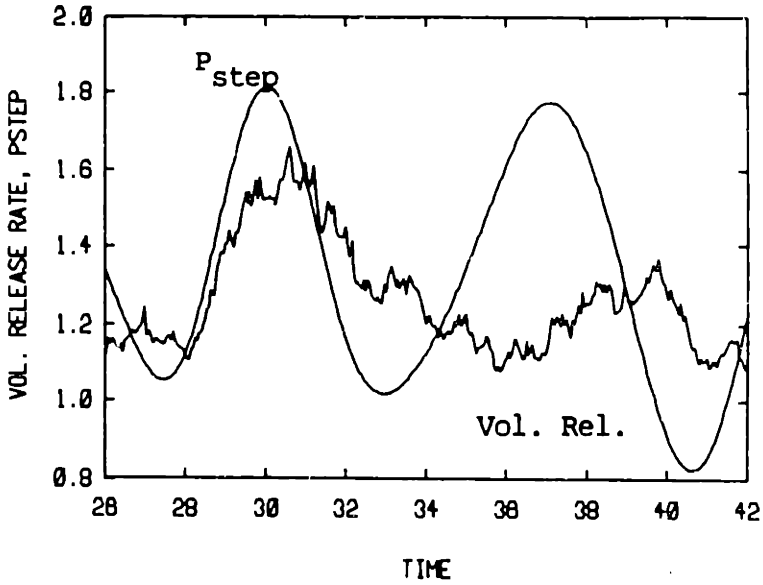

(a)

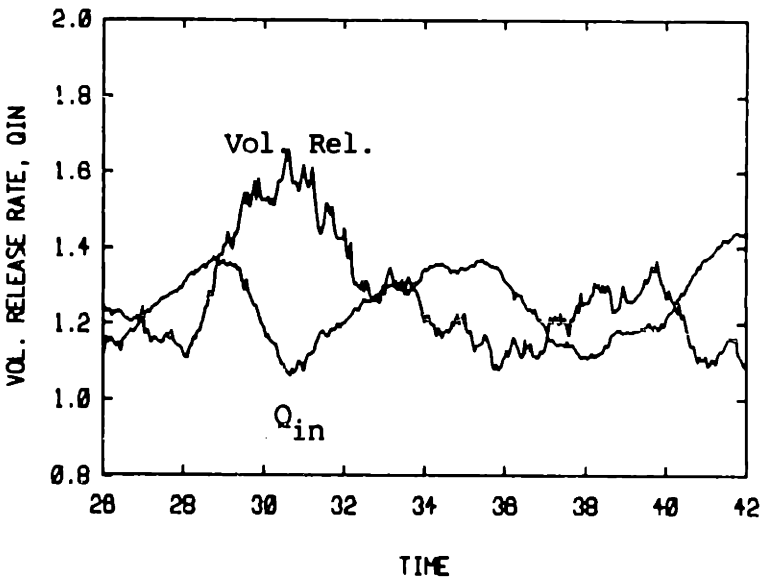

(b)

Figure 5.16 (a)- A close up segment of the plot in Fig. 5.15 showing the 1/4 period phase difference between the step pressure and volume (heat) release traces. (b)- The rate of volume release and inlet flow rate plotted for the same time segment in (a). They are 1/2 period (180 degrees) out of phase.

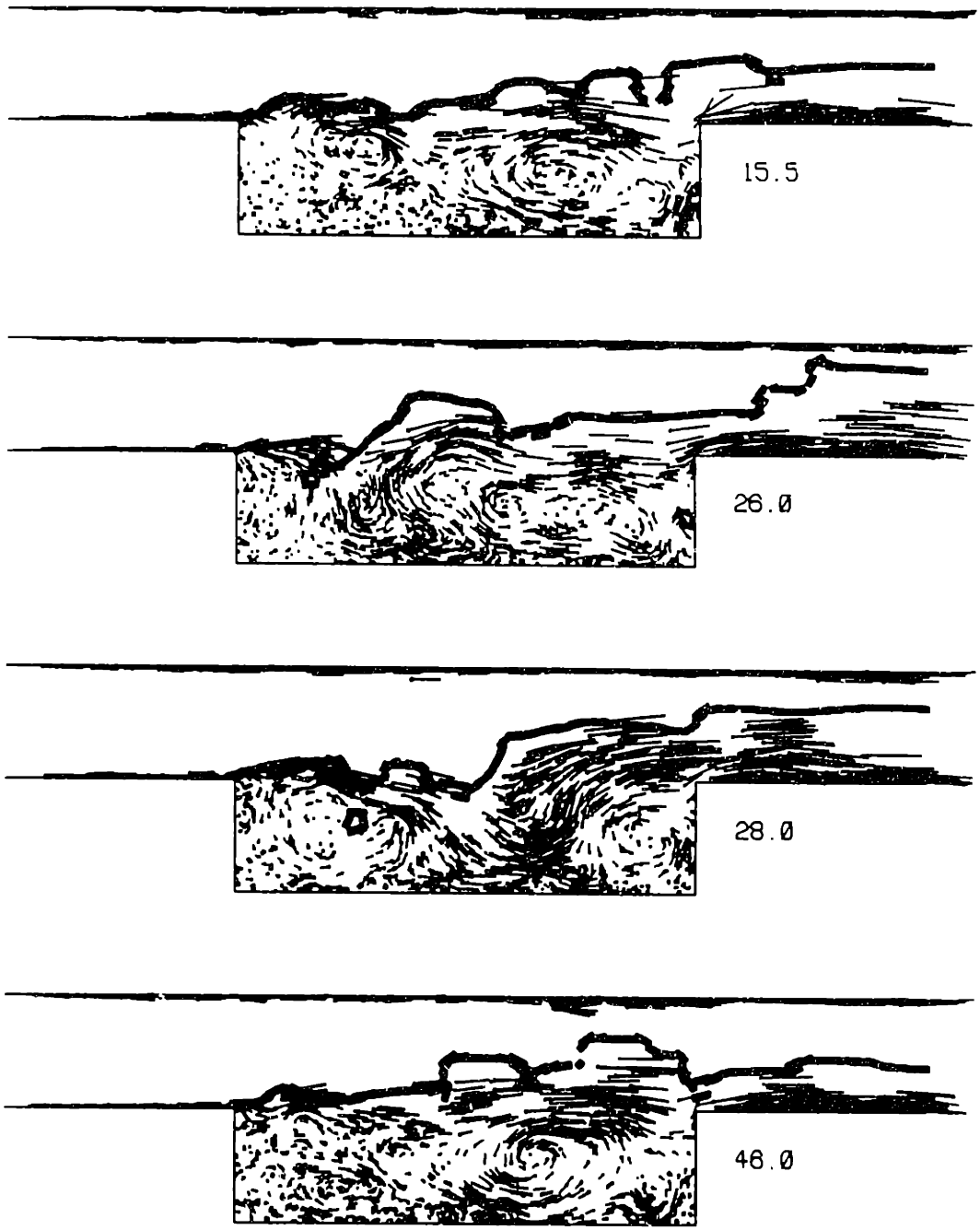

Figure 5.17 Instantaneous frames of the reacting flow field of Fig. 5.1, at times corresponding to heat release minima in Fig. 5.12 depicting the relatively minor contortion and fragmentation of the flame interface at these times.

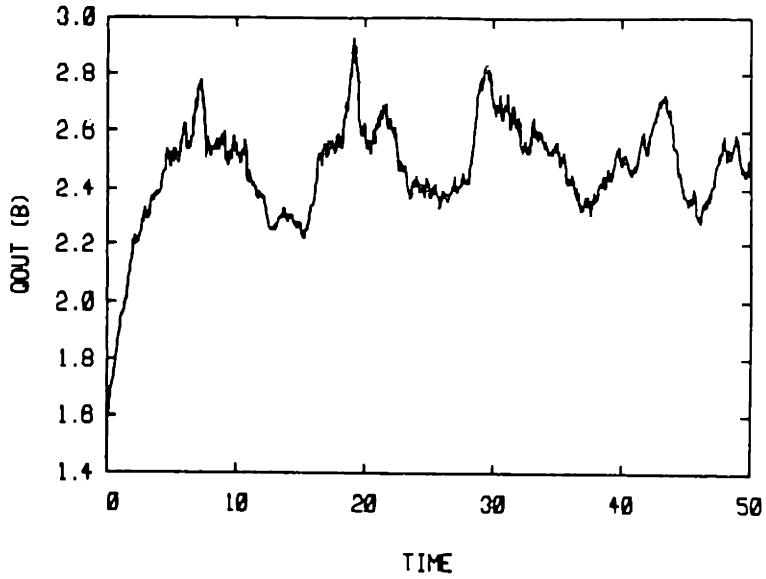

(a)

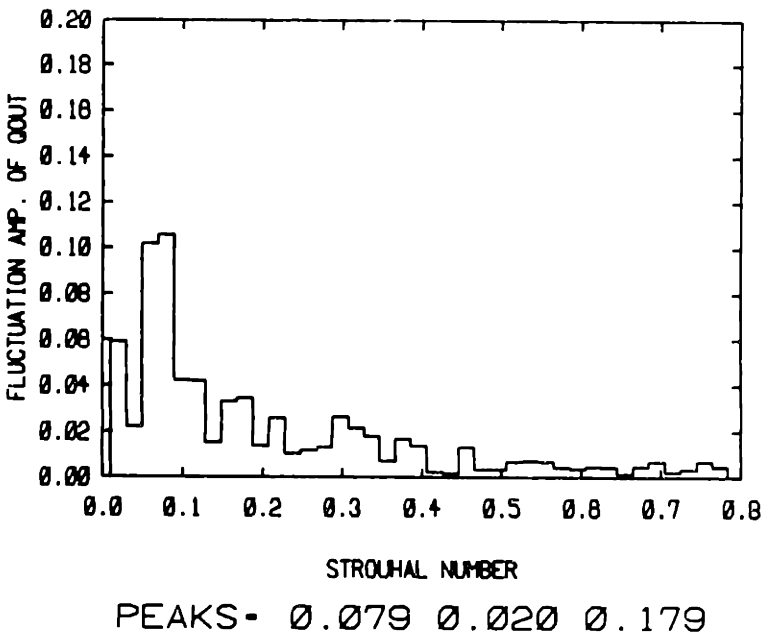

(b)

Figure 5.18 (a)- The volume flow rate out of the combustor, at xmax, plotted against time. (b)- The corresponding spectrum computed for the time period 10-50. The Strouhal number used is based on the cavity depth and mean inlet flow velocity for the time period considered. The dominant peak is around St=0.1.

5.2.2 High Frequency Forcing :

Our immediate objective in this and the following section is to examine the operation of the combustor under specified conditions that include a sinusoidal exit pressure with a given frequency and amplitude. We intend to compare the flow dynamics for two cases that differ only in the amount of heat release. This comparison is expected to provide some understanding of the effect of increased equivalence ratio on combustor operation assuming a specified pressure oscillation in the system.

In particular, in this section we consider a pressure oscillation that is at a frequency significantly higher than the natural frequency observed above, St=0.1. In the next section we consider a lower forcing frequency closer to the natural frequency.

This high-frequency forcing study is intended to demonstrate that the experimentally observed migration from high to low frequencies as the equivalence ratio is increased is not due to the flow in the isolated dump section, but rather it involves the whole system including upstream and downstream configurations. Specifically, we demonstrate that increasing the rate of heat release, under conditions of high frequency forcing, leads to further dampening of the natural low frequency instability of the combustor.

To begin, let us consider the same geometry used above, namely: $L/D=4$, $H/D=1$, $xmin/D=-4$, and $xmax/D=4$. We specify the following flow parameters: $Re_u=10^4$, $S_u/U_r=0.05$, $p_o/p_r=0.375$. Relevant numerical parameters include $\Delta_s/D=0.0095$ for both cases, while $h_s/D=1/3,1/4$ and $\Gamma_m/U_rD=0.0278,0.0208$ for the low and high heat release cases respectively. The exit pressure is specified as a cosine function of amplitude $p_{mx}=2.5$, and frequency, f_f, such that $f_fD/U_r=0.4$. The only significant difference between the two cases is the density ratio across the flame. For the low heat release case, we use $\rho_u/\rho_b=1.5$, while we double this ratio for the high heat release case :

ρ_u/ρ_b=3.0. In the next section we attain the same objective of higher heat (volume) release rate by increasing the burning speed rather than the density ratio. The amount of volume generated at the flame front per time step is proportional to : $S_u(\rho_u/\rho_b-1)$. Consequently, since (ρ_u/ρ_b-1) is increased from 0.5 to 2.0, we expect to see a corresponding four-fold increase in the rate of heat release.

We look first at the low heat release case.

The forcing pressure function at the exit section of the combustor, p_{ex}, and the resulting step pressure trace, P_{step}, are shown in Fig. 5.19. Clearly, the dominant oscillation in P_{step} is at the forcing frequency. The two traces are seen to be in phase. This is expected since, apart from the density jump across the flame front, the flow is incompressible and the pressure drop within the combustor is due to friction and flow acceleration or decceleration. The flow rate into the combustor, Q_{in}, which is plotted versus time in Fig. 5.20, is initialized at 1.0 (dimensionless) and then settles down to a mean value of 0.66. It exhibits organized high frequency oscillation around this mean, with visible low frequency modulation. Again, the dominant oscillation is at the forcing frequency. The spectra of Q_{in} and P_{step}, shown in Fig. 5.21, indicate this dominance of the forcing frequency at St=fD/U=0.603$\pm$0.009 (i.e. fD/U_r=0.4). A small peak exists in both traces at St=0.115$\pm$0.009. The relative amplitude of this peak, with respect to that at the forcing frequency, is higher in the Q_{in} spectrum than in the P_{step} spectrum. This reflects the more prominent low frequency modulation observed in the time trace of Q_{in}, Fig. 5.20, as compared to the P_{step} trace in Fig. 5.19a. As we shall see below, this St=0.115 peak and the associated low frequency modulation is due to the natural instability of the recirculation zone analyzed in Section 5.2.1.

A close up view of the superposition of the Q_{in} and P_{step} traces is shown in Fig. 5.22. The organization of the flow oscillations due to forcing is evident in the repeated consistent phase lag of 1/4 period between the two traces. This phase shift corroborates our above observation in the unforced case.

The rate of heat release and the total flame length are plotted versus time in Fig. 5.23. The correlation between the two traces is evident, as in the unforced case. Spectral analysis of the heat release trace is shown in Fig. 5.24. As expected from the time trace, the forcing frequency is not dominant. Rather, most of the energy is concentrated at low frequencies with a significant amplitude distributed broadly around St=0.1. As we shall see below, this is a manifestation of the fact that the shear layer eddies, which are observed to shed regularly at forcing frequency, merge together or with the large recirculation zone eddy so that the overall burning rate is governed more by the low frequency dynamics than by the high frequency forcing. Finally, the flow rate at the exit plane, Q_{out}, is plotted along with its frequency spectrum in Fig. 5.25. Both the forcing frequency, St=0.603, and the low frequency modulation, at St=0.115, are evident in both plots.

Let us now look at the same global diagnostics, for the high heat release case. The pressure traces, P_{step} and p_{ex}, are shown in Fig. 5.26. The amplitude of the pressure oscillation at the step as well as its mean value are higher than the corresponding quantities in the low heat release case. As we shall see below, this is a manifestation of the higher flow rate, Q_{out}, leaving the combustor in the high heat release case because of the higher rate of expansion at the flame front. This increase in P_{step}, due to the higher heat release at the flame, causes a smaller inlet flow rate, Q_{in}, into the combustor from the upstream reservoir whose stagnation pressure has been

held constant. The plot of Q_{in} versus time, shown in Fig. 5.27, illustrates this fact. The mean value of Q_{in}, after time 10.0, is found to be 0.44, which is significantly less than the vlaue of 0.66 found in the low heat release case. The spectra of Q_{in} and P_{step} are shown in Fig. 5.28. They indicate, again, a dominant high frequency peak at the forcing frequency, $St=fD/U=0.924\pm0.011$, i.e. $fD/U_r=0.4$. Comparison with Fig. 5.21 shows that the effect of increased heat release was to broaden the low frequency peak around St=0.1, as well as to increase the amplitude of the high frequency peak. This suggests that increasing the heat release tends to stabilize the natural low frequency dynamics of the flowfield, that is, to shift more of the flow energy into the small scales and out of the large scales. This is verified below in the detailed observation of the vorticity field.

The phase shift between Q_{in} and P_{step} is still observed to be 1/4 of the forcing high frequency period of oscillation, as in Fig. 5.29.

The rate of heat release is found to be roughly four times that measured in the low heat release case. This is expected, as long as the overall flame length does not change significantly between the two cases, since the rate of expansion at the flame is proportional to $S_u(\rho_u/\rho_b-1)$. The time traces of the heat (volume) release and flame length are shown in Fig. 5.30. The heat release spectrum is shown in Fig. 5.31, and it indicates the same kind of low frequency dominance measured in the low heat release case. The peaks here are higher because of the increased rate of expansion at the flame. The overall flame length, or number of flamelets, is decreased slightly due to the higher rate of heat release, as evident from a comparison of Figs. 5.23b and 5.30b. This can be explained by observing the sequence of frames of each flow field, shown below in Figs. 5.33 and 5.36 for the low and high heat release cases respectively. The larger amplitude of the recirculation zone instability in the low heat release case, and the associated large eddies in the

recirculation zone, cause more entrainement of reactants and contortion of the flame than in the high heat release case, where these natural dynamics are dampened. This decrease in flame length, due to an increase of ρ_u/ρ_b, is evidently not significant enough to offset the tendency toward an increase in the overall rate of heat release from the combustor.

The time trace and spectrum of Q_{out} are shown in Fig. 5.32. The oscillation of Q_{out} is at a higher mean in this case despite the smaller mean Q_{in}. This is due to the 4-fold increase in the rate of high release. The amplitudes of both the high and low frequency peaks in Fig. 5.32b are also higher than those in Fig. 5.25b due, in part to higher heat release as well as, in the case of the high frequency peak, to the more organized nature of the forced Q_{in} oscillation at that frequency.

Let us now examine the flow dynamics for each of the two cases of low and high heat release, using time frame sequences depicting the flow field in terms of the vortex elements and the flame interface. We begin with the low heat release case. Consider the sequence of frames in Fig. 5.33a. This sequence displays the high frequency shedding of shear layer eddies that are more organized than those observed in the unforced case above. This increased organization is due to the pressure forcing. The eddies are seen to cause definite "small" scale modulations of the flame interface. Of much more consequence, however, is the persistent low frequency, large scale, natural dynamics of the cavity flow. These are manifested in the large recirculation zone eddy shedding observed in Fig. 5.33b. One shedding cycle extends roughly from 26.0 to 40.0. Hence, with a period of ~14. The flow dynamics involve a superposition of small scale shear layer eddies generated at the shedding frequency and large scale recirculation zone eddies produced at the natural low frequency mode of the combustor. This result is corroborated by the u-velocity traces at $x/D=\pm 1.0$, $y/D=1.0$, shown in Fig. 5.34, and their

corresponding spectra in Fig. 5.35. The highest peak in both spectra is at St=fD/U=0.115±0.009, (i.e. at fD/U_r=0.076, since U/U_r=0.66 for the time period 10-62.75 considered.) This translates into a period of 13.2, which corresponds to the large eddy shedding in Fig. 5.33b. The second highest peak in the spectra of Fig. 5.35 is that at St=fD/U=0.603±0.009, i.e. fD/U_r=0.40, which is the forcing frequency. This corresponds to a period of 2.5, which is evidently the period of forced shear layer eddy shedding. This can be seen in Fig. 5.33a between frames 32.0 and 34.5, for example.

Therefore, we see that, in the low heat release case, the natural dynamics of the recirculation zone persisted significantly despite the higher frequency forcing. The natural frequency of the flowfield was close to $1/5^{th}$ of the forcing frequency (0.115/0.603=1/5.24).

The results of the high heat release case are quite different. The dynamics are illustrated in the sequence of frames in Fig. 5.36a and 5.36b. The frame sequence in Fig. 5.36a illustrates similar high frequency shear layer eddy shedding, as in the low heat release case. However, the large scale eddy shedding from the recirculation zone has been virtually suppressed due to the increased heat release, as can be seen in Fig. 5.36b. The recirculation zone is still unstable, but the corresponding eddies are relatively incoherent, and small compared to those in the low heat release case. The period of these eddies is roughly 22, extending from time 28 to 50 in the sequence of Fig. 5.36b. This would give a frequency of fD/U_r=0.045, or fD/U=0.1, given that U/U_r=0.44. The u-velocity traces and spectra are shown in Fig's 5.37 and 5.38 respectively. The reduced unsteadiness in the vorticity plots is reflected in the lower amplitude oscillations in the u-traces, and the corresponding lower amplitudes of the peaks in the spectra. Of significance is that the peak at St=0.1 is no longer dominant, as would have been expected from the vorticity plots. The dominant peak at

$St=fD/U=0.924\pm0.011$ corresponds to $fD/U_r=0.4$, which is the forcing frequency. This corresponds to a period of 2.5, which is again that of the forced shear layer eddies, as is evident from Fig. 5.36a - frames 32 to 34.5, or 36 to 38.5. In particular, frames 32 to 34 demonstrate the growth and downstream propagation of flame modulations caused by the forced high frequency shear layer eddy shedding. Vaneveld et. al. (1982) report shclieren pictures of an experimental cavity-type dump combustor under conditions of relatively stable high frequency operation that show similar growth and propagation of flame modulation along the top of the cavity.

The above results indicate that the increase in heat (volume) release leads to the stabilization of the flow, as in the unforced case. Further, increasing the heat release causes a shift towards higher frequencies for dominant dynamics, given high frequency forcing. Hence, this isolated dump (without an acoustically coupled downstream system) cannot cause a transition to lower frequency dominance due to increased heat release. Rather, the opposite is true; under high frequency forcing, the natural low frequency dynamics tend to die out as the heat release increases, as in the unforced case.

It is interesting to note that the position of the flame front with respect to the boundary of the shear layer, or the zone of intense vorticity, depends on the rate of heat release. At low heat release, the flame is essentially tangential to the local streamlines and is stabilized on the boundary of the vorticity zone. The cross-stream distance between the flame front and the boundary of the vorticity zone grows donstream. However, the flame remains almost tangential to the local streamlines. In the high heat release, case, the flame is attached to the zone of high vorticity concentration only upstream and near the step. Downstream, the flame front moves away from the vorticity zone and into the free stream where streamlines

are essentially straight and parallel lines. This explains the observed flat, horizontal, flame interface away from the step in Fig. 5.36.

Results of high frequency forcing emphasize our previous conclusion that heat release stabilizes shear flows. It is evident that the favourable pressure gradient produced by the expansion of the flow as it accelerates to accomodate the extra volume can delay the rollup of the shear layer and suppress the recirculation zone mode. As we will show in the next section, this is true only in case of high frequency forcing, when the recirculation zone mode is not energized. The effect of the favourable pressure gradient on the stabilization of the boundary layer on the top wall is also apparent in all cases.

In the next section we examine the effect of increased heat release on the flow dynamics under conditions of low frequency forcing.

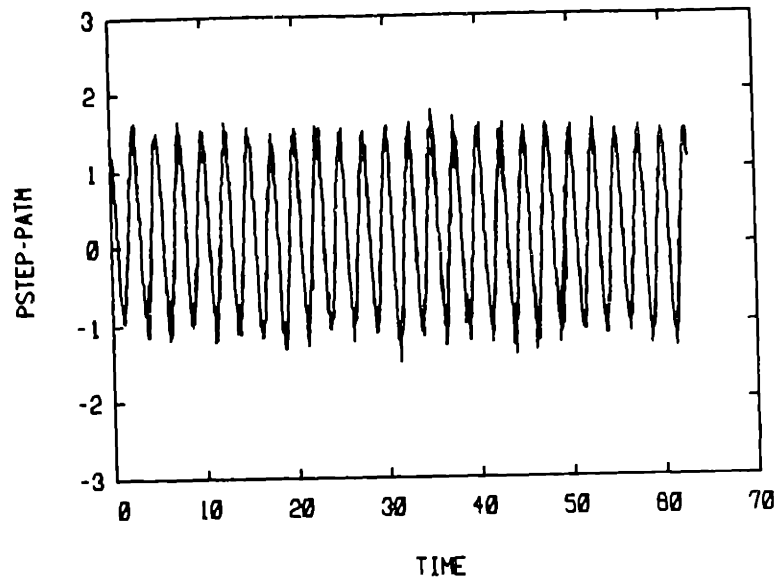

(a)

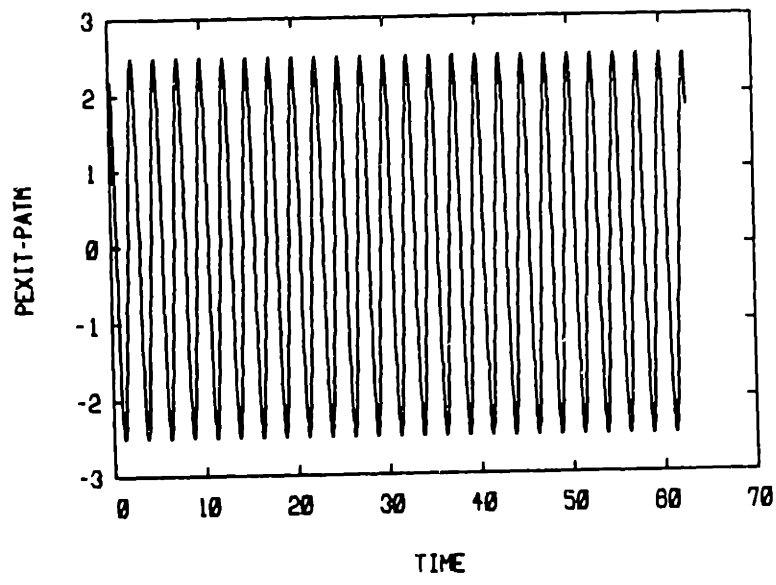

(b)

Figure 5.19 The pressure trace (channel centerline) at the upstream step (a) and the specified exit pressure trace (b) plotted versus time, for the low heat release flow of Fig. 5.33 below.

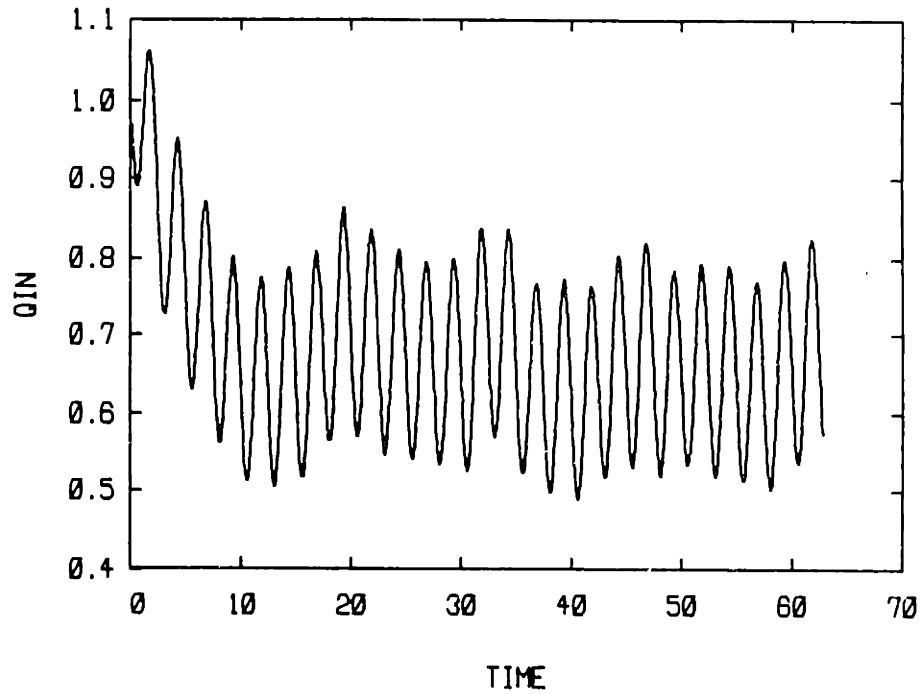

Figure 5.20 The inlet flow rate at xmin plotted against time, for the low heat release flow of Fig. 5.33 below. The mean flow rate for the time period from 10 to 62.75 is 0.66.

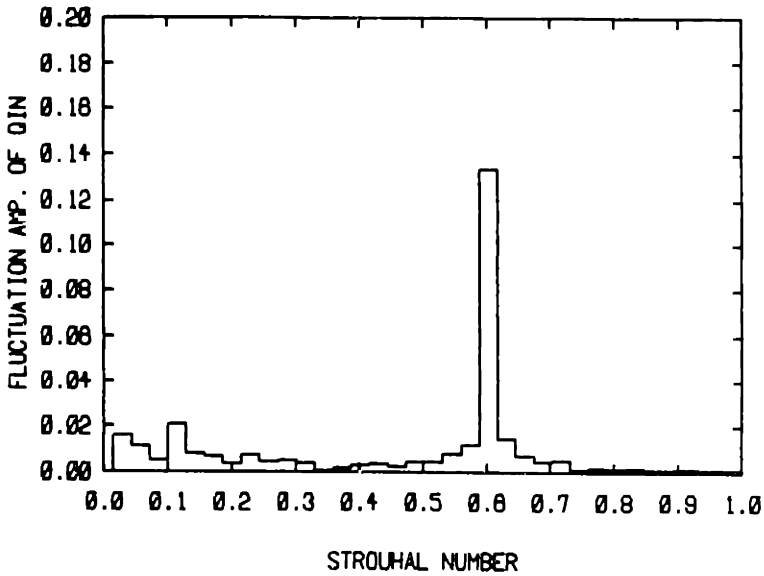

(a)

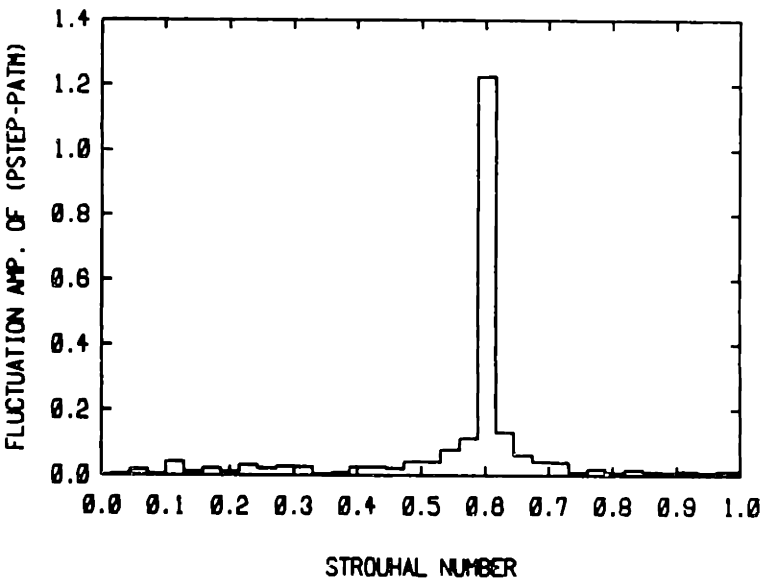

(b)

Figure 5.21 Spectra of the inlet flow rate (a) and upstream step pressure (b), computed from the corresponding time traces in figures 5.20 and 5.19a, for the time period 10-62.75. The Strouhal number used is based on the cavity depth and the mean inlet flow velocity for the time period considered. Both plots exhibit a dominant peak at St=0.6, and a smaller peak around St=0.1.

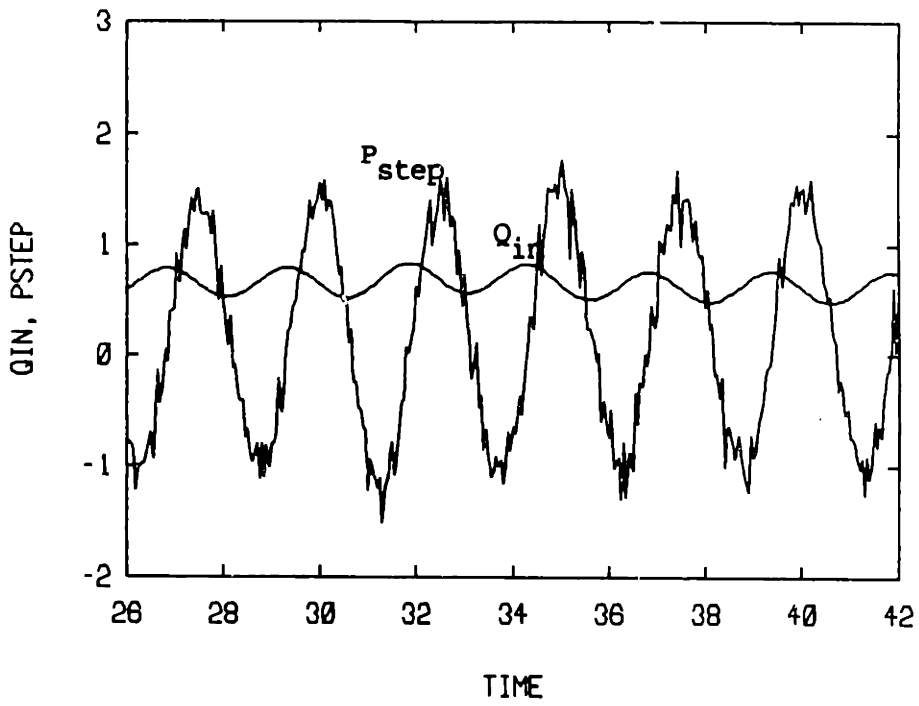

Figure 5.22 A close up segment of the step pressure and inlet flow rate superposed time traces for the low heat release flow of Fig. 5.33 below.

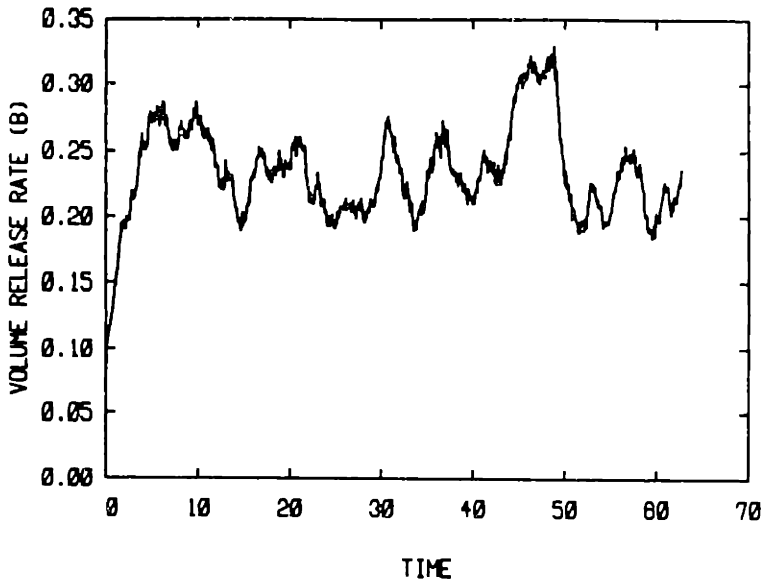

(a)

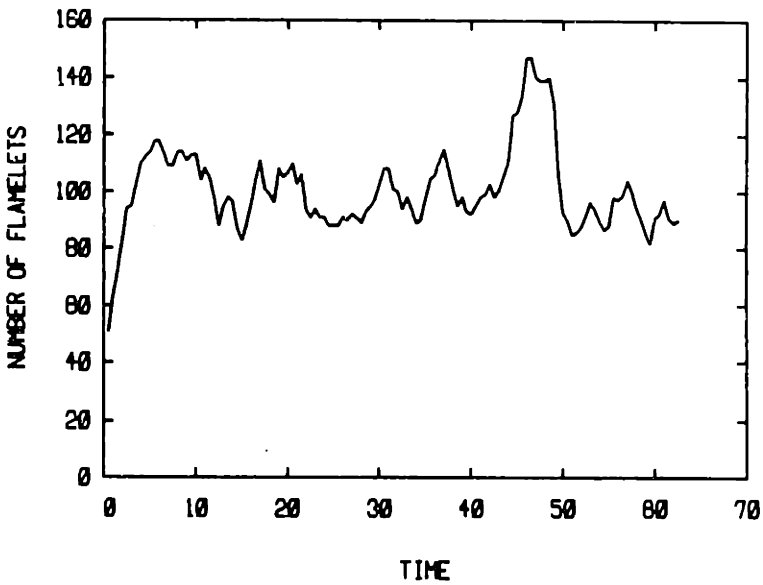

(b)

Figure 5.23 The rate of volume release (heat release) in the combustor (a), and the total number of flame segments (b), plotted against time, for the low heat release flow field shown in Fig. 5.33 below.

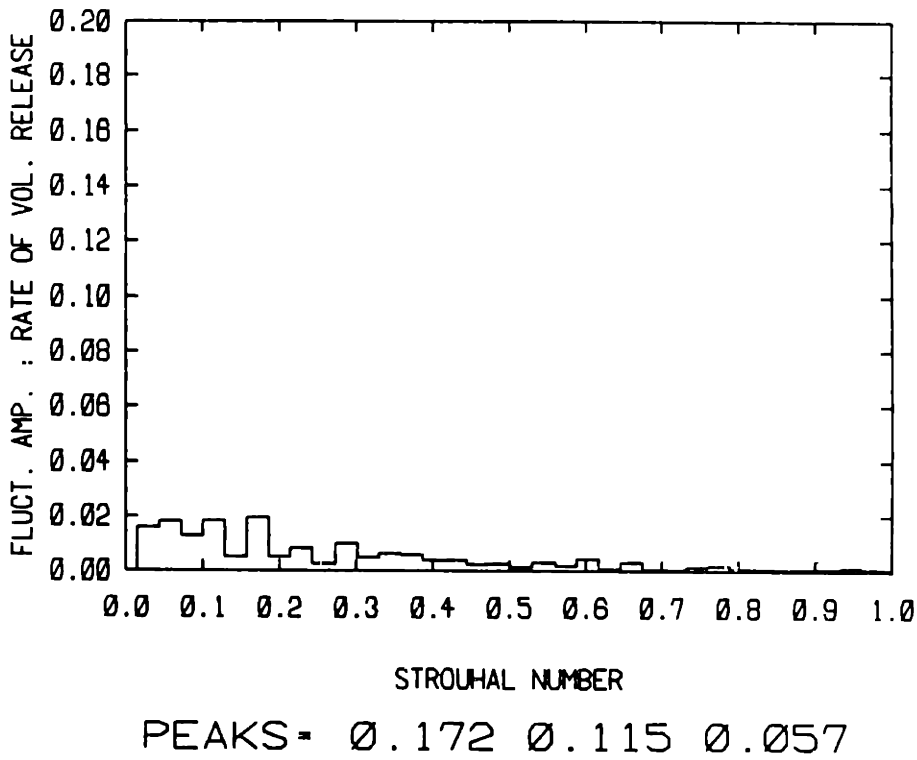

Figure 5.24 Spectrum of the rate of volume release (heat release) in the combustor, computed from the time trace in Fig. 5.23a, for the time period 10-62.75. The Strouhal number used is based on the cavity depth and the mean inlet flow velocity for the time period considered.

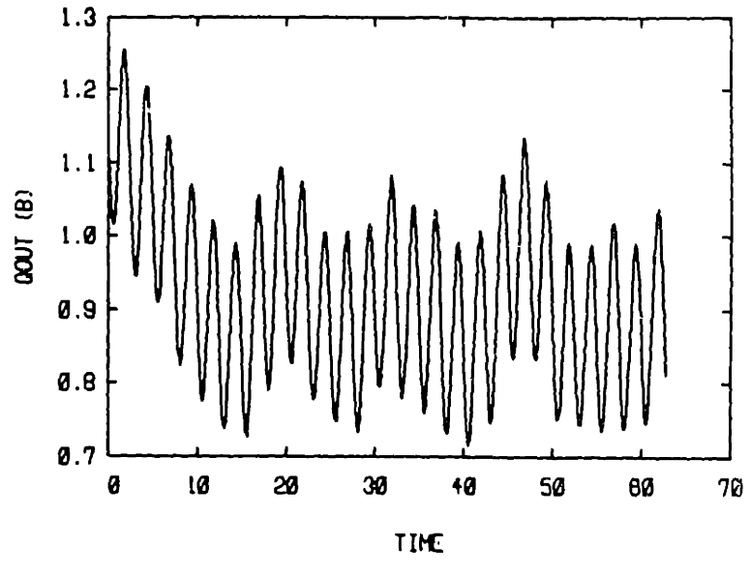

(a)

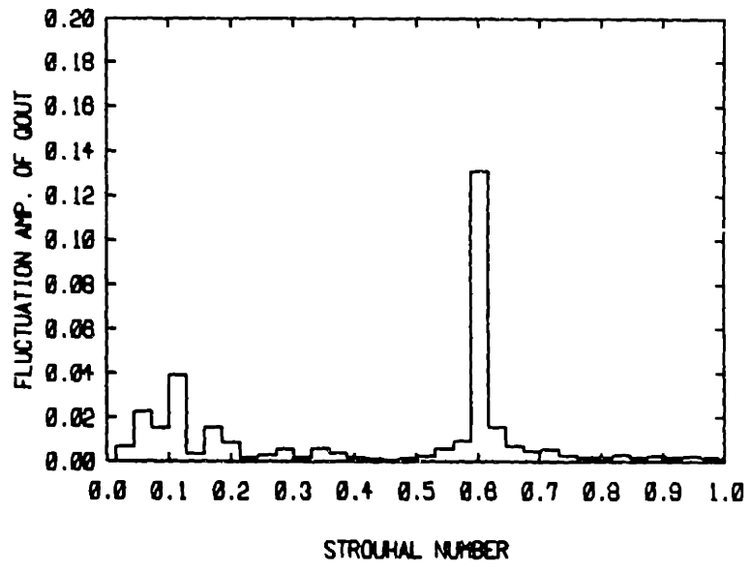

(b)

Figure 5.25 (a)- The volume flow rate out of the combustor, at xmax, plotted against time, for the low heat release flow of Fig. 5.33 below. (b)- The corresponding spectrum computed for the time period 10-62.75. The Strouhal number used is based on the cavity depth and mean inlet flow velocity. The dominant peak is at St=0.6, while a smaller peak lies around St=0.1

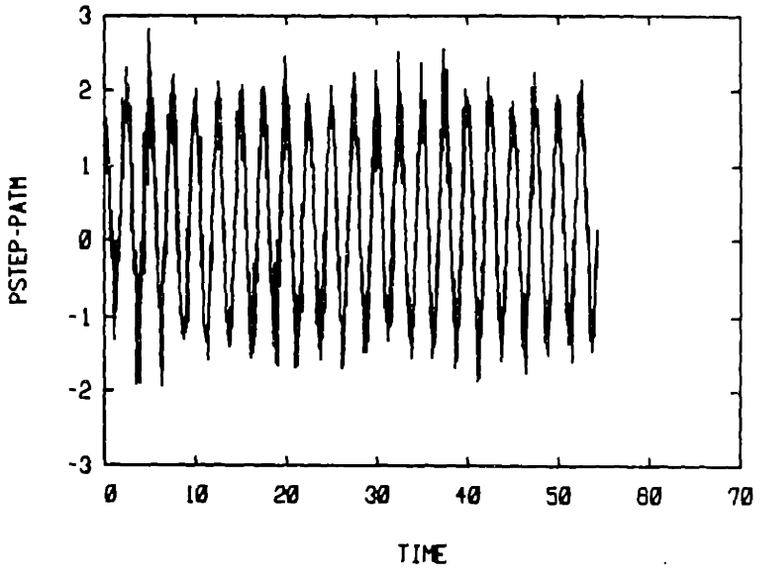

(a)

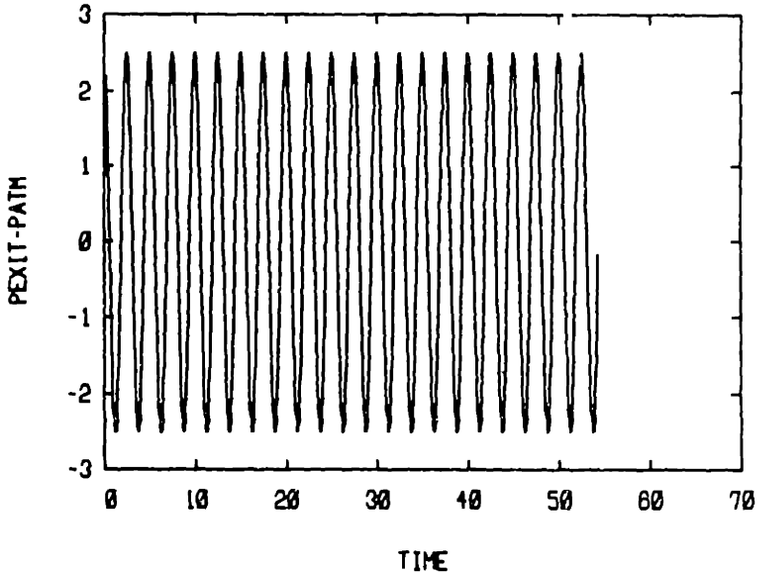

(b)

Figure 5.26 The pressure trace (channel centerline) at the upstream step (a) and the specified exit pressure trace (b) plotted versus time, for the high heat release flow of Fig. 5.36 below.

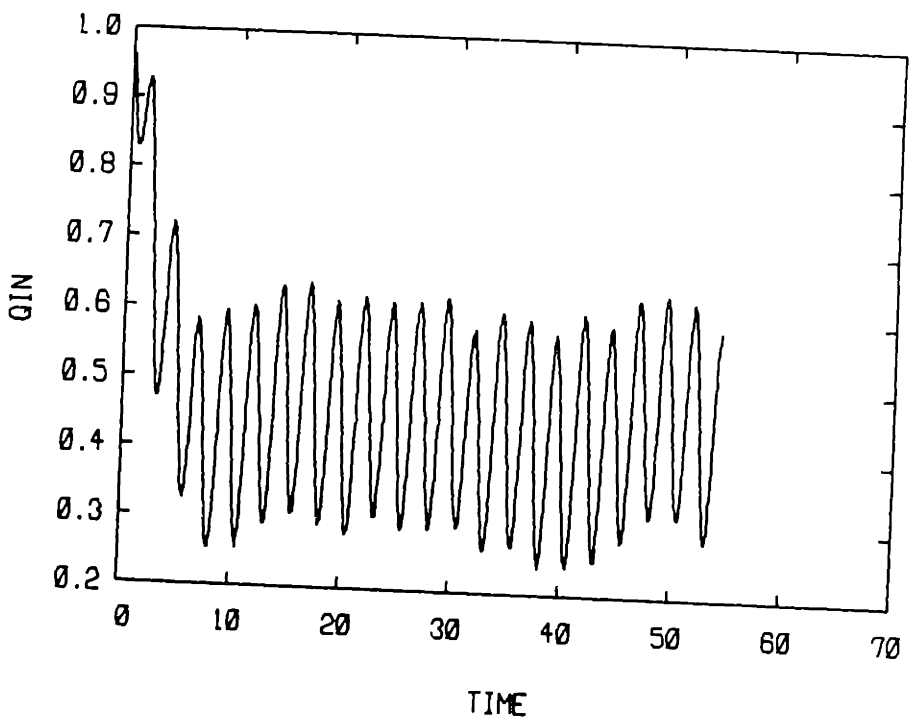

Figure 5.27 The inlet flow rate at xmin plotted against time, for the high heat release flow of Fig. 5.36 below. The mean flow rate for the time period from 10 to 54.25 is 0.44.

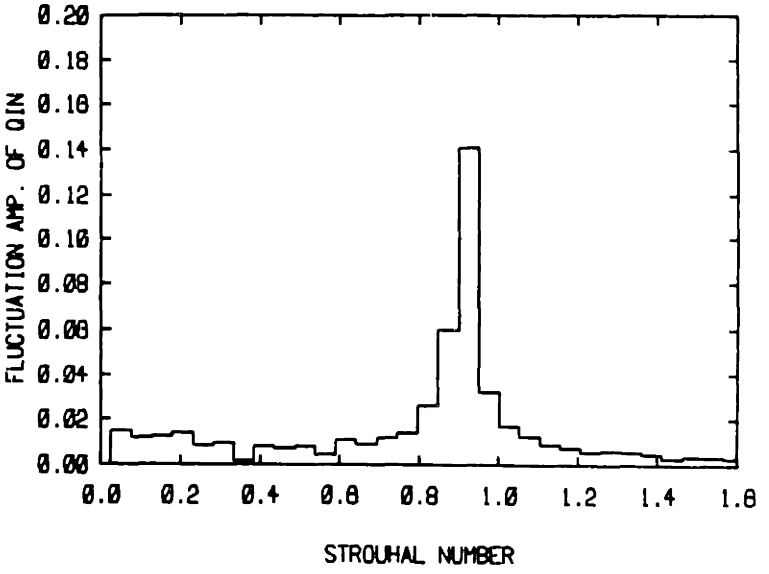

(a)

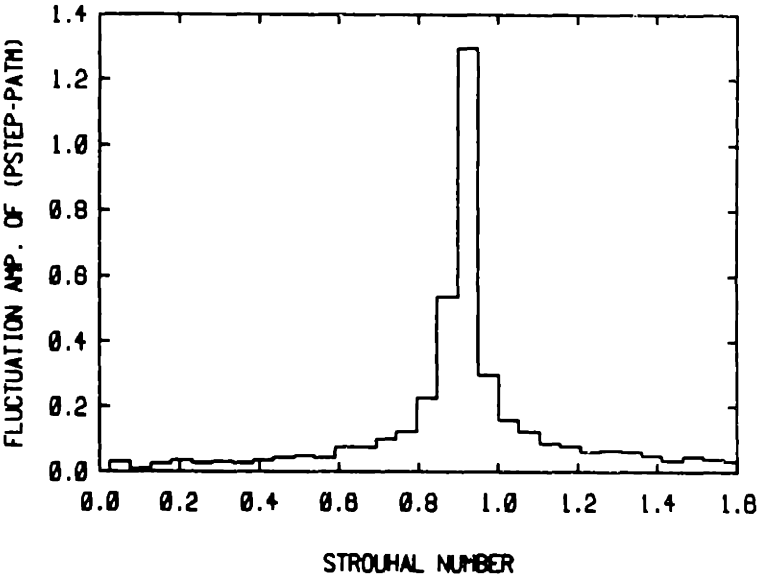

(b)

Figure 5.28 Spectra of the inlet flow rate (a) and upstream step pressure (b), computed from the corresponding time traces in figures 5.27 and 5.26a, for the time period 10-54.25. The Strouhal number used is based on the cavity depth and the mean inlet flow velocity for the time period considered. Both plots exhibit a dominant peak at St=0.9, with a broad spectrum at low St.

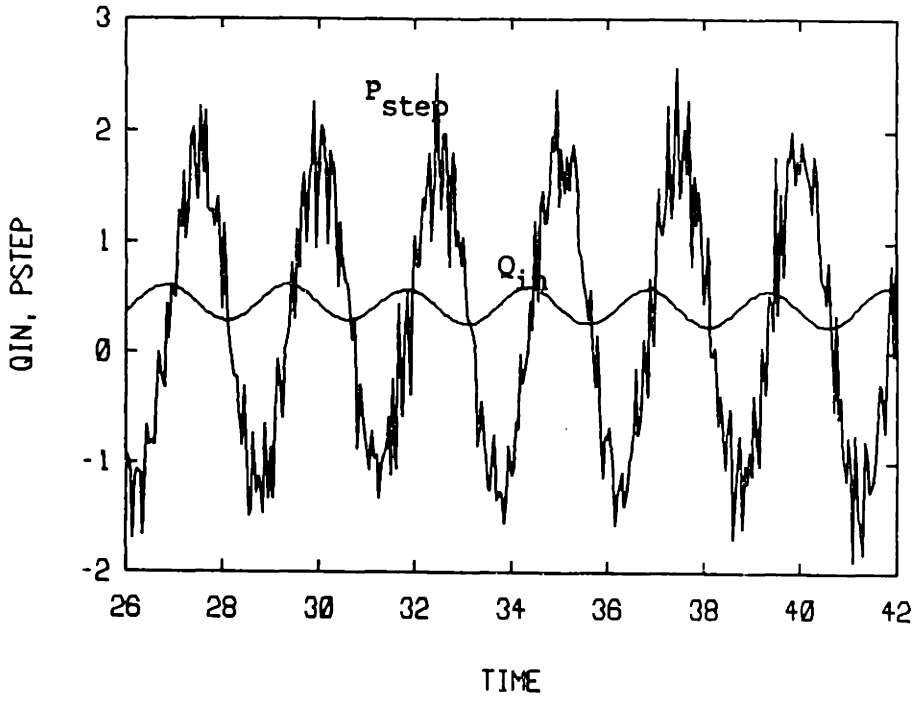

Figure 5.29 A close up segment of the step pressure and inlet flow rate superposed time traces for the high heat release flow of Fig. 5.36 below.

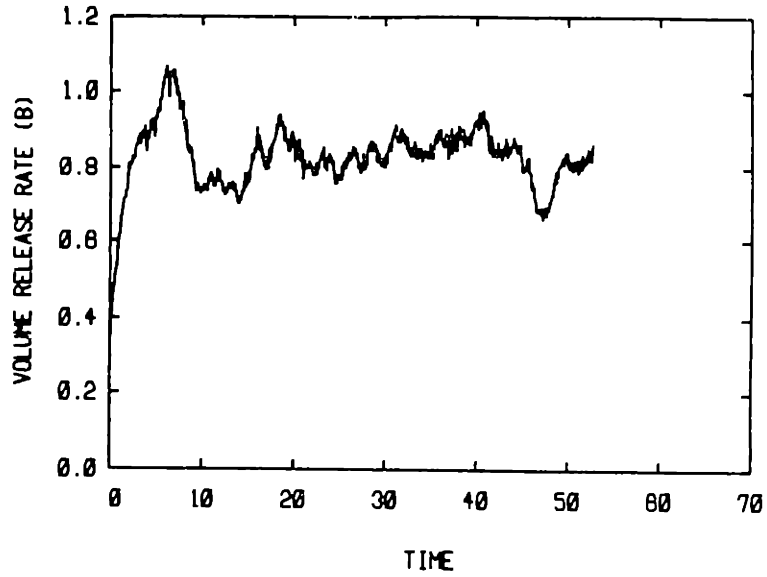

(a)

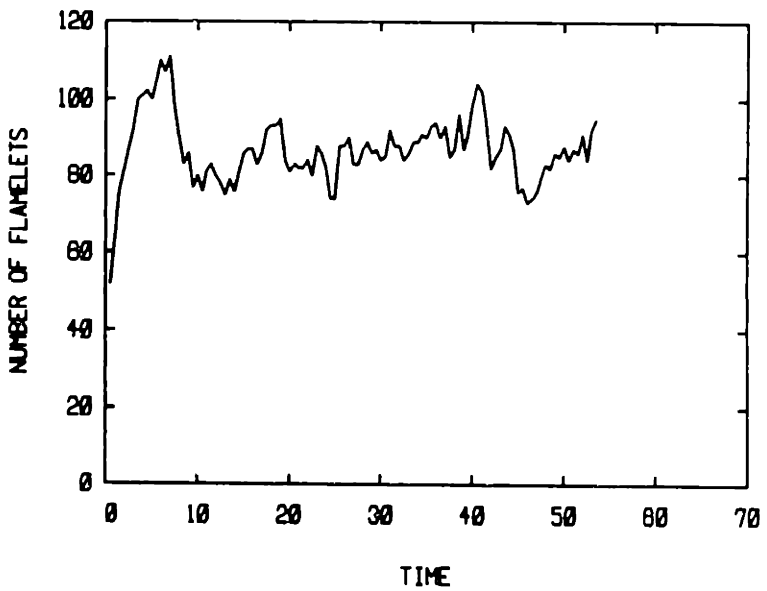

(b)

Figure 5.30 The rate of volume release (heat release) in the combustor (a), and the total number of flame segments (b), plotted against time, for the high heat release flow field shown in Fig. 5.36 below.

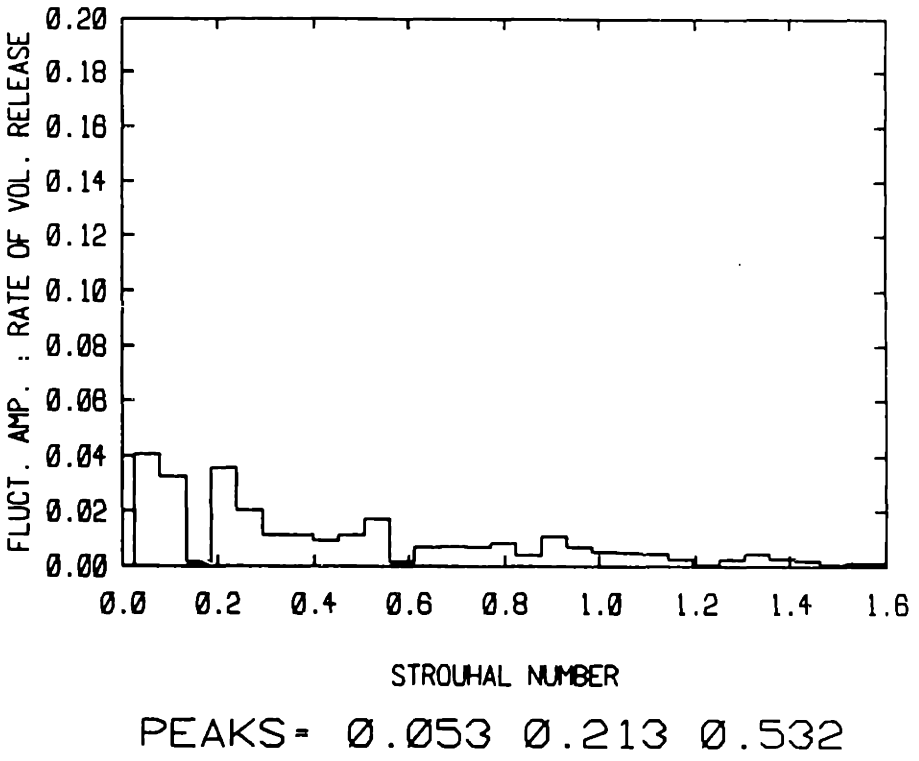

Figure 5.31 Spectrum of the rate of volume release (heat release) in the combustor, computed from the time trace in Fig. 5.30a, for the time period 10-54.25. The Strouhal number used is based on the cavity depth and the mean inlet flow velocity for the time period considered.

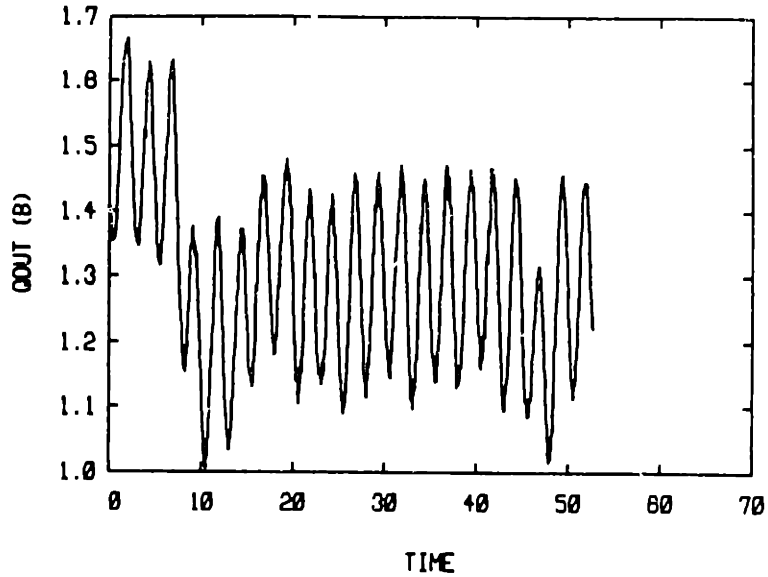

(a)

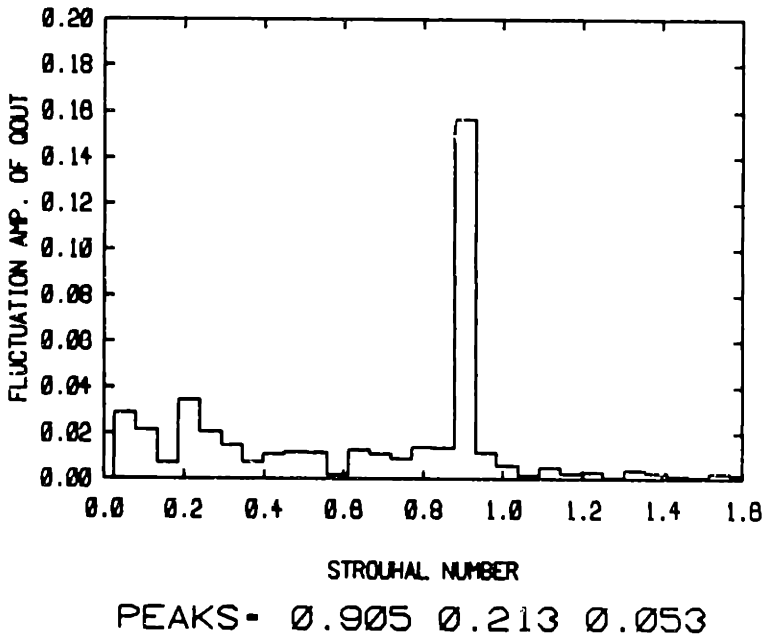

(b)

Figure 5.32 (a)- The volume flow rate out of the combustor, at xmax, plotted against time, for the low heat release flow of Fig. 5.36 below. (b)- The corresponding spectrum computed for the time period 10-54.25. The Strouhal number used is based on the cavity depth and mean inlet flow velocity for the time period considered. The dominant peak is at the forcing St, St=0.9.

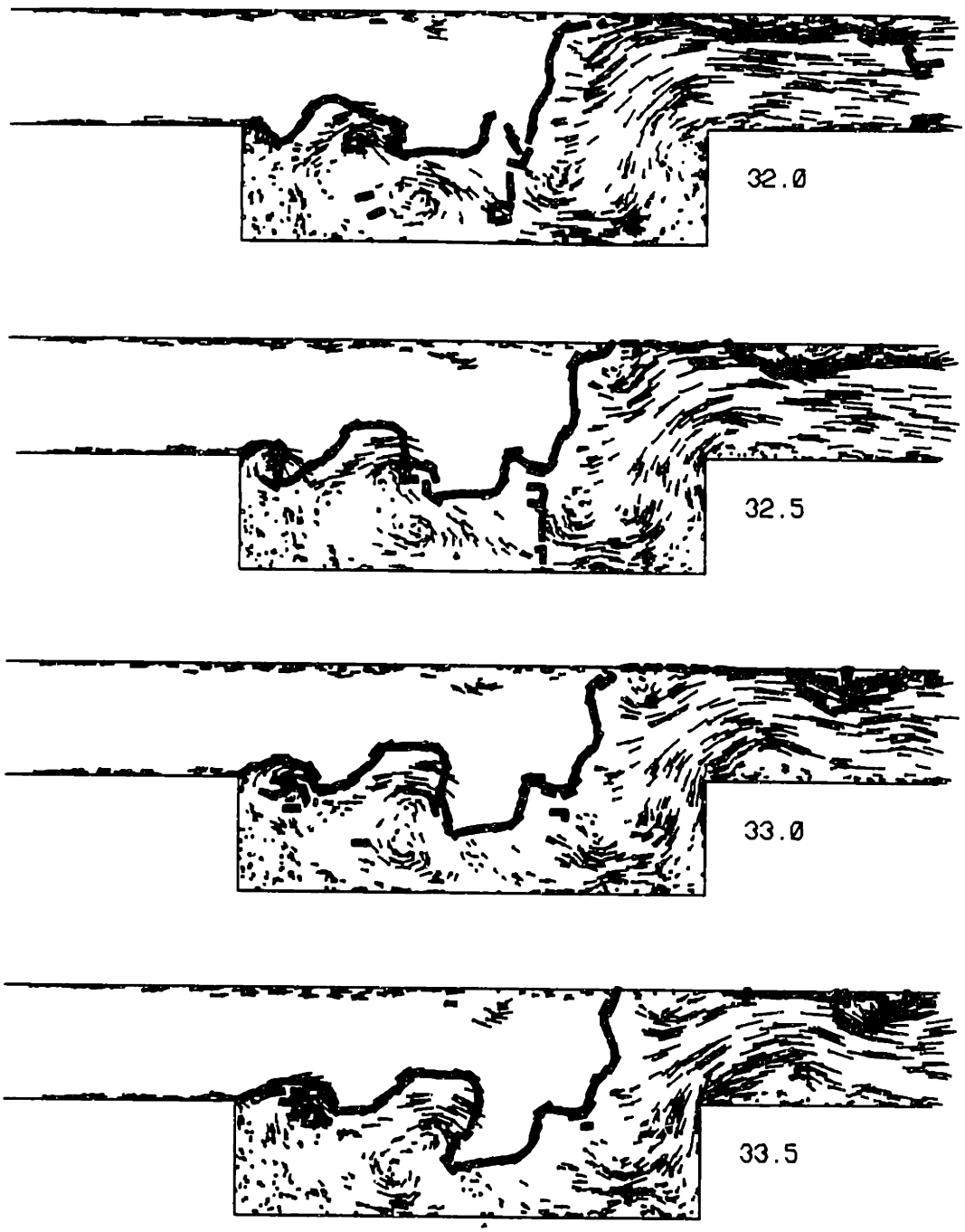

Figure 5.33a For caption see next page.

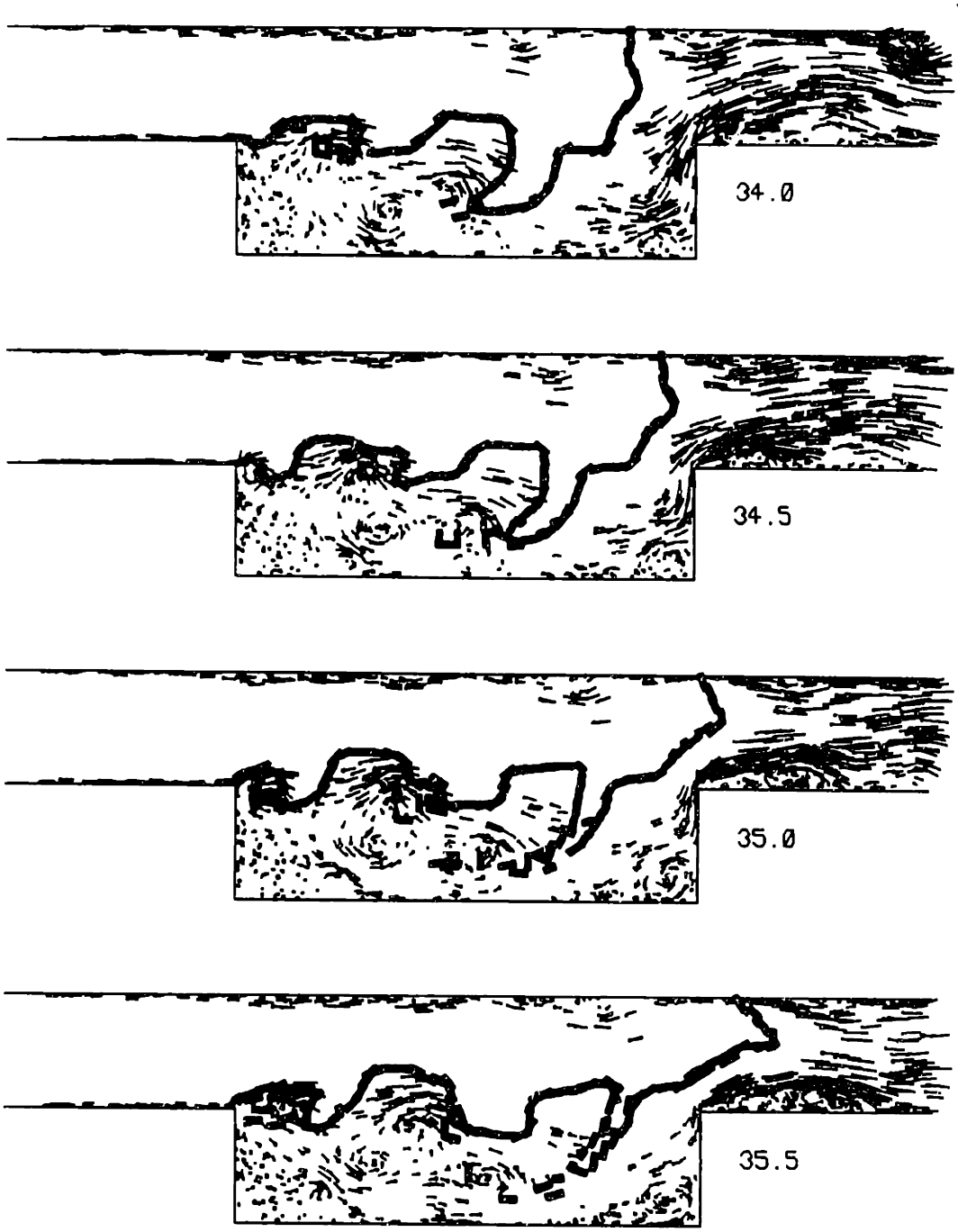

Figure 5.33a A sequence of time frames of the combustor flow field at low heat release, illustrating the fast shear layer eddy shedding at the forcing frequency. The exit pressure is a specified sinusoidal function of time, at fD/U_r=0.4, i.e with a period of 2.5.

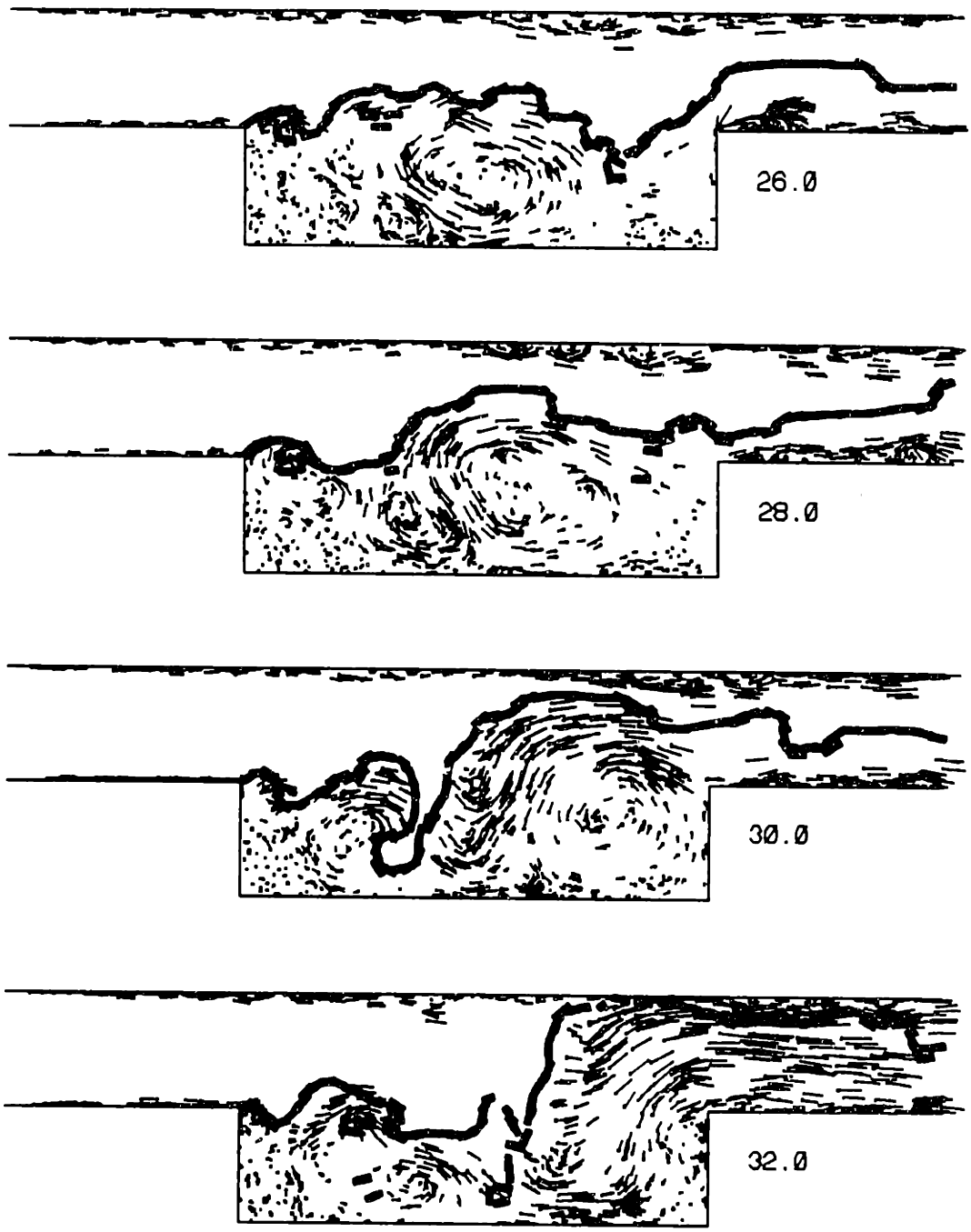

Figure 5.33b For caption see next page.

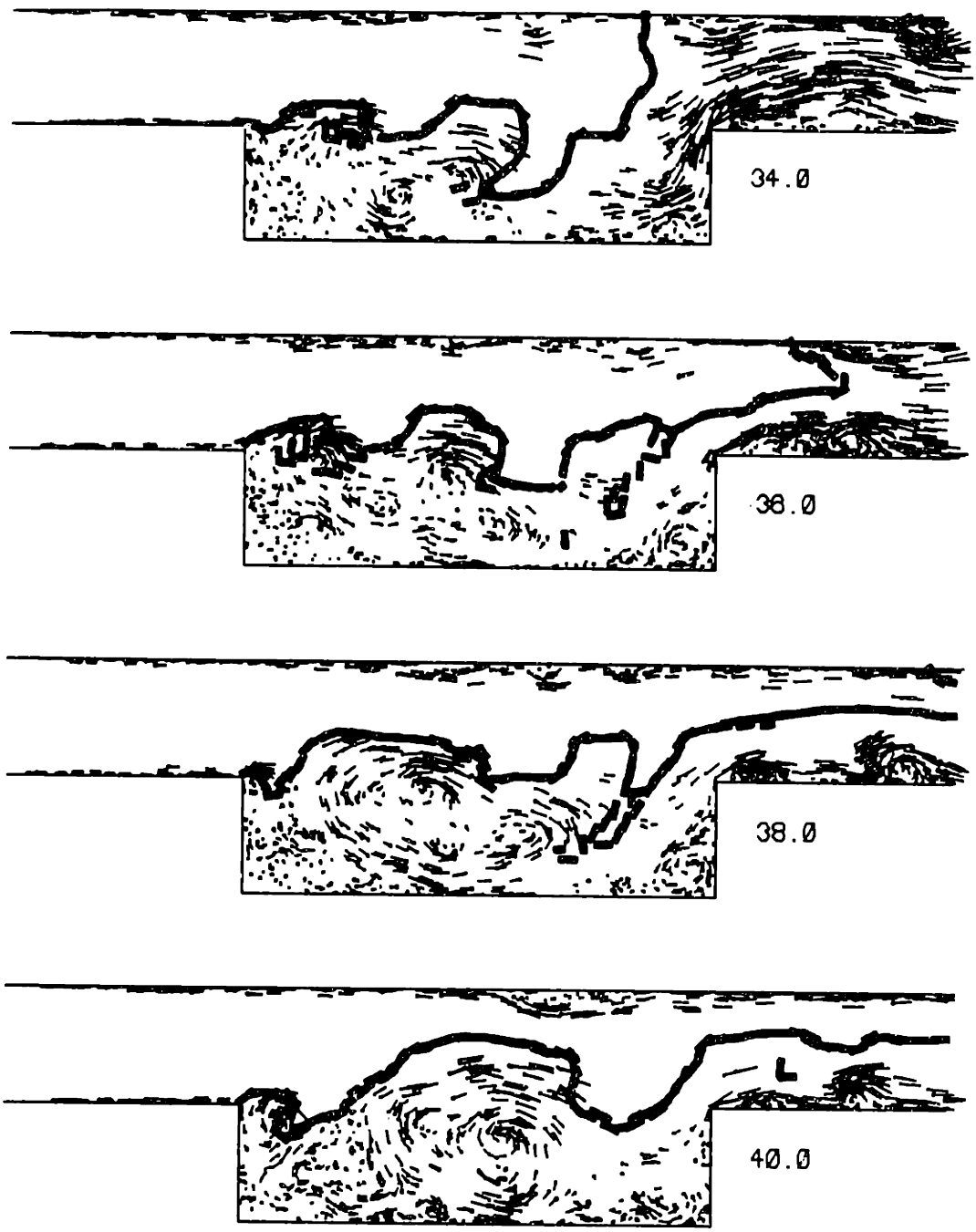

Figure 5.33b A sequence of time frames of the combustor flow field at low heat release, illustrating the slow recirculation zone eddy shedding at the natural frequency. The exit pressure is a specified sinusoidal function of time, at $fD/U_r=0.4$.

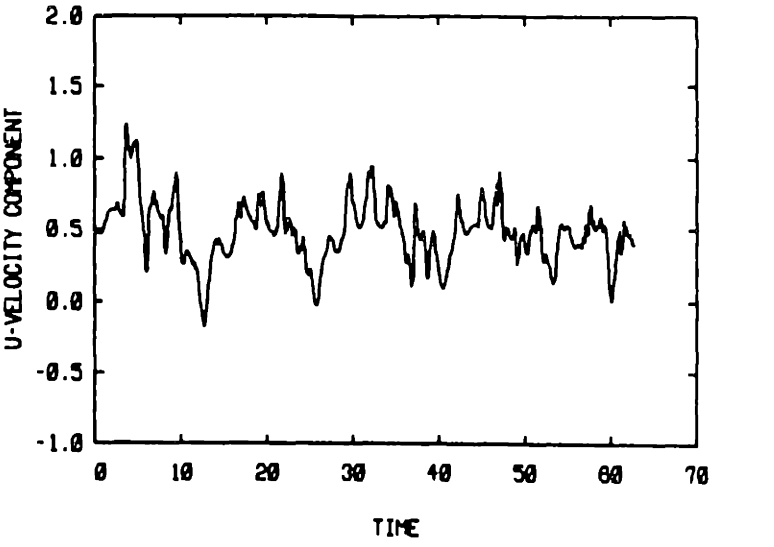

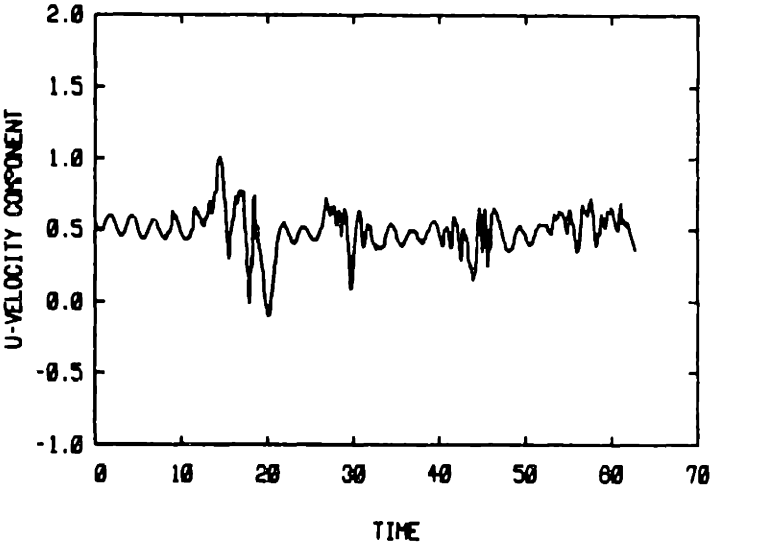

Figure 5.34 Time traces of the streamwise velocity at two points along the top of the cavity, for the low heat release flow field of Fig. 5.33. The numbers identifying the station location are the x and y coordinates, respectively.

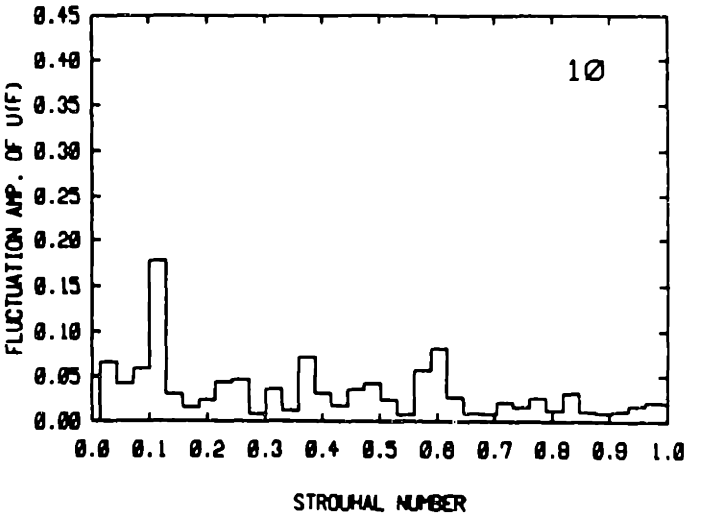

X=-1.000, PEAKS= 0.115 0.603 0.373

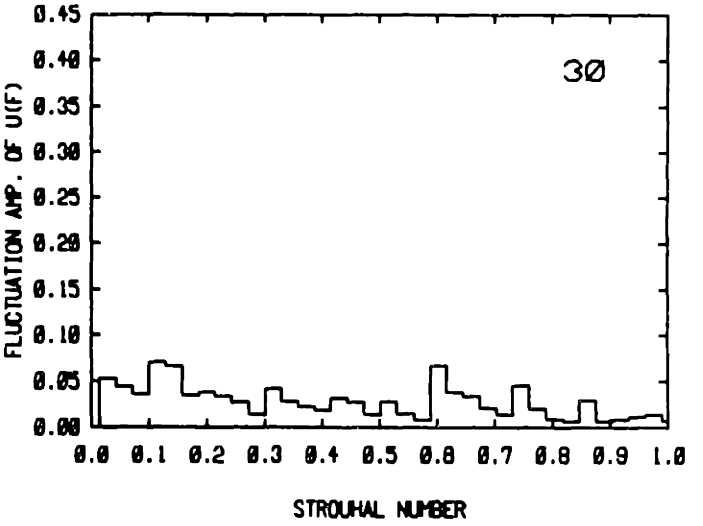

X= 1.000, PEAKS= 0.115 0.603 0.029

Figure 5.35 Spectra of the streamwise velocity fluctuation, computed from the time trace in Fig. 5.34, for the time period 10.0-62.75. The Strouhal number used is based on the cavity depth and the mean inlet flow velocity for the time period considered. The dominant peak is around St=0.1 in both plots, with a smaller peak at the forcing frequency, St=0.6.

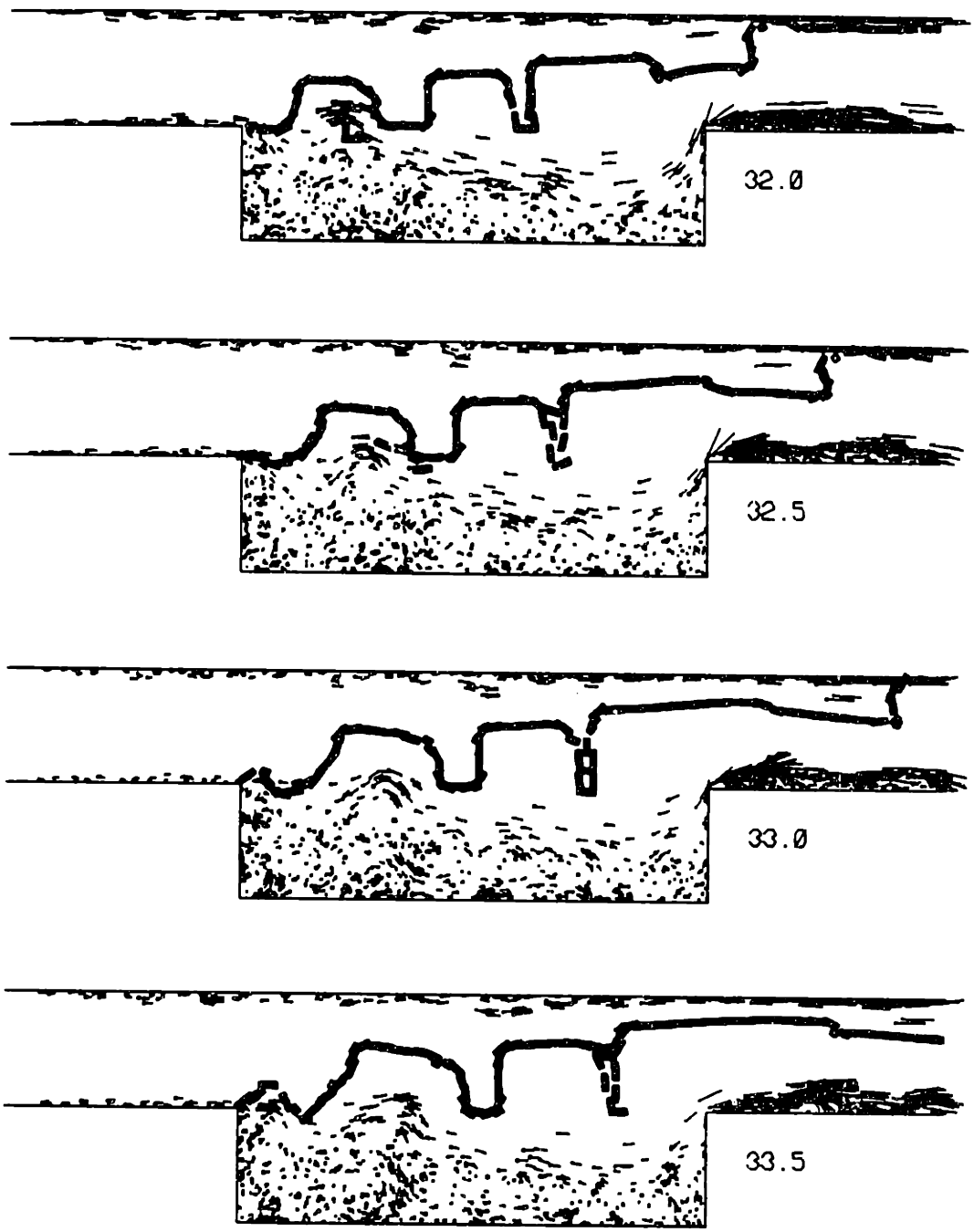

Figure 5.36a Continued on next page, caption at end of sequence.

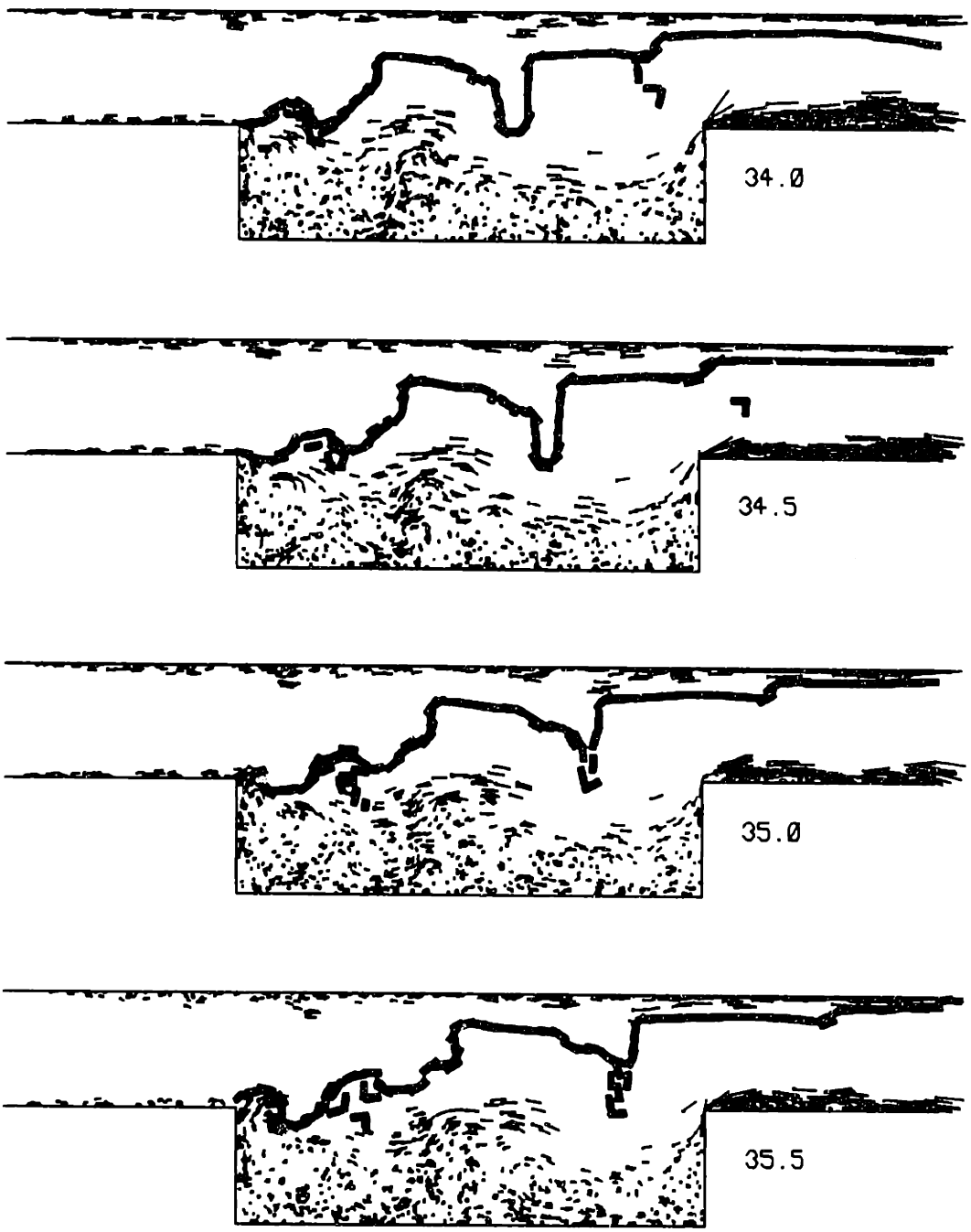

Figure 5.36a Continued on next page, caption at end of sequence.

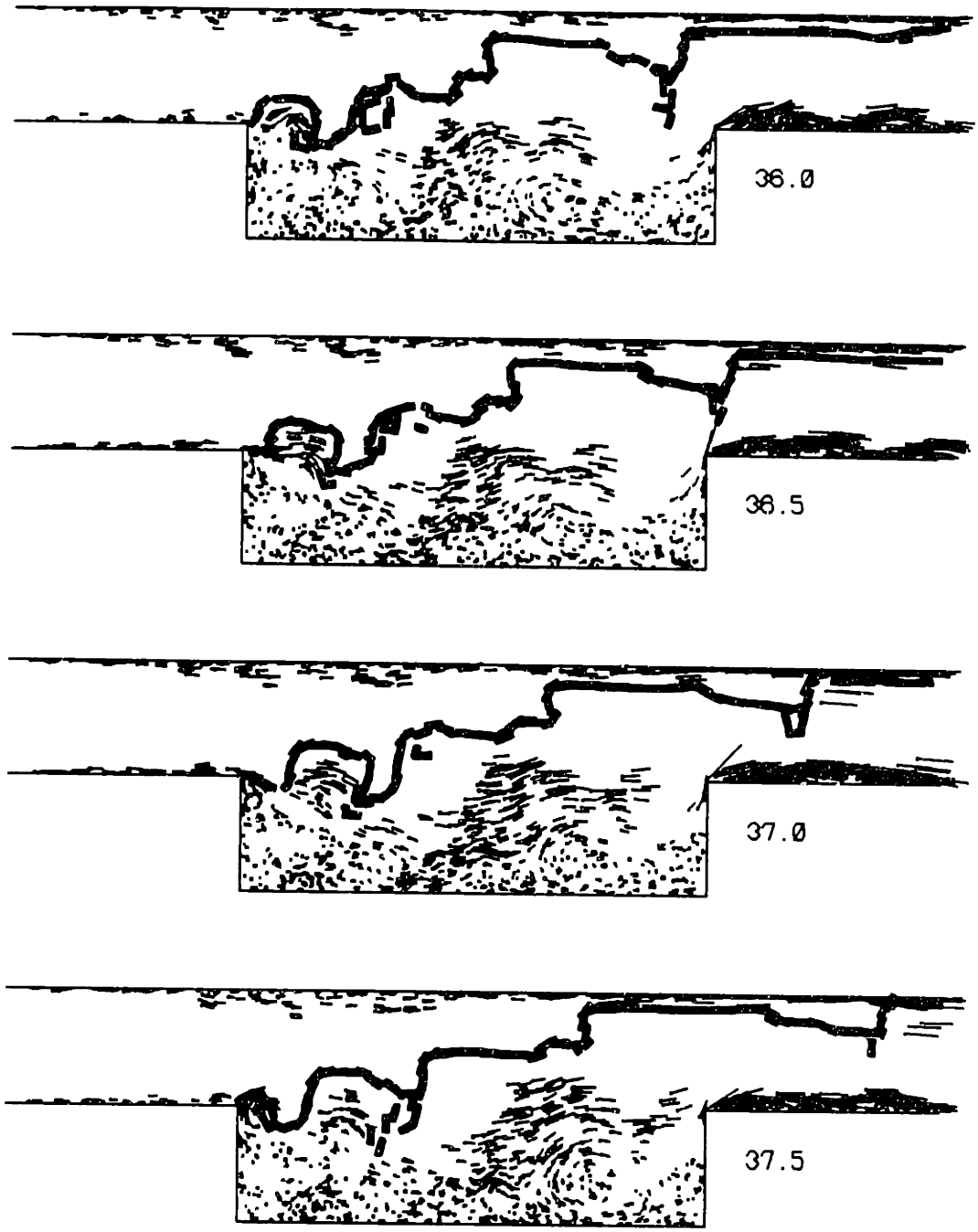

Figure 5.36a For caption see next page.

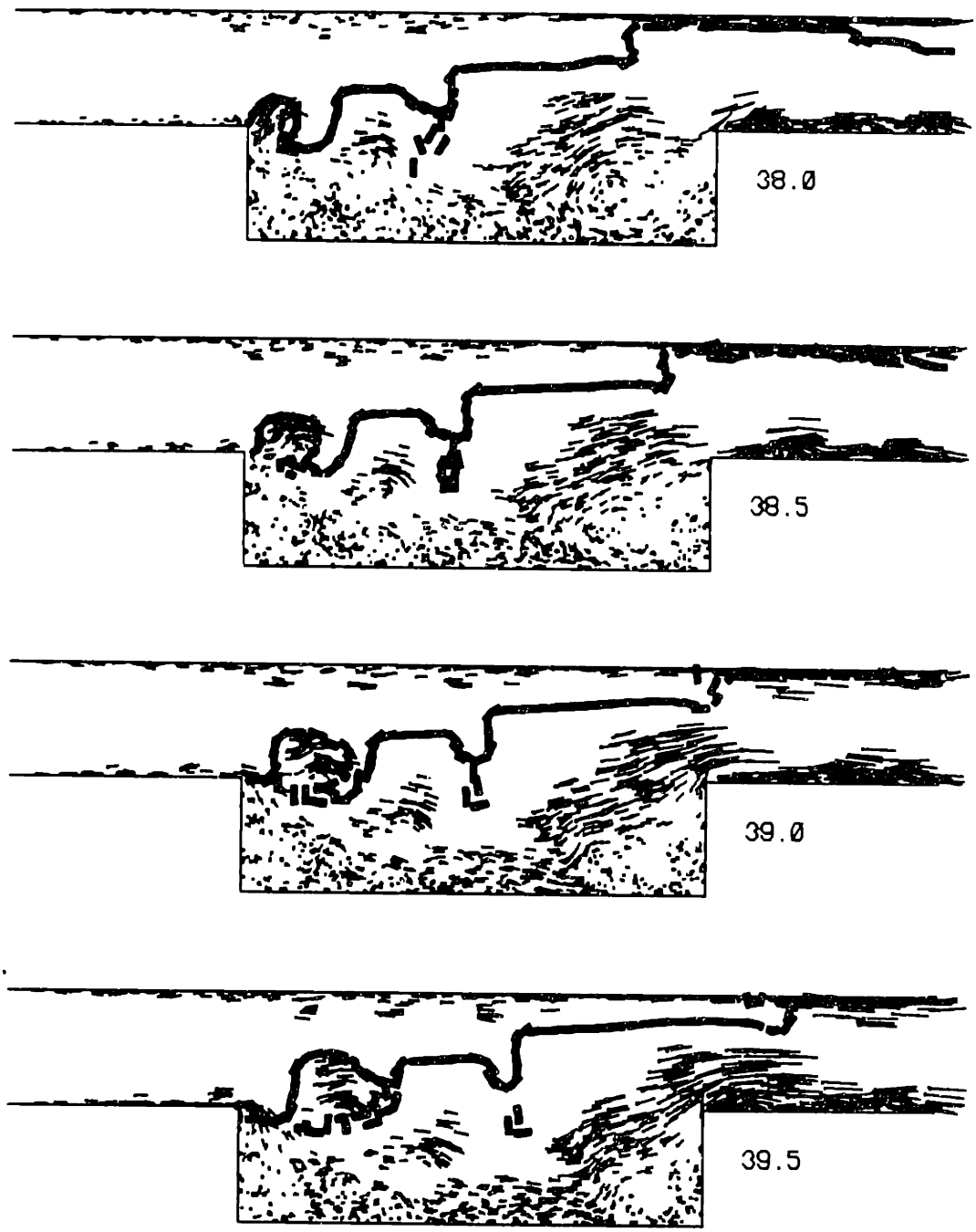

Figure 5.36a A sequence of time frames of the combustor flow field at high heat release, illustrating the fast shear layer eddy shedding at the forced frequency. The exit pressure is a specified sinusoidal function of time, at fD/U_r=0.4, i.e. with a period of 2.5.

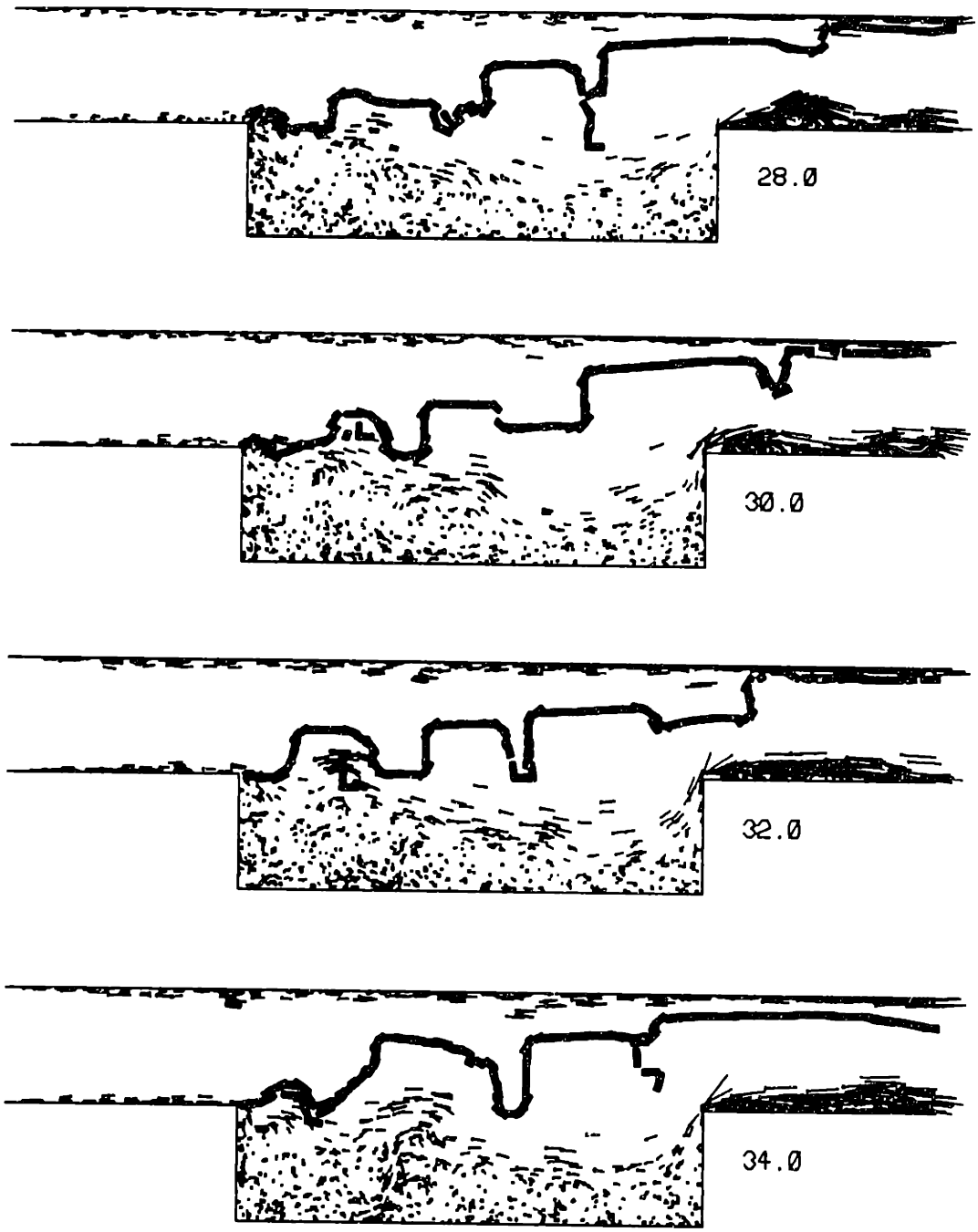

Figure 5.36b Continued on next page, caption at end of sequence.

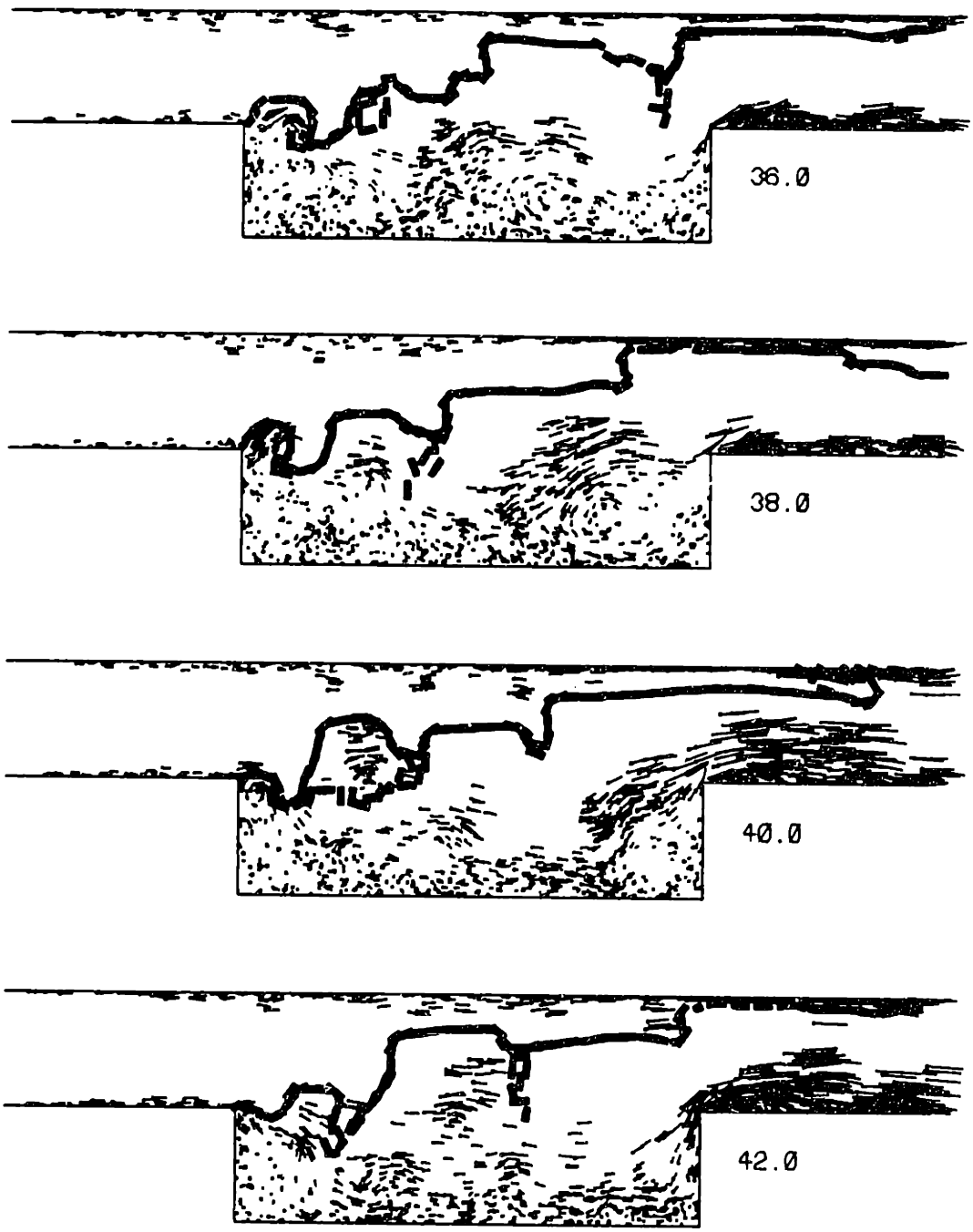

Figure 5.36b For caption see next page.

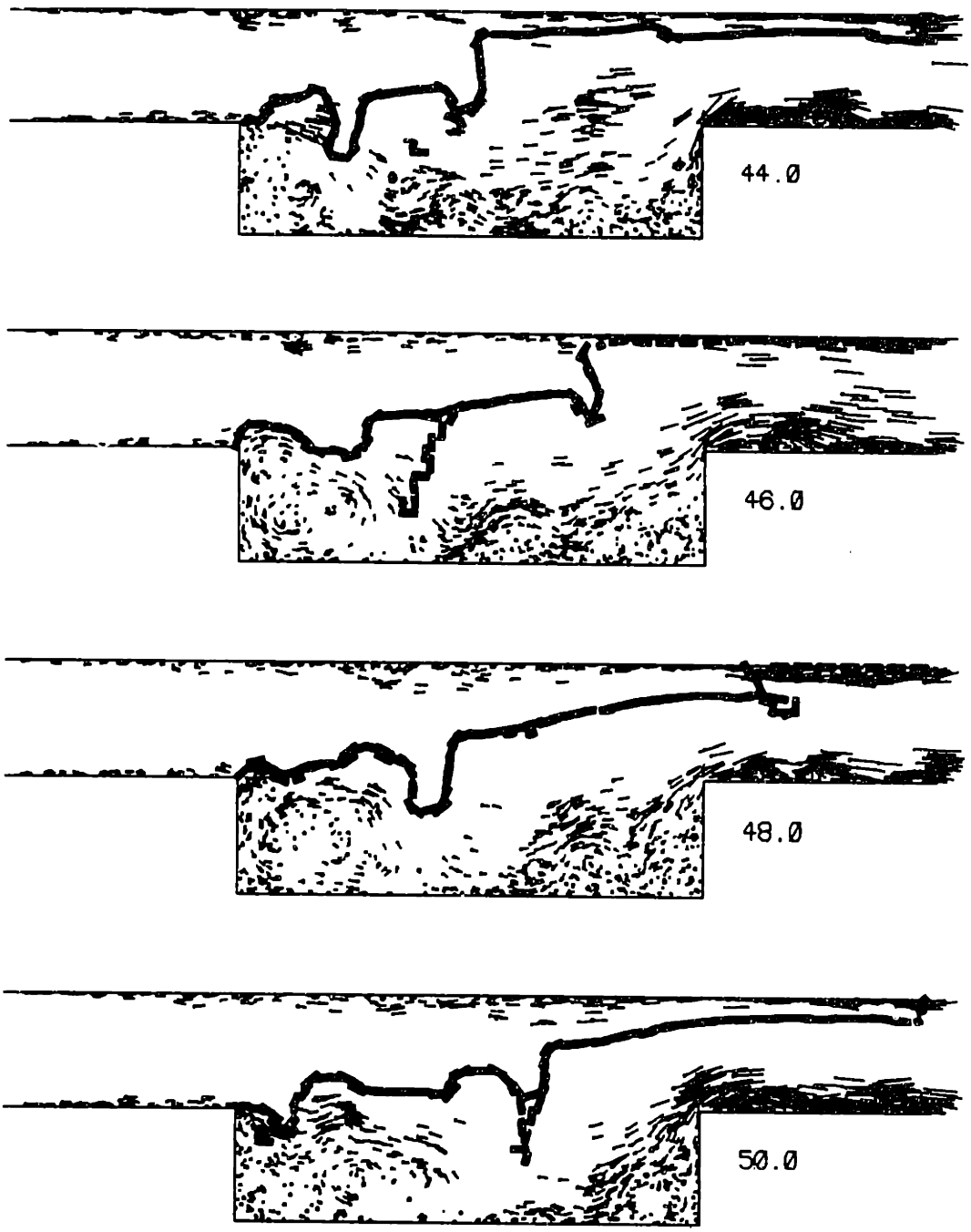

Figure 5.36b A sequence of time frames of the combustor flow field at high heat release, illustrating the slow recirculation zone eddy shedding at the natural frequency. The exit pressure is a specified sinusoidal function of time, at $fD/U_r=0.4$.

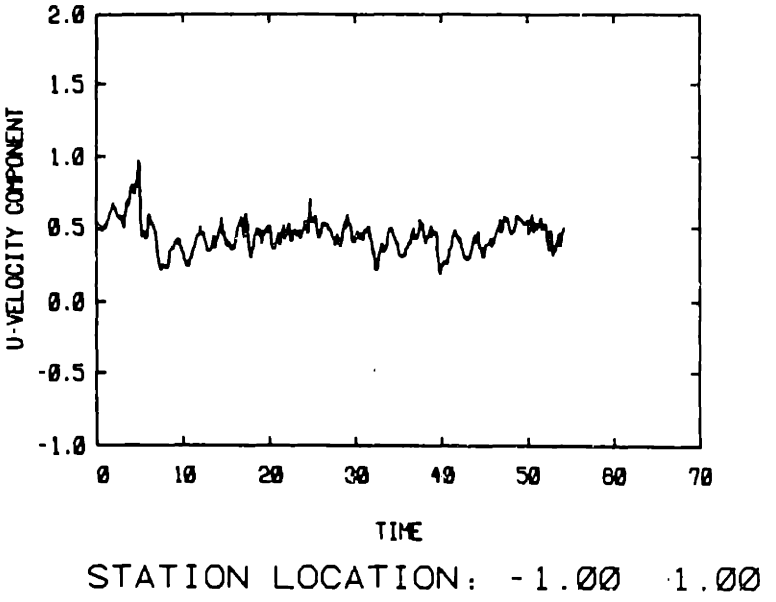

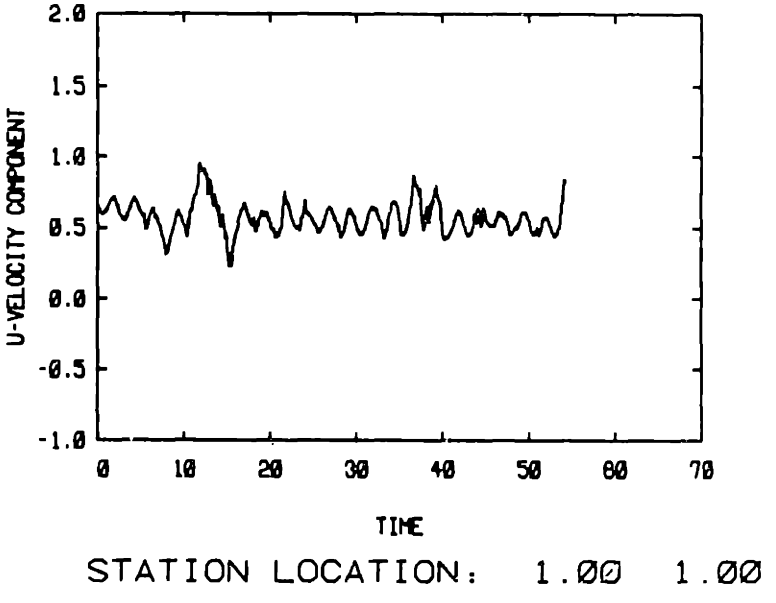

Figure 5.37 Time traces of the streamwise velocity at two points along the top of the cavity, for the high heat release flow field of Fig. 5.36. The numbers identifying the station location are the x and y coordinates, respectively.

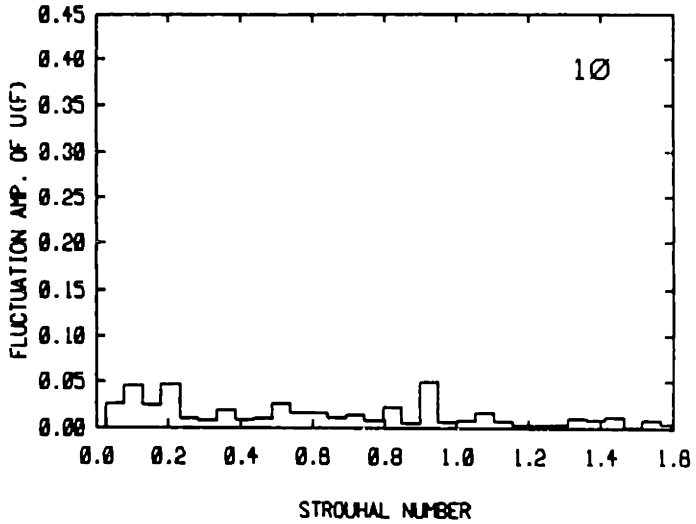

X= -1.000, PEAKS= Ø.924 Ø.205 Ø.103

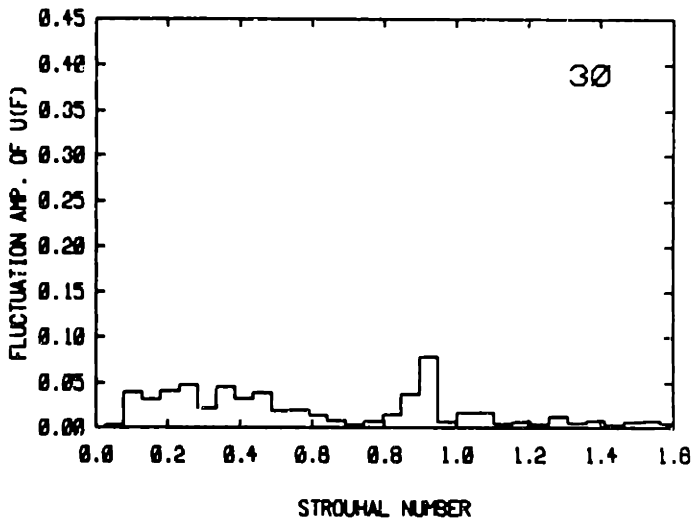

X= 1.000, PEAKS= Ø.924 Ø.257 Ø.360

Figure 5.38 Spectra of the streamwise velocity fluctuation, computed from the time trace in Fig. 5.37, for the time period 10.0-54.25. The Strouhal number used is based on the cavity depth and the mean inlet flow velocity for the time period considered. The dominant peak is around St=0.9, the forcing St, in both plots.

5.2.3 Low Frequency Forcing :

We now examine the effect of heat release on the combustor dynamics, given low frequency forcing of the exit pressure, p_{ex}. We consider three cases that differ only in the amount of heat release. As we shall see below, and contrary to what was observed above under high frequency forcing, the effect of increasing the rate of heat release is to amplify the flow oscillations in the combustor leading to flashback and flow reversal in the inlet channel.

We use the same geometry as above. Namely : $L/D=4$, $H/D=1$, $xmin/D=-4$, and $xmax/D=4$. Relevant flow parameters are : $Re_u=10^4$, $\rho_u/\rho_b=4.0$, and $p_o/p_r=1.0$. All cases use the following set of numerical parameters : $h_s/D=1/3$, $\Delta_s/D=0.0095$, and $\Gamma_m/U_rD=0.02778$. The exit pressure is specified to be a cosine function of time with amplitude $p_{mx}=2.5$, and frequency f_f such that $f_fD/U_r=0.1$. The only difference between the three cases is the value of the normal burning speed of the flame, S_u. For the low heat release case, we use $S_u/U_r=0.025$, while $S_u/U_r=0.035$ is used for the intermediate case, and $S_u/U_r=0.05$ is used for the high heat release case. We recall that the rate of heat release is proportional to S_u, as well as (ρ_u/ρ_b-1), which is fixed here. It is noted that if the flame mean length (area) were to remain unchanged, given the above two fold increase of S_u, then the mean rate of heat release is expected to double accordingly. However, as we shall see below, at $S_u/U_r=0.025$, the flame interface is seen to be considerably more fragmented and contorted, thus having larger area, compared to the $S_u/U_r=0.05$ case. Consequently, the increase in the global rate of heat release in the combustor is less than two-fold.

Let us begin then, by examining the results of the low heat release case with $S_u/U_r=0.025$. The specified p_{ex} trace, and the resulting P_{step} trace, are plotted against time in Fig. 5.39, while the P_{step} spectrum is shown in Fig.

5.40. The inlet flow rate (Q_{in}) and its spectrum are shown in Fig. 5.41. The Strouhal number, in Figs. 5.40 and 5.41b, is St=fD/U, where, as above, U is the mean slug flow inlet velocity. From Fig. 5.41a, U/U_r=0.84, for the time period 8.0-28.4. Using this U/U_r ratio, the peak at St=fD/U=0.117 in both the P_{step} and Q_{in} spectra is found to correspond to fD/U_r=0.10. This is the forcing frequency (time period 10.0, as in Fig. 5.39b). Figure 5.42 illustrates the 1/4 period (90 degrees) phase difference between Q_{in} and P_{step}, as observed by Yu et. al. (1989) and Poinsot et. al. (1987).

The time evolution of the unsteady flow field is shown in the sequence of frames in Fig. 5.43. This sequence exhibits one cycle of the large eddy shedding in the recirculation zone. The flow and flame dynamics are clearly different from those of the high frequency forced case. On the other hand, the correspondence between the flow rate and pressure traces, and the vorticity dynamics, is somewhat similar to that found above for the unforced case. Let us examine these dynamics in detail using both the frame sequence and the Q_{in} and P_{step} traces. As we shall demonstrate below, the flame is observed to undergo large amplitude oscillations (flapping) that cause it to intermittently fill the whole dump section (i.e. the dump and the channel above it), propagate slightly into the upstream channel, and then be swept downstream by the flow in a periodic fashion. This flapping is very explicit in Fig. 5.43, as discussed below.

Let us consider the cycle of events beginning at frame 12.0. At this time, the flame is roughly at its farthest upstream location in its large amplitude flapping cycle. The products have expanded to fill the whole dump section. The flow rate into the combustor is at its minimum, only slightly larger than zero. The pressure is falling rapidly (Fig. 5.42). Due to the small inlet flow rate, Q_{in}, and the expansion of products within the dump, the recirculation zone eddy is seen to fill the whole dump section as well,

from slightly after the upstream step to the downstream step. In the next two frames (times 13.0 and 14.0), the flame and vorticity field are convected downstream by the accelerating inlet flow rate. At time 15.0, the step pressure is minimum, and the inlet flow rate is increasing rapidly. A trailing eddy is being shed at the upstream step while the leading eddy is being convected against the downstream step. The flame interface is dipped strongly into the dump, following the vorticity field, as the trailing eddy grows at the step. The interface is also seen to move downstream, being convected along with the leading eddy, such that it is still approximately normal to the streamlines in the incoming flow. These vertical flame shapes have been observed experimentally under similar conditions, see Vaneveld et. al. (1982).

In frame 16.0 the reactants are being entrained by the growing trailing eddy, and the flame interface is being contorted, thus increasing in area. The flame in the channel is being swept further downstream with the voticity of the previous large leading eddy. This continues in frame 17.0, where, as in Fig. 5.42, the flow rate has attained its maximum while the step pressure is rising rapidly. At this point, the trailing eddy is still growing and entraining reactants as it begins to move away from the step. In frames 18-19, the leading eddy is practically completely swept away, as the trailing eddy is growing, moving downstream, and entraining more reactants. Around time 19.5, the pressure reaches its maximum (2.5 time units, or 1/4 period, after $(Q_{in})_{max}$), and the flow rate is decreasing rapidly.

In frame 20.0, we see that the eddy has filled most of the dump and starts to expand, along with the flame interface, upwards as well as upstream and downstream into the channel. This expansion continues through frame 21.0 and 22.0. At time 22.0 the flow rate reaches its minimum, which is slightly larger than zero, as at time 12.0 above. The pressure is decreasing rapidly

while the flame has reached the channel top wall and expanded into the upstream channel, as in Frame 12.0. The eddy has also expanded to fill the dump and the channel. Starting with frame 23.0, the cycle is repeated as the flow rate starts to increase again, pushing the products and the large expanded eddy downstream towards the combustor exit.

This cycle is seen to repeat itself, with a period of 10.0, i.e. with $fD/U_r=0.1$. This corresponds to the forcing frequency. The u-velocity trace at $x/D=\pm1$, and $y/D=1$, corroborates this observation. These traces are shown in Fig. 5.44. Comparison with the Q_{in} trace, in Fig. 5.41a, reveals similar periodicity. The u-spectra are shown in Fig. 5.45, where the dominant peak is at $St=fD/U=0.117$, with $U/U_r=0.84$. This corresponds to $fD/U_r=0.10$ as above.

This low frequency, large amplitude, flapping of the flame is the precursor to flashback that has been observed extensively in experimental investigations.

The correspondence between the pressure oscillations and the flow field pictures discussed above is in agreement with the results of Yu et. al. (1989). Their schlieren pictures reveal that the minimum step pressure occurs as the trailing eddy starts forming at the upstream step as in frame 15.0 above. Similarly, the maximum pressure is found to correspond to a situation where the flame fills the cavity and is still growing to fill the channel, as in frame 20.0 above.

The global rate of heat (volume) release from the combustor, and the overall flame length, are plotted against time in Fig. 5.46. Comparing this trace with the pressure and inlet flow rate traces, Fig. 5.47, we find, as with Yu. et. al. (1989), that the heat release lags the step pressure by roughly 1/4 of a period, and is roughly 180 degrees (1/2 period) out of phase with the flow rate (see also Poinsot et. al. 1987). This latter result is expected since the pressure lags the inlet flow rate by 1/4 period, as in

Fig. 5.42 above. The rate of heat release is maximum when Q_{in} is minimum. Hence, the heat release maxima correspond to a flow picture where the products, and the contorted flame interface have expanded to fill the whole dump section, as in Fig. 5.43, frames 12.0 and 22.0. Further, the rate of heat release is observed in Fig. 5.46 to rise steeply between times 16 and 20, which corresponds to the time of strong trailing eddy growth and flame contortion in Fig. 5.43. The mean value of the rate of heat release, for time 8-28.4, is found to be 0.97.

The flow rate out of the combustor is plotted versus time in Fig. 5.48, and superposed on the Q_{in} trace in Fig. 5.49. It is seen to be at the same frequency as, and in phase with, the inlet flow rate Q_{in}. The spectra of the rate of heat release and inlet flow rate are shown in Fig. 5.50. Again, the peak at St=0.117, which corresponds to the forcing frequency, is dominant. The mean value of Q_{out} is found to be 1.80, which is expected since $(Q_{in})_{av}$ = 0.84, and 0.84+0.97=1.81~1.80.

The fact that, as shown above, the unsteady heat release is only 1/4 of a period out of phase with the pressure in the combustor is a significant indicator of the combustor dynamics. When the pressure and heat release oscillations are nearly in phase, at the natural frequency of the combustor, it can be expected, using Rayleigh's criterion (Rayleigh, 1945), that sufficient coupling may occur leading to the growth of disturbances and the amplification of the combustor instability. When the combustor exit pressure, p_{ex}, was either fixed or forced at high frequency, as in sections 5.2.1 and 5.2.2 above, the combustor instability was not enhanced by increasing the heat release. The instability of the recirculation zone could not be amplified at its low natural frequency, because of the constraint on the combustor pressure exerted by the specified p_{ex}. In the present case, where the forcing is at low frequency, close to the combustor natural mode, it is

expected that the coupling between heat release and pressure oscillations can cause the amplification of the combustor instability. We demonstrate this fact below, by increasing the burning speed, S_u, and observing the resulting combustor flow dynamics.

We discuss now the intermediate case, with S_u/U_r=0.035. Flow diagnostics are examined, as above, to study the operation of the combustor. The step and exit pressures are shown in Fig. 5.51, while the inlet flow rate is plotted in Fig. 5.52a, and is superposed on the smoothed step presssure trace in Fig. 5.52b. The inlet flow rate is seen to reach negative values in a part of its oscillation cycle, as opposed to what was observed above with S_u/U_r=0.025. Hence, increasing the heat release has lead to flow reversal at the combustor inlet. Consistent with this observation, the smoothed step pressure traces are found to attain slightly higher values in the present case than in the above low heat release case, compare for example Figs. 5.52b and 5.47a. Figure 5.52b also illustrates the 1/4 period phase shift between the step pressure and inlet flow rate traces. The mean inlet flow velocity is computed from the Q_{in} trace for time 10-40, and is found to be U/U_r=0.73. The spectra of Q_{in} and P_{step}, shown in Fig. 5.53, exhibit a dominant Strouhal number St=fD/U=0.137, i.e. fD/U_r=0.100, at the forcing frequency.

The flow dynamics are shown in terms of the vortex elements and the flame interface in the sequence of frames in Fig. 5.54. The flame interface in this case is less contorted than that in the low heat release case, Fig. 5.43. This trend towards less contortion continues upon further increase in S_u, as we shall see below. The flame is also seen to move further upstream, as compared to the low heat release case, by propagating through the boundary layer due to local flow reversal. This can be seen in frame 21.0 in Fig. 5.54, where the inlet flow rate is still positive, Q_{in}=0.06 (dimensionless). The direction of the velocity vectors on the vortex elements in the boundary

layer upstream of the step indicates local flow reversal. Q_{in}, on the other hand, reverses later on (time : 21.3 to 22.25). The extent to which the flame moves upstream along the channel floor is more than that observed in Fig. 5.43 because of stronger local flow reversal and the overall inlet flow reversal in the present case.

The correspondence between the maximum and minimum step pressures in the oscillation cycle and the frame sequence in Fig. 5.54 is similar to that observed in the low heat release case. The maximum pressure is roughly at frame 19, i.e. when the flame and the large recirculation zone eddy fill the cavity and are expanding into the channel, while the minimum pressure occurs at frames 15 and 25, when the trailing eddy is forming at the upstream step. Frames 15 and 25 illustrate that the formation of the upstream trailing eddy is associated with : strong influx of flow into the cavity, a downward dip of the flame interface into the dump, and the entrainement of reactants into the products.

The flow dynamics observed in Fig. 5.54, including the lift-off of the flame in the upstream boundary layer, and the large amplitude flame flapping, are similar to the schlieren pictures from available experiments. The flowfield in the "chucking" mode observed in the experiment by Vaneveld et. al. (1982), which was shown in Fig. 1.2, illustrates similar dynamics to those observed in Fig. 5.54, with St=0.15. Similarly, Fig. 5.55, from Keller et. al. (1981), shows experimental pictures from a step-dump combustor flow that exhibits large amplitude oscillation as that observed here, with St=0.11. Again, we see the same kind of cyclic flapping of the flame and vorticity field, occuring at St=O(0.1).

Further, the above results illustrate the amplification of the natural recirculation zone instability at the forcing frequency, fD/U_r=0.1, i.e. with a period of 10, as can be observed between frames 15 and 25. This visual

observation is corroborated by the above spectra of P_{step} and Q_{in} as well as by the traces and spectra of the u-velocities at $x/D=\pm 1.0$, $y/D=1.0$, in Figs. 5.56 and 5.57. The u-spectra show a dominant low frequency peak at $St=fD/U=0.137$, i.e. $fD/U_r=0.10$.

In the low heat release case, the mean inlet velocity U was such that the forcing Strouhal number was $St=fD/U=0.117$, and the instability of the recirculation zone was seen to exhibit this same St (see Fig. 5.45). In the present case the forcing is at $St=fD/U=0.137$, and we have seen that the recirculation zone response is at this same St. This suggests that when the forcing St is close enough to the 0.1 value, to be within the broad region of instability of the recirculation zone, it couples with this instability and amplifies it. This explains the observed variability of the experimentally measured St around 0.1, due to solely varying the dump length (see Yu et. al., 1989, for example) or other acoustic components of the system.

Let us look next at the overall rate of heat release in the combustor corresponding to the above dynamics. Fig. 5.58 shows the time trace of the heat (volume) release and the flame length. As before, we see that the two traces are in phase. The heat release trace is also shown superposed on the smoothed step pressure and inlet flow rate traces in Fig. 5.59. It is noteworthy, from these superposed traces, that the heat release oscillation is more closely in phase with the pressure oscillation than in the above case. This is due to the faster rate of burning (larger S_u) in this case. The rate of heat release is also higher in the present case than that observed above; compare Figs. 5.58 and 5.46. The mean value computed from the trace in Fig. 5.58a, for time 10-40, is found to be 1.24 as opposed to 0.97 above. Evidently, increasing S_u tends to increase the amplitude of the heat release rate and to decrease the phase lag between it and the pressure oscillation. Both of these factors tend to amplify the combustor dynamics according to the

Rayleigh criterion, as discussed above, and as illustrated by the evidence of flow reversal in the present case.

Since the heat release oscillation is more in phase with the pressure, it is then expected to be only 1/4 period out of phase with the Q_{in} trace, as is evident in Fig. 5.59b.

The Q_{out} trace is shown in Fig. 5.60, plotted against time and superposed on the Q_{in} trace. The two flow rates are in phase, as observed earlier. The amplitude of oscillation of the Q_{out} trace is larger than that in Fig. 5.48 above, again illustrating the amplification of the combustor dynamics by the increased heat release. The spectra of the heat release and Q_{out} oscillation are shown in Fig. 5.61. The dominance of the forcing Strouhal number, at St=fD/U=0.137, is evident. The amplitudes of the dominant peaks in these spectra are higher than those in Fig. 5.50, as expected from the corresponding time traces.

Finally, let us look at the high heat release case, where S_u/U_r=0.05. We observe here similar dynamics as above, but with yet larger amplitude oscillations that result in the motion of the flame further upstream into the inlet channel beyond the edge of the computational domain, xmin.

The forcing function, p_{ex}, which is identical to that used in the two cases above, is plotted along with the step pressure in Fig. 5.62. The resulting inlet flow rate trace is shown in Fig. 5.63. Two cycles of oscillation are observed, and they exhibit a growth in the amplitude of flow and pressure oscillation from one cycle to the next. The oscillation amplitude in the second cycle exceeds that measured in the above cases, and causes significant flow reversal at the inlet plane, with Q_{in} reaching a minimum of ~ -0.6. Thus, the further increase in S_u to S_u/U_r=0.05 has caused a concomitant increase in the amplitude of oscillations in the flowfield. The mean inlet flow velocity is found to be U/U_r=0.57, for the time period 3.0-

23.3. The Q_{in} and P_{step} spectra exhibit a dominant peak at St=fD/U=0.173, which corresponds to fD/U_r=0.10; this is the forcing frequency. Again we find that the flow dynamics are amplified at the forcing St, with the latter being close to 0.1. The phase difference between the P_{step} and Q_{in} traces is observed to be ~1/4 of the period, as in all the above results.

The flow dynamics are illustrated in the flame sequence in Fig. 5.64. Large amplitude flame oscillations are observed, similar to the above two cases, but with the flame propagating even further into the upstream channel and exiting the computational domain at xmin, as in frame 23.0. This necessitated the interruption of the computation.

We observe, as expected from the higher S_u, less flame contortion and fragmentation than that in the above two cases. On the other hand, the correspondence between the flow rate and pressure traces and the frame sequence in Fig. 5.64 is similar to that observed above. Note that the flame is observed to separate away from the vorticity field, more so than in the above two cases. This is similar to what was observed earlier in the high frequency forcing study, upon increasing the rate of heat release. It is a result of the increased strength of the expansion field at the flame, which causes it generally to ride higher above the cavity in the channel.

The period of the recirculation zone eddy shedding is observed to be roughly 10, as for example between frames 8 and 18-19. The recirculation zone eddies are being shed at the forcing frequency, i.e. at ~ $St=fD/U_r=0.1$.

The u-velocity traces at $x/D=\pm1$ and $y/D=1$, are shown in Fig. 5.65. Their spectra exhibit the same dominant low frequency peak at St=fD/U=0.173 as the Q_{in} and P_{step} spectra.

The rate of heat release and the overall flame length (area) are plotted against time in Fig. 5.66. They are seen to follow each other closely as above. The heat release is seen to rise steeply for time 16-18, which

corresponds to the period of strong entrainement in the above frame sequence. It is also seen to attain a higher maximum in the second cycle than that observed above, as expected from the higher S_u.

The heat release trace is superposed over the smoothed step pressure and the inlet flow rate traces in Fig. 5.67. In the second cycle of oscillation, the heat release and the pressure are seen to rise simultaneously, with the heat release peak occuring slightly before the pressure peak and staying high for the duration of the latter peak. As indicated above, both this phase relationship and the large amplitude of the heat release peak lead to the amplification of the combustor dynamics according the Rayleigh criterion. The heat release rate, being almost in phase with the pressure oscillation, is expected to be ~ 1/4 period out of phase with the inlet flow rate oscillation, as shown in Fig. 5.67b.

Q_{out} is plotted in Fig. 5.68a, and is superposed over the Q_{in} trace in Fig. 5.68b. As expected, the amplitude of the Q_{out} oscillation is larger than in the above two cases, with Q_{out} and Q_{in} roughly in phase.

To summarize then, we have shown that under conditions of low frequency forcing, where the forcing Strouhal number is close to the natural St of the combustor, increasing the rate of heat release causes the recirculation zone dynamics to be amplified. This results in inlet and exit flow rate and pressure oscillations that increase in amplitude as the heat release is increased. At high rates of heat release, intermittent inlet flow reversal and flame "flashback" into the upstream channel are observed.

By contrast, under high frequency forcing, the combustor dynamics are stabilized upon increasing the rate of heat release.

Thus, the stability of the combustor flow is related to the pressure oscillation in the system as a whole. The specific frequency range at which flashback occurs is predetermined by the recirculation zone, namely it is

St=fD/U=O(0.1) for low Mach number flow. However, if the combustor pressure is constrained by some forcing mechanism such that it cannot oscillate with large amplitude at the natural frequency of the recirculation zone, then flashback can not occur.

In particular, for the same flow and high heat release conditions as the S_u/U_r=0.05 case above, forcing the combustor at a high frequency (fD/U_r=0.4) dampens the combustor dynamics such that the amplitude of the inlet flow rate oscillation is significantly less than that measured above. The results that support this conclusion are shown in Figs. 5.69-5.72. Figure 5.69 shows the step and exit pressure traces illustrating the high frequency forcing. The resulting Q_{in} trace is shown in Fig. 5.70. Q_{in} is observed to oscillate between 0.4 and 1.0 as opposed to the high amplitude oscillation in Fig. 5.63. For the time period : 10 to 26.6, the mean inlet flow velocity is U/U_r=0.77. The spectra of Q_{in} and P_{step} are shown in Fig. 5.71. The high frequency peak is at St=fD/U=0.55, i.e. fD/U_r=0.4 - the forcing frequency. The small amplitude peak at low frequency is at St=fD/U=0.16, in the vicinity of 0.1. This peak is the result of the natural response of the combustor, and it is reflected in the low frequency modulation of the time traces. This situation of a dominant peak at the high forcing frequency and a small amplitude peak at the low natural frequency has been observed above in the high frequency forcing study. Clearly, the large amplitude flow oscillation at the natural frequency, observed above under low frequency forcing for otherwise identical flow conditions, is absent from these high frequency forced results. This fact is also illustrated in the sequence of frames shown in Fig. 5.72, which shows weak recirculation zone eddy shedding as compared to the sequence in Fig. 5.64. Therefore, these, and earlier high frequency forcing results, indicate that high frequency forcing is a feasible mechanism

for the suppression of the combustor instability. This conclusion is in agreement with the experimental evidence of McManus et. al. (1989).

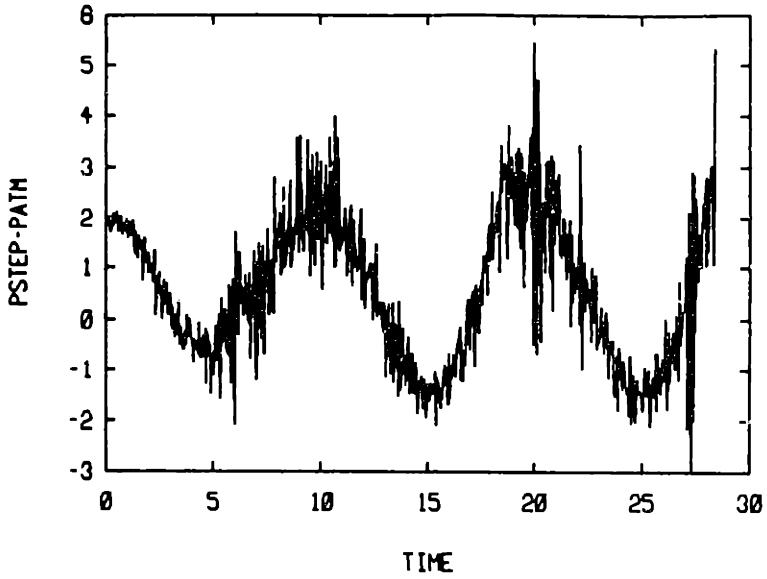

(a)

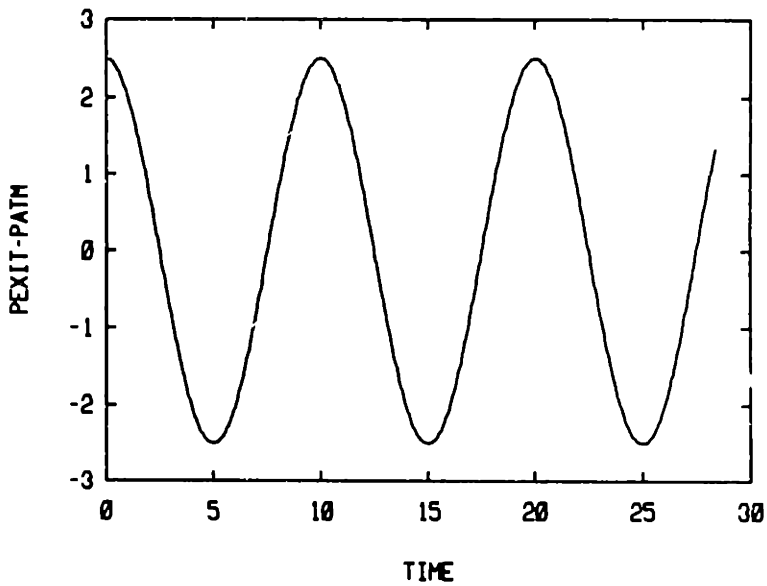

(b)

Figure 5.39 The pressure trace (channel centerline) at the upstream step (a) and the specified exit pressure trace (b) plotted versus time, for the low heat release flow of Fig. 5.43 below.

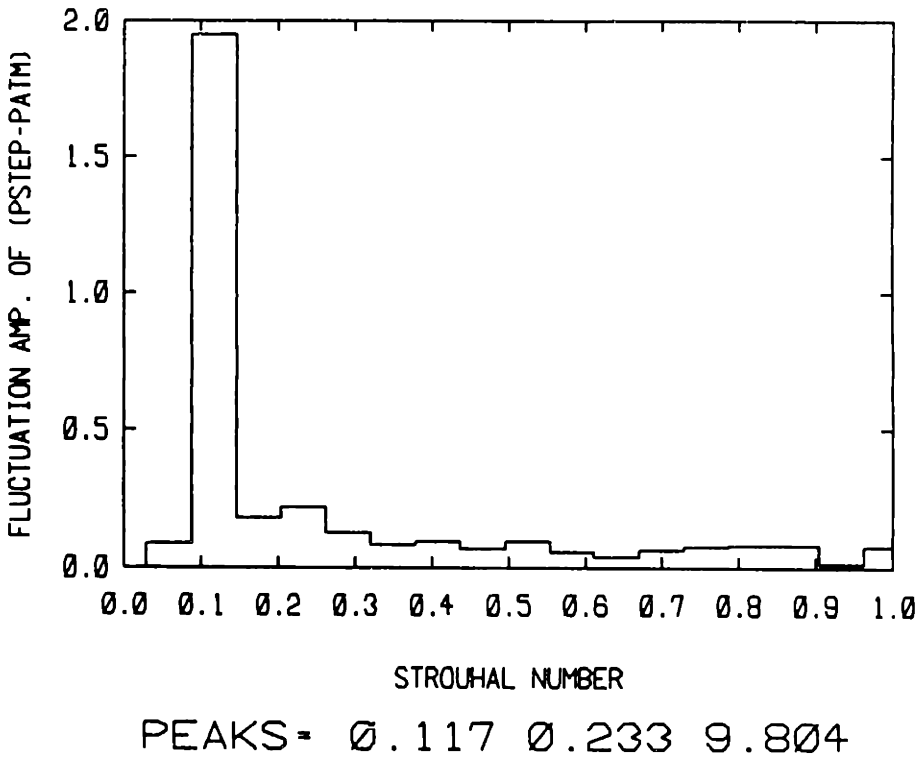

Figure 5.40 Spectrum of the step pressure, computed from the time trace in Fig. 5.39a, for the time period 8-28.4. The Strouhal number used is based on the cavity depth and the mean inlet flow velocity for the time period considered. The dominant peak at St=0.117 corresponds to the forcing frequency.

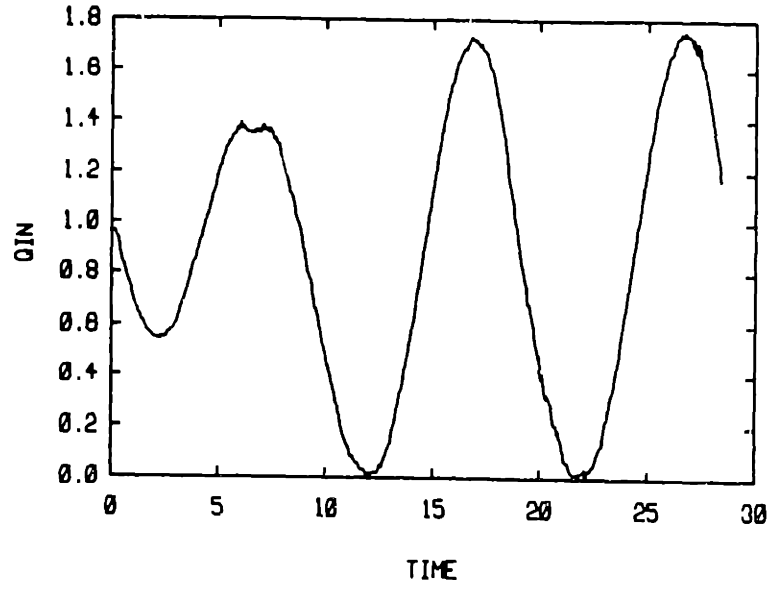

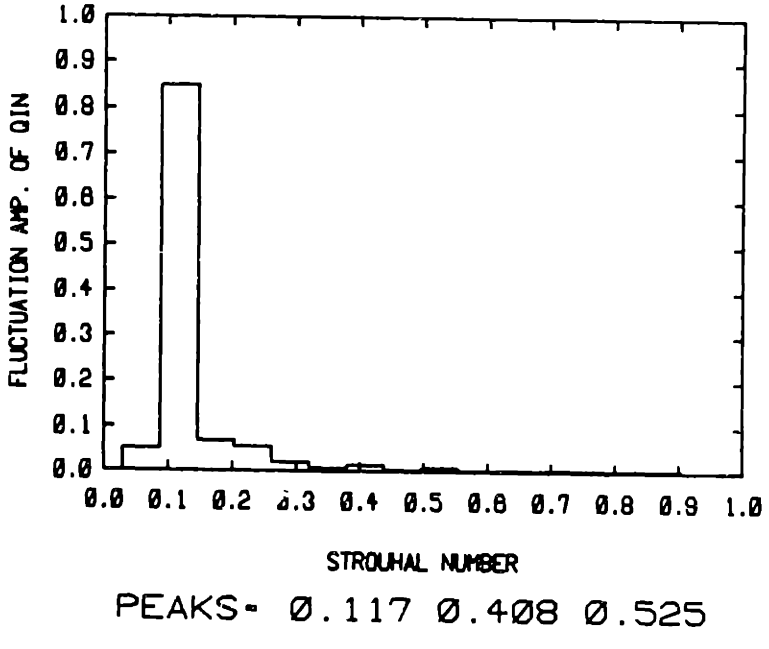

Figure 5.41 The time trace (a) and spectrum (b) of the inlet flow rate at xmin, for the low heat release flow of Fig. 5.43 below. The mean flow rate for the time period from 8 to 28.4 is 0.84.

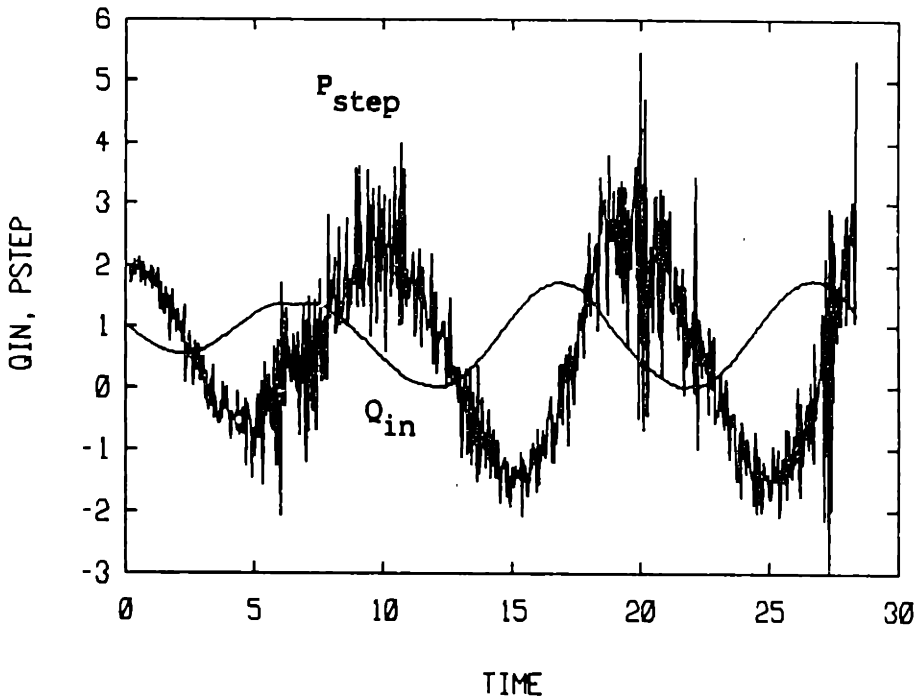

Figure 5.42 The step pressure and inlet flow rate superposed time traces for the low heat release flow of Fig. 5.43 below.

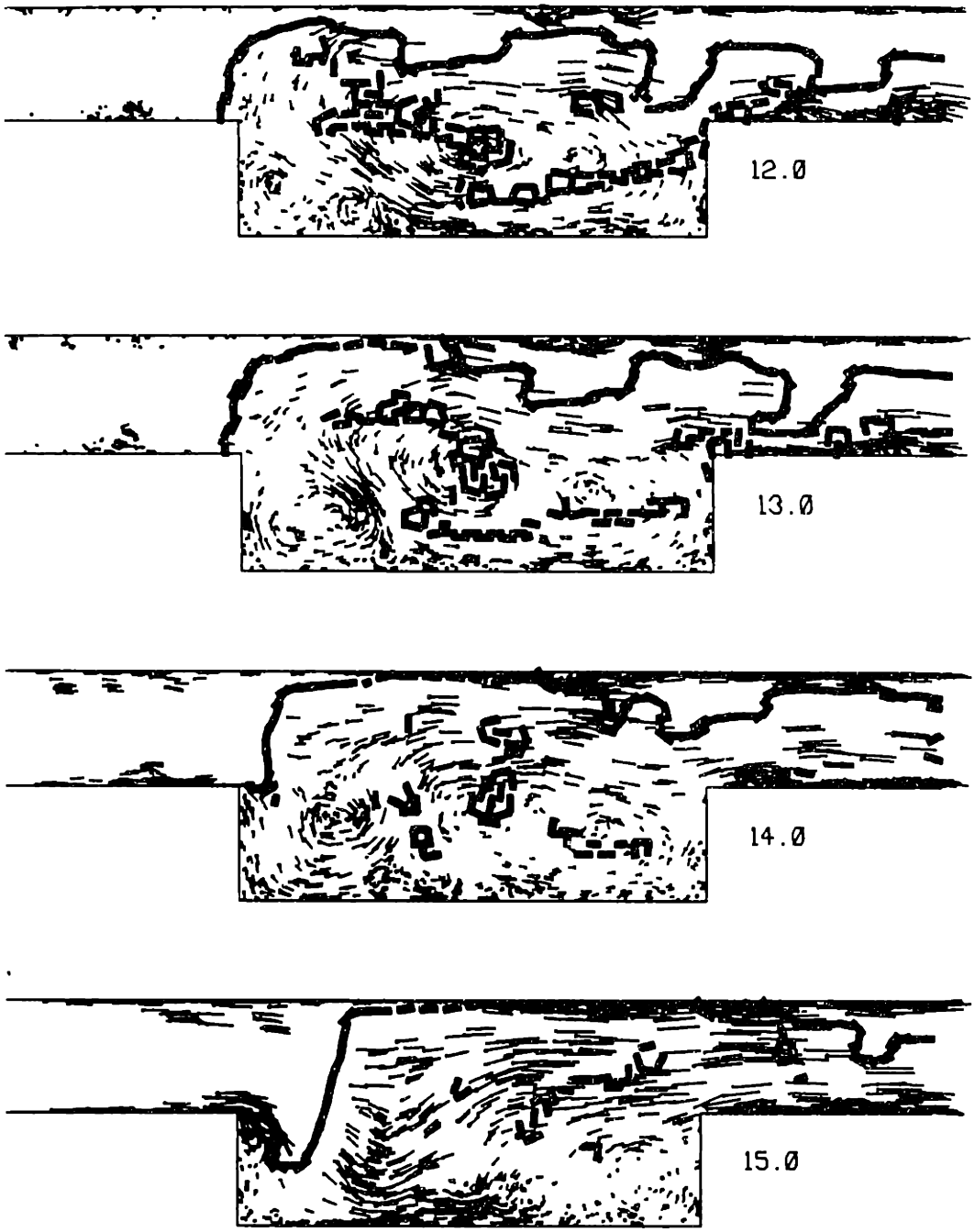

Figure 5.43 Continued on next page, caption at end of sequence.

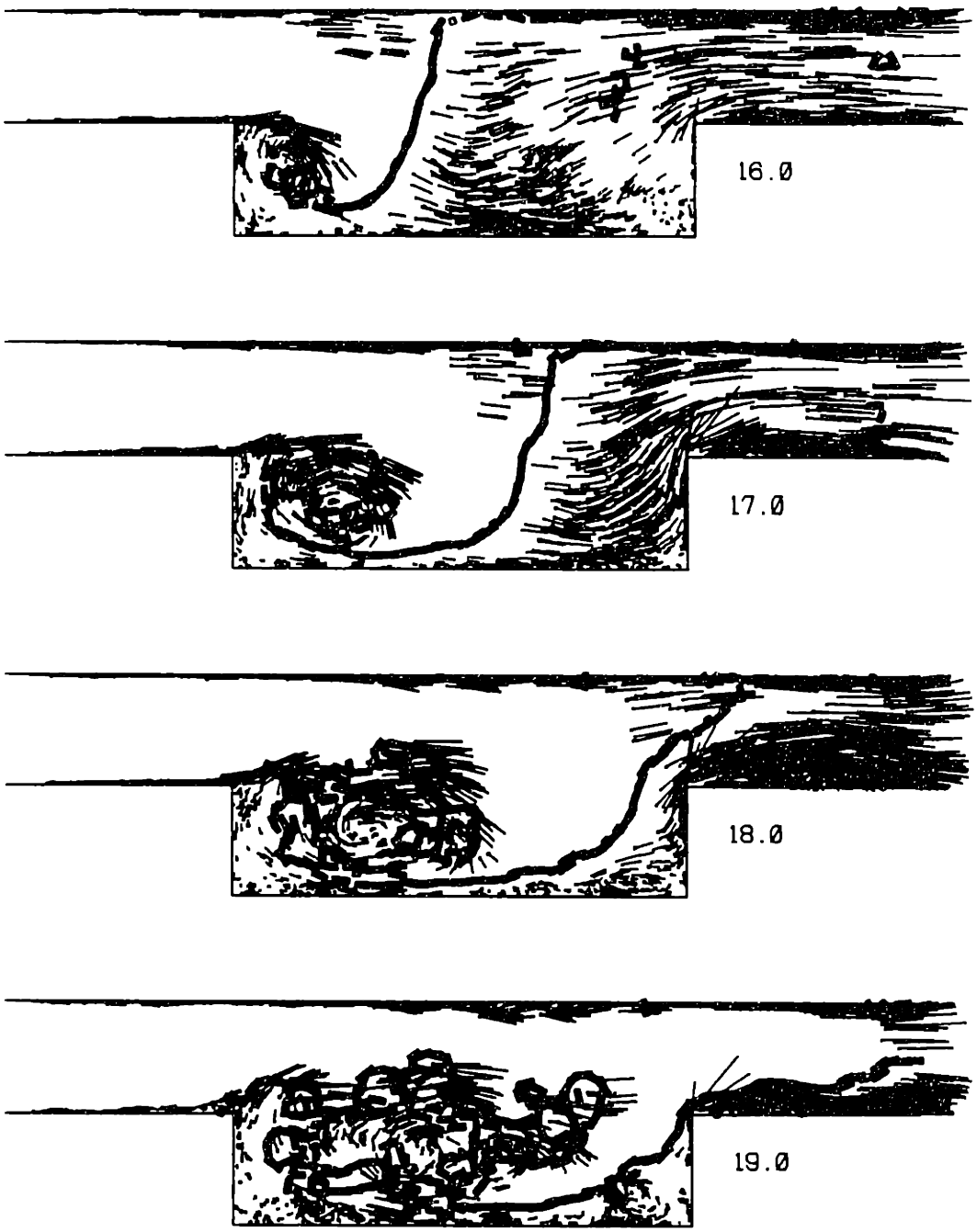

Figure 5.43 Continued on next page, caption at end of sequence.

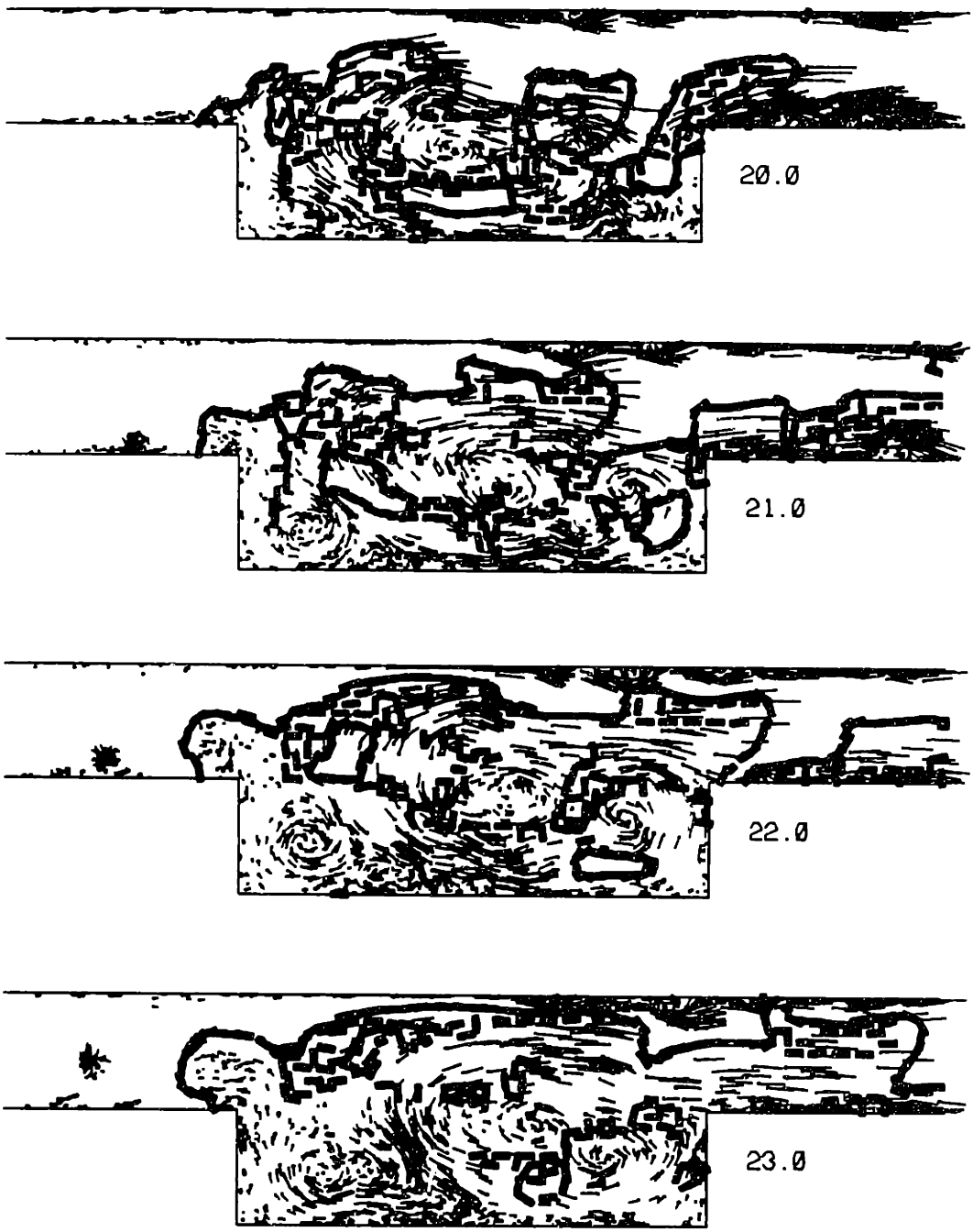

Figure 5.43 For caption see next page.

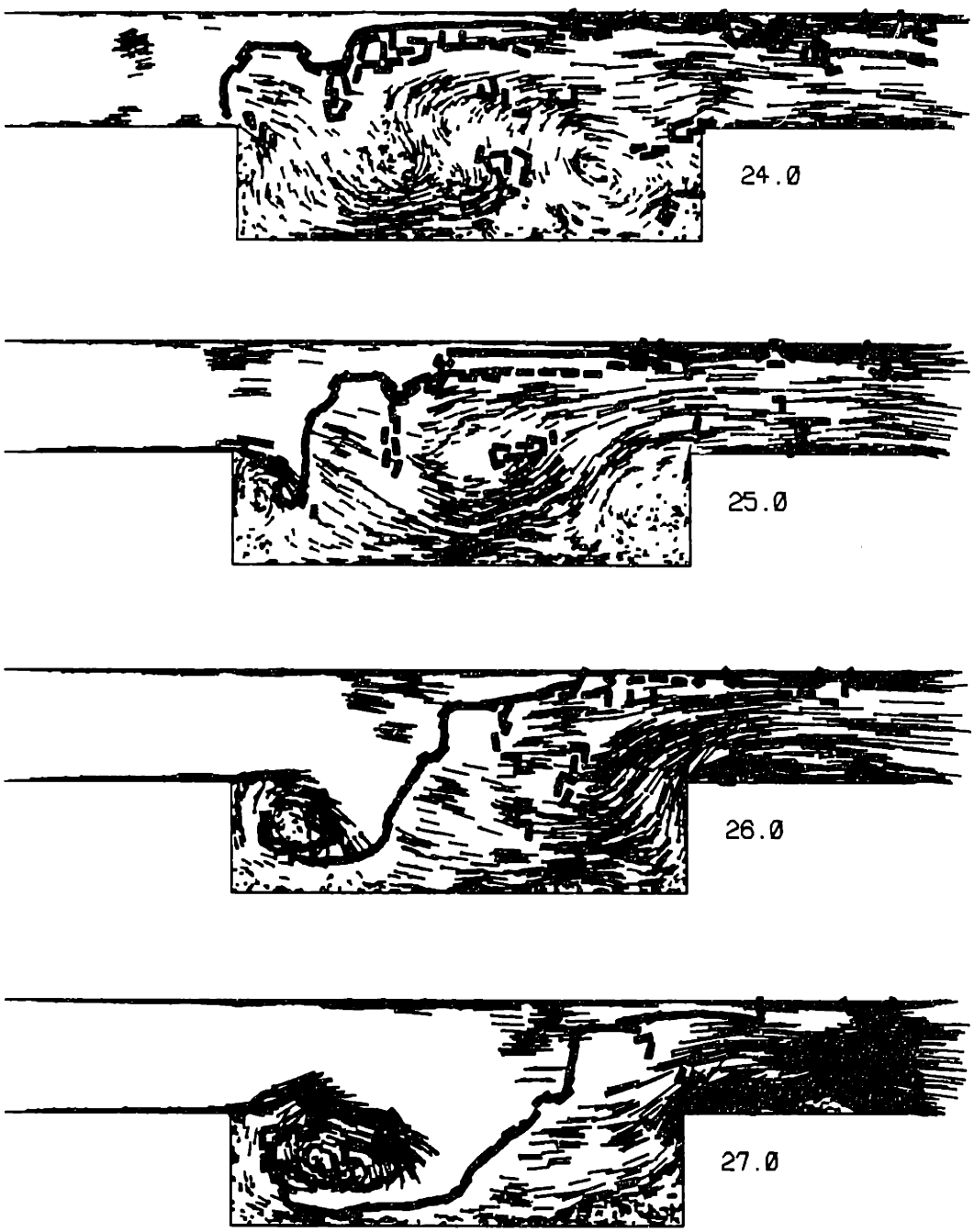

Figure 5.43 A sequence of time frames of the combustor flow field at low heat release and low forcing frequency, illustrating the large amplitude flapping of the flame, and the associated large eddy shedding. The exit pressure is a specified sinusoidal function of time, at fD/U_r=0.1.

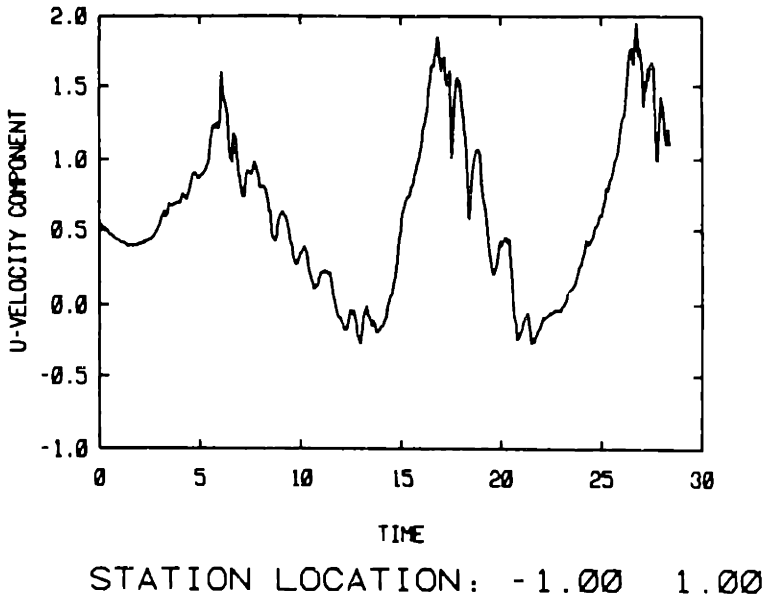

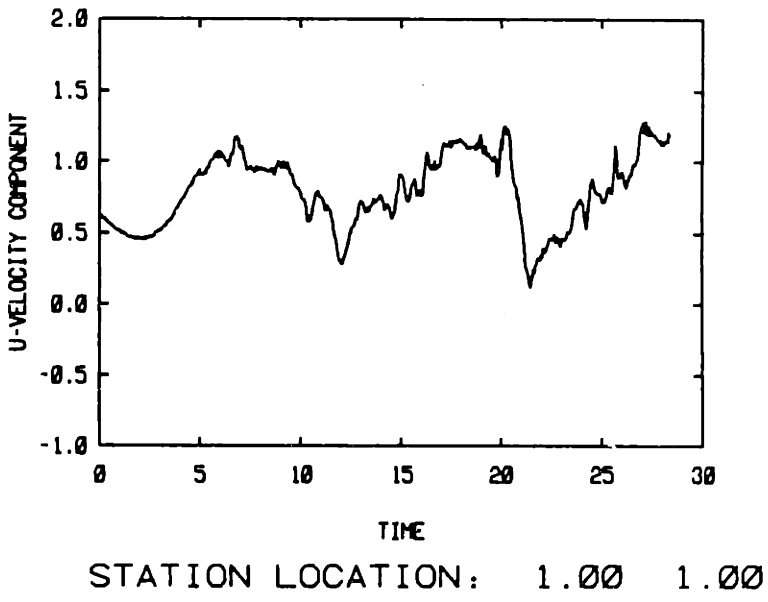

Figure 5.44 Time traces of the streamwise velocity at two points along the top of the cavity, for the flow field of Fig. 5.43. The numbers identifying the station location are the x and y coordinates, respectively.

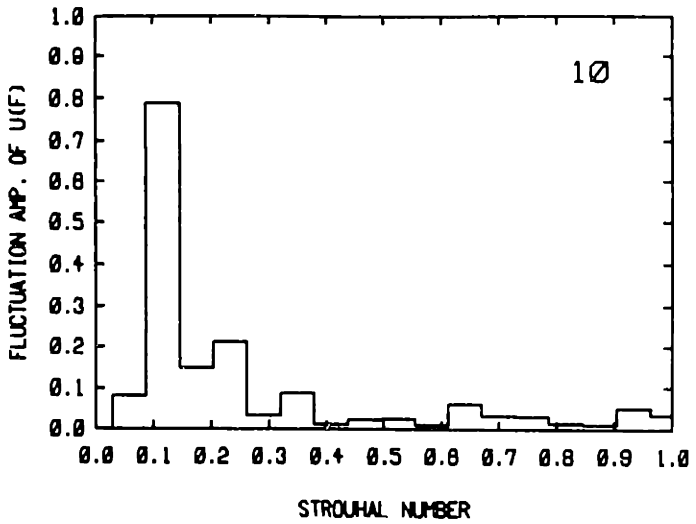

X=-1.000, PEAKS= 0.117 0.233 0.350

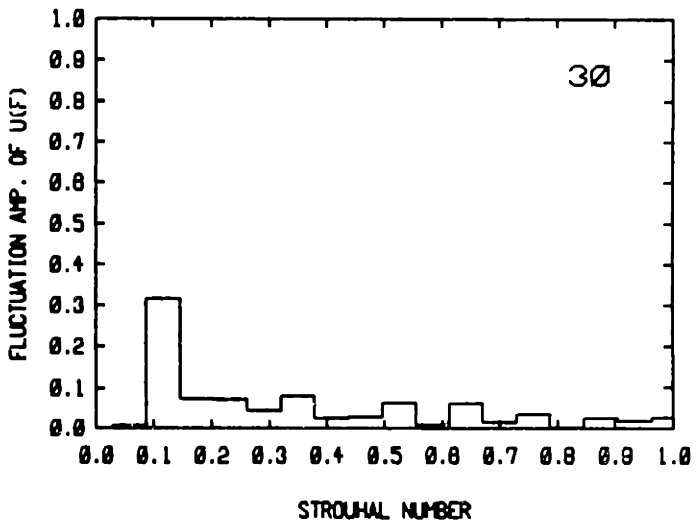

X= 1.000, PEAKS= 0.117 0.350 0.525

Figure 5.45 Spectra of the streamwise velocity fluctuation, computed from the time traces in Fig. 5.44, for the time period 8-28.4. The Strouhal number used is based on the cavity depth and the mean inlet flow velocity for the time period considered. The dominant peak is at St=0.117 in both plots.

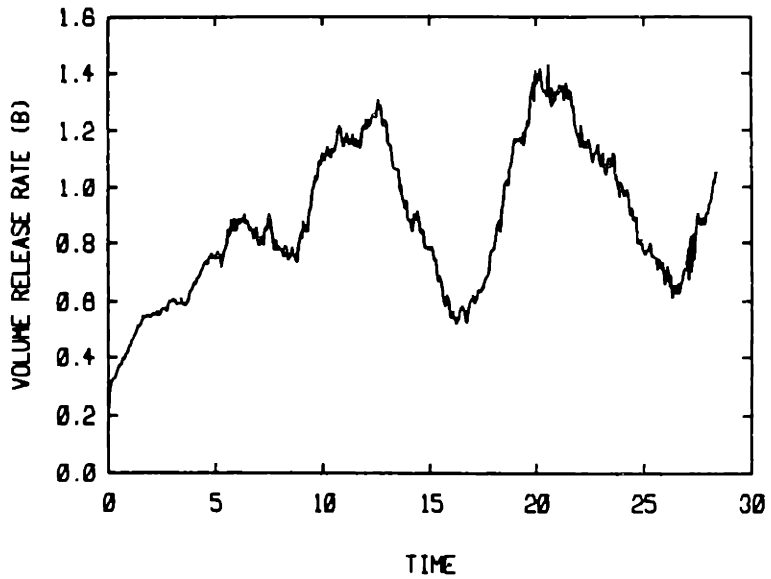

(a)

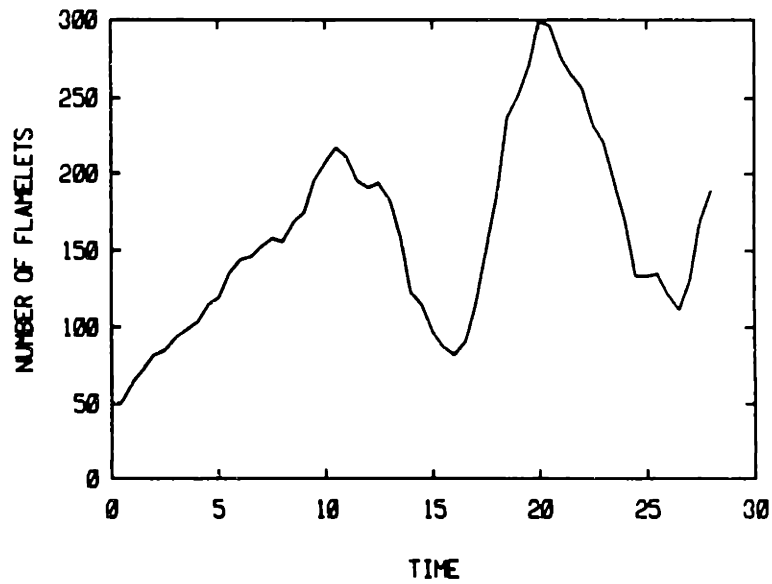

(b)

Figure 5.46 The rate of volume release (heat release) in the combustor (a), and the total number of flame segments (b), plotted against time, for the low heat release flow field of Fig. 5.43.

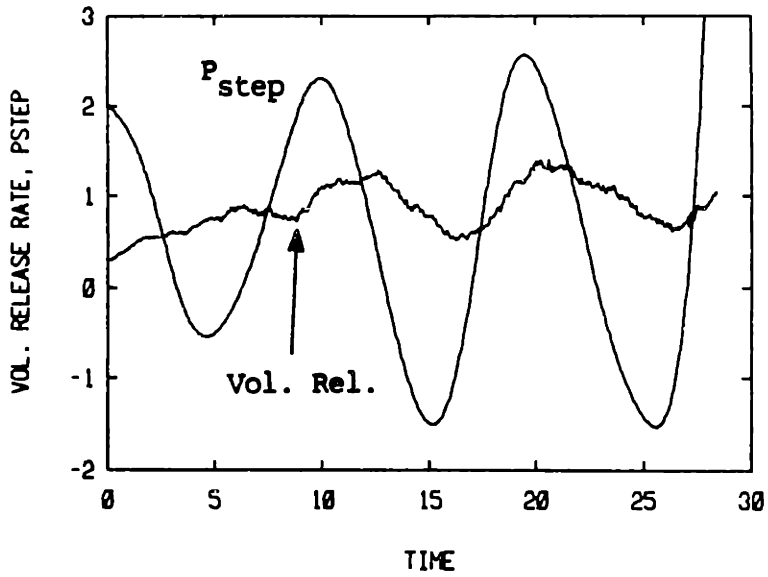

(a)

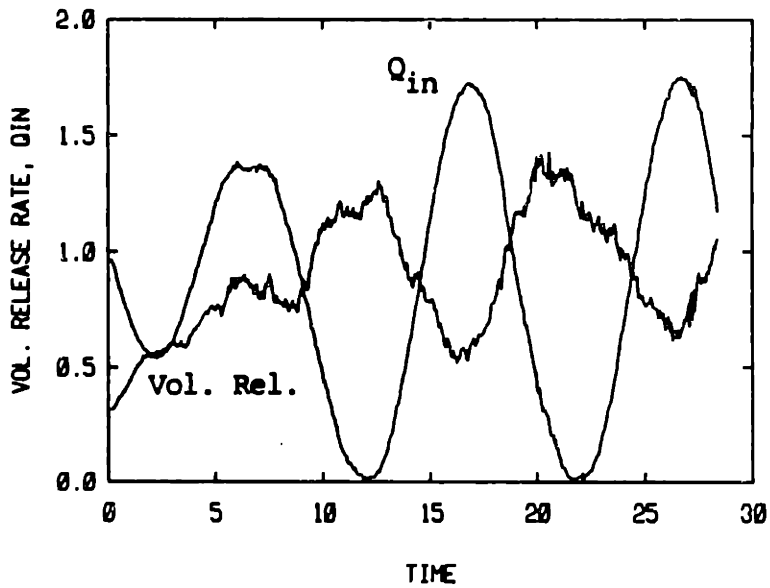

(b)

Figure 5.47 Superposition of the time traces of the rate of volume release and : (a) the step pressure, (b) the inlet flow rate. Both plots are for the low heat release flow of Fig. 5.43.

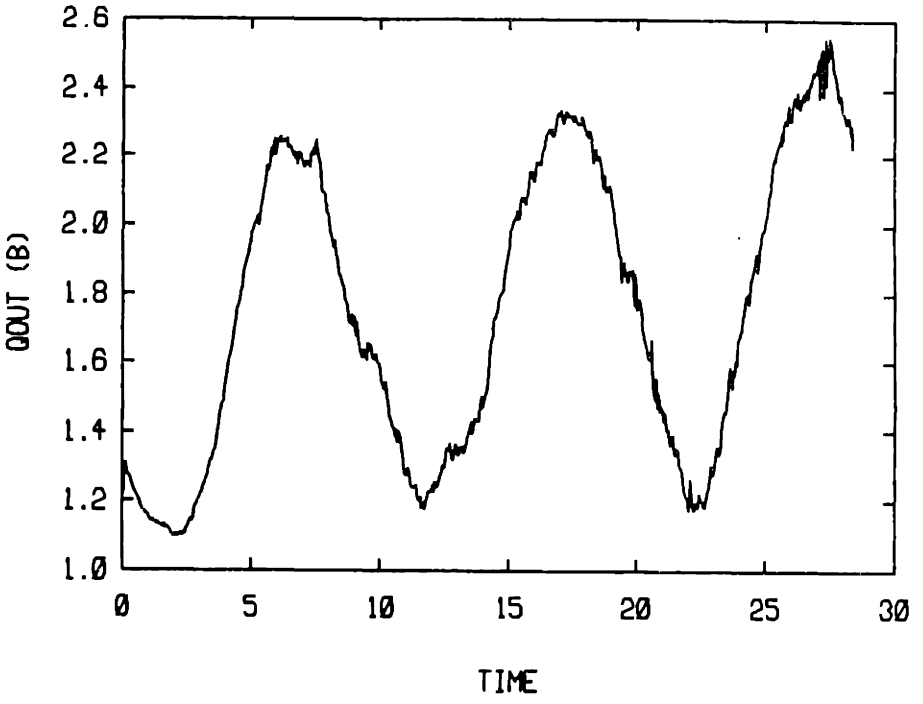

Figure 5.48 The volume flow rate out of the combustor, at xmax, plotted against time, for the low heat release flow of Fig. 5.43.

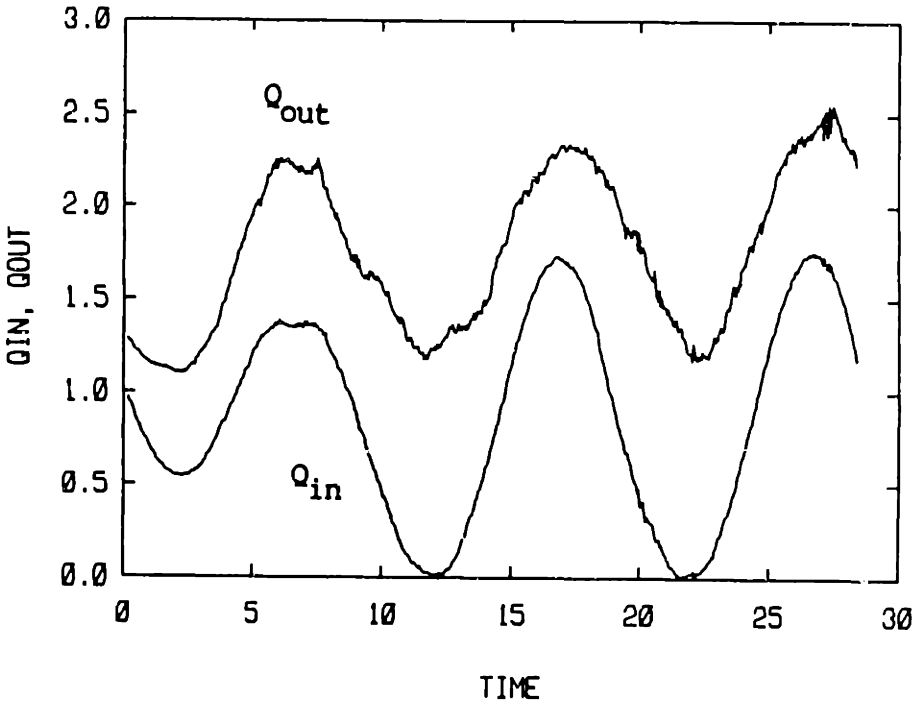

Figure 5.49 Superposition of the time traces of the inlet and exit flow rates of the combustor, for the low heat release flow of Fig. 5.43.

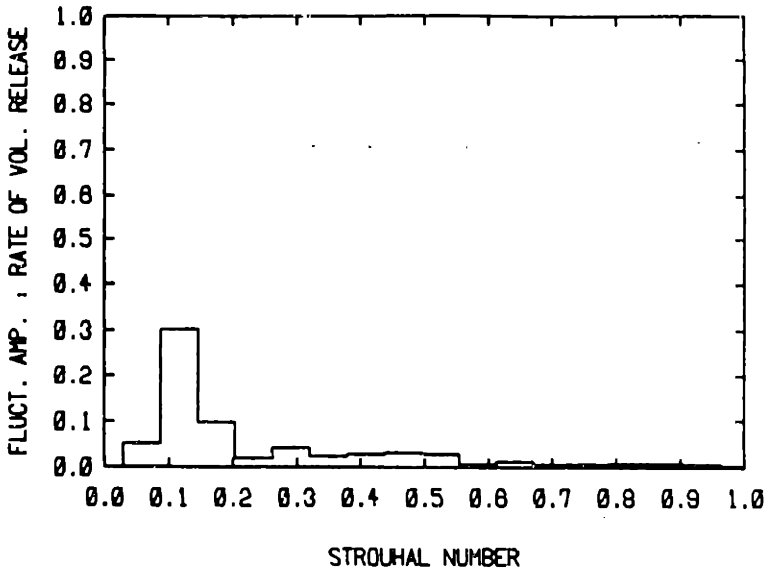

(a)

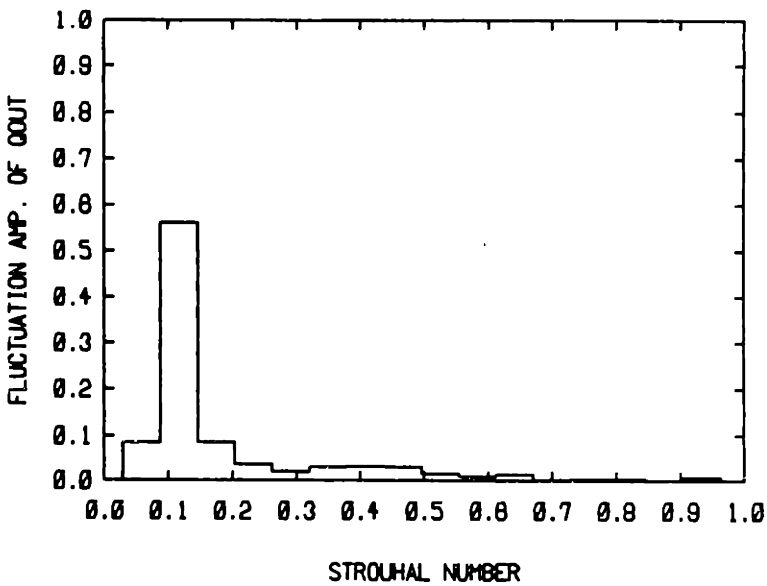

(b)

Figure 5.50 Spectra of the rate of volume release (a), and of the exit flow rate (b), for the low heat release flow of Fig. 5.43, computed from the corresponding time traces for the time period 8–28.4. The Strouhal number used is based on the cavity depth and mean inlet flow velocity. The dominant peak is at St=0.117.

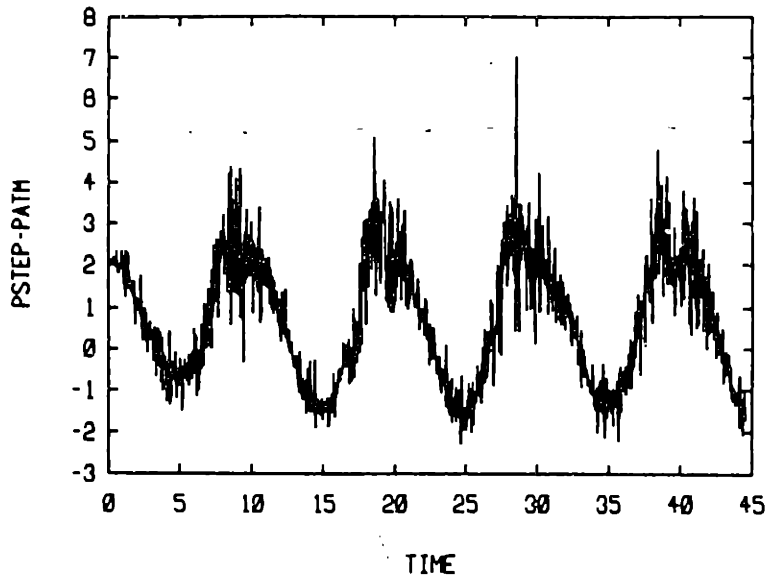

(a)

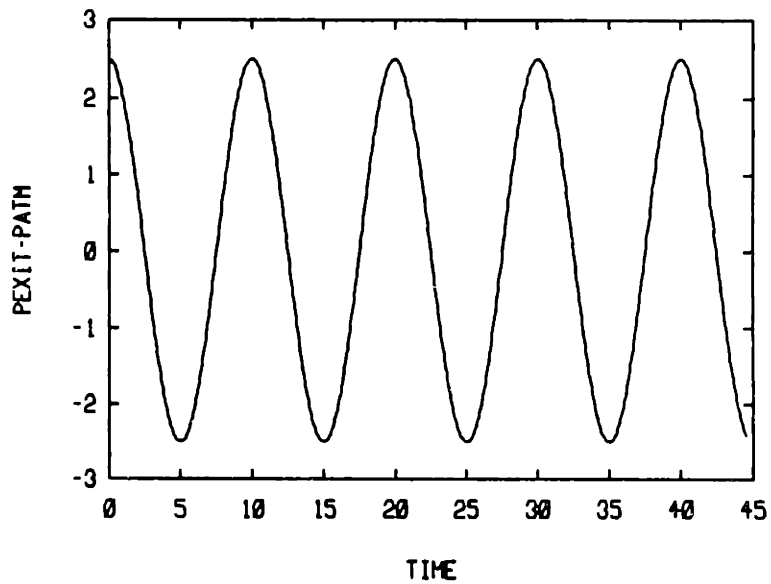

(b)

Figure 5.51 The pressure trace (channel centerline) at the upstream step (a) and the specified exit pressure trace (b) plotted versus time, for the intermediate heat release flow of Fig. 5.54 below.

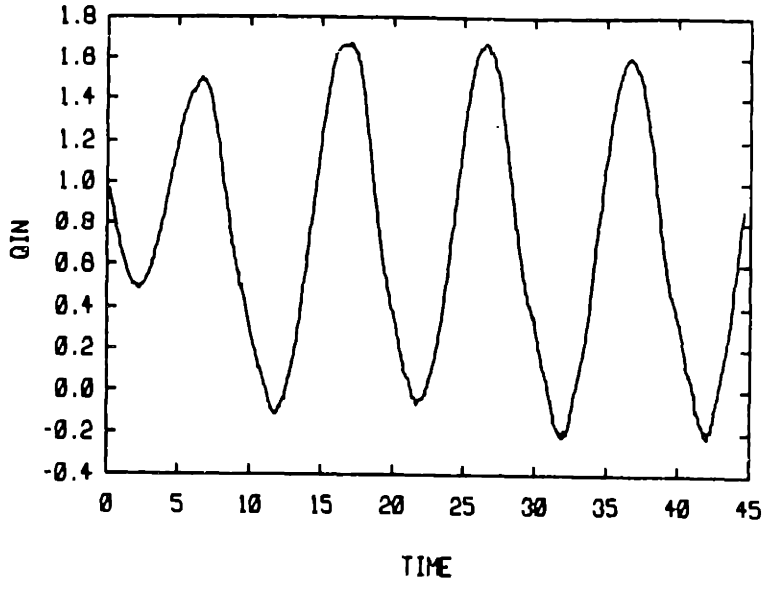

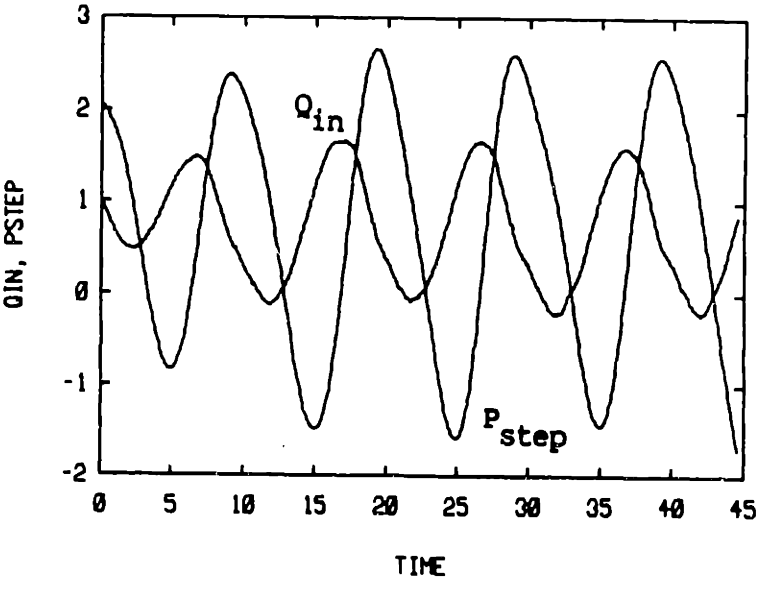

Figure 5.52 (a)- The time trace of the inlet flow rate at xmin, and (b)- the superposition of the inlet flow rate and smoothed step pressure traces, for the intermediate heat release flow of Fig. 5.54 below. The mean flow rate for the time period from 10 to 40 is 0.73.

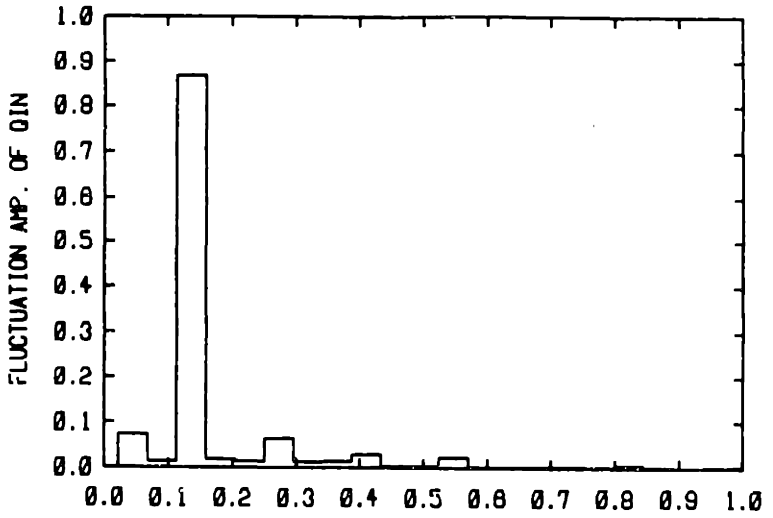

(a)

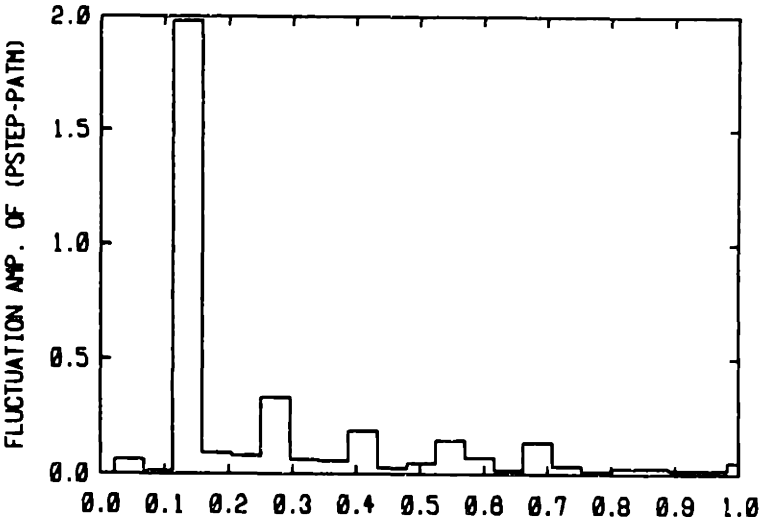

(b)

Figure 5.53 Spectra of the inlet flow rate (a) and upstream step pressure (b), computed from the corresponding time traces in figures 5.51a and 5.52a, for the time period 10-40. The Strouhal number used is based on the cavity depth and the mean inlet flow velocity for the time period considered. Both plots exhibit a dominant peak at St=0.137.

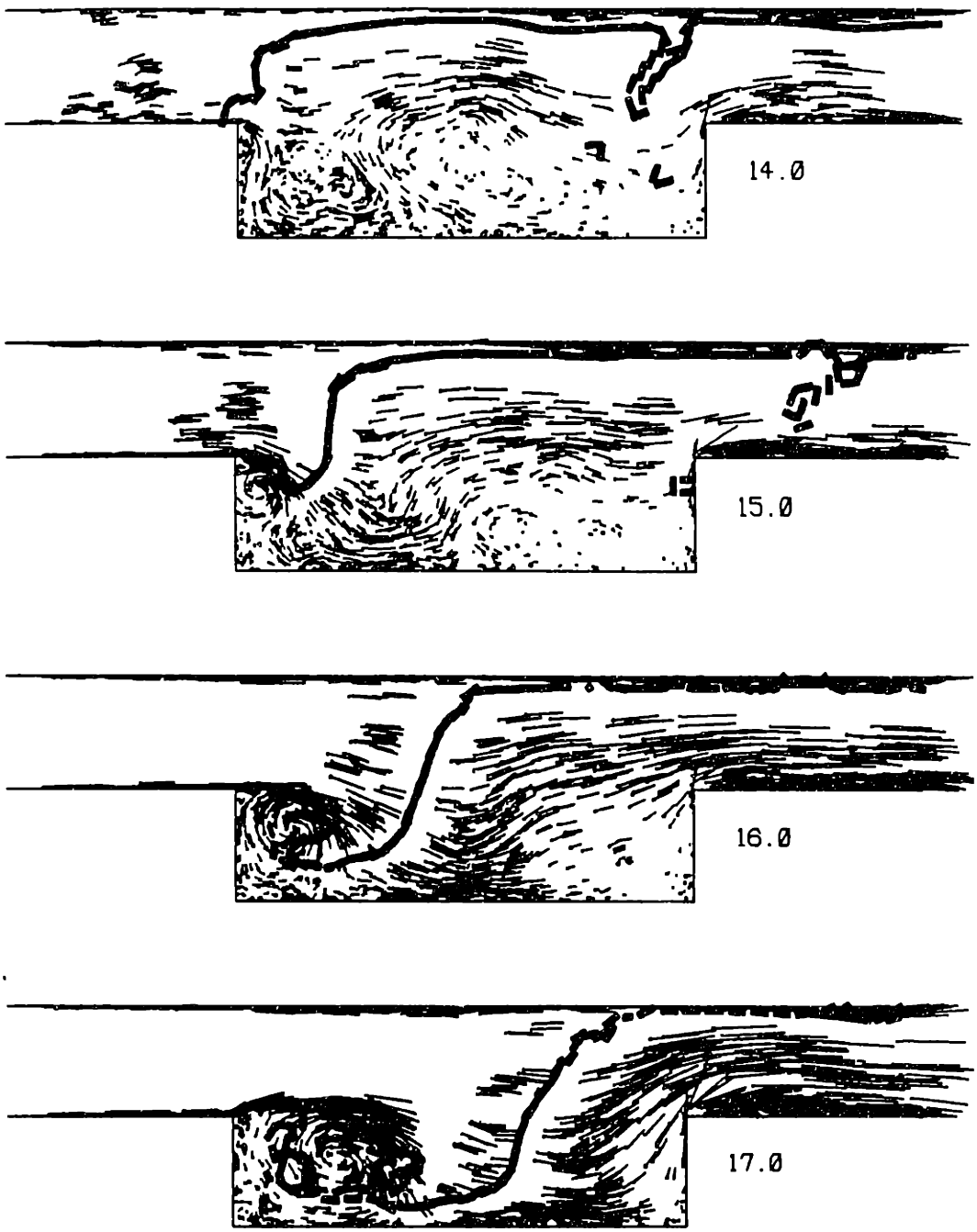

Figure 5.54 Continued on next page, caption at end of sequence.

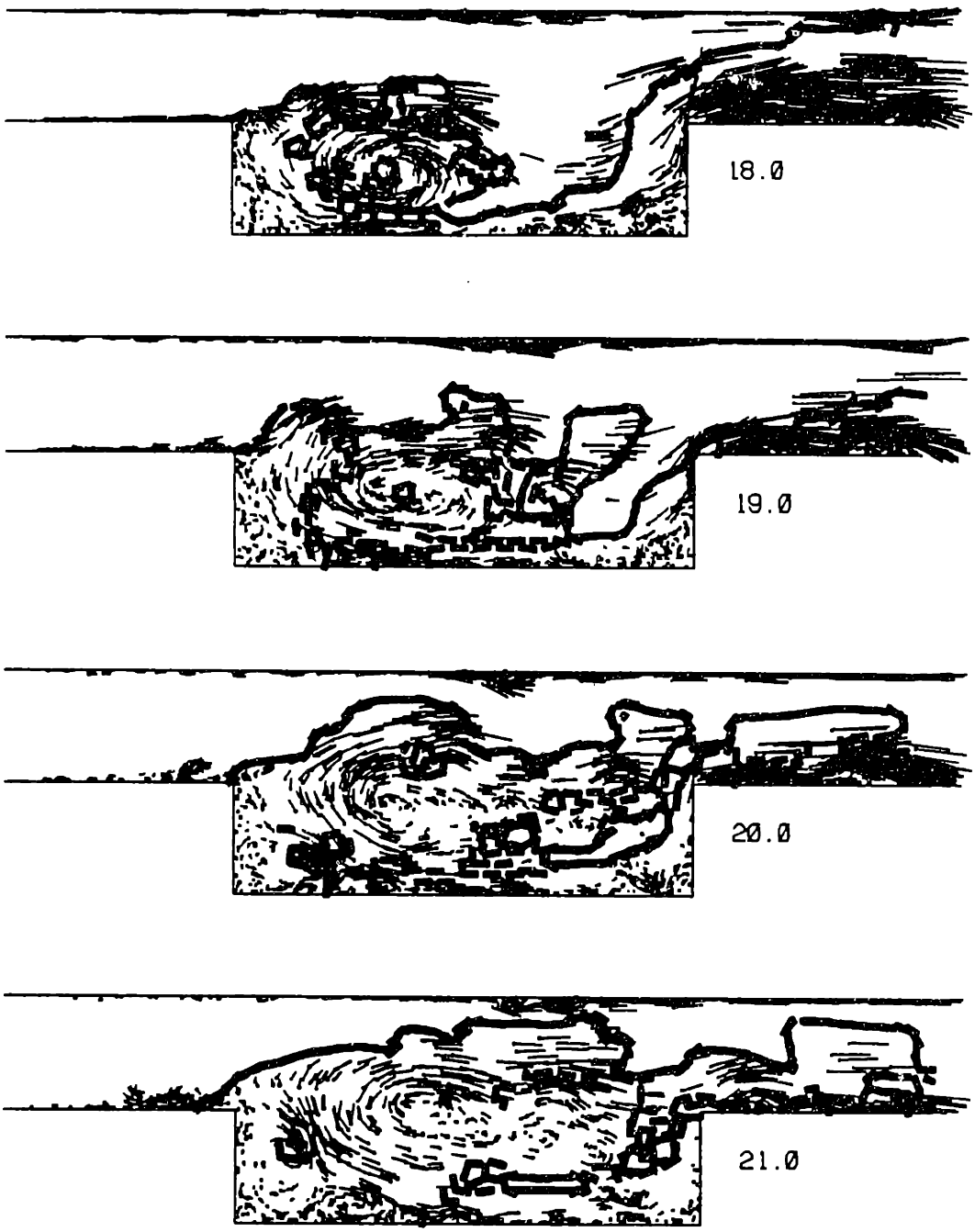

Figure 5.54 For caption see next page.

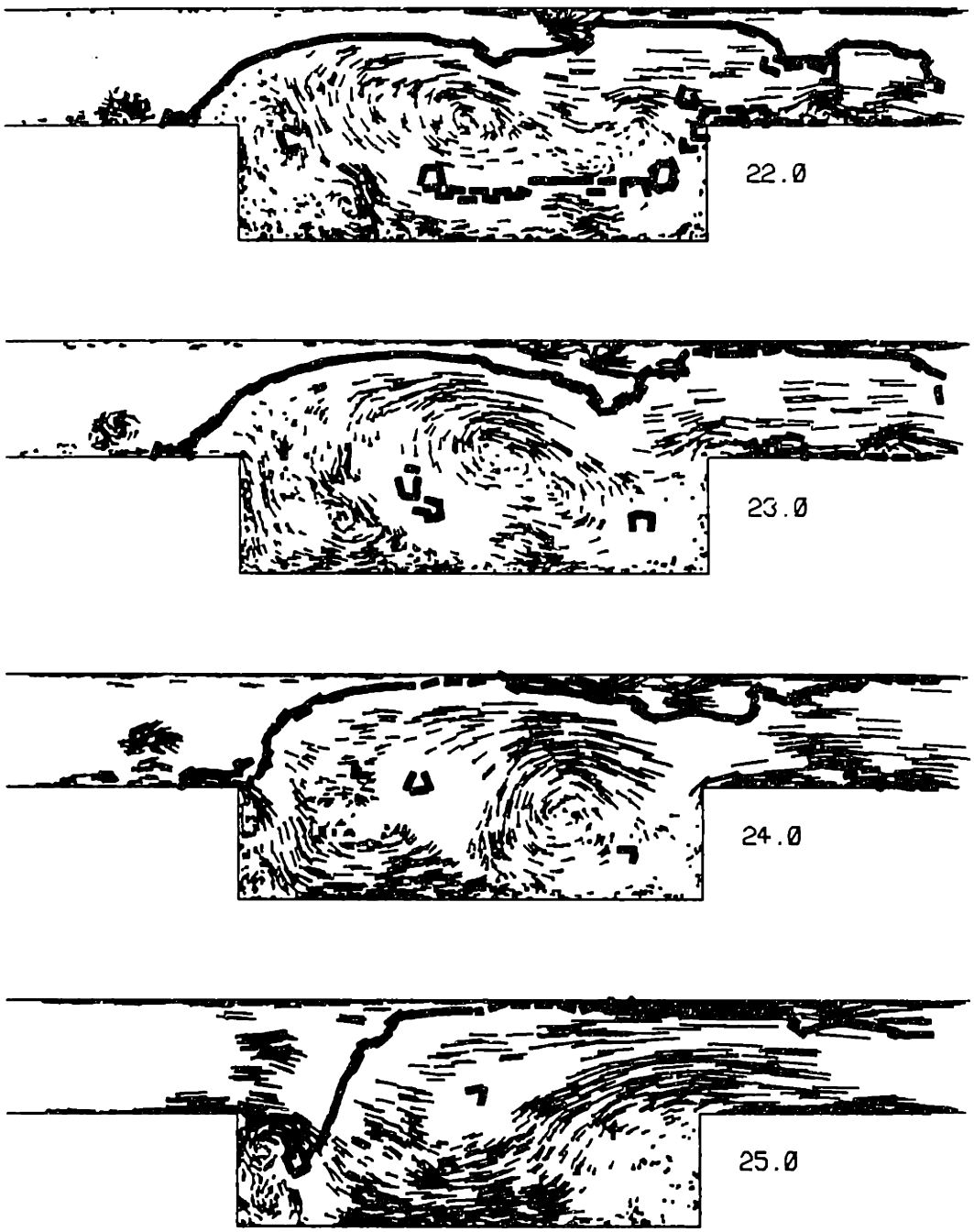

Figure 5.54 A sequence of time frames of the combustor flow field at intermediate heat release and low forcing frequency, illustrating the large amplitude flapping of the flame, and the associated large eddy shedding, and flow reversal. The exit pressure is a specified sinusoidal function of time, at $fD/U_r=0.1$.

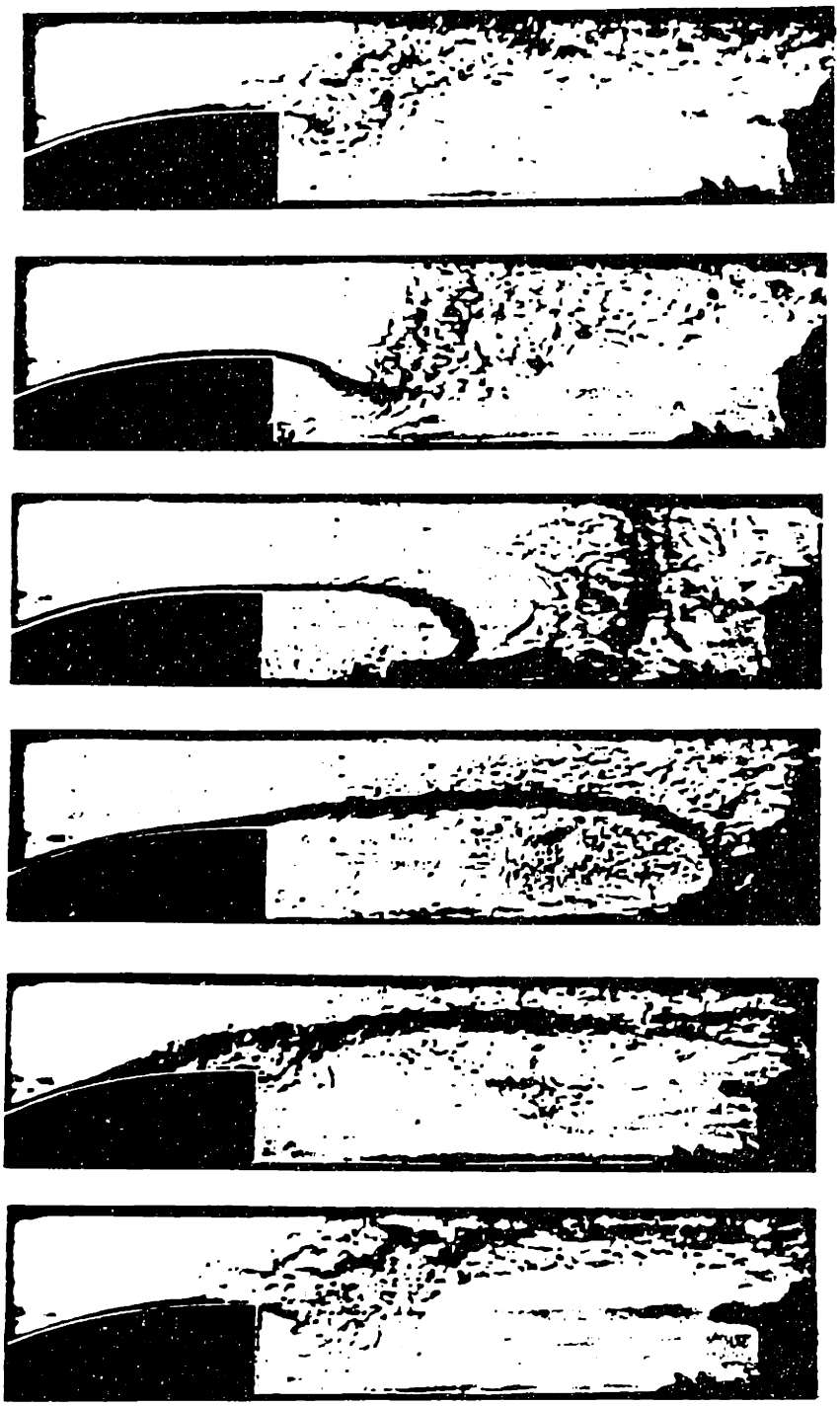

Figure 5.55 Schlieren record of large amplitude flame flapping, ϕ=0.85, time interval between frames: 4 ms. St=fD/U=0.11. Reproduced from Keller et. al. (1981).

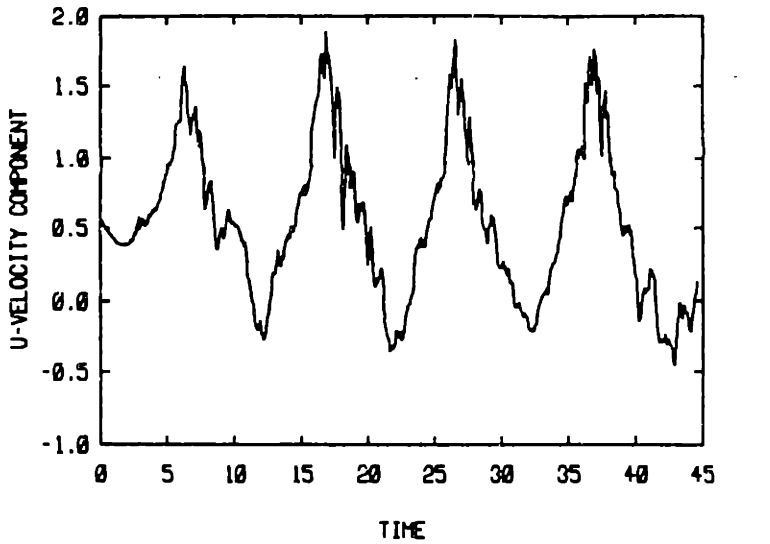

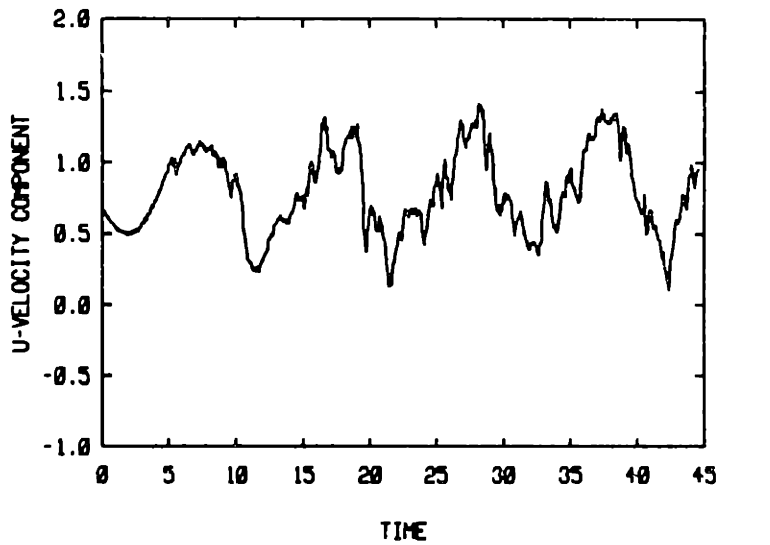

Figure 5.56 Time traces of the streamwise velocity at two points along the top of the cavity, for the flow field of Fig. 5.54. The numbers identifying the station location are the x and y coordinates, respectively.

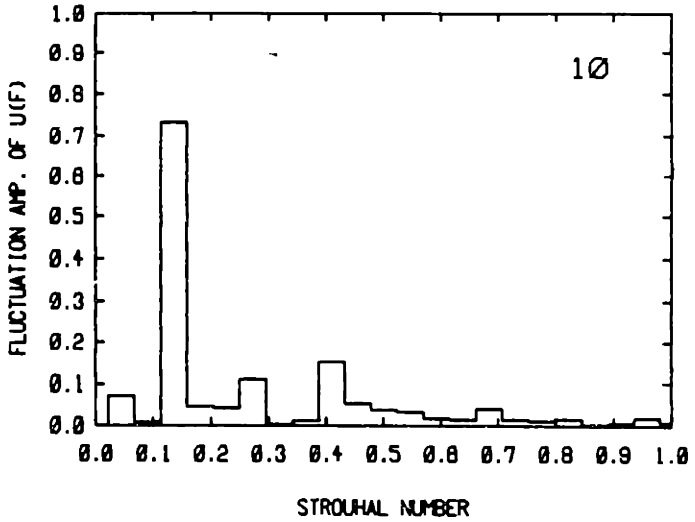

X= 1.000, PEAKS= Ø.137 Ø.411 Ø.274

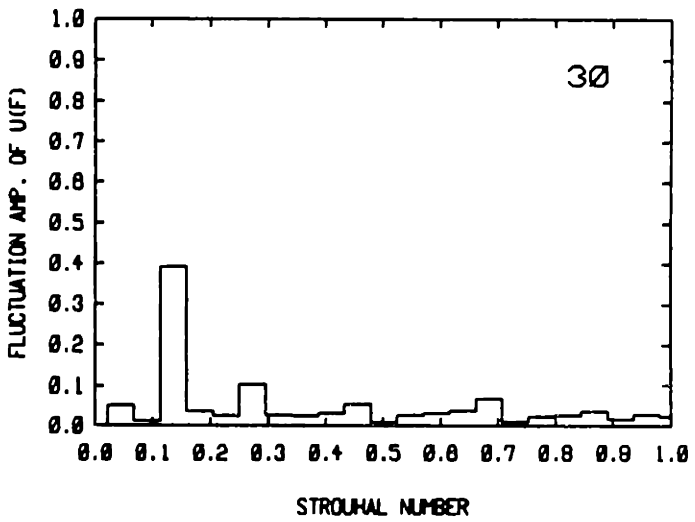

X= 1.000, PEAKS= Ø.137 Ø.274 Ø.685

Figure 5.57 Spectra of the streamwise velocity fluctuation, computed from the time traces in Fig. 5.56, for the time period 10.0–40.0. The Strouhal number used is based on the cavity depth and the mean inlet flow velocity for the time period considered. The dominant peak is at St=0.137 in both plots.

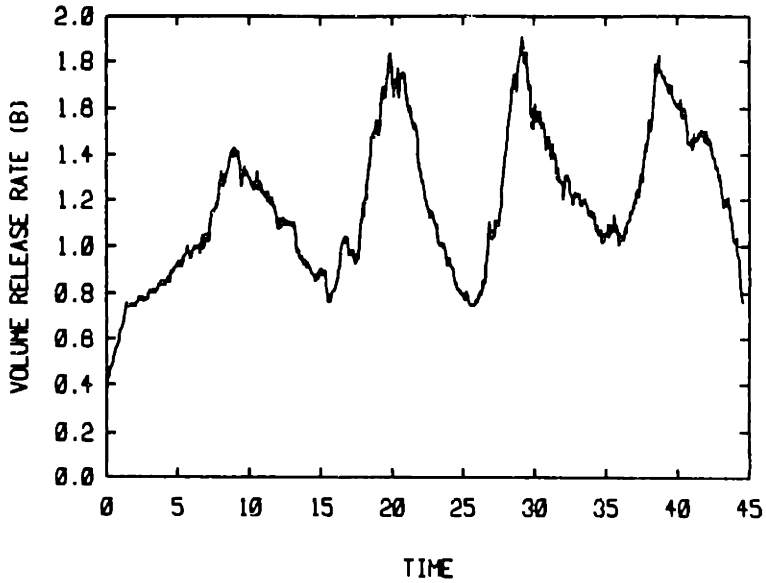

(a)

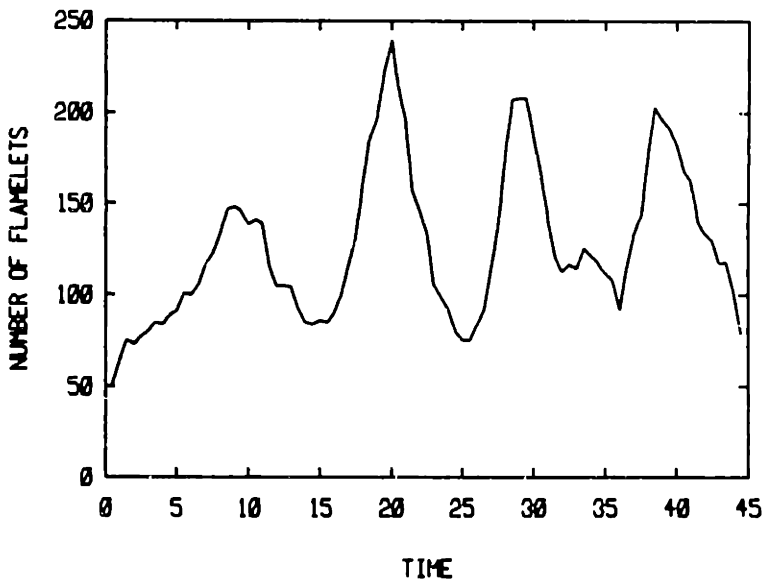

(b)

Figure 5.58 The rate of volume release (heat release) in the combustor (a), and the total number of flame segments (b), plotted against time, for the intermediate heat release flow field of Fig. 5.54.

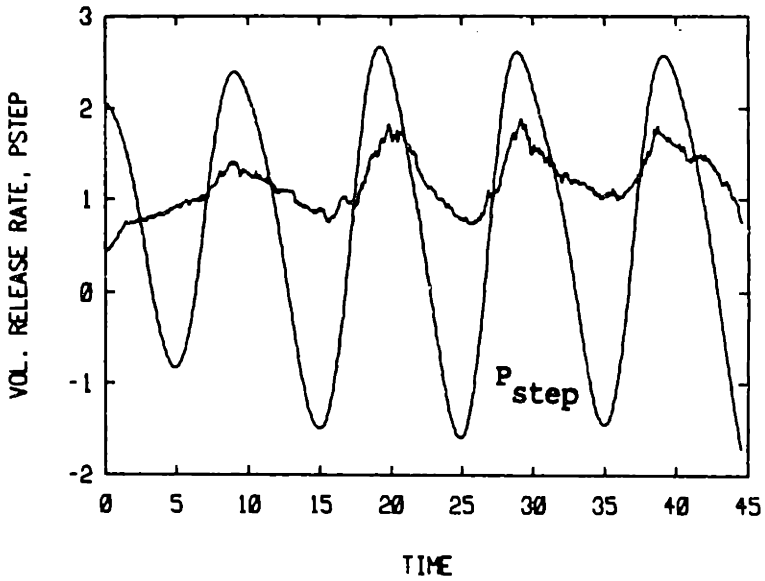

(a)

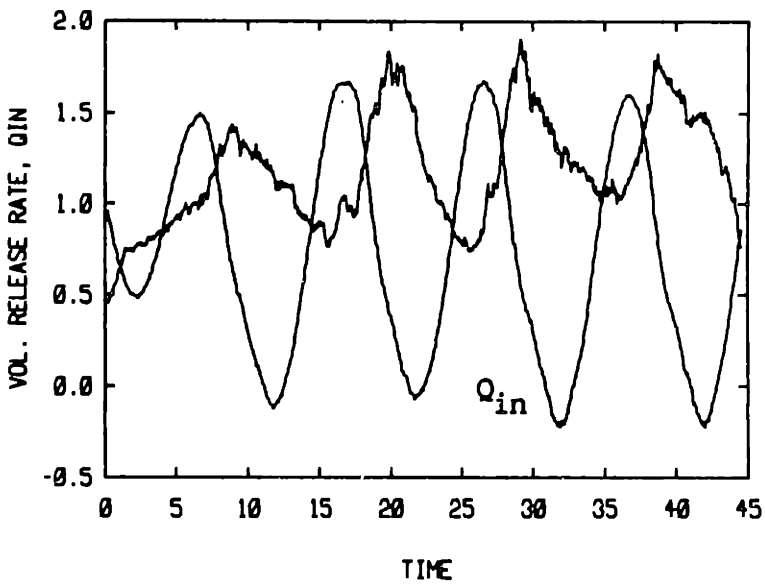

(b)

Figure 5.59 Superposition of the time traces of the rate of volume release and : (a) the step pressure, (b) the inlet flow rate. Both plots are for the intermediate heat release flow of Fig. 5.54.

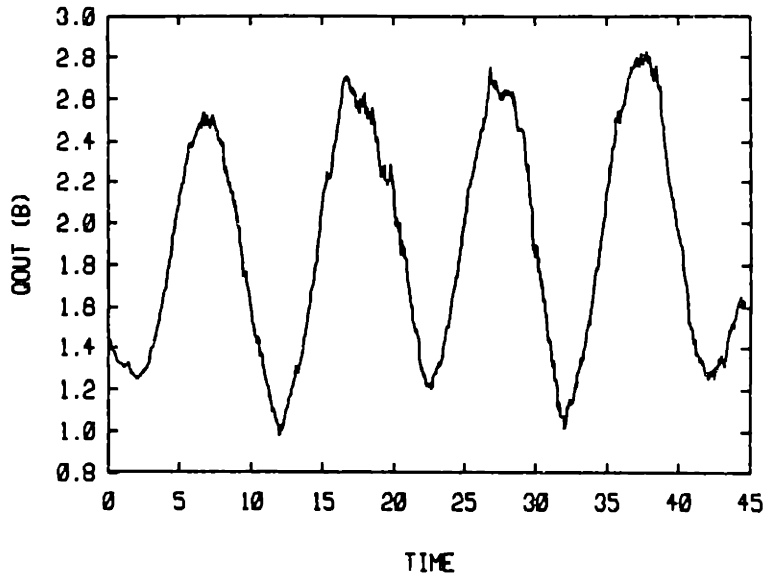

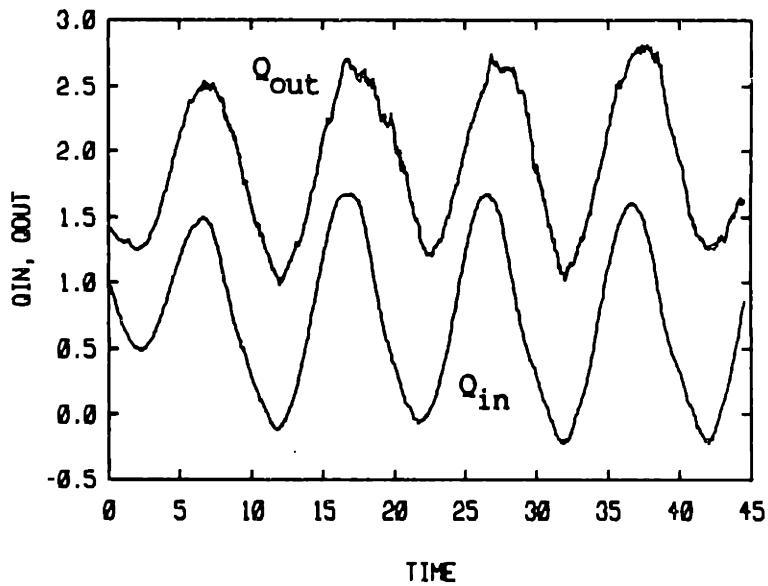

Figure 5.60 (a)- The exit flow rate plotted against time and (b)- superposed on the time trace of the inlet flow rate into the combustor, for the intermediate heat release flow of Fig. 5.54.

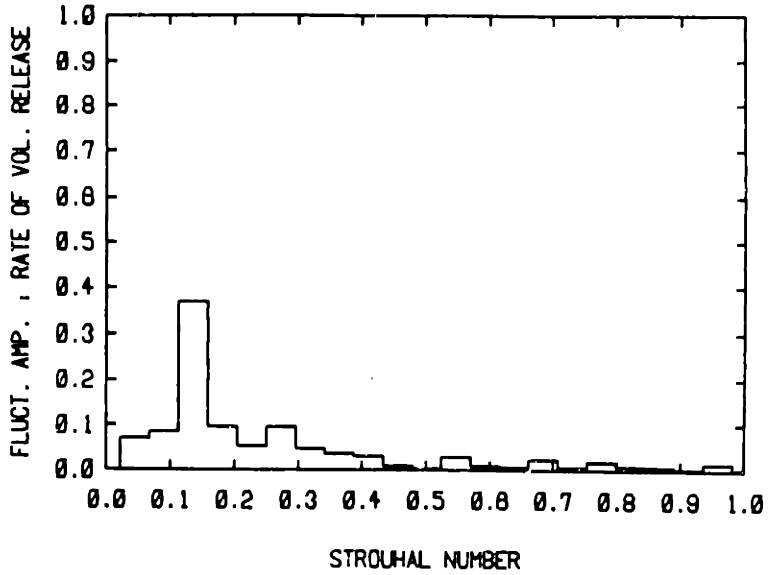

(a)

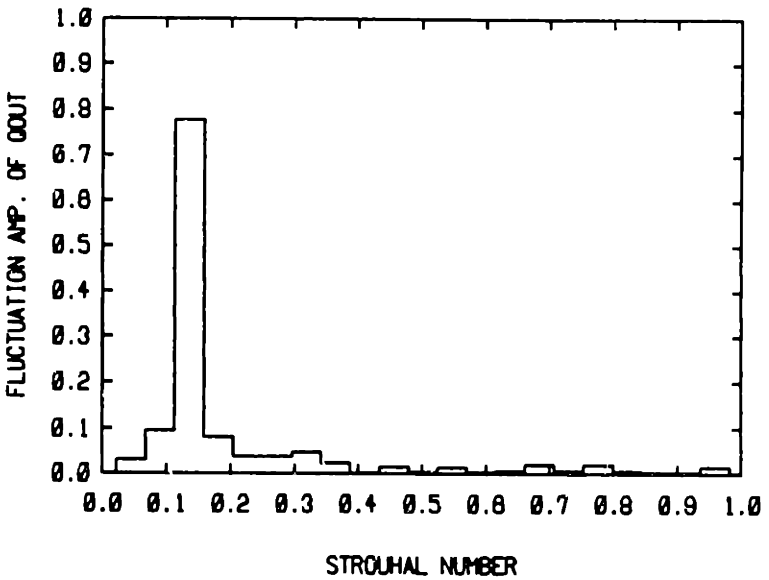

(b)

Figure 5.61 Spectra of the rate of volume release (a), and of the exit flow rate (b), for the intermediate heat release flow of Fig. 5.54, computed from the corresponding time traces for the time period 10-40. The Strouhal number used is based on the cavity depth and mean inlet flow velocity. The dominant peak is at St=0.137.

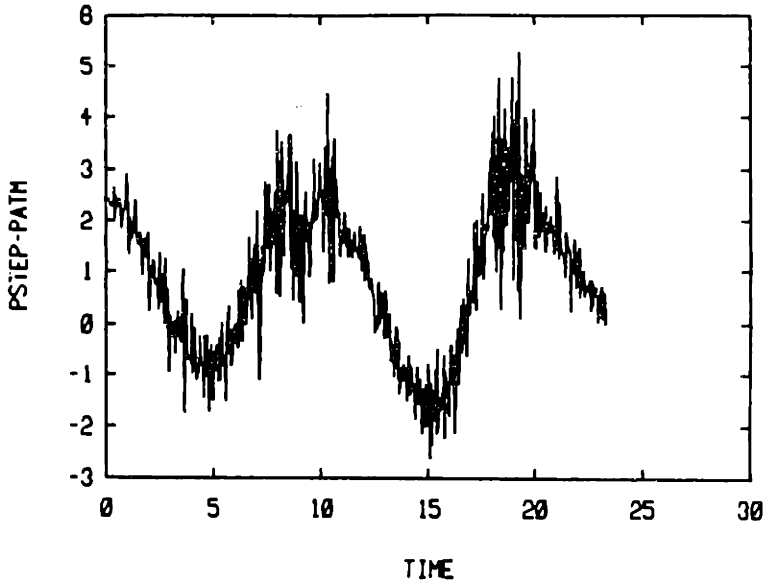

(a)

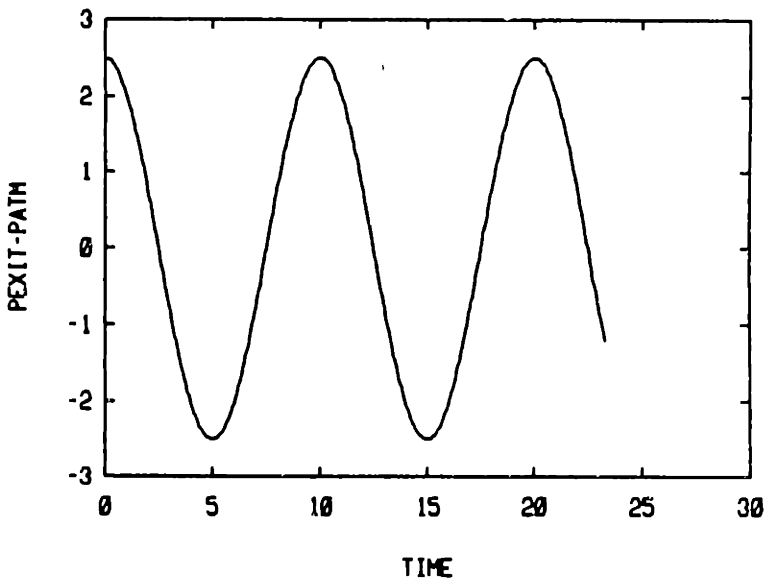

(b)

Figure 5.62 The pressure trace (channel centerline) at the upstream step (a) and the specified exit pressure trace (b) plotted versus time, for the high heat release flow of Fig. 5.64 below.

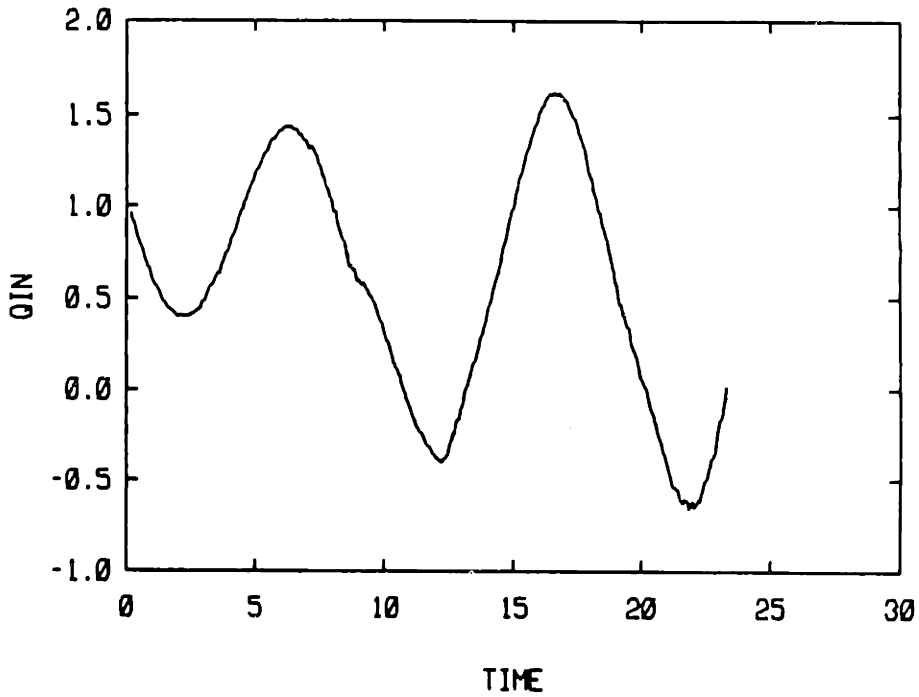

Figure 5.63 The time trace of the inlet flow rate at xmin, for the high heat release flow of Fig. 5.64 below. The mean flow rate for the time period from 3.0 to 23.3, is 0.57.

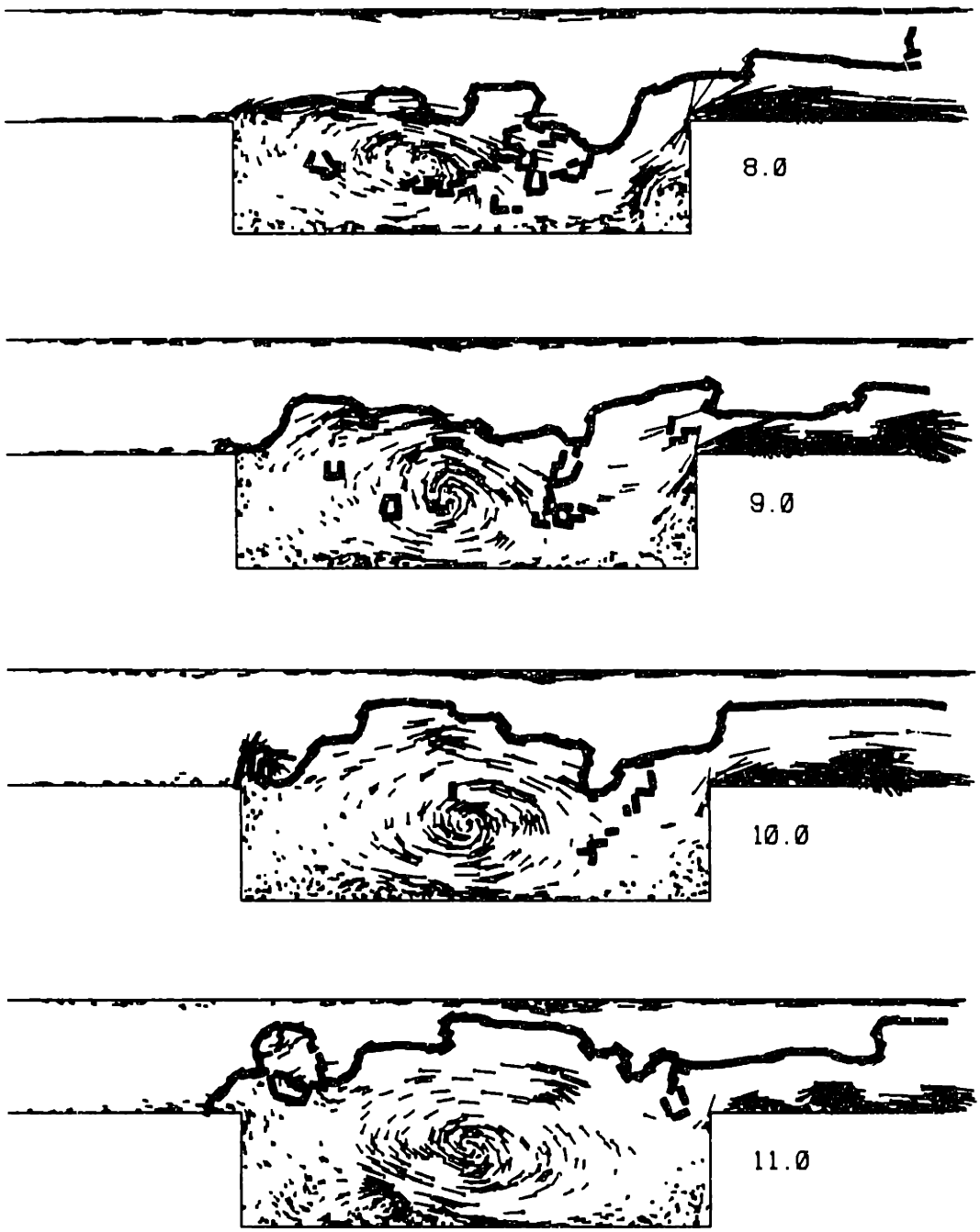

Figure 5.64 Continued on next page, caption at end of sequence.

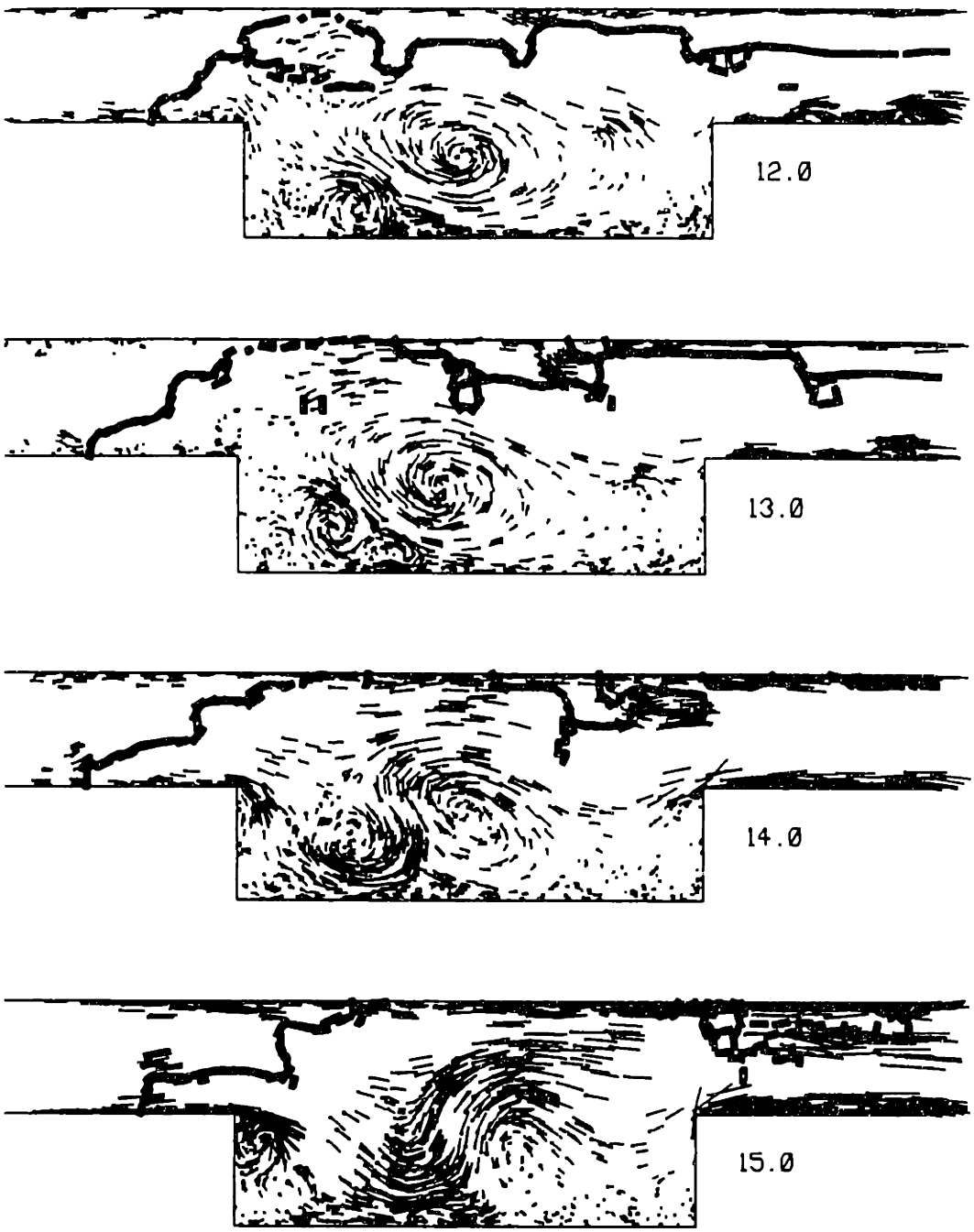

Figure 5.64 Continued on next page, caption at end of sequence.

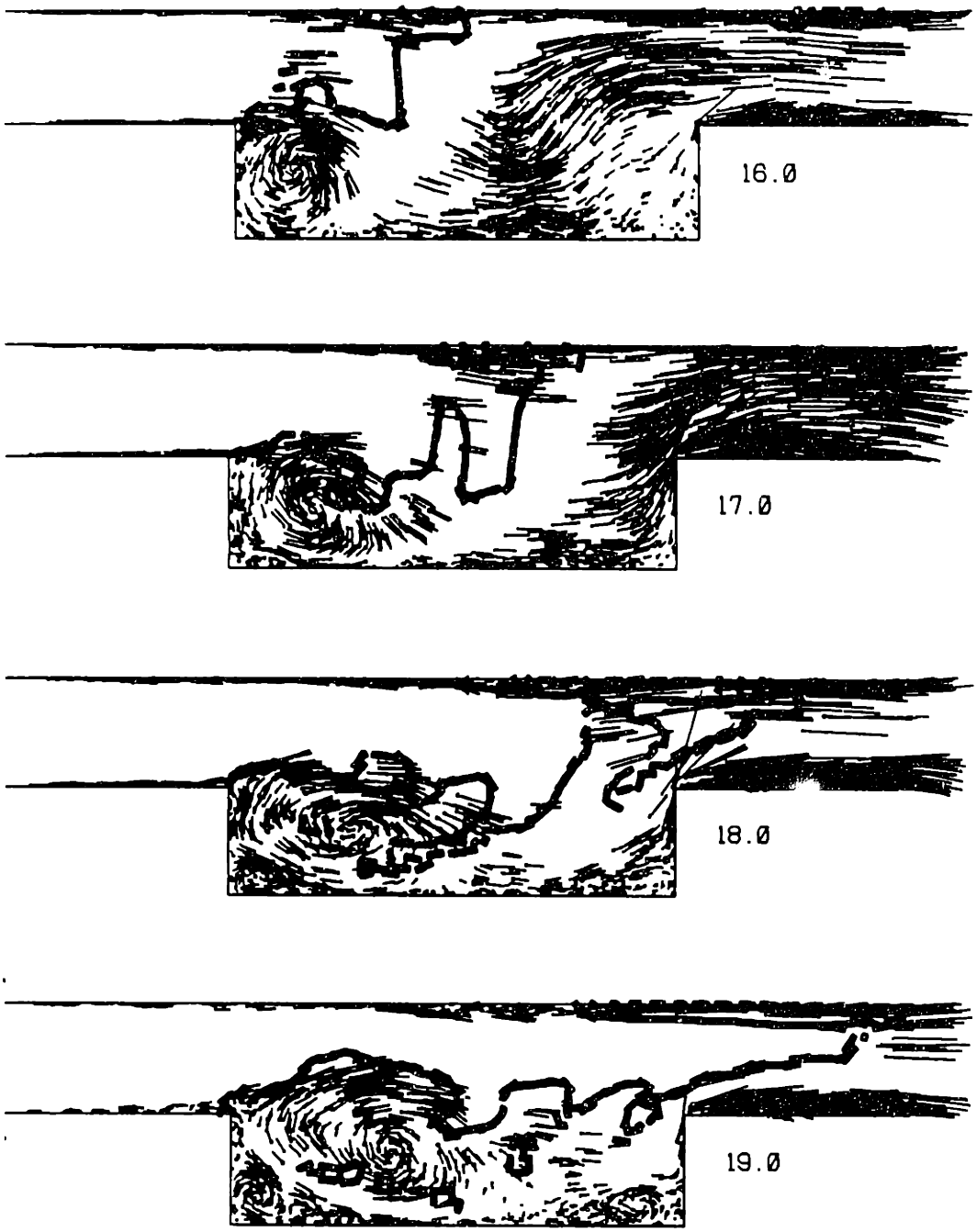

Figure 5.64 For caption see next page.

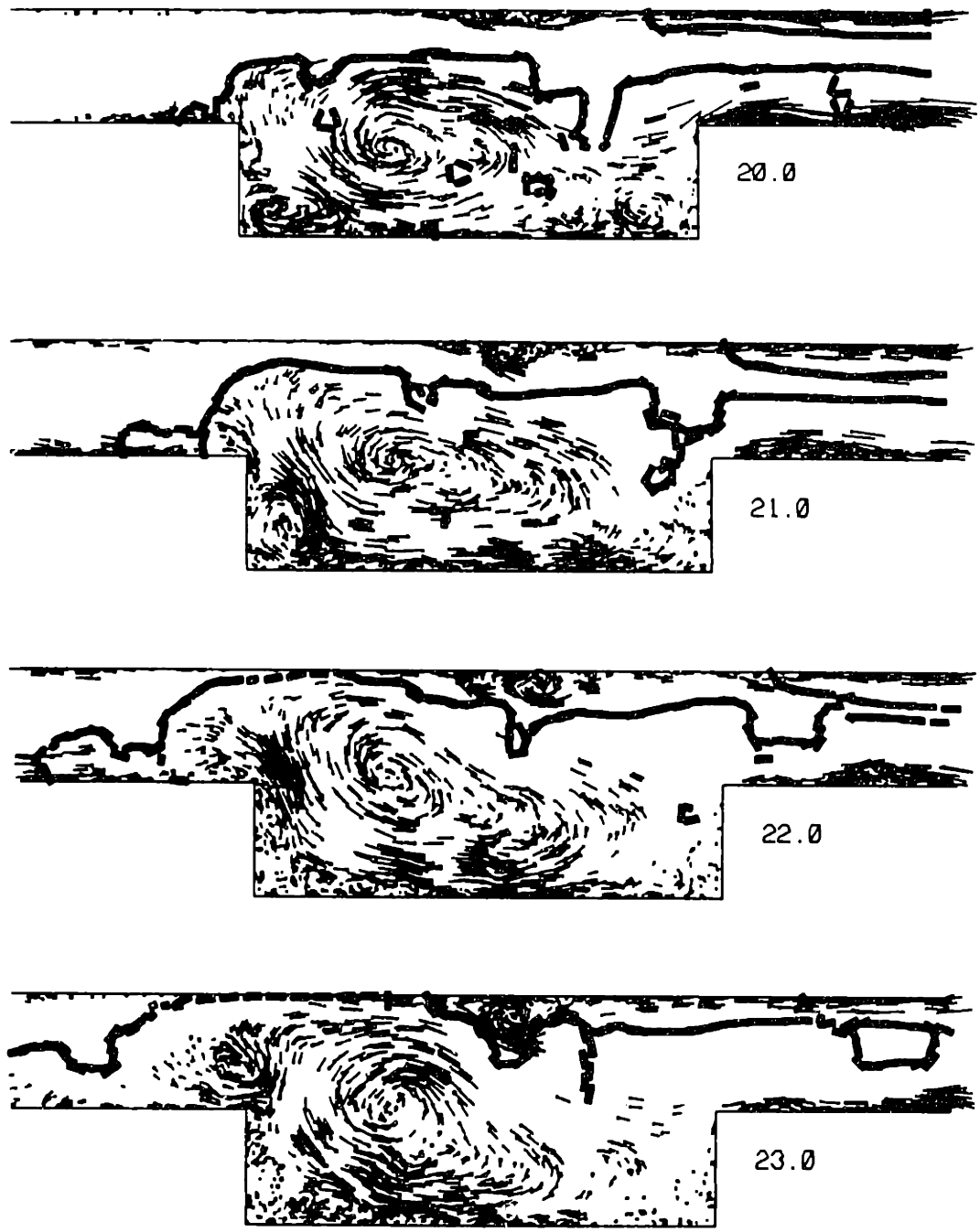

Figure 5.64 A sequence of time frames of the combustor flow field at high heat release and low forcing frequency, illustrating the large amplitude flapping of the flame, and the associated large eddy shedding, and flow reversal. The exit pressure is a specified sinusoidal function of time, at $fD/U_r=0.1$.

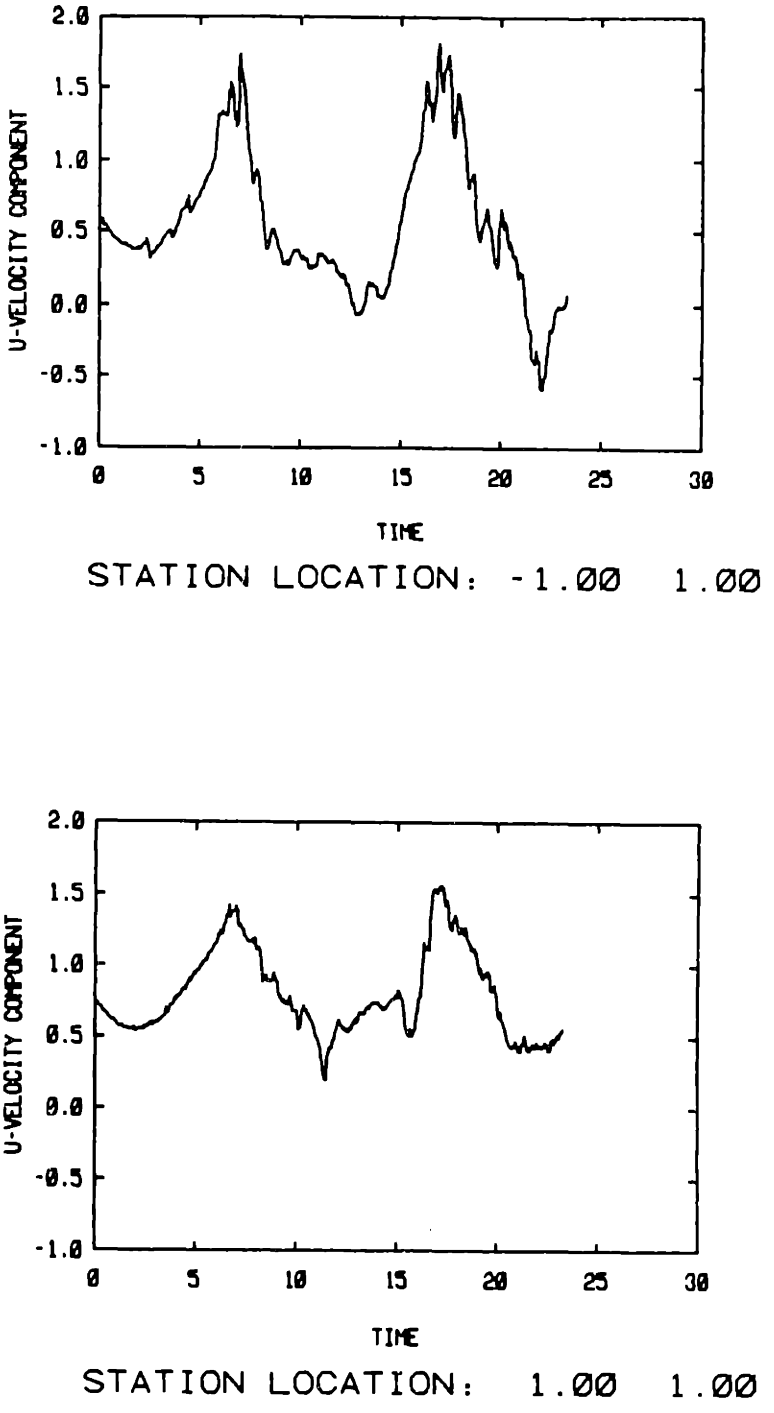

Figure 5.65 Time traces of the streamwise velocity at two points along the top of the cavity, for the flow field of Fig. 5.64. The numbers identifying the station location are the x and y coordinates, respectively.

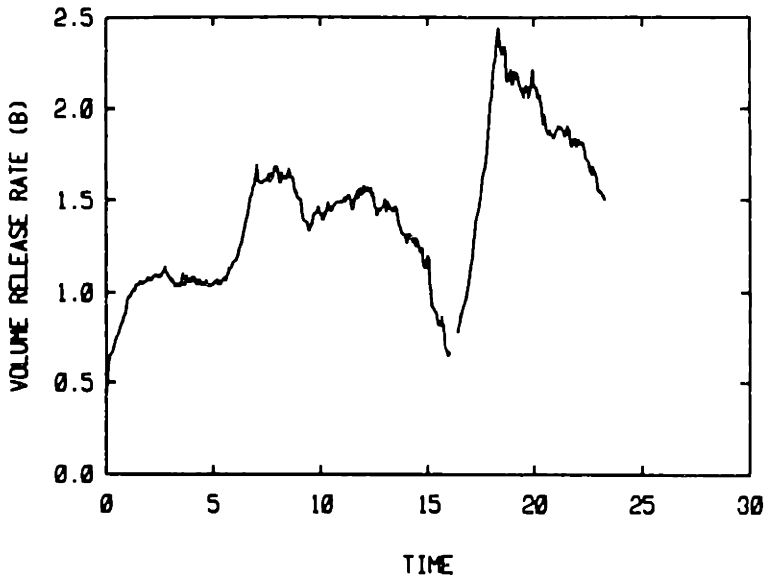

(a)

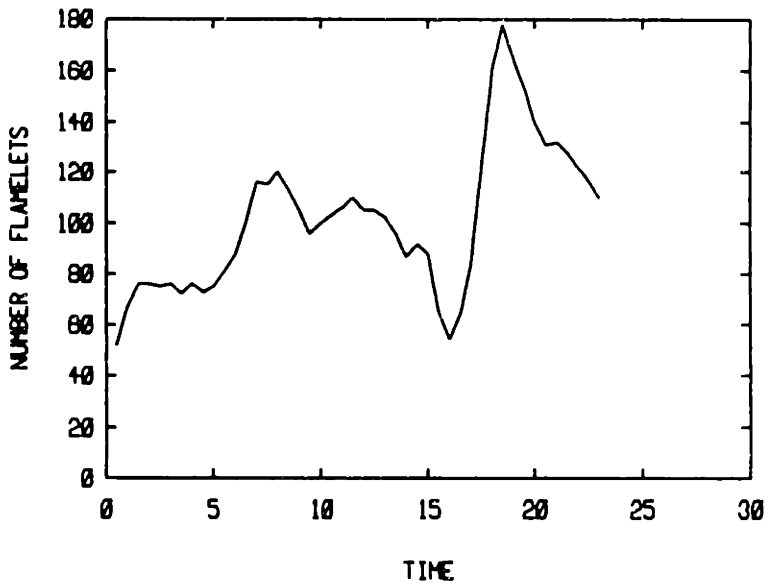

(b)

Figure 5.66 The rate of volume release (heat release) in the combustor (a), and the total number of flame segments (b), plotted against time, for the high heat release flow field of Fig. 5.64.

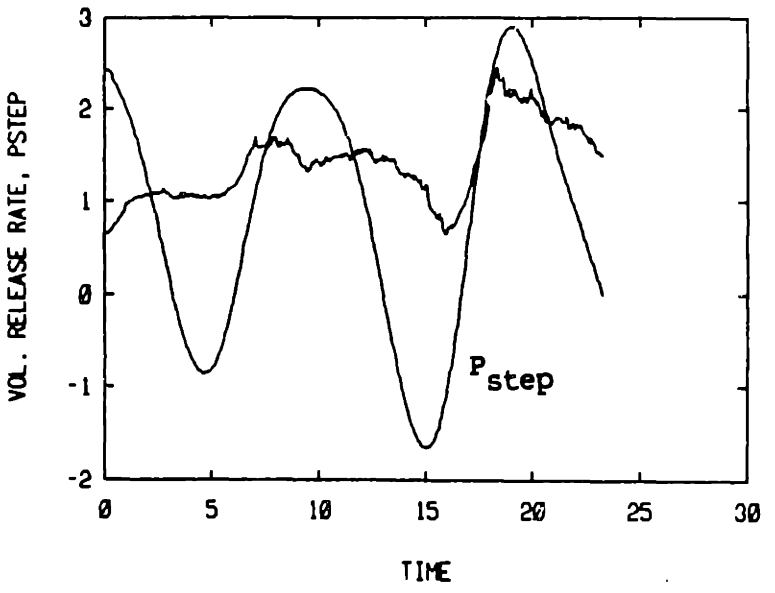

(a)

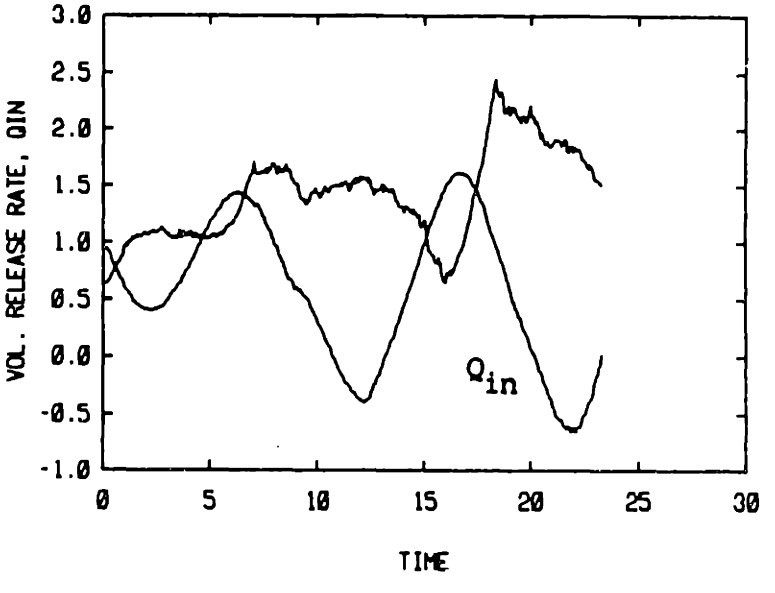

(b)

Figure 5.67 Superposition of the time traces of the rate of volume release and : (a) the step pressure, (b) the inlet flow rate. Both plots are for the high heat release flow of Fig. 5.64.

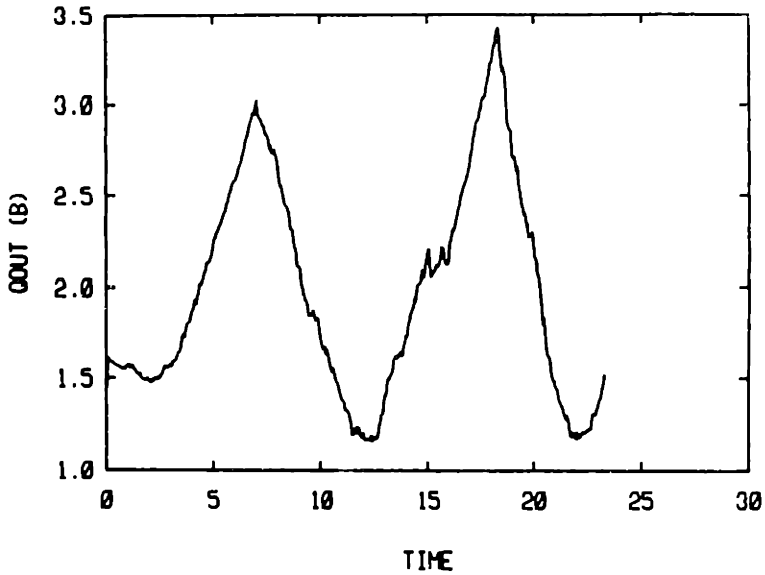

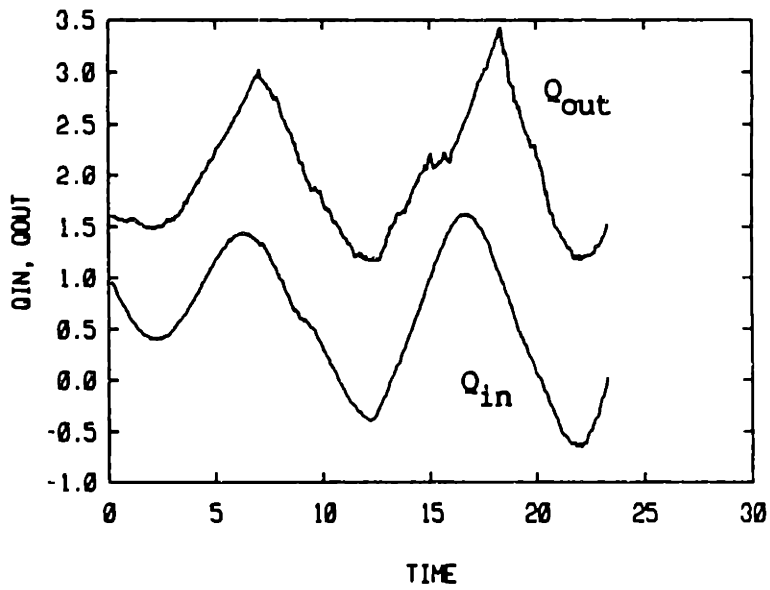

Figure 5.68 (a)- The exit flow rate plotted against time and (b)- superposed on the time trace of the inlet flow rate into the combustor, for the high heat release flow of Fig. 5.64.

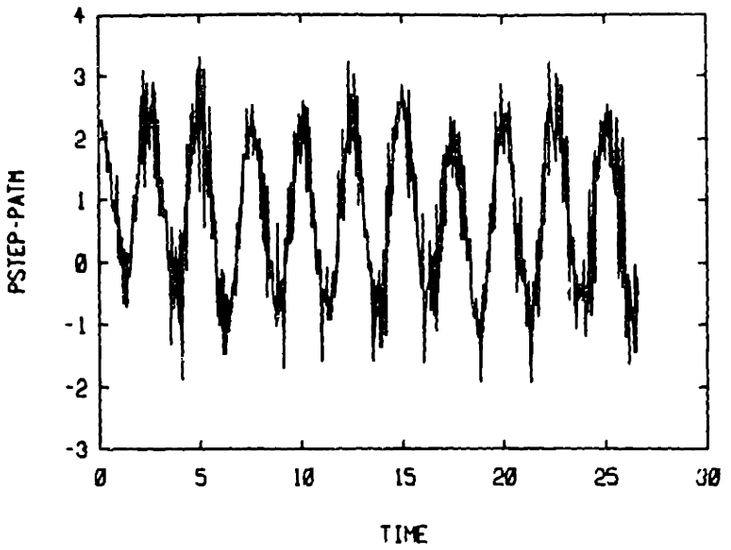

(a)

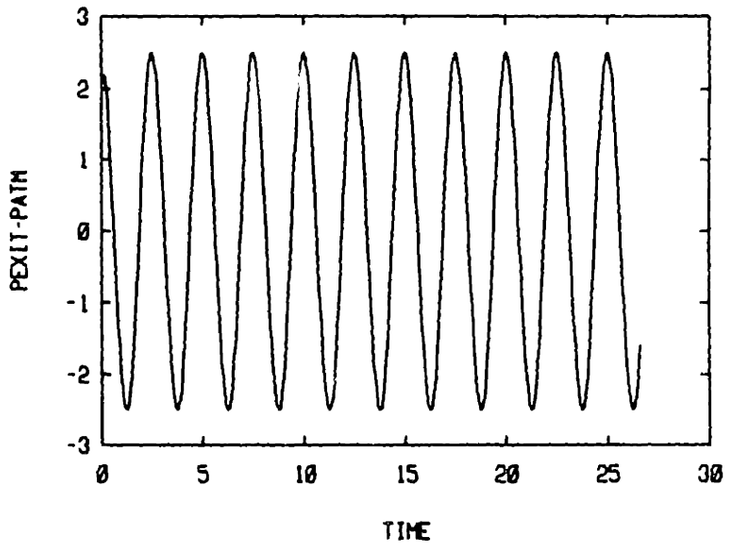

(b)

Figure 5.69 The pressure trace (channel centerline) at the upstream step (a) and the specified exit pressure trace (b) plotted versus time, for the high heat release and high forcing frequency flow of Fig. 5.72 below.

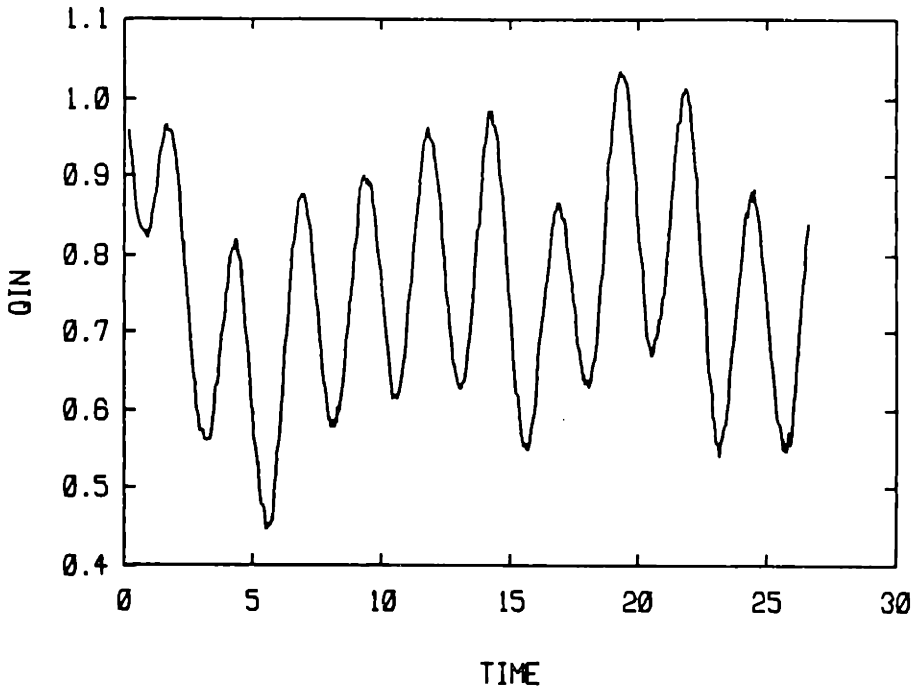

Figure 5.70 The time trace of the inlet flow rate at xmin, for the high heat release and high forcing frequency flow of Fig. 5.72 below. The mean flow rate for the time period from 10 to 26.6, is 0.77.

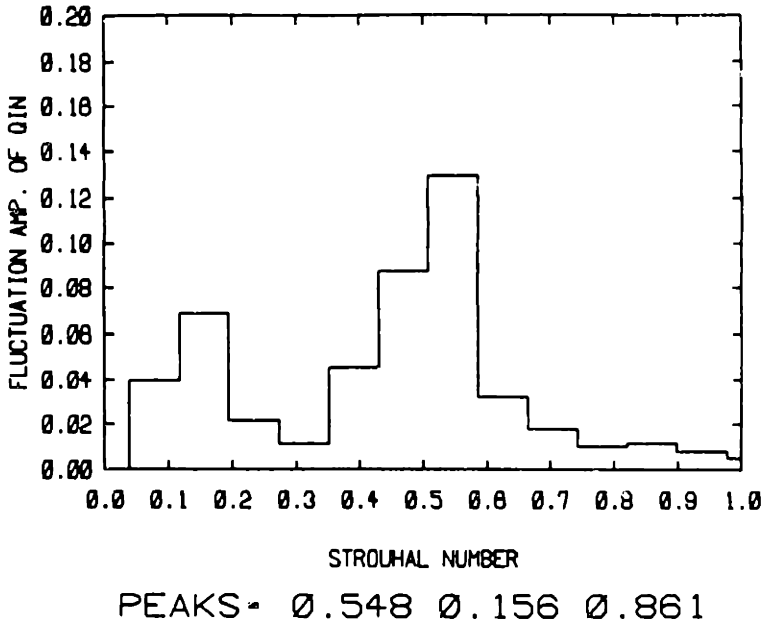

(a)

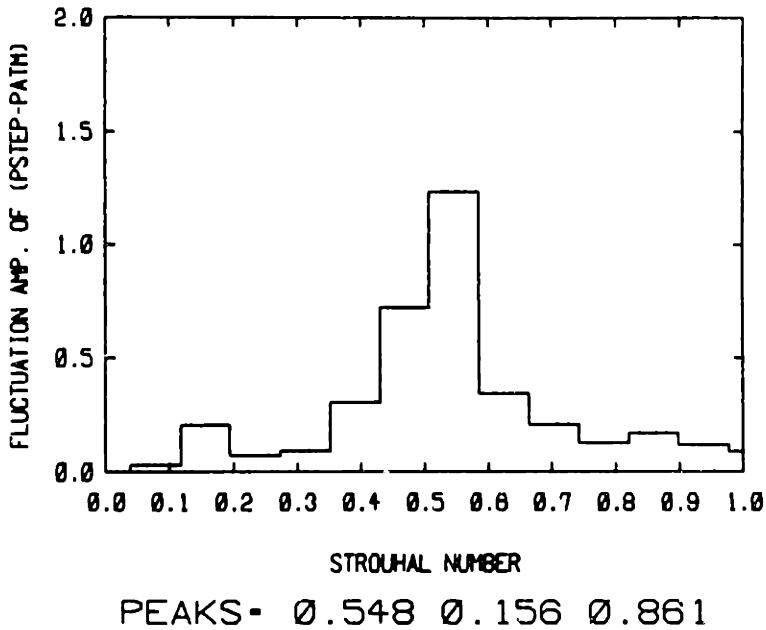

(b)

Figure 5.71 Spectra of the inlet flow rate (a) and upstream step pressure (b), computed from the corresponding time traces in figures 5.69a and 5.70, for the time period 10-26.6. The Strouhal number used is based on the cavity depth and the mean inlet flow velocity for the time period considered.

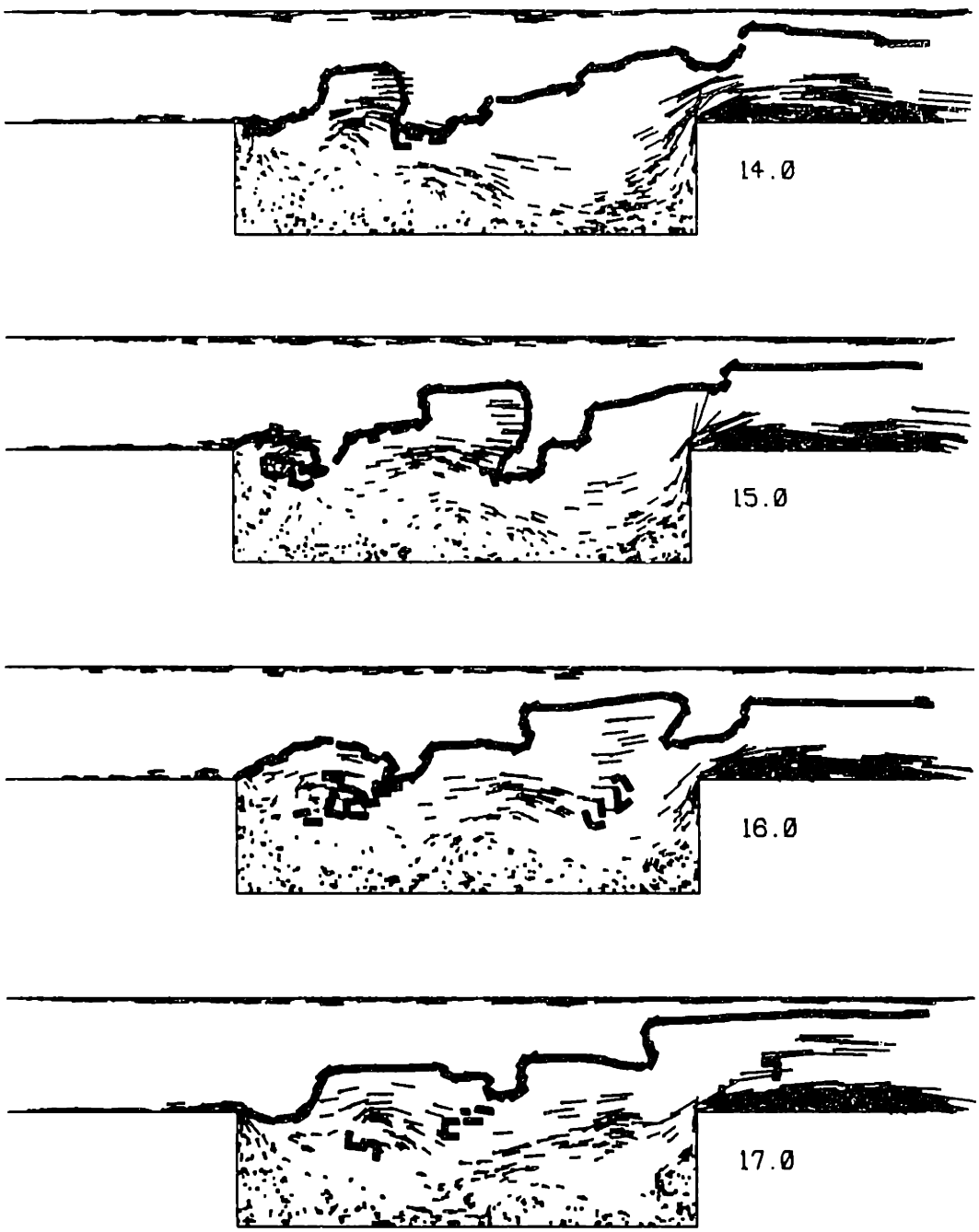

Figure 5.72 Continued on next page, caption at end of sequence.

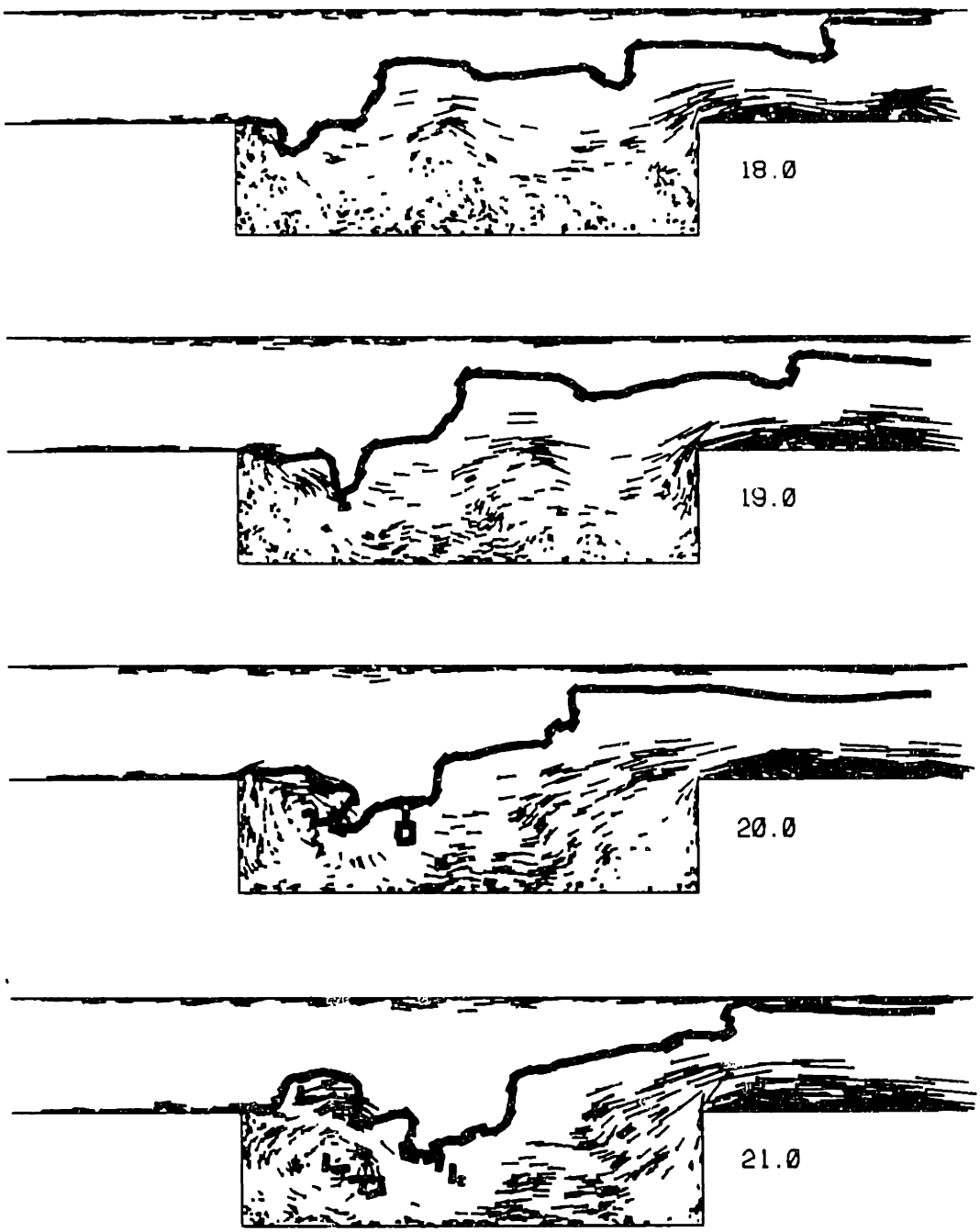

Figure 5.72 For caption see next page.

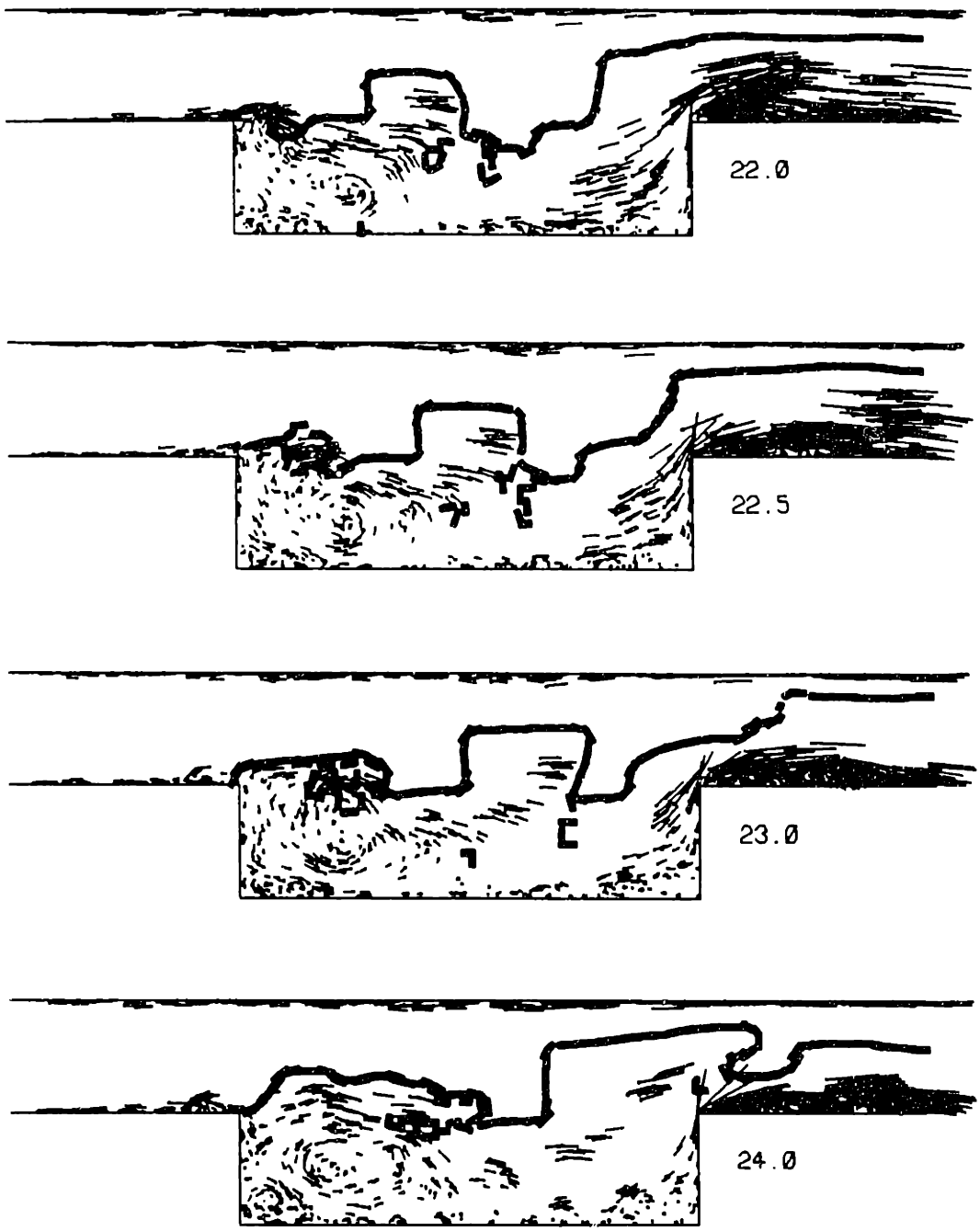

Figure 5.72 A sequence of time frames of the combustor flow field at high heat release and high forcing frequency, illustrating the relatively stable combustor operation and the weak recirculation zone eddy shedding. The exit pressure is a specified sinusoidal function of time, at fD/U_r=0.4.

5.2.4 Closing Remarks :

In closing, we note that the above forcing study is relevant for the purpose of both studying the combustion system operation and controlling the combustor instability.

In a real combustion system, the piping leading to and from the combustor is known to respond to the reacting flow dynamics in the dump section such that the pressure imposed at the combustor experiences significant oscillation; see, for example, Vaneveld et. al. (1982). In the above forcing study, we have endeavored to examine the operation of the combustor under different conditions of system pressure oscillation. By imposing this pressure oscillation at the combustor exit, we have lumped the system acoustic components in the downstream flow apparatus.

The study of this lumped downstream acoustic system, and its response to the reacting flow dynamics in the combustor, is an interesting extension of this work. In Chapter 3, we described the formulation for the solution of the inviscid compressible gas dynamics equations in a long 1D channel. We report in Appendix D some results using this 1D model, coupled to the combustor model used hitherto. These results inllustrate that the response of the oscillator involves pressure modulation at the combustor exit with specific frequencies, as observed experimentally. Further, since the particular results reported correspond to a choice of oscillator length and burnt gas temperature that result in a high oscillation frequency, the corresponding combustor response is found to be similar to that in the above high frequency forced case. Future work on this problem should be targeted at providing a thourough understanding of the response of the oscillator to the combustor exit flow rate oscillation.

The use of the above forced results for devising strategies for controlling the combustor instability has also been indicated above. Forcing

the combustor exit pressure at high frequency, and limiting its low frequency oscillation to low amplitudes, is essential in controlling the flashback instability.

While in the above study it was easy to force the exit pressure to have a specified amplitude and frequency of oscillation, the control of the pressure in actual systems is a difficult task. In fact, as reported by McManus et. al. (1989), experiments have required considerable controller power to overcome the natural pressure oscillations in the system, especially at high heat release. It seems evident that a combination of proper system design, as well as active control, is required for significant control of the combustor instability.

6. CONCLUSIONS

A numerical model was developed and implemented to study the dynamics of non-reacting and reacting flow in a dump combustor. The random vortex method along with the "Simple Line Interface Calculation" (SLIC) method are used to compute the low Mach number flow in a 2D compact combustor. The pressure is introduced in order to provide the necessary coupling between the compact combustor domain and the inlet and exit flow problems. The diagram shown in Fig. 6.1 illustrates the coupling between various component models that, together, provide a full combustion system model. The pressure information is transmitted upstream via (1) the specification of the combustor exit pressure, p_{ex}, using the downstream flow model, (2) the integration of the streamwise pressure gradient from the combustor exit to its inlet, and the computation of the inlet pressure, p_{in}, and (3) the use of p_{in} as the exit pressure for the upstream flow problem model. The flow rate information, on the other hand, travels downstream. The inlet flow rate to the combustor, Q_{in}, is specified by the upstream flow model. The combustor exit flow rate, Q_{out}, is the sum of Q_{in} and the rate of volume generation by the flame expansion field, and Q_{out} is used as the inlet flow rate to the downstream flow model.

The non-reacting flow in the combustor geometry was studied with regard to understanding the essential mechanism behind its instability. Two elements of the flowfield, the separating shear layer and the recirculation bubble in the dump, were found to be significant in determining the flow dynamics, depending on the dump (cavity) geometry. The shear layer Kelvin-Helmholz instability leads to the formation of organized vortex eddies that grow in size as they travel downstream. The recirculation zone exhibits similar shedding, with lower frequency and larger eddy sizes, which is reminiscent of

the eddy shedding in the wake behind a bluff body. For short cavities, $L/D < 2$, the shear layer eddies ride over a relatively quiescent recirculation zone. They are shed at the upstream separation point, travel downstream along the cavity top, and impinge on the downstream edge. The recirculation zone oscillation causes low frequency modulation of the shear layer instability, and is manifested in small amplitude flapping of the layer. For longer cavities, $L/D > 3$, the recirculation zone instability dominates the dynamics. Shear layer eddies are engulfed by the large recirculation zone eddies, and play otherwise no role in the flow dynamics. In the recirculation zone, eddies are shed at the upstream step, concomitant with a strong downward dip of the shear layer into the cavity. They grow by engulfing vortical fluid from the shear layer, and are then detached from the step and convected downstream in the cavity as they continue to grow by engulfing irrotational channel fluid. At the downstream step, an eddy is either destroyed or climbs over the step and is convected downstream in the channel. These eddies, being of the scale of the cavity depth, are larger than shear layer eddies. They are also shed and convected at lower frequency. We have found that, for $L/D > 3$, this frequency is independent of L/D and it scales with the cavity depth D, and the mean inlet velocity U, such that $fD/U=O(0.1)$. This supports the analogy between the recirculation zone dynamics and the wake behind bluff-body, since we know that the eddy shedding behind a bluff-body is at $fD/U=O(0.1)$ where D is the dimension of the bluff body.

Since cavity-type dump combustors generally use $L/D > 3$, the long cavity dynamics are more relevant to combustor flow than those of short cavities. In particular, this large scale, low frequency, "wake mode" shedding in the recirculation zone is the essential element of the flow in a dump combustor.

The reacting flow was studied with regard to the effect of the flame heat release on the overall combustor stability, under different conditions of exit pressure modulation.

The flame was generally observed to ride on the edge of the recirculation zone eddies. The frequency of the recirculation zone instability is the same as in the non-reacting flow, at $fD/U=O(0.1)$.

For a fixed amplitude, the frequency of modulation of the exit pressure is found to determine the combustor response to an increase in heat release. When this pressure is fixed, or forced at a frequency that is higher than the natural frequency of the combustor, the effect of increasing the rate of heat release is to cause the dampening of the recirculation zone instability. On the other hand, when the exit pressure is forced at low frequency, close to the combustor natural frequency, the recirculation zone dynamics are amplified by an increase in the rate of heat release, ultimately leading to flow reversal and flame flashback.

These observations conform with the instability requirement based on the Rayleigh criterion (Rayleigh, 1945), which states that sufficient coupling may occur between the pressure and the heat release leading to the growth of disturbances and the amplification of the natural combustor instability, when the pressure and heat release oscillations are in phase at the natural frequency of the combustor. Given that the flowfield in the combustor is at low Mach number, it is expected that constraining the exit pressure will also constrain the pressure everywhere in the combustor, at least at low frequencies. When the exit pressure is modulated at high frequency, or is fixed, its fluctuation component at the low natural frequency is zero and hence cannot be amplified by the heat release. On the other hand, when the exit pressure is modulated at low frequency, close to the combustor natural frequency, this amplification is possible. As we have seen, this

amplification is enhanced by both the increased amplitude of the rate of heat release and the smaller phase discrepancy between the heat release oscillation and the pressure oscillation.

We have also shown that, for either high frequency exit pressure forcing or for fixed exit pressure, increasing the rate of the heat release in fact causes the dampening of the low frequency component of the combustor dynamics. This stabilization is due to the favourable pressure gradient imposed by the flame expansion field and is similar to the stabilization of boundary layers and shear layers by favourable pressure gradients. It is also in agreement with experimental evidence in bluff body stabilized flames where no appreciable acoustic resonance may exist in the system.

Further, our results indicate that, at a given high rate of heat release and for given combustor operating conditions, increasing the frequency of the exit pressure modulation, at the same amplitude, leads to the stabilization of the combustor dynamics. We have also found that reducing the amplitude of the exit pressure oscillation at the same low frequency, leads to similar stabilization.

These results suggest various methods of controlling the combustor instability by specified forcing of the exit pressure. Clearly, controlling the amplitude of the pressure oscillation at the natural combustor frequency is the key to preventing the amplification of the recirculation zone instability at high heat release. Enforcing a high frequency exit pressure oscillation or a fixed exit pressure dampens the combustor instability. Similarly, limiting the amplitude of the pressure oscillation, even if the frequency is close to the natural mode, tends to stabilize the combustor. In an actual combustion system these effects may be achieved by active or passive means, or a combination of both.

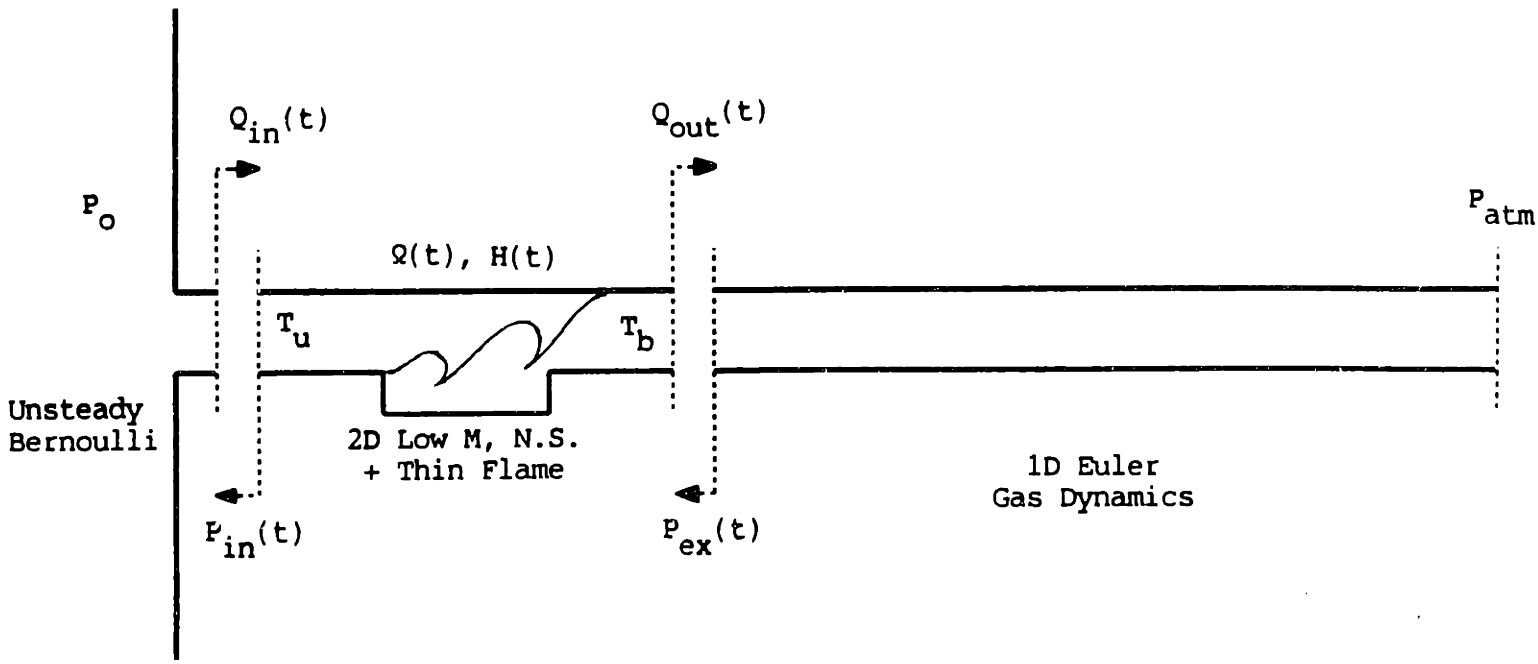

Figure 6.1 A schematic diagram showing the combustor coupling to the upstream and downstream flow elements.

7. REFERENCES

Anderson, D.A., Tannehill, J.C., and Pletcher, R.H., (1984), "Computational Fluid Mechanics and Heat Transfer", Hemisphere Pub. Co., NY.

Barr, P.K. and Ashurst, W.T., (1984), "An Interface Scheme for Turbulent Flame Propagation", Sandia Report SAND 82-8773, Sandia National Laboratories.

Batchelor, G.K., (1985),"An Introduction to Fluid Dynamics", Cambridge University Press, England.

Beale, J.T., and Majda A., (1981), "Rates of convergence for viscous splitting of the Navier-Stokes equations", Math. of Computation, 37, No.156, pp. 243-259.

Berndt, S.B., (1966), "The Vorticity Jump Across a Flow Discontinuity", J. Fluid Mech., 26, part 3, pp. 433-436.

Brown, G.L. and Roshko, A., (1974), "On Density Effects and Large Structures in Turbulent Mixing Layers", J. Fluid Mech., 64, pp. 775-816.

Cheng, S.I., and Kovitz, A.A., (1957a), "Ignition in the Laminar Wake of a Flat Plate", Sixth Symposium (International) on Combustion, at Yale University, New Haven, Connecticut, 1956; Reinhold Pub. Corp.; pp. 418-427.

Cheng, S.I., and Kovitz, A.A., (1957b), "Theory of Flame Stabilization by a Bluff Body", Sixth Symposium (International) on Combustion, at Yale University, New Haven, Connecticut, 1956; Reinhold Pub. Corp.; pp. 681-691

Cherry, N.J., Hillier, R., and Latour, M.E.M.P., (1984), "Unsteady Measurements in a separated and Reattaching Flow", J. Fluid Mech., 144, pp. 13-46.

Chorin, A.J., (1980), "Flame Advection and Propagation Algorithms", J. Comp. Phys., 35, 1-11.

Chorin, A.J., (1972), "Numerical study of slightly viscous flow", J. Fluid Mech., 57, part 4, pp. 785-796.

Chorin, A.J., (1978), "Vortex sheet approximation of boundary layers", J. of Comp. Phys., 27, pp.428-442

Chorin, A.J., and Marsden, J.E., (1979), "A mathematical introduction to fluid mechanics", Springer Verlag.

Choudhury, P.R., Gerstein, M., and Mojaradi, R., (1981), "A Novel Feedback Concept for Combustion Instability in Ramjets", JANNAF meeting, 1981.

Chung, S.H., and Law, C.K., (1984), "An Invariant Derivation of Flame Stretch", Combustion and Flame, 55, pp. 123-125.

Driver, D.M., Seegmiller, H.L., and Marvin, J.G., (1987), "Time-Dependent Behavior of a Reattaching Shear Layer", AIAA Journal, 25, no. 7, pp. 914-919.

Eaton, J.K. and Johnston, J.P., (1981), "Low Frequency Unsteadiness of a Reattaching Turbulent Shear Layer", Third International Symposium on Turbulent Shear Flows - selected papers, ed. Bradbury, L.J., Durst, F., Launder, B.E., Schmidt, F.W. and Whitelaw, J.H., Springer-Verlag.

Emmons, H.W., (1958), "Fundamentals of Gas Dynamics", Ed. W.H. Emmons, Vol. 3, "Highspeed Aerodynamics and Jet Propulsion", chap. 2, Princeton University Press.

Ethembabaoglu, S., (1973), "On the Fluctuating Flow Characteristics in the Vicinity of Gate Slots", Division of Hydraulic Engineering, University of Trondheim, Norwegian Inst. of Technology.

Fristrom, R.M. and Westenberg, A.A., (1965), "Flame Structure", McGraw-Hill, New York.

Gangi, A.R., and Sawyer, R.F., (1979), "An Experimental Study of the Flow Field and Pollutant Formation in a Two Dimensional, Premixed, Turbulent Flame", AIAA-79-0017, 17th Aerospace Sciences Meeting, New Orleans.

Gangi, A.R., and Sawyer, R.F., (1980), "Experimental Study of the Flowfield of a Two-Dimensional Premixed Turbulent Flame", AIAA Journal, 18, no. 7, pp. 817-824.

Gangi, A.R., and Sawyer, R.F., (1978), "Blowout and Flashback in a Two Dimensional Lean Premixed Combustor", Dept. of Mech. Eng'g, Univ. of Calif. Berkeley, part of PhD Thesis by Gangi.

Gerald, C.F., and Wheatley, P., (1984), "Applied Numerical Analysis", Addison Welsey.

Ghaddar, N.K., (1985), "Numerical Investigation of Heat Transfer Enhancement due to Oscillatory Flow Over Furrowed Walls", Ph.D. Thesis, Mechanical Engineering, M.I.T.

Ghaddar, N.K., Magen, M., Mikic, B.B., and Patera, A.T., (1986), "Numerical Investigation of Incompressible Flow in Grooved Channels. Part 2. Resonance and Oscillatory Heat-Transfer Enhancement", J. Fluid Mech., 168, pp. 541-567.

Gharib, M., (1987), "Response of the Cavity Shear Layer Oscillations to External Forcing", AIAA Journal, 25, no. 1.

Gharib, M. and Roshko, A., (1987), "The Effect of Flow Oscillations on Cavity Drag", J. Fluid Mech., 177, pp. 501-530.

Ghoniem, A.F., Chorin, A.J., and Oppenheim, A.K., (1982), "Numerical Modelling of Turbulent Flow in a Combustion Tunnel", Philos. Trans. Roy. Soc. London, Sr. A, vol. 304, pp. 303-325.

Ghoniem, A.F., (1986), "Computational Methods in Turbulent Reacting Flow", Lectures in Applied Mathematics, 24, pp. 199-265.

Ghoniem, A.F., and Gagnon, Y., (1987), "Vortex Simulation of Laminar Recirculating Flow", J. Comp. Phys., 68, No. 2, pp. 346-377.

Ghoniem, A.F. and Ng, K., (1987), "Numerical study of the dynamics of a forced shear layer", Phys. Fluids, 30, No.3, pp.706-721.

Ghoniem, A.F. and Sherman, F.S., (1985), "Grid Free Simulation of Diffusion using Random Walk Methods", J. Comp. Phys., 61, pp. 1-37.

Glassman, I., (1987), "Combustion", Academic Press, 2nd ed., p. 187.

Greenberg, M.D., (1978), "Foundations of Applied Mathematics", Prentice-Hall.

Hald, O., (1985), (PAM-270), Center for Pure and Applied Mathematics, Univ. of California, Berkley.

Hardin, J.C., and Mason, J.P., (1977), "Broadband Noise Generation by a Vortex Model of Cavity Flow", AIAA Journal, 15, no. 5. (Experimental flow visualization by H. Werle, ONERA).

Hayes, W.D., (1957), "The Vorticity Jump Across a Gas Dynamic Discontinuity", J. Fluid Mech., 2, pp. 595-600.

Hildebrand, F.B., (1976),"Advanced Calculus for Applications", Prentice-Hall.

Ho, C. and Huang, L., (1982), "Subharmonics and Vortex Merging in Mixing Layers", J. Fluid Mech., 119, pp. 443-473.

Honji, H., (1975), "The Starting Flow Down a Step", J. Fluid Mech., 69, pp. 229-240.

Hussain, A.K. and Zamman, K.B., (1978), "The Free Shear Layer Tone Phenomenon and Probe Interference", J. Fluid Mech., 87, pp. 349-383.

John, F., (1982), "Partial differential equations", Springer Verlag, 4th. ed.

Jones, R.E., (1978), "Gas Turbine Engine Emissions - Problems, Progress, and Future", Prog. Energy Combust. Sci., 4, pp. 73-113.

Jou, W.-H., and Menon, S., (1987), "Simulations of Ramjet Combustor Flow Fields. Part II - Origin of Pressure Oscillations", AIAA paper 87-1422.

Kailasanath, K., Gardner, J., Boris, J. and Oran, E., (1986), "Interactions Between Acoustics and Vortex Structures in a Central Dump Combustor", AIAA Paper No. 86-1609.

Kailasanath, K., Gardner, J.H., Boris, J.P., and Oran, E.S., (1987), "Acoustic - Vortex Interactions and Low Frequency Oscillations in Axisymmetric Combustors", AIAA paper No. 87-0165.

Karamcheti, K., (1980), "Principles of Ideal-Fluid Aerodynamics", Krieger, Malabar, Florida.

Keller, J.O., Vaneveld, L., Korschelt, D., Hubbard, G.L., Ghoniem, A.F., Daily, J.W. and Oppenheim, A.K., (1981), "Mechanism of Instabilities in Turbulent Combustion Leading to Flashback", AIAA Paper No. 81-0107R.

Kiya, M. and Sasaki, K., (1983), "Structure of a Turbulent Separation Bubble", J. Fluid Mech., 137, pp. 83-113.

Kiya, M. and Sasaki, K., (1985), "Structure of Large-Scale Vortices and Unsteady Reverse Flow in the Reattaching Zone of a Turbulent Separation Bubble", J. Fluid Mech., 154, pp. 463-491.

Knio, O.M., (1984), "Low Mach Number Simulation of Combustion in Closed Chambers", S.M. Thesis, Mechanical Engineering, Mass. Inst. of Tech.

Knisely, C. and Rockwell, D., (1982), "Self-Sustained Low-Frequency Components in an Impinging Shear Layer", J. Fluid Mech., 116, pp. 157-186.

Kuwahra, K., and Takami, H., (1973), "Numerical studies of two-dimensional vortex motion by a system of point vortices", J. Phys. Soc. Japan, 34, No. 1, pp. 247-253.

Landau, L.D. (1944), "On the Theory of Slow Combustion", appears in 3 publications, (1) J. Exp. Theor. Phys. (ZhETF), 14(6), 240 (In Russian); (2) Acta Phys. Chim. URSS, 19, 77; and (3) Collected Papers of L.D.Landau, Ed. D. Ter Haar, Gordon and Beach Science Publisher, London, and Pergamon Press, (1967).

Lewis, B. and Von Elbe, G., (1961), "Combustion, Flame, and Explosions of Gases", 2nd ed., pp. 228-261, Academic Press.

Lighthill, M. (1963), "Introduction: Boundary Layer Theory", in : Laminar Boundary Layer Theory, L. Rosenhead, Ed., p. 46, Oxford Univ. Press., London.

Masutani, S.M., Kobayashi, H., Azuhata, S., Miyadera, H., Hishinuma, Y., (1987), "Plane Mixing Layers with Streamwise Pressure Gradient", 6th Symposium on Turbulent Shear Flows, Tolouse, France, paper 10-2.

Masutani, S.M., Kobayashi, H., Azuhata, S., Arashi, N., and Hishinuma, Y., (1988), "Confined Plane Mixing Layers with Streamwise Pressure Gradient. Part 1. The Single Phase Flow", Hitachi Research Lab., Hitachi ltd., Submitted to J. Fluid Mech., Dec. 1988.

Matalon, M., and Matkowsky, B.J., (1982), "Flames as Gasdynamic Discontinuities", J. Fluid Mech., 124, pp. 239-259.

Majda, A. and Sethian, J., (1985), "The Derivation and Numerical Solution of Equations for Zero Mach Number Combustion", Combustion Sci. and Tech., 42, pp. 185-205.

McManus, K.R., Vandsburger, U., and Bowman, C.T., (1987), "Modification of Combustion Characteristics of a Dump Combustor using Shear Layer Excitation", Mechanical Engineering Dept, Stanford University.

McManus, K.R., Vandsburger, U., and Bowman, C.T., (1989), "Combustor Performance Enhancement Through Direct Shear Layer Excitation", Submitted to "Combustion and Flame".

Menon, S., and Jou, W.H., (1987), "Simulations of Ramjet Combustor Flow Fields, Part I - Numerical Model, Large-Scale and Mean Motions", AIAA Paper No. 87-1421.

Milinazzo, F. and Saffman, (1977), "The Calculation of Large Reynolds Number Fluid Flow using Discrete Vortices with Random Walk", J. comp. Phys., 23, pp. 380-392

Morton, B.R., (1984), "The generation and decay of vorticity", Gheophys. Astrophys. Fluid Dynamics, 28, pp.277-308.

Neary, M.D., and Stephanoff, K.D., (1987) "Shear-Layer-Driven Transition in a Rectangular Cavity", Phys. Fluids, 30, no. 10.

Nehari, Z., (1975), "Conformal Mapping", Dover, New York.

Najm, H.N., and Ghoniem A.F., (1987) "Numerical simulation of the convective instability in a dump", AIAA-87-1874, AIAA/SAE/ASME/ASEE/ 23rd Joint Propulsion Conference.

Noh, W.T. and Woodward, P. (1976), "SLIC (Simple Line Interface Calculation)", Proc. 5th Int. Conf. Numer. Meth. Fluid Mech., Berlin, Springer-Verlag.

Oster, D. and Wygnanski, I., (1982), "The Forced Mixing Layer Between Parallel Streams", J. Fluid Mech., 123, pp. 91-130.

Parker, R., and Welsh, M.C., (1983), "Effects of Sound on Flow Separation from Blunt Flat Plates", Int. J. Heat & Fluid Flow, 4, no. 2.

Payne, R.B., (1958), "Calculations of Unsteady Viscous Flow past a Circular Cylinder", J. Fluid Mech., 4, p. 81.

Pindera, M.Z., and Talbot, L., (1986), "Flame Induced Vorticity: Effects of Stretch", Twenty-first Symposium (International) on Combustion/The Combustion Institute, pp. 1357-1366.

Pitz, R.W., and Daily, J.W., (1981), "Experimental Study of Combustion in a Turbulent Free Shear Layer Formed at a Rearward Facing Step", AIAA Paper No. 81-0106.

Pitz, R.W., and Daily, J.W., (1983), "Combustion in a Turbulent Mixing Layer Formed at a Rearward-Facing Step", AIAA Journal, 21, 11, pp. 1565-1570.

Plee, S.L., and Mellor, A.M., (1978), "Review of Flashback Reported in Prevaporizing/Premixing Combustors", Combustion and Flame, 32, pp. 193-203.

Poinsot, T.J., Trouve, A.C., Veynante, D.P., Candel, S.M., Esposito, E.J., (1987), "Vortex-Driven Acoustically Coupled Combustion Instabilities", J. Fluid Mech., 177, pp. 265-292.

Potter, M.C., and Foss, J.F., (1982), "Fluid Mechanics", Great Lakes Press.

Rayleigh, J.W.S., (1945), "The Theory of Sound: Vol. II", Dover, New York.

Rockwell, D. and Knisely, C., (1979), "The Organized Nature of Flow Impingement Upon a Corner", J. Fluid Mech., 93, pp. 413-432.

Rosenhead, L., (1932), "The formation of vortices from a surface of discontinuity", Proc. Roy. Soc. London, Ser. A, 134, pp. 170-192.

Saffman, P.G., and Baker, G.R., (1979), "Vortex Interactions", Ann. Rev. Fluid Mech.", pp. 95-122.

Sarohia, V., (1977), "Experimental Investigation of Oscillations in Flows Over Shallow Cavities", AIAA Journal, 15, pp. 984-991.

Schlichting, H., (1979), Transl. J. Kestin, "Boundary Layer Theory", McGraw Hill, New York.

Schadow, K. and Wilson, K., (1985), "Characterization of Large-Scale Structures in a Forced Ducted Flow with Dump", AIAA Paper No. 85-0080.

Schadow, K., Wilson, K., Crump, J., Foster, J. and Gutmark, E., (1984), "Interaction Between Acoustics and Subsonic Ducted Flow with Dump", AIAA Paper No. 84-0530.

Sethian, J., (1984), "Turbulent Combustion in Open and Closed Vessels", J. Comp. Phys., 54, pp. 425-456.

Sinha, S.N., (1978), "Two Dimensional Laminar and Turbulent Separating Flows Over Backward Facing Steps and Rectangular Cavities", Ph.D. Thesis, Indian Institute of Technology, Kanpur, India, (available from University Microfilms International).

Sivashinsky, G.I., (1976), "On a Distorted Flame Front as a Hydrodynamic Discontinuity", Acta Astronautica, 3, (11-12), pp. 889-918.

Sivashinsky, G.I., (1979), "Hydrodynamic theory of flame propagation in an enclosed volume", Acta Astronautica, 6, pp. 631-645.

Smith, D. and Zukoski, E., (1985), "Combustion Instability Sustained by Unsteady Vortex Combustion", AIAA Paper No. 85-1248.

Strehlow, R.A., (1984), "Combustion Fundamentals", McGraw-Hill, New York.

Tani, I., Iuchi, M., and Komoda, H., (1961), "Experimental Investigation of Flow Separation Associated with a Step or a Groove", Aeronautical Research Institute, University of Tokyo, Report No. 364.

Thompson, P.A., (1984), "Compressible-Fluid Dynamics", Maple Press Co.

Tien, C.L., and Lienhard, J.H., (1979), "Statistical Thermodynamics", Hemisphere Pub. Co., Washington.

Trefethen, L.N., (1979), "Numerical Computation of The Schwartz-Christoffel Transformation", STAN-CS-79-710, Computer Science Dept., School of Humanities and Sciences, Stanford University.

Van Dyke, M., (1975), "Perturbation Methods in Fluid Mechanics", The Parabolic Press, Stanford, CA.

Vaneveld, L., Hom, K. and Oppenheim, A.K., (1982), "Secondary Effects in Combustion Instabilities Leading to Flashback", AIAA Paper No. 82-0037.

Williams, F.A., (1985), "Combustion Theory", Benjamin/Cummings Pub. Co., 2nd ed., pp. 504-505.

Wright, F.H., and Zukoski, E.E., (1962), "Flame Spreading from Bluff-Body Flameholders", Eighth Symposium (International) on Combustion, at the California Inst. of Tech., Pasadena, Calif., 1960; The Williams & Wilkins Company. pp. 933-943.

Yu, K., Lee, S., Stewart, H.E., and Daily, J.W., (1987), "Vortex-Nozzle Interactions in Ramjet Combustors", AIAA Paper No. 87-1871.

Yu, K., Trouve, A., Keanini, R., Bauwens, L., (1989), "Low Frequency Pressure Oscillations in a Model Ramjet Combustor - The Nature of Frequency Selection", AIAA-89-0623.

Ziada, S. and Rockwell, D., (1982), "Vortex-Leading-Edge Interaction", J. Fluid Mech., 118, pp. 79-107.

APPENDIX A

Derivation of The General Equations

Given the assumptions stated in section 2.1, the following discussion demonstrates the derivation and non-dimensionalization of the equations listed in Table 2.1. Dimensional quantities are denoted by a tilde (~). The reference quantities for non-dimensionalization are listed in Table 2.2. Additional nomenclature is described in Table 2.3.

A.1 Mass Conservation : We begin by the dimensional form as below,

$$\frac{D\tilde{\rho}}{D\tilde{t}} + \tilde{\rho}\,\nabla.\tilde{\mathbf{u}} = 0$$

then, introduce $\tilde{\rho}_r$, $\tilde{U}$, and $\tilde{L}$, the reference density, velocity and length respectively, where, $\rho = \tilde{\rho}/\tilde{\rho}_r$, $u_i = \tilde{u}_i/\tilde{U}$, $t = \tilde{t}/\tilde{t}_r = \tilde{t}/(\tilde{L}/\tilde{U})$, and $x_i = \tilde{x}_i/\tilde{L}$, we get:

$$\frac{D\rho}{Dt} + \rho\,\nabla.\mathbf{u} = 0$$

which is equation (2.2) in Table 2.1.

A.2 Momentum : The dimensional momentum conservation equation, for a compressible fluid with zero body forces and bulk viscosity, is given by : [Schlichting (1979), Batchelor (1985)]

$$\tilde{\rho}\,\frac{\tilde{D}\tilde{\underline{u}}}{\tilde{D}t} = -\,\tilde{\nabla}\tilde{p} + \tilde{\nabla}.\tilde{\underline{\tau}}$$

where, $\tilde{\underline{\tau}} = \tilde{\mu}\underline{\tau}'$, $\underline{\tau}'=(\tau'_{ij})$, and $\tau'_{ij} = \left(\frac{\partial \tilde{u}_i}{\partial \tilde{x}_j} + \frac{\partial \tilde{u}_j}{\partial \tilde{x}_i} - \frac{2}{3}\delta_{ij}\nabla.\tilde{\mathbf{u}} \right)$

and, $\nabla.\tilde{\underline{\tau}} = \tilde{\mu}(\nabla.\underline{\tau}') + (\nabla\tilde{\mu}).\underline{\tau}' = \tilde{\mu}\left(\nabla^2\tilde{\mathbf{u}} + \frac{1}{3}\nabla(\nabla.\tilde{\mathbf{u}}) \right) + (\nabla\tilde{\mu}).\underline{\tau}'$

Then, using the reference quantities for $\tilde{\rho}$, $\tilde{\mathbf{u}}$, $\tilde{t}$, and $\tilde{\mathbf{x}}$, and using:

$$p = \tilde{p}/\tilde{p}_r, \quad \tilde{p}_r = \tilde{\rho}_r\tilde{R}\tilde{T}_r$$

$$M_o = \tilde{U}/(\gamma\tilde{R}\tilde{T}_r)^{1/2}$$

$$\mu = \tilde{\mu}/\tilde{\mu}_r, \quad Re_o = \tilde{\rho}_r\tilde{U}\tilde{L}/\tilde{\mu}_r$$

$$\tilde{\underline{\tau}} = (\tilde{\mu}_r\tilde{U}/\tilde{L})\ \underline{\tau}$$

we arrive at equation (2.3), namely :

$$\gamma M_o^2\ \rho\frac{Du}{Dt} = -\,\nabla p + \frac{\gamma M_o^2}{Re_o}\nabla.\underline{\tau}$$

A.3 Energy : We begin by writing the dimensional energy conservation equation as follows (White 1974) :

$$\tilde{\rho}\,\frac{\tilde{De}}{\tilde{Dt}} = \frac{\tilde{p}}{\tilde{\rho}}\,\frac{\tilde{D\rho}}{\tilde{Dt}} + \tilde{\Phi} + \nabla.(\tilde{k}\nabla\tilde{T}) + \tilde{\rho}\tilde{\xi}$$

where,

$\tilde{e}$ = internal energy per unit mass of fluid

$\tilde{\xi}$ = rate of heat generation per unit mass of fluid

$\tilde{\Phi}$ = dissipation function, as defined in Table 2.1 in 2-D, using dimensional quantities

Then, using :

$$\nabla.(\tilde{k}\nabla\tilde{T}) = -\nabla.\tilde{q}$$

and, if we assume that both reactants and products can be modeled as perfect gases with constant $\tilde{c}_p$, $\tilde{c}_v$, and gas constant $\tilde{R}$, then we can write :

$$\tilde{e} = \tilde{e}(\tilde{T})$$

$$\tilde{c}_v = (\partial\tilde{e}/\partial\tilde{T})_v = d\tilde{e}/d\tilde{T}$$

hence, following a fluid element,

$$\frac{\tilde{De}}{\tilde{Dt}} = \tilde{c}_v\,\frac{\tilde{DT}}{\tilde{Dt}}$$

further, $\tilde{p} = \tilde{\rho}\tilde{R}\tilde{T}$, and,

$$\frac{\tilde{D\rho}}{\tilde{Dt}} = \frac{1}{\tilde{R}}\,\frac{\tilde{D}}{\tilde{Dt}}\left(\frac{\tilde{p}}{\tilde{T}}\right) = \frac{1}{\tilde{R}}\left(\frac{\tilde{T}}{\tilde{T}}\,\frac{\tilde{Dp}}{\tilde{Dt}} - \frac{\tilde{p}}{\tilde{T}}\,\frac{\tilde{DT}}{\tilde{Dt}}\right)\frac{1}{\tilde{T}^2}$$

After substituting in the above energy equation, we get,

$$\tilde{\rho}\tilde{c}_v\,\frac{\tilde{DT}}{\tilde{Dt}} = \frac{1}{\tilde{T}}\left(\tilde{T}\,\frac{\tilde{Dp}}{\tilde{Dt}} - \tilde{p}\,\frac{\tilde{DT}}{\tilde{Dt}}\right) + \tilde{\Phi} - \nabla.\tilde{q} + \tilde{\rho}\tilde{\xi}$$

or, $$\tilde{\rho}\,(\tilde{c}_v + \tilde{R})\,\frac{\tilde{D}\tilde{T}}{\tilde{D}\tilde{t}} - \frac{\tilde{D}\tilde{p}}{\tilde{D}\tilde{t}} = \tilde{\Phi} - \nabla.\tilde{q} + \tilde{\rho}\tilde{\xi}$$

but, $\tilde{c}_v + \tilde{R} = \tilde{c}_p = \frac{\tilde{\gamma}\tilde{R}}{\tilde{\gamma}-1}$

also, let us express $\tilde{\xi}$ as : $\tilde{\xi} = \tilde{Q}\dot{\tilde{W}} / \tilde{\rho}$, where

$\tilde{Q}$ = heat of reaction, J/(kg of reactants burnt), > 0.

$\dot{\tilde{W}}$ = rate of generation of products, kg/m^3, (=rate of burning of reactants), > 0.

then, we get,

$$\tilde{\rho}\,\frac{\tilde{D}\tilde{T}}{\tilde{D}\tilde{t}} - \frac{\tilde{\gamma}-1}{\tilde{\gamma}\tilde{R}}\,\frac{\tilde{D}\tilde{p}}{\tilde{D}\tilde{t}} = \frac{\tilde{\gamma}-1}{\tilde{\gamma}\tilde{R}}\,(\tilde{\Phi} - \nabla.\tilde{q} + \tilde{Q}\dot{\tilde{W}})$$

Next, we proceed to non-dimensionalize this equation, using the following,

$$\rho = \tilde{\rho} / \tilde{\rho}_r \qquad T = \tilde{T} / \tilde{T}_r \qquad t = \tilde{t} / (\tilde{L}/\tilde{U})$$

$$p = \tilde{p} / (\tilde{\rho}_r\tilde{R}\tilde{T}_r) \qquad \Phi = \tilde{\Phi} / (\tilde{\mu}_r\tilde{U}^2/\tilde{L}^2) \qquad q = \tilde{q} / (\tilde{k}_r\tilde{T}_r/\tilde{L})$$

$$Q = \tilde{Q} / (\tilde{c}_p\tilde{T}_r) \qquad \dot{W} = \dot{\tilde{W}} / \dot{\tilde{W}}_r$$

get,

$$\rho\,\frac{DT}{Dt} - \frac{\gamma-1}{\gamma}\,\frac{Dp}{Dt} = \frac{\gamma-1}{\gamma}\,\frac{\tilde{\mu}_r\tilde{U}}{\tilde{\rho}_r\tilde{T}_r\tilde{R}\tilde{L}}\,\Phi - \frac{\gamma-1}{\gamma}\,\frac{\tilde{k}_r}{\tilde{R}\tilde{L}\tilde{\rho}_r\tilde{U}}\,\nabla.q + \frac{\gamma-1}{\tilde{\gamma}\tilde{R}}\,\frac{\tilde{c}_p\tilde{L}}{\tilde{\rho}_r\tilde{U}}\,\dot{\tilde{W}}_r\,\dot{Q}W$$

now, note that

$$\frac{\gamma-1}{\gamma}\,\frac{\tilde{\mu}_r\tilde{U}}{\tilde{\rho}_r\tilde{T}_r\tilde{R}\tilde{L}} = \frac{(\gamma-1)M_o^2}{Re_o}$$

further, $\tilde{c}_p = (\gamma-1)/\tilde{\gamma}\tilde{R}$, hence,

$$\frac{\gamma-1}{\gamma}\,\frac{\tilde{k}_r}{\tilde{R}\tilde{L}\tilde{\rho}_r\tilde{U}} = \frac{\tilde{k}_r}{\tilde{c}_p\tilde{L}\tilde{\rho}_r\tilde{U}} = \lambda$$

and, if we choose,

$$\dot{\tilde{W}}_r = \frac{\tilde{\rho}_r\tilde{c}_p\tilde{U}^2}{\tilde{k}_r}\,\tilde{\rho}_r$$

we have,

$$\frac{\gamma-1}{\tilde{\gamma}\tilde{R}}\,\frac{\tilde{c}_p\tilde{L}}{\tilde{\rho}_r\tilde{U}}\,\dot{\tilde{W}}_r = \frac{1}{\lambda}$$

Finally, substituting above, we get the non-dimensional energy equation listed in Table 2.1, namely,

$$\rho\frac{DT}{Dt} - \frac{\gamma-1}{\gamma}\frac{Dp}{Dt} = -\lambda\,\nabla.\mathbf{q} + \frac{(\gamma-1)M_o^2}{Re_o}\,\Phi + \frac{Q}{\lambda}\,\dot{W}$$

A.4 Species : We begin this formulation by writing the species conservation equation for a control volume, from which we get that, at every point in the fluid,

$$\frac{\partial}{\partial \tilde{t}} (\tilde{\rho} \tilde{C}) = - \nabla.(\tilde{\rho} \tilde{C} \tilde{u}) - \nabla.\tilde{g} - \dot{\tilde{W}}$$

where, $\tilde{C}$ = mass of Reactants per unit mass of fluid (nondimensional)

$\tilde{g}$ = diffusive flux of Reactants per unit area (kg/m^2s)

$= - \tilde{d} \nabla C$, where $\tilde{d}$: kg/ms.

$\dot{\tilde{W}}$ = rate of burning of reactants per unit volume (kg/m^3s)

then we develop this equation as follows,

$$C \frac{\partial \tilde{\rho}}{\partial \tilde{t}} + \tilde{\rho} \frac{\partial C}{\partial \tilde{t}} = - \tilde{u}.\nabla(\tilde{\rho} C) - \tilde{\rho} C \nabla.\tilde{u} - \nabla.\tilde{g} - \dot{\tilde{W}}$$

$$= - \tilde{\rho} \tilde{u}.\nabla C - C \tilde{u}.\nabla \tilde{\rho} - \tilde{\rho} C \nabla.\tilde{u} - \nabla.\tilde{g} - \dot{\tilde{W}}$$

hence, $$C \frac{D\tilde{\rho}}{D\tilde{t}} + \tilde{\rho} \frac{DC}{D\tilde{t}} = \tilde{\rho} C \left(\frac{1}{\tilde{\rho}} \frac{D\tilde{\rho}}{D\tilde{t}} \right) - \nabla.\tilde{g} - \dot{\tilde{W}}$$

or, $$\tilde{\rho} \frac{DC}{D\tilde{t}} = - \nabla.\tilde{g} - \dot{\tilde{W}}$$

Then, to arrive at a non-dimensional form, we use the same reference values for $\tilde{\rho}$, $\dot{\tilde{W}}$, and $\tilde{t}$, as above, in addition to : $g = \tilde{g} / (\tilde{d}_r/\tilde{L})$ where $\tilde{d}_r$ is the reference value for $\tilde{d}$. We get,

$$\rho \frac{DC}{Dt} = - \frac{\tilde{d}_r}{\tilde{\rho}_r \tilde{U} \tilde{L}} \nabla.g - \frac{\tilde{L} \tilde{c}_p \tilde{U} \tilde{\rho}_r}{\tilde{k}_r} \dot{W}$$

$$= - \frac{\tilde{c}_p \tilde{d}_r}{\tilde{k}_r} \frac{\tilde{k}_r}{\tilde{c}_p \tilde{\rho}_r \tilde{U} \tilde{L}} \nabla.g - \frac{1}{\lambda} \dot{W}$$

Therefore, as listed in Table 2.1,

$$\rho \frac{DC}{Dt} = - \frac{\lambda}{Le_o} \nabla . \mathbf{g} - \frac{1}{\lambda} \dot{W}$$

A.5 State Equation : Given the dimensional perfect gas equation :

$$\tilde{p} = \tilde{\rho}\tilde{R}\tilde{T}$$

the non-dimensional equation is easily derived by using :

$$\rho = \tilde{\rho} / \tilde{\rho}_r \qquad T = \tilde{T} / \tilde{T}_r \qquad p = \tilde{p} / (\tilde{\rho}_r \tilde{R} \tilde{T}_r)$$

The equation listed in Table 2.1 is then found, namely :

$$p = \rho RT$$

A.6 Arrhenius Equation : For a first or second order chemical reaction (Strehlow, 1984; Fristrom & Westenberg, 1965) the rate constant $\tilde{\xi}$ (s^{-1}) is given quite accurately by the Arrhenius equation :

$$\tilde{\xi} = \tilde{A}\, e^{-\tilde{E}_a/\tilde{R}\tilde{T}}$$

where, $\tilde{A}$ (s^{-1}) and $\tilde{E}_a$ (J/kg) are the frequency factor and activation energy, respectively.

Further, for a simplified version of the combustion process, where we assume a first order irreversible reaction such as : R → P, $\tilde{\xi}$ is defined as:

$$\tilde{\xi} = \frac{-1}{[\tilde{R}]} \frac{d[\tilde{R}]}{d\tilde{t}}$$

where, $[\tilde{R}]$ is the concentration of reactants, in kg/m^3. Then, since,

$$[\tilde{R}] = \tilde{\rho}C$$

and,

$$\dot{\tilde{W}} = \frac{d[\tilde{P}]}{d\tilde{t}} = -\frac{d[\tilde{R}]}{d\tilde{t}}$$

we get, $\tilde{\xi} = \dot{\tilde{W}}/\tilde{\rho}C$. Substituting in the above Arrhenius equation, we arrive at the following dimensional expression:

$$\dot{\tilde{W}} = \tilde{A}\tilde{\rho}C\, e^{-\tilde{E}_a/\tilde{R}\tilde{T}}$$

Then, to arrive at a non-dimensional form, we use,

$$A = \tilde{A}/\tilde{A}_r = \tilde{A}\tilde{k}_r/(\tilde{\rho}_r \tilde{c}_p \tilde{U}^2)$$

$$T_a = \tilde{E}_a/\tilde{R}\tilde{T}_r$$

and the reference value $\dot{\tilde{W}}_r$ defined above. The final equation is as below,

$$\dot{W} = A\rho C\, e^{-T_a/T}$$

as listed in Table 2.1 .

Appendix B

Self Induced Velocity

This section describes the formulation of the self induced velocity of a point vortex in a 2D domain with impermeable walls, when the Schwartz-Christoffel mapping is used to map the flow configuration from the physical plane (w-plane) to the upper half plane (ζ-plane) and to map the flow velocities back from the ζ-plane to the w-plane. This relates to section 3.B in the thesis.

Consider a point vortex with strength Γ_o at $w=w_o$ ($w=x+iy$, $i=(-1)^{1/2}$) in domain D in the w-plane, with boundary ∂D. Let ∂D_1 be the impermeable part of ∂D. Further, let $(u(w),v(w))$ be the velocity field in D having zero normal component along ∂D_1, and circulation Γ_o along curves in D which have w_o in their interior. Let $(u_o(w),v_o(w))$ be the velocity field induced in the w-plane by a free point vortex at w_o.

The self-induced velocity of the point vortex in the presence of impermeable boundaries is then given by :

$$V_o = \lim_{w \to w_o} [\ (u(w)-iv(w)) - (u_o(w)-iv_o(w))\ ] \qquad (B.1)$$

Let $\zeta=\zeta(w)$ ($\zeta=\xi+i\eta$) be a conformal mapping of D onto the upper half plane, ($Im(\zeta)\geq 0$). Then, we have, by potential theory :

$$W(w) = u(w)-iv(w) = \frac{d\zeta(w)}{dw}\ (\mu(\zeta)-i\nu(\zeta)) = F(w)\ S(\zeta) \qquad (B.2)$$

where W and S are the complex velocities in the w and ζ plane respectively. Then we have (sec'n 3.B):

$$W(w) = \frac{-i\Gamma_o}{2\pi}\ \left(\frac{1}{\zeta-\zeta_o} - \frac{1}{\zeta-\zeta_o^*} \right)\ F(w) \qquad (B.3)$$

where, $\zeta=\zeta(w)$, $\zeta_o=\zeta(w_o)$, and "*" denotes the complex conjugate, pertaining to the image of the point vortex with respect to the Real axis in the ζ-plane.

The velocity $(u_o(w),v_o(w))$ due to the free vortex is given by:

$$W_o(w) = u_o(w)-iv_o(w) = -i\Gamma_o/2\pi(w-w_o) \tag{B.4}$$

Then, we write :

$$\begin{aligned} V &= (u(w)-iv(w)) - (u_o(w)-iv_o(w)) \\ &= \frac{-i\Gamma_o}{2\pi}\left(\frac{F(w)}{\zeta-\zeta_o} - \frac{F(w)}{\zeta-\zeta_o^*} - \frac{1}{w-w_o}\right) \\ &= \frac{-i\Gamma_o}{2\pi}\left(\frac{F(w)(w-w_o) - (\zeta-\zeta_o)}{(\zeta-\zeta_o)(w-w_o)} - \frac{F(w)}{\zeta-\zeta_o^*}\right) \end{aligned} \tag{B.5}$$

Using the taylor expansion of $\zeta(w)$ around w_o, we get:

$$\begin{aligned} \zeta-\zeta_o = \zeta(w)-\zeta(w_o) &= \left(\frac{d\zeta}{dw}\right)_{w_o}(w-w_o) + \frac{1}{2}\left(\frac{d^2\zeta}{dw^2}\right)_{w_o}(w-w_o)^2 + O[(w-w_o)^3] \\ &= F(w_o)\ (w-w_o) + \frac{1}{2}F'(w_o)\ (w-w_o)^2 + O[(w-w_o)^3] \end{aligned} \tag{B.6}$$

where, $F'=dF/dw$. Substituting in the numerator of the first term above, we get :

$$V = \frac{-i\Gamma_o}{2\pi}\left(\frac{\frac{F(w)-F(w_o)}{w-w_o} - \frac{1}{2}F'(w_o) - O(w-w_o)}{\frac{\zeta-\zeta_o}{w-w_o}} - \frac{F(w)}{\zeta-\zeta_o^*}\right) \tag{B.7}$$

Hence, in the limit as w tends to w_o, V tends to V_o, as in eq. (B.1), i.e. :

$$V_o = \frac{-i\Gamma_o}{2\pi}\left(\frac{1}{2}\frac{F'(w_o)}{F(w_o)} - \frac{F(w_o)}{\zeta-\zeta_o^*}\right) \tag{B.8}$$

but, $$\frac{F'(w)}{F(w)} = \frac{dF/dw}{d\zeta/dw} = \frac{dF(w)}{d\zeta} \tag{B.9}$$

then,

$$V_o = \frac{-i\Gamma_o}{2\pi} \left[\frac{1}{2} \left(\frac{dF}{d\zeta}\right)_{w=w_c} - \frac{F(w_o)}{\zeta-\zeta_o^*} \right] \tag{B.10}$$

The second term on the right is due to the image vortex in the ζ-plane, while the first term is the one referred to in eq. (3.).

It is noted that we have based the above discussion on a point vortex concept, while the computational elements used in this work are vortex blobs with a specified cutoff radius δ. This is not inconsistent when δ is smaller than the distance from the blob to the nearest domain wall, because the self induced complex velocity V_o is due solely to the presence of the walls. The wall velocities, computed at a distance r from the vortex element, are identical whether one is using a point vortex or a blob model, as long as $r > \delta$ (nb. $\kappa(r/\delta)=1$ for $r > \delta$).

Appendix C

Potential Flow Solution given an Expansion field in an Unbounded Simply Connected Domain

This discussion concerns the solution of the poisson eq. (3.42b). Namely, the solution for the potential function ϕ_e on an unbounded simply connected domain, where :

$$\nabla^2\phi_e = (QS_u/T_u)\ \delta(x-\chi_f) \tag{C.1}$$

given that $u_e=\nabla\phi_e \to 0$ as $x\to\infty$.

This solution, is given by:

$$\phi_e(x) = \int_A G(x-x')\ (QS_u/T_u)\delta(x'-\chi_f)\ dA \tag{C.2}$$

where $x=(x,y)$, $r=|x|$, $G(x) = \ln(r)/2\pi$ is the Green function, $dA=dx'dy'$, and the integral is taken over an area A that contains the flame interface defined by the surface $\chi_f(t)$.

The corresponding velocity field, u_e, is given by :

$$\begin{aligned} u_e = \nabla\phi_e &= \int_A K(x-x')\ (QS_u/T_u)\delta(x'-\chi_f)\ dA \\ &= \int_A K(x-x')\ \varepsilon(x')\ dA \end{aligned} \tag{C.3}$$

where

$$K(x) = \nabla G(x) = (x,y)/2\pi r^2 \tag{C.4}$$

Let us approximate the integral (C.3), analogous to eqs. (3.19) (3.23), by a summation over elemental areas A_j containing the flame interface (see also Ghoniem et. al., 1982; Chorin, 1973). Hence,

$$u = \sum_{j=1}^{N} K(x-x_j)q_j \tag{C.5}$$

where,

$$q_j = \int_{A_j} \varepsilon(x')\, dA \tag{C.6}$$

and x_j is the center of gravity of the section of the flame interface lying in area A_j. By eqs. (C.5) and (C.4), the velocity due to the expansion field from one elemental area A_j is :

$$u_j = K(x-x_j)q_j = q_j\, r_j/2\pi|r_j|^2 \tag{C.7}$$

where $r_j = x-x_j$. This is the flow field due to a 2D potential point source of strength q_j at x_j (see Potter & Foss, 1982). Hence, q_j, which is the total rate of expansion in area A_j, can be lumped in one point source j located at x_j, and the summation (C.5) is done over a finite set of point sources along the flame interface.

Therefore, the solution of eq. (C.1) in an unbounded simply connected domain is given by the velocity field (C.5) due to a set of point sources of strengths q_j located along the flame front. The evaluation of the value of q_j is done in section 3.3.2 above.

In order to guarantee a finite velocity field, as was done with the vorticity field, we use "source blobs" instead of point sources, hence we replace the point source kernel $K(x)$ defined in eq. (C.4) by the modified kernel $K_c(x)$ defined by :

$$K_c(x) = K(x)\ \min(1, r/c) \tag{C.8}$$

where $r=|x|$, and c is the cutoff (core) radius of the source blob. c_j is determined from a specified maximum allowed velocity due to a source (V_m) by:

$$c_j = q_j/2\pi V_m \tag{C.9}$$

The specification of V_m is discussed in section 3.3.2 above.

The velocity due to a collection of N source blobs is thus given by :

$$u_e = \sum_{j=1}^{N} u_{ej} = \sum_{j=1}^{N} \frac{q_j}{2\pi} \frac{r_j}{|r_j|^2} \min(1, |r_j|/c_j) \tag{C.10a}$$

$$= \sum_{j=1}^{N} \frac{q_j}{2\pi} \frac{r_j}{|r_j|^2} g(|r_j|/c_j) \tag{C.10b}$$

where

$$g(r) = \begin{cases} 1 & r > 1 \\ r & r \le 1 \end{cases} \tag{C.11}$$

i.e.

$$u_{ej} = \begin{cases} \dfrac{q_j}{2\pi} \dfrac{r_j}{|r_j|^2} & \text{for } |r_j| > c_j \\ \dfrac{q_j}{2\pi c_j} \dfrac{r_j}{|r_j|} & \text{for } |r_j| \le c_j \end{cases} \tag{C.12}$$

or, if we use polar coordinates (r,θ) centered at source k, then

$$u_{ej} = (u_r, u_\theta) = \begin{cases} q_j/2\pi r & \text{for } r > c_j \\ q_j/2\pi c_j = V_m & \text{for } r \le c_j \end{cases} \tag{C.13}$$

Appendix D

Oscillator Response to the Combustor Dynamics

The interaction between the combustor and the oscillator is a complex process that involves coupling between the combustor dynamics and the "acoustic" characteristics of the inlet and exhaust manifolds, which we lump in one unit as an "oscillator". In actual systems, this coupling is observed to result in pressure oscillations that invariably migrate to lower frequencies as the rate of heat release is increased, leading eventually to large amplitude, low frequency oscillations that can cause inlet flow reversal and flame flashback.

The 1D downstream channel model developed in Chapter 3 is implemented here to examine some of the basic features of this coupled system. This study is intended to shed some light on the complex combustor-system coupling in real systems. In particular, we wish to identify the mechanism by which the oscillator amplifies the perturbation generated within the combustor in the form of vorticity and heat release time variation and to determine the response frequency of the oscillator.

This 1D oscillator has been studied separately before coupling it with the combustor. This involved examining its response to specified input flow rate functions. The results exhibit typical properties of a forced oscillator. For a given forcing function, the response includes a transient period before the system settles into a stationary phase. In the transient phase the response is a combination of the natural fundamental frequency of the oscillator along with the forcing frequency and the harmonics of each. Once the system reaches a stationary state, the natural response dies out leaving the forcing frequency and its harmonics. The natural frequency is

determined by the "mean" sonic speed, c_o, and the oscillator length L_o. Given our boundary conditions, explained in Chapter 3, the natural fundamental frequency corresponds to a 1/4 wavelength mode along the length of the oscillator, such that $f_n=c_o/4L_o$. Hence,

$$\frac{f_n D}{U_r} = \frac{c_o/U_r}{4\ (L_o/D)}$$

With this in mind, we now consider the coupling between the two systems, the oscillator and the combustor.

At the outset, we recall the coupling between the combustor and the oscillator used in this model. The exit flow rate from the combustor, Q_{out}, is the inlet flow to the downstream 1D channel (oscillator), while the pressure computed from the oscillator flow at its inlet specifies p_{ex} at the combustor exit. For Q_{out} positive, the temperature at the oscillator inlet is specified as the temperature of the products, T_b, which is a constant.

Let us examine a flow case with relatively low heat release. Of primary interest is the frequency of velocity and pressure oscillation in this coupled system, as well as the associated flow dynamics in the combustor.

We use the same reference quantities described above. We also specify the temperature of the reactants T_u=293 K, the gas constant R=287 mN/kgK, and the ratio of specific heats $\gamma=c_p/c_v$=1.4. The combustor geometry is also as above : xmin/D=-4, xmax/D=4, H/D=2, and L/D=4. The flow parameters are given by : $Re_u=10^4$, p_o/p_r=0.375, S_u/D=0.05, and ρ_u/ρ_b=1.5. The length of the oscillator is : L_o = 1.5 meters, or L_o/D=60. The corresponding fundamental natural frequency of the oscillator is found to be: f_nD/U_r=0.267. Relevant numerical parameters are : h_s/D=0.25, Δ_s/D=0.0079, Γ_m/U_rD=0.025, and $\Delta tU_r/D$=0.05, for the combustor flow. In the oscillator, we use $\Delta x/D$=0.870, and $\Delta tU_r/D$=0.0125, such that the usual CFL condition is satisfied at all x and t.

Let us examine first the time traces of the step and exit pressures, shown in Fig. D.1, and the inlet flow rate into the combustor in Fig. D.2a. The amplitude of the pressure oscillation is seen to grow slowly with time reaching values of $\pm 15 p_r$ at the combustor exit after 2000 time steps (time 100). Similar behaviour is exhibited by the flow rate oscillation. This growth seems to be a result of resonance involving the coupled system dynamics. Because of the slow growth rate associated with the long transient of this undamped oscillator, and given the computational facilities at our disposal, it was not possible to run the code for sufficiently long time to achieve a stationary state in terms of the global elements of the flowfield, such as the pressure and the flow rate. On the other hand, as we shall see below, the flow velocities in the cavity exhibited relatively stationary behaviour associated with the shedding of vortex eddies and the oscillation of the flame front.

The frequency spectra of the pressure and flow rate traces are shown in Figs. D.2b and D.3. These are computed for time 10 to 100, where the mean inlet velocity was : $U/U_r=0.75$. The Strouhal number in the spectra is $St=fD/U$. We recall, the combustor natural instability frequency is given by $St=fD/U=O(0.1)$. The oscillator fundamental frequency, given this scaling, is found to be such that $St=fD/U=0.356$. Clearly, neither frequency is evident in the pressure and flow rate spectra. Instead we observe a set of four large amplitude peaks at frequencies given by : $St=fD/U=$ 0.593, 1.230, 1.881, and 2.548. The last three Strouhal numbers are harmonics of the fundamental at 0.593, being related to it roughly through multiplication by 2, 3, and 4. They are clearly characteristics of the full coupled system involving the oscillator, the combustor, and the upstream reservoir inlet.

Given the p_{ex} spectrum in Fig. D.3b, we expect the cavity flowfield to look somewhat similar to that observed under high frequency forcing in

section 5.2.2, where the natural dynamics of the recirculation zone in the dump persisted, albeit being damped compared to the low frequency forcing case, while small shear layer eddies were shed at the high forcing frequency. The sequence of frames in Fig. D.4a illustrates the organized shear layer eddy shedding at a period of ~ 2-2.5 which corresponds to the dominant high frequency peak at St=0.6, while those in Fig. D.4b show the large recirculation zone eddy shedding in the dump. These frames exhibit dynamics similar to those observed in the high frequency forcing, low heat release, results in Fig. 5.33b. The corresponding velocity traces at $x/D=\pm 1$, $y/D=1$, are shown in Fig. D.5, and their spectra are shown in Fig. D.6. Remarkably, and as observed earlier in the high frequency forcing study in Fig. 5.35, these spectra exhibit dominant peaks in the low frequency range, corresponding to the natural recirculation zone shedding, at $St=fD/U=O(0.1)$, as opposed to the high forcing frequency range. They reflect the local vorticity dynamics more so than the global flow rate fluctuation. The dominant low frequency peak is at $St=fD/U=0.074$, which corresponds to $fD/U_r=0.056$, or a time period of 18. This period is consistent with the shedding observed in the frame sequence in Fig. D.4b.

The correspondence between the rate of heat release and the overall flame length is observed in the time traces shown in Fig. D.7. The large amplitude, low frequency oscillations evident in the heat release and flame length traces correspond to the recirculation zone eddies in the combustor. The frequency spectrum of the heat release trace is shown in Fig. D.8. As expected from the corresponding time trace, the dominant peaks are at low frequencies, around 0.1. This low frequency dominance under high frequency exit pressure oscillation has been observed in our forced study above, see Figs. 5.24 and 5.31. The heat release fluctuation at high frequencies is, by necessity, of small amplitude because high frequency perturbations of the

flame interface, which are associated with the shedding of shear layer eddies, are small with respect to the those associated with the shedding of recirculation zone eddies, at low frequency.

Finally, we present the time trace and frequency spectrum of the exit flow rate from the combustor, Q_{out}, shown in Fig. D.9. The oscillation of Q_{out} is similar to that seen with Q_{in} in Fig. D.2. The spectra of each exhibit the same "high" St peaks associated with the coupled system, with relatively insignificant oscillation at the low natural frequency of the combustor. We also observe that the amplitude of the Q_{out} oscillation is seen to grow with time, as expected from the similar growth of Q_{in}. Again we note that no stationary state oscillation was reached, given our limited computational resources.

The present model has been useful for observation of the basic coupled system properties. The fact that the oscillator response causes oscillation of the combustor exit pressure at well defined frequencies supports the relevance of the modulation/forcing study in Chapter 5 as a means of studying the combustor response under specified system conditions. Also of interest is the origin of the coupled system dominant frequency of 0.6. The selection of this frequency involves the various system components, namely the oscillator, the vorticity and flame dynamics in the dump, and the upstream reservoir.

We note on the other hand, that a stationary state corresponds to a more realistic operating situation than the transient phase, and is necessary for studying the physical characteristics of the coupled system under specified conditions. The introduction of a certain amount of damping into the oscillator model may be considered as a possible means of shortening the transient. The only diffusion in the present model is numerical, associated with the discretization of gradients on a finite grid.

The oscillator model can be also improved by implementing a more detailed coupling at the combustor exit. In particular, the specification of a constant temperature, T_b, can be improved upon. The mixture leaving the combustor at xmax includes both reactants and products, and the relative percentage of each can be used to compute the mean temperature of the fluid at the oscillator inlet at each time step.

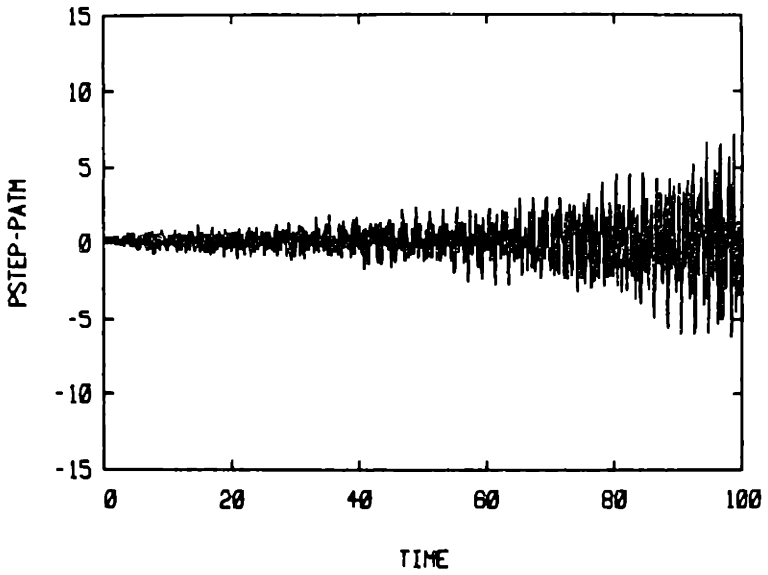

(a)

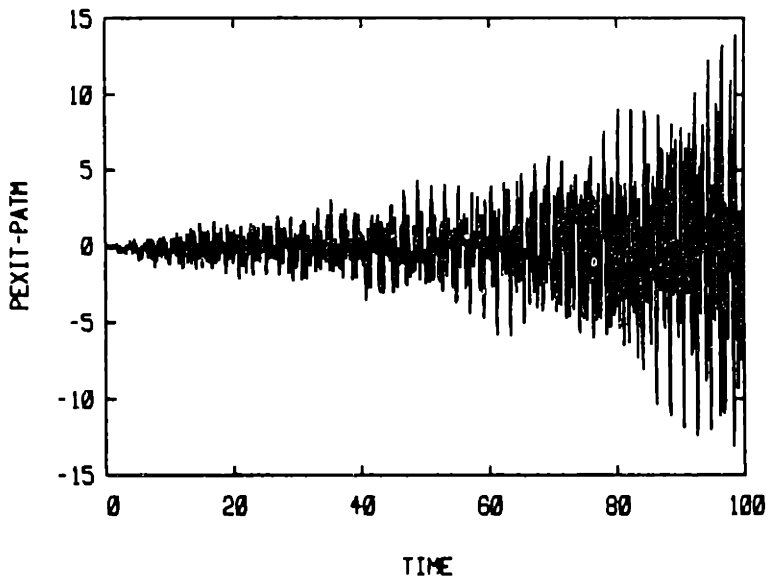

(b)

Figure D.1 The pressure trace (channel centerline) at the upstream step (a) and the exit pressure trace (b) plotted versus time, for the flow of Fig. D.4 below.

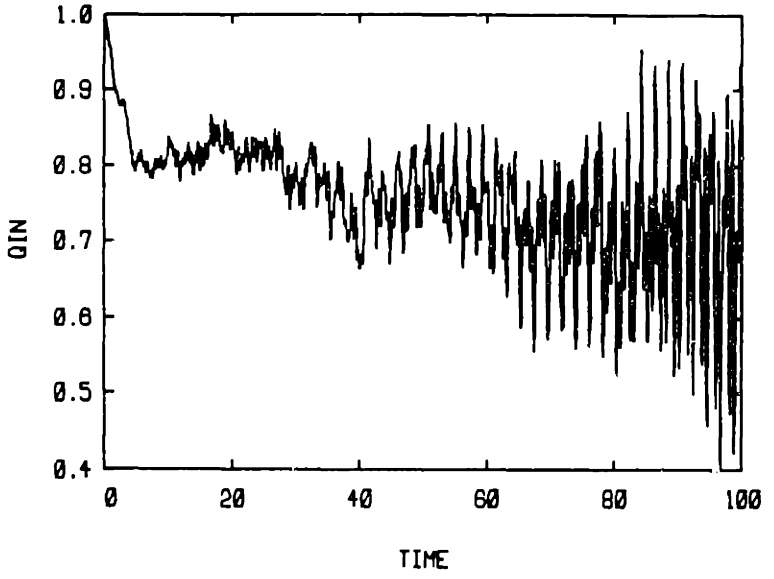

(a)

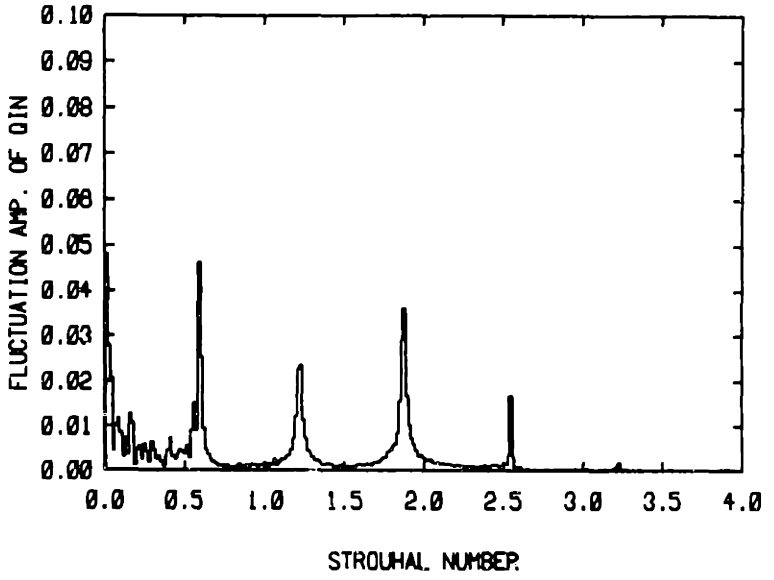

(b)

Figure D.2 The time trace (a) and the spectrum (b) of the inlet flow rate at xmin, for the flow of Fig. D.4 below. The mean flow rate for the time period from 10 to 100 is 0.75. The Strouhal number is St=fD/U.

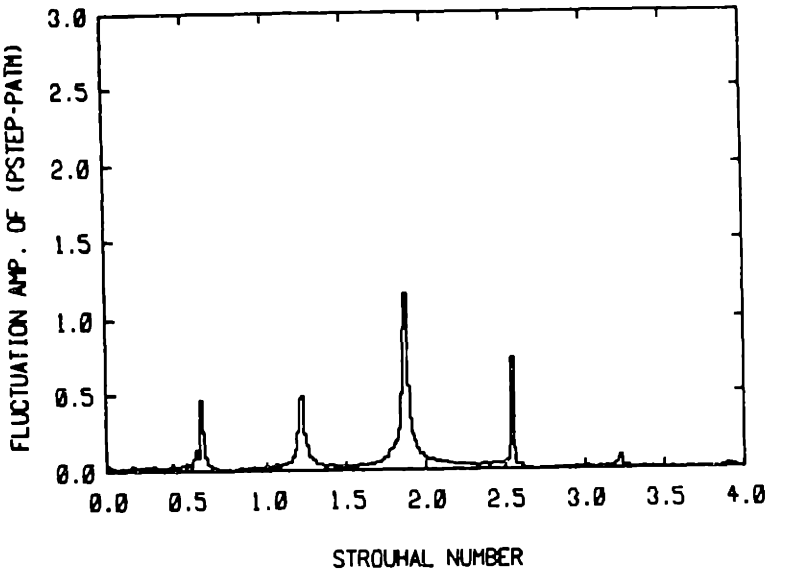

(a)

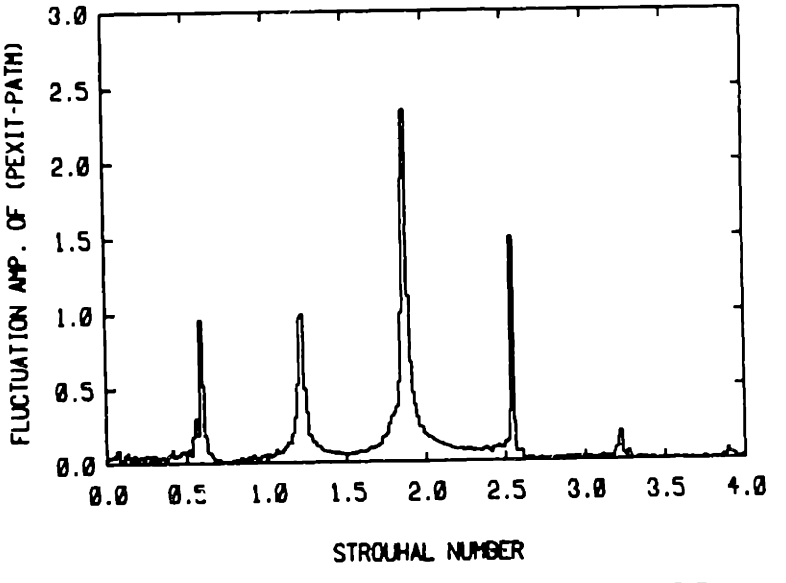

(b)

Figure D.3 The spectra of the step pressure (a) and the exit pressure (b), for the flow of Fig. D.4 below. The Strouhal number is St=fD/U.

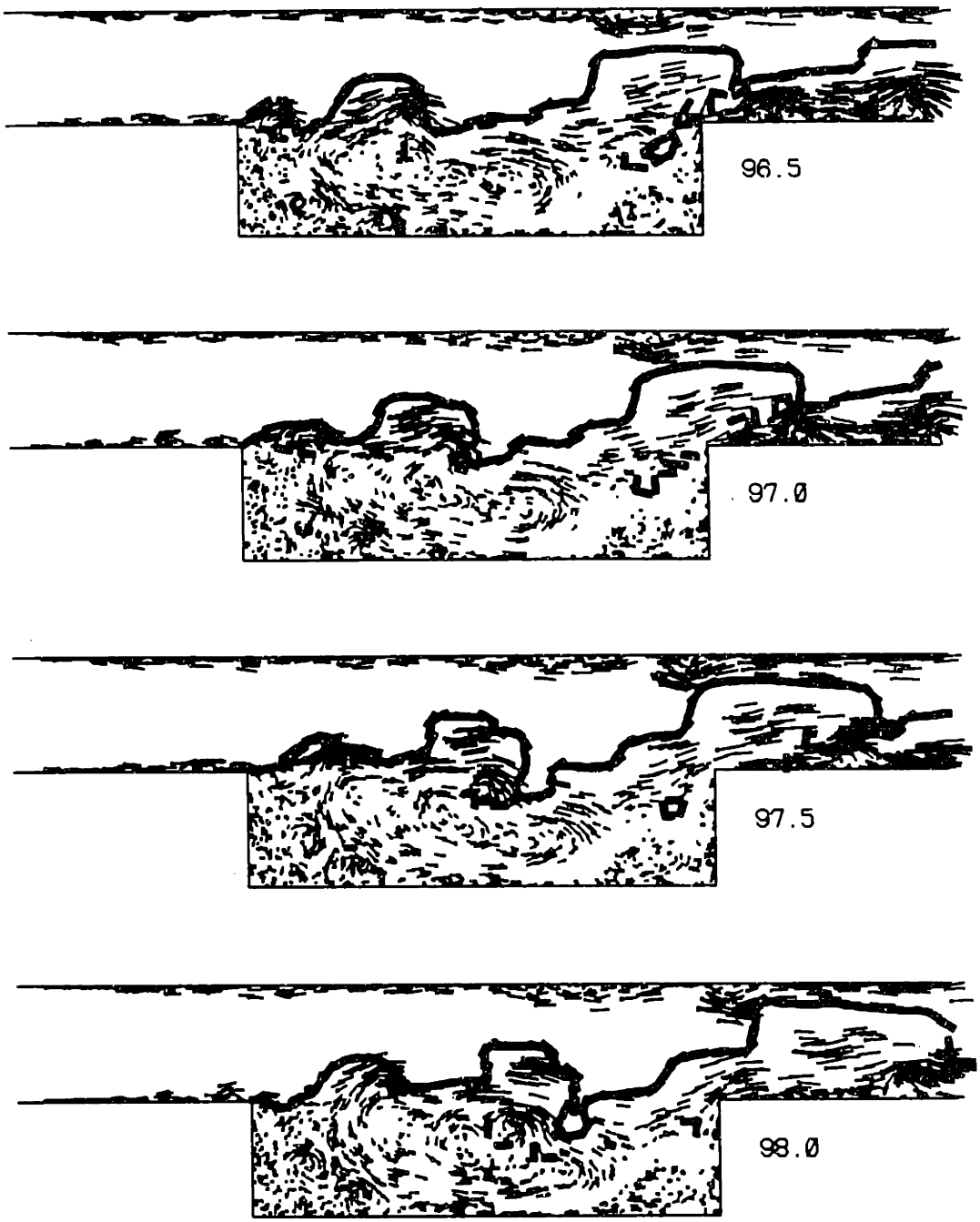

Figure D.4a For caption see next page.

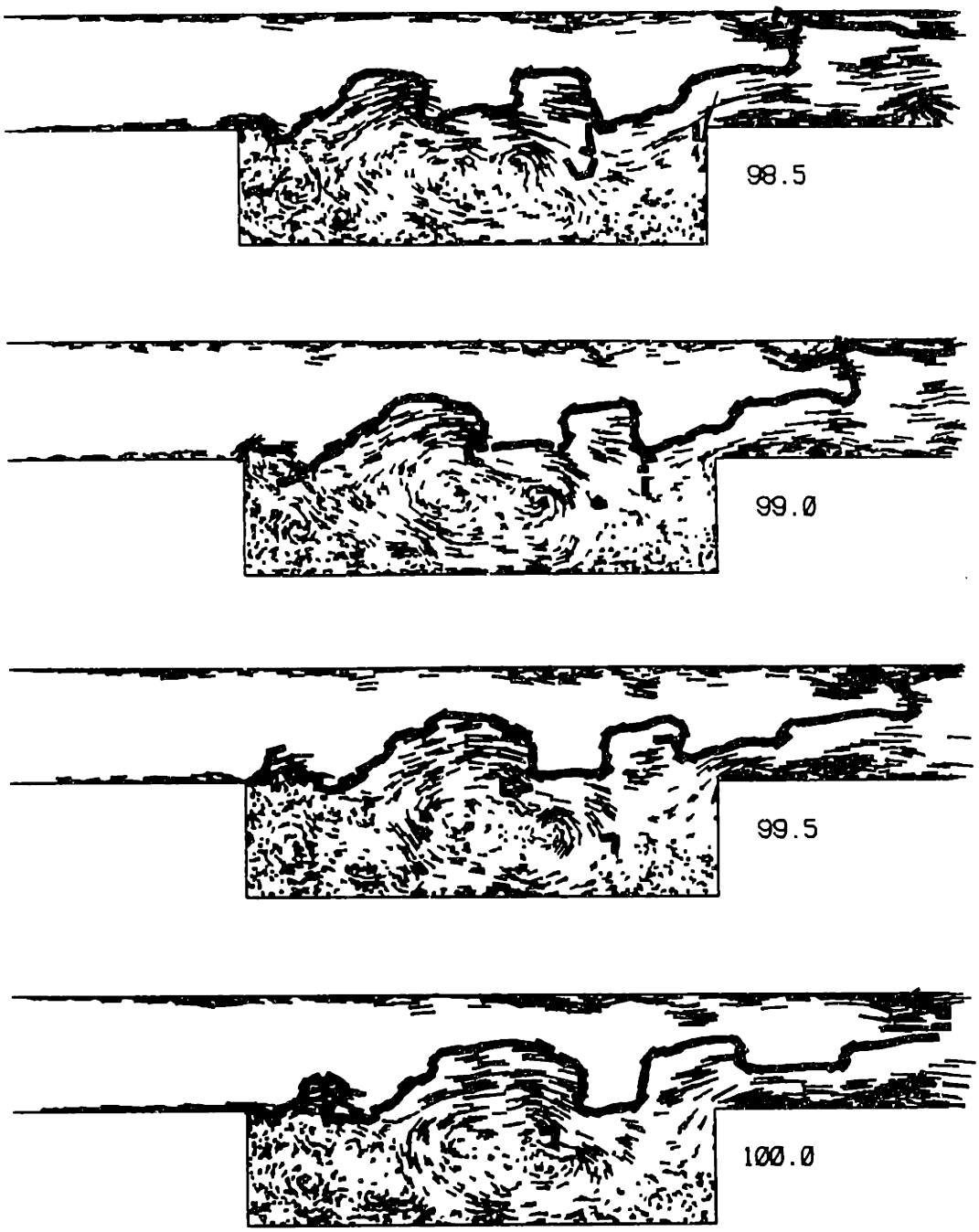

Figure D.4a A sequence of time frames of the combustor flow field with the exit pressure provided by the 1D oscillator, illustrating the fast shear layer eddy shedding at the dominant high frequency of pressure and flow rate oscillation, fD/U_r=0.44, i.e. with a period of 2.25.

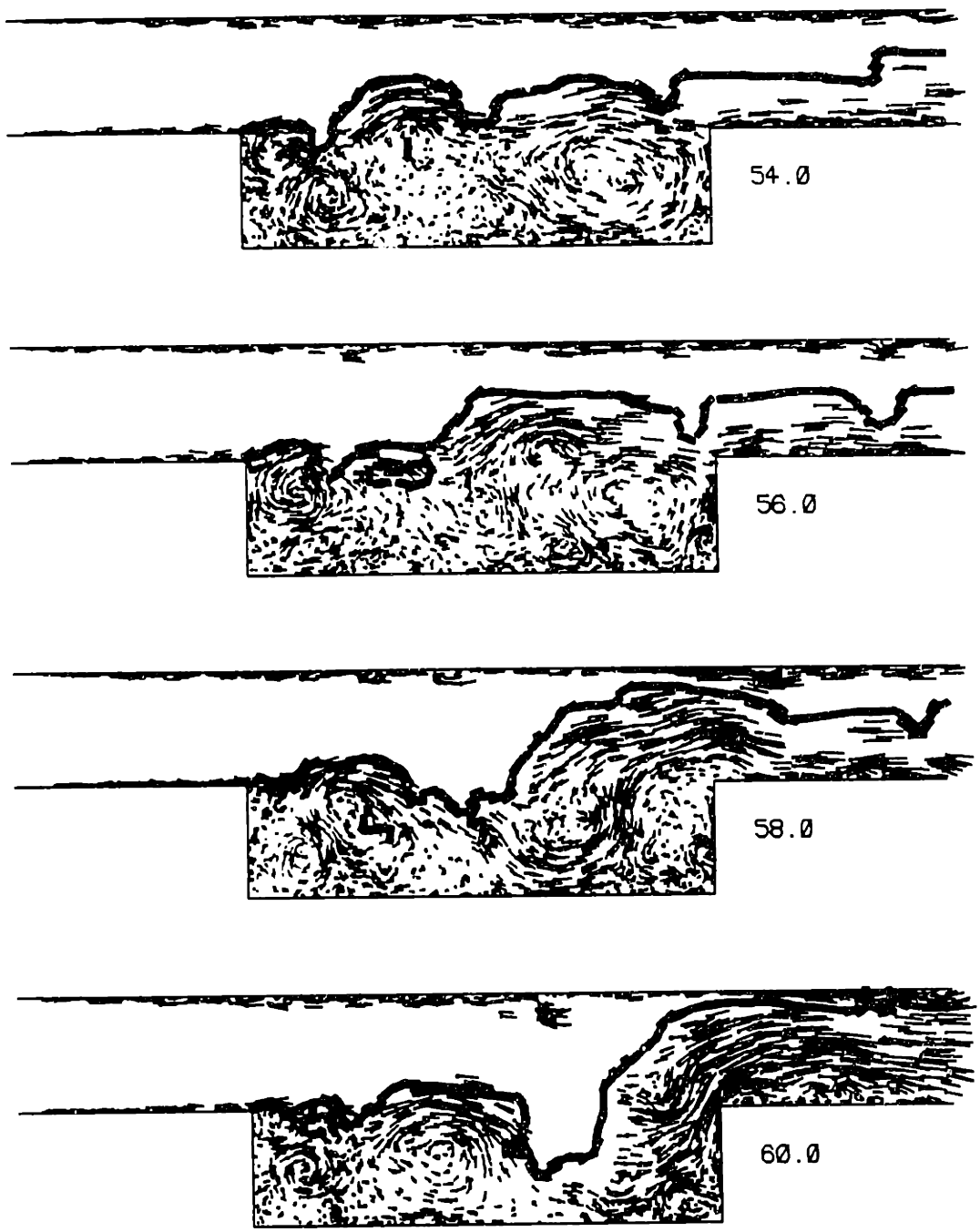

Figure D.4b Continued on next page, caption at end of sequence.

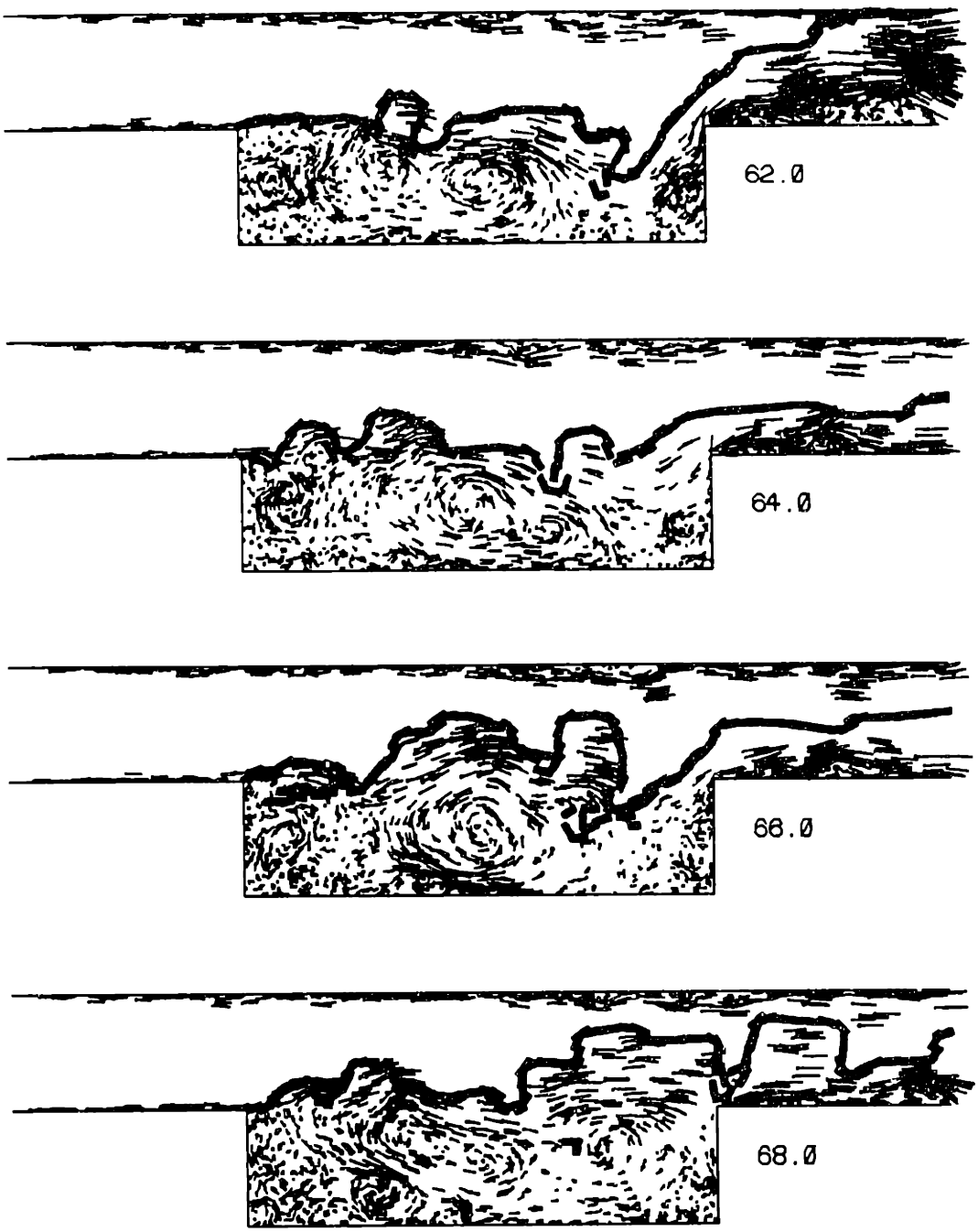

Figure D.4b Continued on next page, caption at end of sequence.

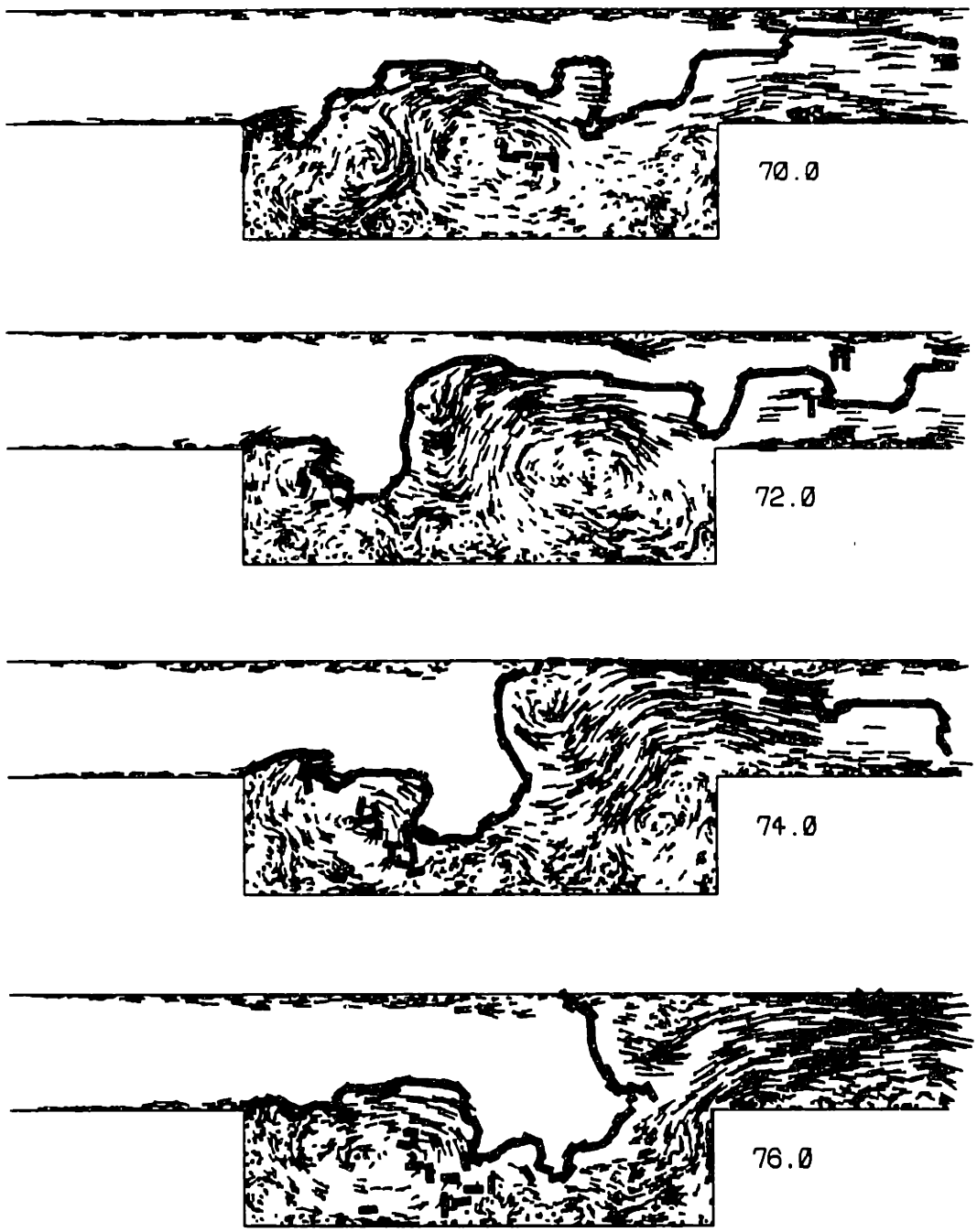

Figure D.4b For caption see next page.

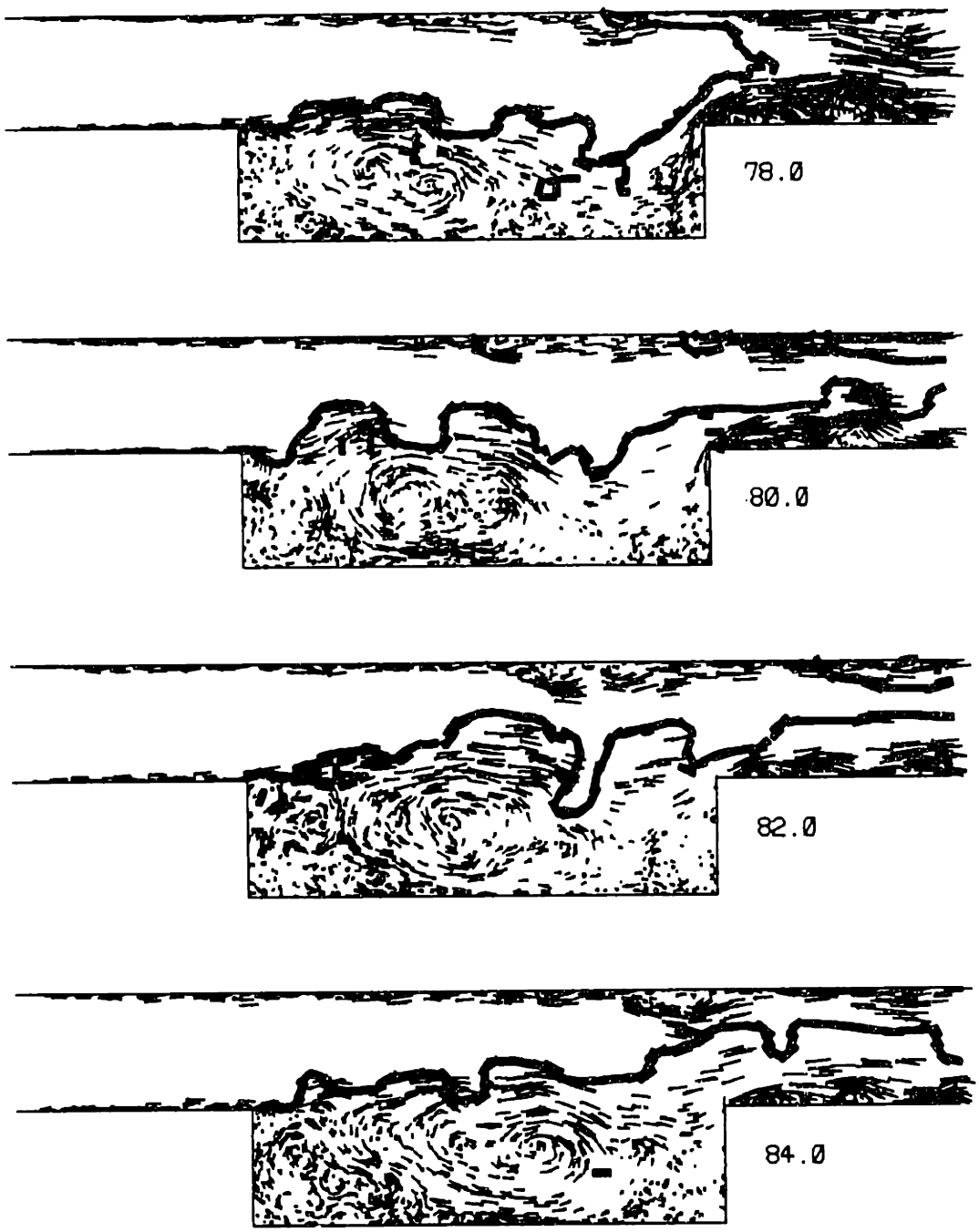

Figure D.4b A sequence of time frames of the combustor flow field with the exit pressure provided by the 1D oscillator, illustrating the relatively stable large eddy shedding, similar to the low heat release, high frequency forcing results.

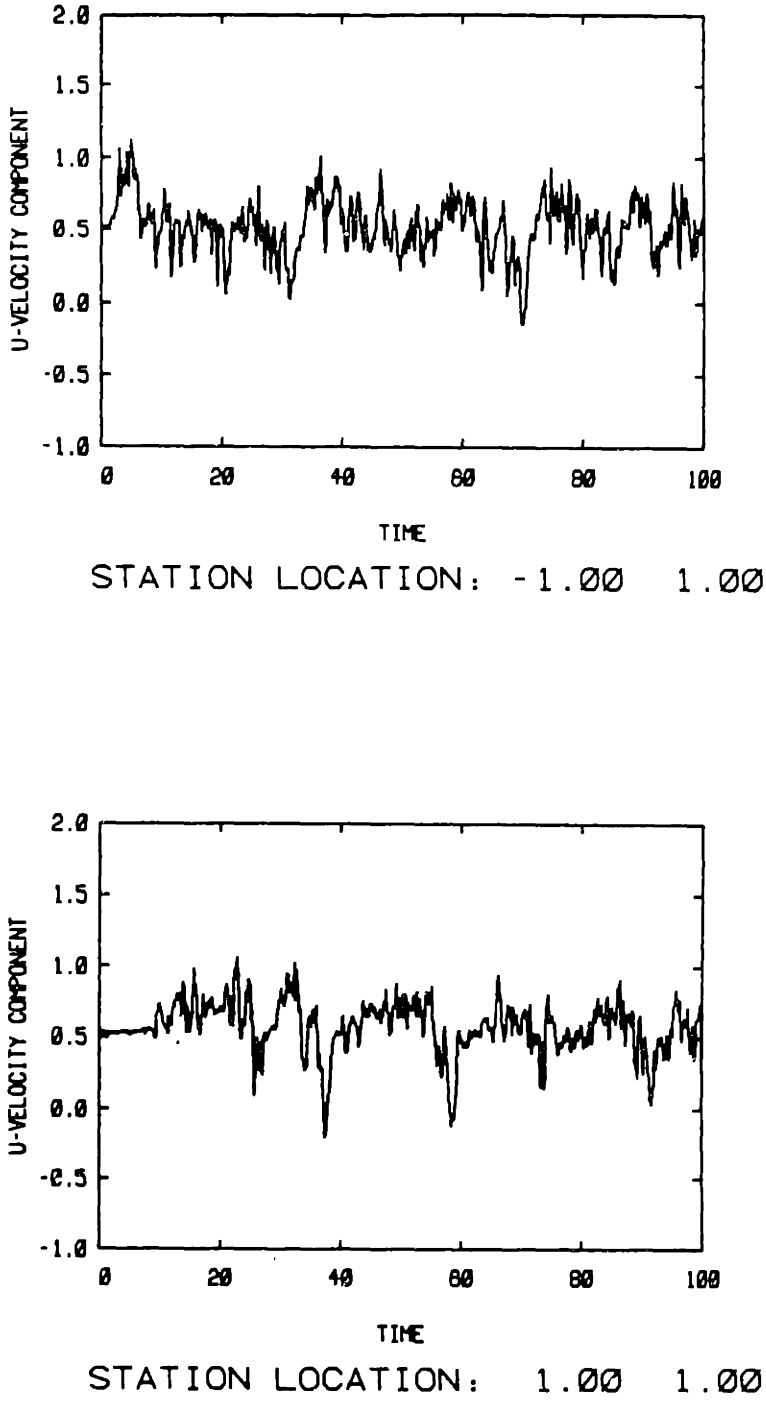

Figure D.5 Time traces of the streamwise velocity at two points along the top of the cavity, for the flow field of Fig. D.4. The numbers identifying the station location are the x and y coordinates, respectively.

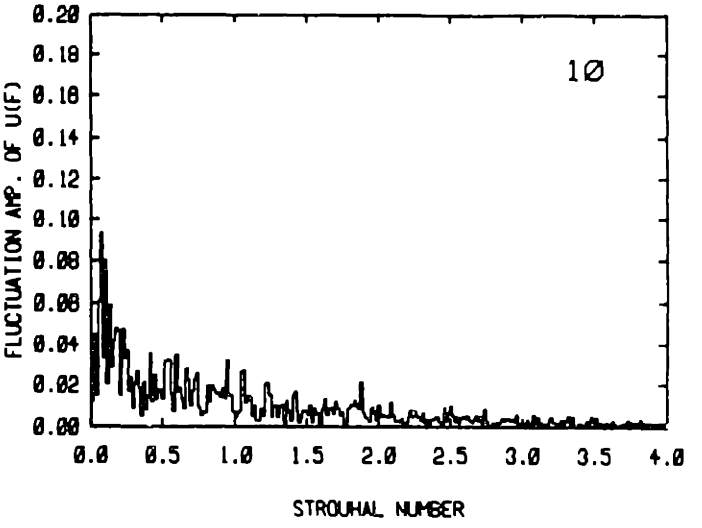

X= -1.000, PEAKS= Ø.Ø74 Ø.1Ø4 Ø.133

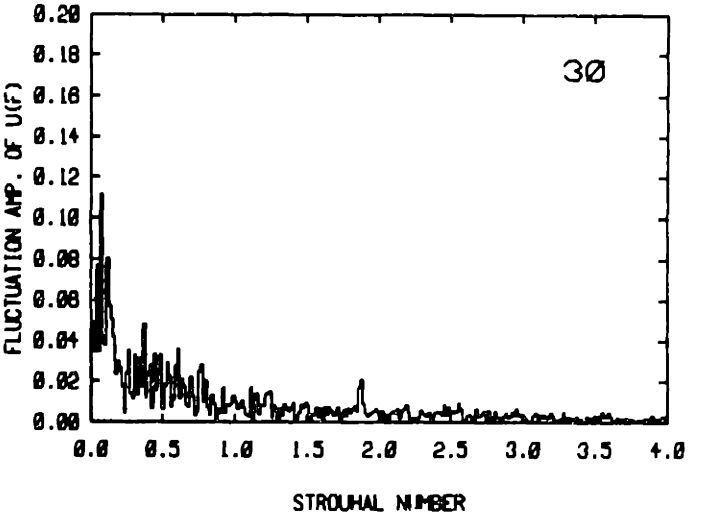

X= 1.000, PEAKS= Ø.Ø74 Ø.119 Ø.Ø44

Figure D.6 Spectra of the streamwise velocity fluctuation computed from the time traces in Fig. D.4, for the time period 10-100. The Strouhal number is based on the cavity depth and the mean inlet flow velocity for the time period considered.

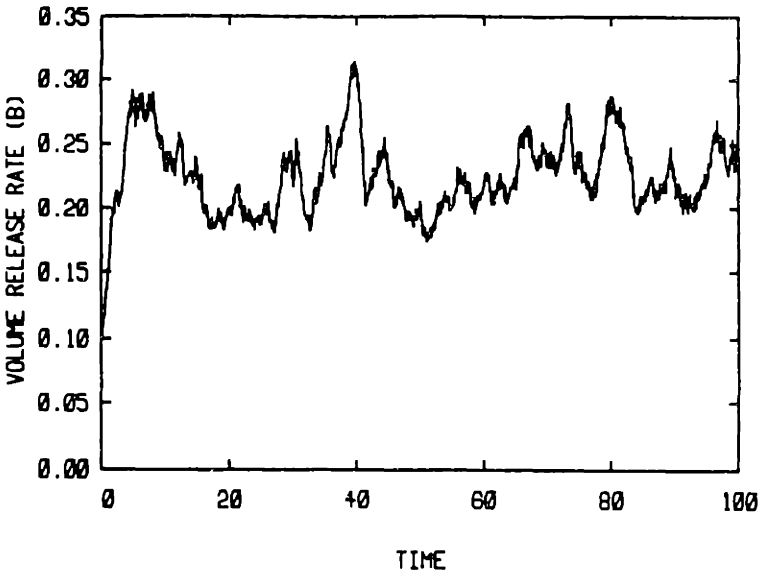

(a)

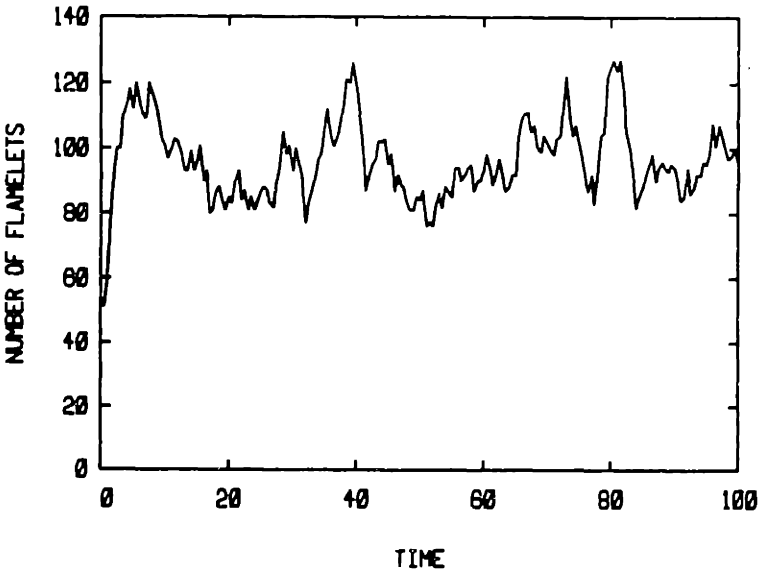

(b)

Figure D.7 The rate of volume release (heat release) in the combustor (a), and the total number of flame segments (b), plotted against time, for the flow field of Fig. D.4.

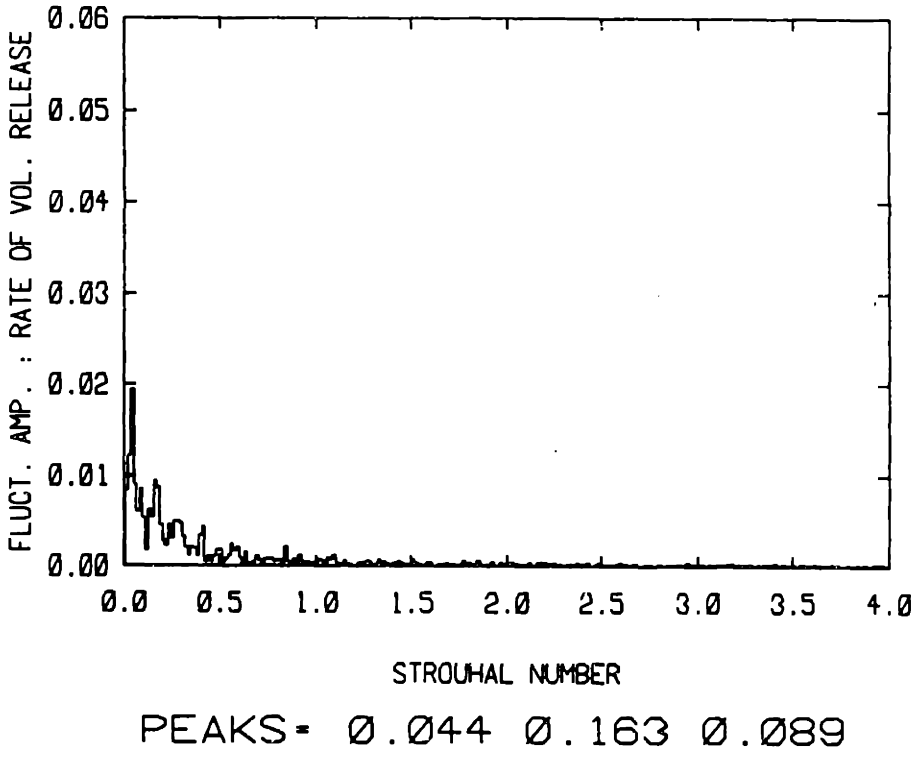

Figure D.8 Spectrum of the rate of heat release fluctuation computed from the trace in Fig. 5.7a, for the time period 10 to 100. The Strouhal number is based on the cavity depth and the mean inlet flow velocity.

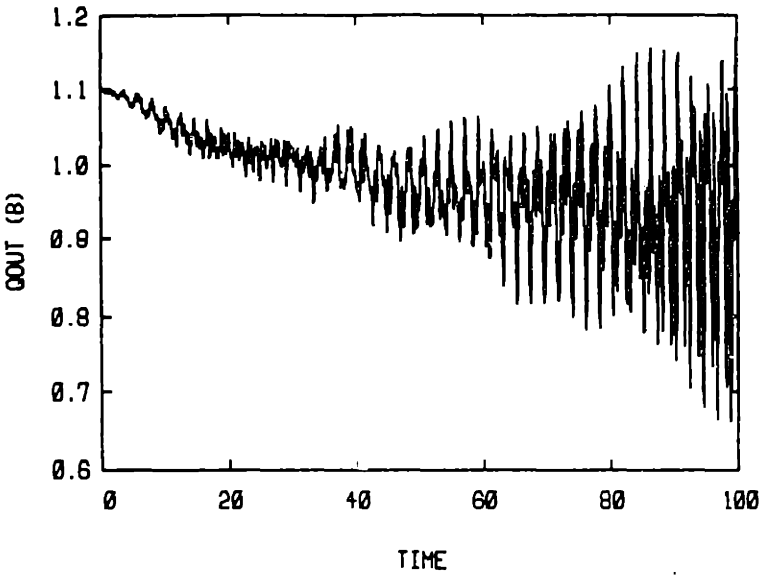

(a)

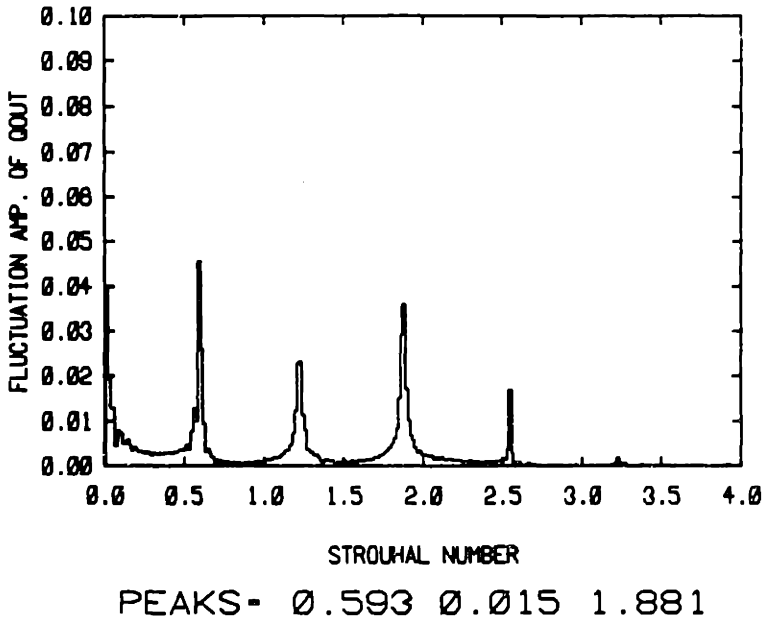

(b)

Figure D.9 The time trace (a) and spectrum (b) of the exit flow rate from the combustor, for the flow in Fig. D.4. The spectrum is based on the time period 10 to 100. The Strouhal number is based on the cavity depth and the mean inlet velocity.